SAPIENZA
UNIVERSITÀ DI ROMA

Faculty of Civil and Industrial Engineering

Department of Structural and Geotechnical Engineering

Damage Sensitive Features From Classic Parameters to New Indicators

PhD Candidate
Eleonora Maria Tronci

Advisor:
Prof. Maurizio De Angelis

Co-Advisor :
Prof. Raimondo Betti

Rome, June 2019

Abstract

Structural Health Monitoring (SHM) is the discipline that concerns about the health condition of engineering structures, mechanical systems, aerospace models, at every moment during their utility life. The primary object of SHM is to spot damage, if present, in the observed system and give a consequent diagnosis. Damage can be considered as a variation in the properties of the system that permanently affects the performance of the structure. This variation is meaningless unless contextualized as a comparison between two different states: damaged and healthy. It is precisely this deviation from normal conditions that approaches like vibration-based algorithms are looking for. Vibration-based SHM aims to implement a strategy to correctly detect damage through the assessment of changes in the identified vibration response of civil structures. The structural response is represented, employing a compact representation of its primary traits, called damage sensitive features (DSFs). It can be stated, therefore, that the effectiveness of vibration-based methodology in identifying damage depends on the robustness of the chosen DSFs. They need to be sensitive enough in spotting anomalies in the structural behavior, but at the same time, they need to be insensitive as much as possible towards temporary or seasonally variation of the structural properties that fall into the common behavior of structural systems.

In this dissertation, two typologies of DSFs are investigated: the first type, well known in the SHM research community, is derived from the response of the system using user's dependent extraction algorithms, while the other is directly computed from the response of the system using digital signal processes alone. In both approaches, the effects of external conditions, like the seasonal variation of air temperature, are accounted for. Within the first kind of DSFs, an automated procedure is proposed to reduce the interdependency of the algorithm from the user's abilities, leading to a robust identification procedure, more suitable for long-term monitoring purposes. The second health indicator here proposed offers a very low-burden computation cost, with almost non-existing dependency from the user and its extraction process makes these features less sensible to external variation like temperature. The two DSFs and the associated extraction processes are investigated and validated both numerically and experimentally.

Experience is simply the name we give our mistakes.
Oscar Wilde

Acronyms

ADF	Augmented Dickey-Fuller
ASE	Audio Spectrum Envelope
AR	Auto-Regressive
AVT	Ambient Vibration Test
CC	Cepstral Coefficient
Cov-SSI	Covariance-Stochastic Subspace Identification
DBSCAN	Density-Based Spatial Clustering of Applications with Noise
DD-SSI	Data-Driven Stochastic Subspace Identification
DSF	Damage Sensitive Feature
EMA	Experimental Modal Analysis
FEM	Finite Element Model
FT	Fourier Transform
FVT	Forced Vibration Test
GK	Gaussian Kernel
HVC	Hard Validation Criteria
IDCT	Inverse Discrete Cosine Transform
LK	Linear Kernel
MFCC	Mel-Frequency Cepstral Coefficient
MPEG	Moving Picture Experts Group
MSD	Mahalanobis Square Distance
NASE	Normalized Audio Spectrum Envelope
NC TMD	Non-Conventional Tuned Mass Damper
OMA	Operational Modal Analysis
PS	Power Spectrum
RVM	Relevance Vector Machine
SPR	Statistical Pattern Recognition
SSI	Stochastic Subspace Identification
SVM	Support Vector Machine
SVR	Support Vector Regression
SHM	Structural Health Monitoring
TMD	Tuned Mass Damper
VAR	Vector AutoRegression

Contents

List of Figures

List of Tables

Chapter 1

Introduction to Structural Health Monitoring

Structural Health Monitoring (SHM) is, in short, any automated monitoring practice that seeks to assess the condition or health of a structure. Its beginnings as an area of interest to engineers can be traced back as far as the time when tap-testing for fault detection became common, although the field did not really become established in research communities until the 1980s, when much interest was generated in the structural condition of oil rigs, and later in aerospace structures and their health. Nowadays, SHM is a popular and still growing research field, which is more and more becoming a focus of the civil infrastructure community.

This chapter aims to provide a general overview of SHM. The potential benefits of implementing SHM within a Statistical Pattern Recognition (SPR) framework will be outlined before discussing the common issues arising when attempting to create/implement such a system.

1.1 What is SHM?

This dissertation focuses on the key role of the indicators chosen to represent the health status of structures within SHM. We talk about SHM every time that the objective of the investigation is assessing the health condition of a system under observation that could suffer from some malfunctioning. Therefore, SHM methodologies have been implemented for different kind of systems: civil structures, mechanical and aerospace models. The work concentrates on civil structures, but

many topics and methodologies addressed in this work are interdisciplinary and come from different expertise areas and therefore, can be as well transferred to different research areas.

SHM takes care of identifying damage in civil structures and gives informed decisions about their health condition along with their service life. Accurate and updated information about the performance level of a building or a bridge, implemented within a real-time damage assessment framework, can promptly alert the community that infrastructure is serving towards immediate danger. Moreover knowing the actual condition of the structure allows to design optimized extraordinary maintenance plans, update the ordinary ones, and coordinate regular inspections to report the condition of the infrastructure.

SHM approaches have been in constant evolution for decades; indeed, on the one hand, they are designed for structures which evolve in turn and on the other, they need face the continuous upgrade of the sensor technology and data analytics. Nowadays, structures are build in a *Big-Data* scenario (Alampalli et al. 2016), where many measurements related to the response of structures and their health conditions can be easily collected. The innovation stays in finding methodologies to efficiently analyze and read the data collected to improve the safety conditions of the infrastructures and of the community that uses them.

Considering the crucial role that infrastructures play in our lives, it is essential to carry on this check up on their health status, trying not to interfere with their ordinary performance. Sensor technology allows us to equip structural systems with sensor networks and record their behavior during both operational and extraordinary conditions, without shutting down the facilities and their services. Accelerometers are the most common sensors adopted for SHM purposes, and consequently, we are used to seeing the structure response in terms of acceleration time histories. Recently the research attention has focused on also other types of quantities representing the structural behavior, like strain, displacement, velocity (Sohn et al. 2001; Xia et al. 2005) and also different technologies to acquire them: MEMS, cameras (Lee and Shinozuka 2006; Lynch et al. 2003). Regardless of the quantity measured, the health condition of almost the totality of mechanical systems, including civil structures, can be read in their vibration response. Vibration-based SHM methodologies are the ones looking for strategies to efficiently spot damages and anomalies in a structures performance, only working with its recorded vibrations response. They look for changes in the regular pat-

tern of the structures attitude because vibration-based techniques rely on the fact that damage is represented by any variation in the material and/or geometric properties of the structure that will hinder its current or future performance (Farrar and Worden 2012). Then, it is intuitive that this alteration reflects in the structural behavior, but it can be recognized only keeping in mind the healthy state because this deviation exists only with respect to a reference condition. Continually measuring the structural vibration response allows to keeping track of the structural condition along with time and it offers robust information of the structure in undamaged situations so that when the structural response is measured after the damage occurred, the deviation from normal behavior will be neat.

The methodology just described would work beautifully if only the mechanical properties of structures, and consequently, their structural behavior depends only on damage variation; unfortunately, this is not the case. It is vital to remember that mechanical systems are built in an environment which is going to interact with the system itself. Environmental and operational conditions inevitably affect the structural behavior, and there are several studies and research that confirm it. Intuitively, something like temperature fluctuation may change the material properties and the geometry characteristics of a structure. It is essential to keep in mind that the variation caused by environmental and operational changes could be, in some cases, higher than the ones due to damage and consequently they could hide damage occurrence or also give a false alarm regarding the structural health. Peeters and De Roeck 2001, for example, established a nonlinear correlation between the ambient temperature and the fundamental frequencies of the Z24 Bridge, a bridge in Switzerland kept under monitoring for a whole year. The influence of temperature variation on frequencies became prominent when the temperature fell below the freezing point with variation up to 15%. Alampalli 1998 shows evidence of the discrepancy observed on the dynamic behavior of a bridge under different temperature conditions. The study case is a steel-stringer bridge with a concrete deck, that is subjected to artificial damage: the bottom flanges of the two main girders are damaged. In this work, the modal response of the structure characterizes the dynamic behavior, directly derived from the acceleration response of the bridge excited by impulse force hammer. Two different studies are carried on: one in which the air temperature is above the freezing point and a second one in which is below it. In the first case, the damage is identified comparing the modal parameters extracted from the acceleration time histories of the

bridge in undamaged conditions with the ones computed from the measurements in damaged ones. The artificial cuts in the bottom flanges of the girders, cause a reduction of the elements stiffness which automatically reflects in the frequencies, being directly proportional stiffness. The first three frequencies indeed show a drop after damage occurrence. This observation does not remain consistent when the temperature reaches values below freezing point and in this particular case, the frequencies extracted under damaged condition result to be higher than the ones computed in the undamaged situation. This unexpected behavior is justified by a change in the boundary conditions of the bridge caused by the shallow temperature, which, instead of acting as a simply supported system, is behaving more like a partially fixed one.

The systematic observation that can be derived from these experimental studies is that the environmental influence on the structure needs to be taken into account in the application and implementation of any vibration-based damage detection methodology. The problem can be managed at two different levels of a damage detection approach: model or feature level. One proposition could be of having a methodology based on a model that can learn the regular pattern and behavior of structures under common environmental and operation fluctuations. This knowledge would consequently allow distinguishing the changes related to damage from the ones coming from other external factors. Another approach could be working on the features adopted in the representation of the structural behavior of the system. Choosing parameters that are less sensitive as possible to environmental conditions and more influenced by damage would strengthen the procedure. These two ways of solving the problems are both valuable, and they are both investigated in this work. The two can be developed and optimized by solving the SHM problem within the context of *statistical pattern recognition*.

1.2 A Statistical Pattern Recognition Framework for SHM

As aforementioned, vibration-based approaches look for deviations from the observed behavior of a system along with time. These changes can be caused by damage or oscillating environmental and operational conditions. The goal is to learn, which is the acceptable fluctuation around a regular behavior and use it to

spot anomalies caused by damage. This can be done comparing during the monitoring period, every new and unknown information with the established model of the healthy structure, and whenever the new information falls far from that, damage occurrence can be presumed.

The discipline that is best up for this role is pattern recognition. According to Bishop 2006 pattern recognition investigates the discovery of regularities in data through the use of computer algorithms and after learning these regularities, the final aim is to classify the data into different categories. Three keywords arise from the previous definition: regularities, learning, and categories. For each problem that is going to be solved within a pattern recognition framework, it is fundamental to specify how these three points are defined as respect to the specific study case. Because the principal aim of SHM is being able to say if a structure is damaged or not, the definition of categories is pretty straightforward; the system can be classified either in damage or healthy category. However, what can be defined as a *pattern*? In pattern recognition, patterns represent features summarizing the necessary information of the objects that have to be classified. The patterns regarding SHM problems that can represent the typical characteristics of the two classes are called damage sensitive features (DSFs). As previously pointed out, the damage is related to a variation in the material/geometrical properties of the structure, and it reflects in a change of the systems behavior. However, it has been stressed out how the structural properties are also affected by the fluctuation of environmental and operational conditions, like seasonal temperature variation or a sudden change in the exciting conditions of the structure, like a wind storm. All these effects are temporary and do not compromise the structural performance on a long period. Therefore it is crucial to choose, when it is possible, DSFs that are less sensitive to these factors. If this is not possible, all these uncertainties can still be taken into account, if the DSFs in SHM framework are modeled as random variables and characterize them statistically.

The extraction of DSFs is one of the key steps in the implementation of the SHM framed within the SPR scheme. Farrar et al. 2001 proposed a framework for SHM, which is built using the statistical pattern recognition approach. This paradigm results in the following steps:

1. Operational evaluation;

2. Data acquisition;

3. Damage sensitive feature extraction;
4. Statistical modeling;
5. Decision Making.

The first task of the framework concerns about the context in which the specific SHM problem takes place. The operational evaluation consists in identifying the initial information regarding the study case, answering questions like:

1. What are the economic and/or life safety motives for performing the monitoring?
2. How is damage defined for the monitored system?
3. What are the conditions, both operational and environmental, under which the system to be monitored functions?
4. What are the limitations on acquiring data in the operational environment?

Therefore, operational evaluation lays the foundation to build a suitable damage assessment approach, completely customized on the structure. To give an example of how the operational evaluation of a specific problem may be formulated, let us consider the case where the owner of a highway overpass decides to monitor the deflection level of the deck under traffic load after ten years of service life. Many factors over the years could have affected the performance of the overpass reducing its service life before the ordinary maintenance. Monitoring the maximum deflection of the deck is an easy way to check the conditions of the structure in comparison with the original design. These infrastructures are often designed considering inputs that evolve with time like traffic, and often they are caught under heavier loads than the designed ones. During the operational evaluation, it could then be decided that displacement transducers and accelerometers could allow the monitoring the deck deflection so to trigger an alarm whenever such values exceed the safe thresholds. During this time, seasonal cycles of high and low temperature would also cause variation in the dynamic of the structure and, accordingly, instrumentation, like thermocouples, apt to measure these effects of such external conditions must then be provided, in order to distinguish their effects from those triggered by traffic load. Additionally, the instrumentation must

be placed in accessible locations without interfering with traffic, while the number of sensors must be sufficient and well placed to accurately and uniquely monitor the maximum displacement of the deck. Feasible and optimal sensor placement is then another aspect to consider during operational evaluation.

Once the monitoring system is designed and installed, the SHM procedure requires the acquisition of the data. The type of sensors and their position on the structure are discussed in the previous section, but in the data acquisition step, there other important decisions to make regarding the measurement process. For example, an important case dependent consideration expressed in this step is how often the data should be collected. If the principal aim is to check the behavior of a structure under fatigue, the data need to be collected continuously; otherwise, if the object is checking the condition of a bridge under long-return period earthquakes, the acquisition can be set at relatively long time intervals.

Such data cannot be used directly but must be processed to ensure their accuracy. Data are collected under varying conditions, and a post-process to normalize them becomes vital to use them correctly. Disciplines like digital signal processing offer several different procedures to normalize the data efficiently, but the correct methodology depends on the context and on the type of features that are going to be extracted from that data. In some cases, it can be useful to normalize the data with respect to the measured inputs or try to come up with a normalization technique that allows getting rid of sources of variability like environmental or operating conditions.

Once the data acquisition and cleaning step is complete, the feature extraction process is performed. The best features for damage detection are typically application specific because their choice is optimized for the monitoring purpose. Accordingly, to the DSFs chosen to represent the structural behavior of the system, the vibration response is manipulated to derive these traits. Since SPR approaches are interdependent with machine learning algorithms, it is essential to present the features in the best way to process. In this context, DSFs are assumed to be assembled into vectors. The dimensions of the feature space need to be well-calibrated: it should not be too big to reduce the computational cost in the actual analysis of data, but at the same time, these vectors cannot be too small otherwise there will not be enough information to characterize the structural properties correctly. An essential point of the SPR strategy is that there are no restrictions on the adopted features nature or regarding their combinations

in the feature vector. For example, for taking into account the environmental fluctuations of a bridge within a damage assessment approach, a valid choice for the feature vector might be: the first four structural frequencies of the bridge, the time when the measurements were made, and temperature and humidity reading from the system.

The two final steps of the SPR paradigm concern the statistical modeling of features extracted from the response of the system and the decisions process that comes from the outcomes of the statistical investigation.

The development of statistical models, built over damage sensitive features, is designed and optimized with the final object of identifying the damaged. As already mentioned, the algorithms used in statistical model development usually can be classified as supervised or unsupervised approaches, depending on the availability or not of labeled data. Regardless the specific nature of the chosen statistical model, the construction of the model per se is carried on in the so-called *training phase*, where the real learning process happens, together with the definition of the boundaries of what has been called the region of conformity with the typical structural conditions. The successive testing phase represents the incipit of the decision-making process. Once the integrity state of the structure has been assessed, such information must be fed into a cost-benefit analysis aimed at determining what is the best action to take to optimize the infrastructures management. This dissertation mainly addresses strategies to perform the third and fourth steps of these methodologies.

1.3 Learning Patterns in an Unsupervised Way

The pattern recognition action is achieved in the learning phase of the statistical model construction. This process needs to be defined because usually, there exist different pattern recognition methodologies according to the type of the chosen learning procedure. When the learning experience is based on a data set for which the corresponding class is known a priori, meaning that the data are already correctly labeled, the recognition process is called *supervised learning*. The learning starts from an established pair of inputs and outputs to infer a function that could be later used to map new examples into the correct category. Unfortunately this kind of learning process, for SHM, would require the availability of

response time histories of the system under both healthy and damaged conditions, however, measurements during damaged situations are rarely available and this ill-condition the learning experience. This problem regards all mechanical health monitoring. Think, for example, in a machine monitoring system, the acquisition of measurements of the machine in its healthy state is inexpensive and easy to obtain. On the contrary, recordings during the damaged conditions of the machine implied the failure of those machines. Therefore, it is extremely rare to have a very well-sampled negative class (He and Garcia 2008).

Unsupervised learning, on the other hand, comes from the neuroscientific theory proposed by Hebb 1949. The learning mechanism for Hebbian relies only on inputs coming into the system to produce patterns of activity. Thus, such models can learn without needing to produce particular responses, without any explicit tasks or directed attempts to learn, and without requiring teaching signals. Therefore unsupervised learning is equivalent to a blind search for patterns in the unlabeled data that can then be later used to determine the correct output value for new data instances. The latter is the preferable mode in the context of civil engineering, and for this reason, in this dissertation, unsupervised pattern recognition strategies are explored to identify damage occurrence.

Among the unsupervised methodology, cluster analysis and novelty detection are the most robust and used methodologies. However, the body of methods concerned with the SPR problem performed under unsupervised learning mode is *novelty detection*. Generally, pattern recognition problems focus on the classification of two or more classes. In novelty detection; instead, the problem is approached within the framework of one-class classification (Moya et al. 1993): one class, the regular class, has to be separated from all other possibilities. The basic assumption is that the positive class is well defined, with enough samples, while the other class(es) is/are severely under-sampled. The scarcity of negative examples can be due to high measurement costs, or the low frequency at which abnormal events occur. Unsupervised classifiers methodologies try separate as much as possible the categories that they identify in the data and that they recognize to have no similarities. In structural damage detection, they should be able to perform this task between features associated with the damaged scenarios and the ones related to the health conditions.

Within the novelty analysis, the problem is solved in two phases. During the first phase, called *training*, the damage sensitive features are extracted from

the response of the undamaged system under different external conditions. This population of features is used to construct a statistical model, called the training model, which represents the normal state of the system. The second phase, called *testing*, occurs when the systems integrity must be assessed. At this time, the DSFs are extracted from the systems response under unknown conditions, and their conformity to the training model is tested. If the new features are found unlikely to be realizations of the training model, they are labeled as *outliers*, i.e., representative of a damaged condition.

Searching for patterns in data and learn those behaviors can be exploited, not only in the damage detection assessment along with the service life of a structure but also within the features extraction process itself. In this work, both these ways of using unsupervised learning are addressed.

1.4 Damage Sensitive Features: Literature Review

The feature extraction step, presented in the SPR paradigm is one of the most critical points in the research area of SHM. It represents the process of computing the damage sensitive properties directly from the vibration response of the structure. DSFs are the parameters allowing to detect the damage in a monitored system.

Before diving into the different existing type of DSFs and their extraction, it is essential to point out that, for almost all the features, it is better to perform some form of data processing, compression and fusion procedures to optimize the extraction process itself and the reading of information from the features.

The modal parameters (frequencies, damping ratios, and mode shapes) are the first features that come in mind when thinking about DSFs for detecting damage detection in civil structures. They were the first indicators to be used for this purpose because their relationship with the structural properties was believed to guarantee high sensitivity to damage. Moreover having features linked directly to structural, mechanical properties allows to interpret their variation better and relate them to physical causes. It has been proved with time, numerically and experimentally, though, that especially frequencies are not always reliable damage sensitive features. Indeed, there are two main issues in using them as DSFs. First

of all, they are not sensitive only to damage, but they tend to be also affected by external variations like environmental fluctuations and changes in the operational conditions. Vandiver 1975 addresses the influence of operational variations over frequencies in one of his investigation of the dynamic response of an offshore light station tower. He extracted the frequencies associated with the first two bending modes and first torsional mode of the system. The author observed 1% shifts in frequencies caused by a fluctuation in the effective mass of the tower caused by the sloshing of fluid in tanks mounted on the deck. The same entity of variation is observed by systematically removing members from a numerical model, showing that damage of most members produces comparable changes to the ones observed in normal working conditions. Farrar et al. 2000 carried on two crucial studies on the Alamosa Canyon and the I-40 bridges, both in New Mexico, in which they investigated their dynamic response under temperature variation. They observed the changing in the first natural frequency between 1996 and 1997, and then ten years later. They derived that the first natural frequency of the Alamosa Canyon Bridge varies by 5% during a 24-hour cycle due to the temperature differential across the bridge deck. Similar fluctuations of the first natural frequency were observed in the I-40 bridge, where it was also possible to simulate four damage scenarios of increasing severity, by gradually cutting one of the girders. Farrar and his colleagues observed that the change in the first modal frequency generated by damage presents a comparable magnitude with the one induced by the effect of temperature. Even more counter-intuitive was the finding that, under the first two damage scenarios, the value of the first natural frequency increased, rather than decreasing. Again, this unexpected result was found to be caused by in-service temperature conditions variations.

Another important disadvantage is that modal frequencies represent a global property of the structure. Consequently, it is challenging to derive information from frequencies shifts other than the presence or absence of damage. For example, frequencies rarely can give information about the possible location of the damage. Doebling et al. 1996b show that lower modal frequencies are little sensitive to localized and contained damage, while environmental effects may significantly alter them. On the other hand, higher modal frequencies, being related to localized behavior of the structure, could be more sensitive to damage but remain very difficult to identify due to their low modal participation factor.

When structural damage happens at different locations, it reflects in multiple

variations in terms of frequencies, associated with distinct combinations of changes in modal frequencies. However, usually, it is not possible to identify all the frequencies needed to find the location of the damage uniquely. Therefore, the use of frequencies as DSFs right know results to be more efficient when these variations can be precisely measured in a controlled environment, such as for quality control in manufacturing.

Damping properties have not been used for damage detection problems as consistently as frequencies and mode shapes. However, there are some cases in which damping coefficients could represent a good choice as DSF. When investigating crack detection in a structure, for example, damping coefficients perform better than frequencies and mode shapes as DSFs because damping changes help to detect the nonlinear, dissipative effects associated with cracks. Modena et al. 1999 show that cracks, which could not be detected with simple visual inspections, produce small variations in structural frequencies and require higher mode shapes to be detected. On the contrary, these same cracks reflect with more significant changes in the damping parameters, sometimes of the order of 50%. The authors focus on finding manufacturing defects or structural damage in precast reinforced concrete elements. The peculiar dynamic response of reinforced concrete justifies the use of damping and nonlinear responses as DSFs. They implement two new techniques based on changes in damping to detect cracks. The first method, which is applicable for a classically damped system, estimates stiffness on the measurements of the modal damping variations and the bending curvatures. The second methodology, instead, involves the viscous and friction components of damping and the identification of damage through friction detection and characterization.

Among modal parameters, mode shapes result to be more suitable DSFs because their nature makes them informative about the dynamic spatial configuration of the system. The disadvantages associated with the mode shapes are the requirements and assumptions that need to be maid to extract them correctly. The efficiency in mode shapes derivation entirely depends on the correct positioning of the sensors. A strategic localization of the sensors leads to richer information and also allows to limit the search of changes in smaller areas. Ahmadian et al. 1997 built a procedure for localizing damage that adopts measured displacements of a structure combined with an analytical model to locate faults. When damage occurs only in some parts of the structure, the associated substructures modes are affected and show a variation, but the ones related to other substructures will be

unaffected. Damage in a particular substructure changes the participation factors of the higher modes of that subpart, but not the ones of the others subparts. The authors constructed their procedure, relying on this observation.

Modal curvature is an extremely effective DSF which can be directly derived by mode shapes, and it is potentially the most sensitive to damage. Maeck and De Roeck 1999 implemented a stiffness-based procedure for doing damage detection, localization, and quantification, and they validate it using the data recorded on the Z24 bridge in Switzerland. Frequencies and mode shapes are used to compute the dynamic stiffness of the system. The method depends on the assumption that the bending stiffness of a beam is equal to the ration of the bending moment and the corresponding curvature, which is the second derivative of the bending deflection. Changes in the dynamic stiffness, given by changes in the modal curvature, indicate the presence of damage. This relationship makes the modal curvature way more sensitive to local damage than modal displacements. However, modal curvature needs to be used carefully because even if extremely sensitive to damage is also the one most prone to variance induced by error sources Doebling et al. 1996a.

Kullaa 2003 offered a very robust example of how the modal parameters could be correctly used as DSFs within a SPR paradigm. He used modal frequencies combined with mode shapes and modal damping ratios to built a control chart to identify damage. He validated this approach using the measurement recordings of the Z24 bridge in Switzerland, which was intentionally subjected to damage scenarios of increasing severity.

Control charts are tools ordinarily used in statistical quality control to determine if the manufacturing of a product is in a state of statistical control. Variation of the quality in any manufactured product is assumed to be driven either by aleatory uncertainties, which are inevitable or by epistemic uncertainties, which can ideally be detected and corrected Allan 1959. Control charts are plots of the limits within which variations of the process properties are considered to be natural, values of the process properties falling outside such limits indicate the occurrence of changes in the process that are generally attributed to epistemic uncertainties, and that are then, in principle, correctable. There exist different versions of control charts that vary depending on the modalities of computation of the control limits. Kulla proposed several different options for the control chart, all based on the common idea that the structure is declared damaged whenever

an index, function of the modal properties, exceeds the upper control limit.

This dissertation stresses another critical point which arises when using modal parameters as DSFs. Even when frequencies result to be the best damage sensitive feature, their extraction procedure is exceptionally dependent on the users expertise. Several methodologies can be applied to extract modal parameters, some more simple than others, but all of them require some level of competence, which makes their computation affected by a high level of variability and uncertainty.

The Fourier analysis of the measured response offers a potent tool to derive DSFs different from the modal properties. Worden et al. 2000 demonstrated the use of outlier analysis as a valuable mean to conduct structural damage detection using transmissibility functions and spectrum characteristics of simulated and experimental data. The proposed method works with the Mahalanobis Squared Distance (MSD) (Mahalanobis 1936), a weighted Euclidean distance of a random vector from the mean of a population of random vectors, where the covariance matrix of the population represents the weight. MSD is used to measure the similarity level of a new incoming feature with the training model, represented by the mean and covariance matrix of the population of features extracted from the response of the system under healthy conditions. In damage detection, an outlier is represented by a damage sensitive feature manifesting a behavior different from that shown by the same features extracted from the response of the system under conditions known to be undamaged. In order to conclude whether the observed discordancy is to be considered alarming, the MSD of the possible outliers feature is compared against a threshold value. In Worden et al. 2000, it is suggested the threshold be determined by first generating a set of identically and normally distributed random numbers, by then evaluating their MSD and picking the maximum value, and by finally repeating the same procedure numerous times to select as threshold the value exceeded only by the 5% of the resulting maxima.

There is a family of DSFs which follows a completely different approach with respect to the features previously cited and it still dominantly used in statistical pattern recognition problems for SHM: the ARMA family models and the wavelets. Their relation to structural properties is less straightforward (Nair et al. 2006) than the one showed by the modal properties or frequency spectra because these features come from directly processing the response time histories.

Wavelet transform permits the analysis of a signal in the time-frequency domain. The use of the energies of the Haar and Morlet wavelet transform coeffi-

cients, intended as the sum of the squares of the wavelet coefficients, were analyzed as potential DSF (Nair and Kiremidjian 2009; Young Noh et al. 2011). The main contribution of this work was that of demonstrating how the energies of the wavelet coefficients are related to the structural properties, then satisfying the condition to be feasible candidates as DSFs. Further advantages related to the use of the wavelet-based DSFs are their compactness and the fact that they can be extracted from the response of a system under nonlinear conditions. Staszewski et al. 1997 extended the concept of wavelet analysis. They proposed a wavelet-transform-based technique to enhance defect detection in a carbon fiber composite plate tested using ultrasonic Lamb waves, additionally incorporating an optical fiber receiver. The authors applied the fundamental symmetric Lamb waves into the sample plates adopting a piezoelectric transducer (operating frequency 250 kHz). They introduced an embedded single-mode optical fiber forming the signal arm of an optical fiber Mach-Zehnder interferometer to monitor the acoustic pulses. Low amplitude direct Lamb wave reflections from delaminations were observed in the sample plates, and there was a sharp improvement in the defect visibility given by the use of wavelet-transform-based novelty technique.

Sohn et al. 2001 were the first to use AR/ARX coefficients within statistical process control techniques. Initially, an Auto-Regressive (AR) model is fit to the acceleration time histories of an undamaged system. The coefficients of the AR model are computed and chosen as the DSFs for the control chart analysis. Then, the AR coefficients obtained from new data are compared with the baseline AR coefficients. Any significant deviation from the baseline of AR coefficients would indicate either a change in environmental conditions or damage. Several projection techniques such as principal component analysis and linear/quadratic projections are also applied to transform the time series from multiple measurement points into a single time series to reduce the dimensionality of the data and enhance the discrimination between features from undamaged and damaged structures. Finally, the statistical procedure, combined with the AR time prediction model, is applied to vibration test data acquired from a concrete bridge column as the column is progressively damaged.

Sohn et al. 2001 also proposed novelty detection approach where AR coefficients are adopted as DSFs within a framework similar to the one used by Worden et al. 2000, to demonstrate the potentials of pattern recognition as an efficient alternative to the more usual frequency approaches. Nair et al. 2006 also employ

a combination of the first three AR coefficients modeling the measured response time histories of the ASCE benchmark structure, described in Johnson et al. 2001, as DSFs. The authors solve the damage detection problem by using hypothesis testing. In particular, they use the t-test, under the null hypothesis that the mean of the training and testing populations of AR-based DSFs are the same, i.e., that the system is undamaged. In the same work, the authors also propose an AR-based index able to locate damage, based on the Euler distance between the cluster of undamaged and unknown damage sensitive features.

1.5 Thesis Scope and Organization

Over the last few years, there has been an increasing trend in the civil and structural engineering community of instrumenting dense sensor networks on structures for SHM purposes. Such sensor networks commonly stream measurement data continuously, collecting and storing a massive amount of information daily. Although this is an encouraging trend for SHM, very often it seems that little is done with the data collected.

The academic research has proposed several methodologies in the past twenty years to use vibration monitoring data for damage assessment and SHM, but there has always been a lag in the application of these approaches to experimental monitoring data and real civil study case. One of the main reasons behind this slowdown is the high computational cost that is often required by these methodologies and the dependency of almost all of them on the users expertise. Indeed, a suitable framework should have a small computational burden to speed up the analysis of big monitoring data and, at the same time, it should be user-friendly so to be used without any particular expertise background on the methodology itself.

Looking at SHM within a SPR framework, the integrity level of a structure is determined by the observation of DSFs, which represent the structural behavior. It is the choice of these indicators and their extraction process that often represents the sensitive and time-consuming step in all damage detection strategies.

This dissertation focuses on looking for suitable DSFs to be used for vibration-based damage detection methodologies, implemented for SHM cases. Initially, the thesis explores the well-known modal parameters and their extraction process

(Part I), while, later on, it focuses on the investigation of new indicators (Part II). The third part (Part III) of this dissertation is dedicated to the monitoring analysis of the historic Civic Tower in Rieti.

In **Chapter 2**, an alternative way to derive the modal parameters from the vibration response of structures is presented. The proposed approach consists of five steps, for which the number of choices that user has to make is highly minimized and, additionally, precise information is given to set the parameters driving the methodology. An initial introduction on state of the art about automatized methodologies to extract modal parameters is given, followed by the definition of the problem statement. The framework is built on the application of the Data-Driven Subspace Stochastic Identification algorithm, and a theoretical overview of this system identification technique is provided. Subsequently, the proposed extraction process is presented in every single step. The application of this procedure can be found in the last chapter of this dissertation (**Chapter 5**).

In **Chapter 3** the use of audio indicators as novel damage sensitive feature is investigated. The performance of two different features, usually used in the field of speaker and speech recognition is here tested to carry on damage detection on civil structures. These audio features are the Cepstral Coefficients (CCs) and MPEG-7, which are commonly adopted to give a compact representation of the speechs signal. They can be easily extracted from the structural response by means of digital signal processes alone. Given its primary focus, this chapter will also be instrumental in better appreciating the role, and properties of the DSFs in the context of SPR approaches. Outlier analysis will be then exploited to distinguish the damaged from the undamaged states of the structure. The technicalities of the application of the proposed algorithm will be studied with particular emphasis on the problem of data normalization concerning external factors. The validity of the proposed algorithm is studied on numerical data from simulated shear-type systems.

In **Chapter 4**, the cointegration technique is introduced for the normalization of DSFs. This approach is well-known in the field of econometrics, where it is used to remove trend from nonstationary time series. Here, cointegration is used to clean Cepstral Coefficients from environmental dependency. The first part of the chapter focuses on the theoretical background of the methodology, addressing both the original and a novel formulation. A numerical and an experimental application are provided to show first how the temperature variation affects Cep-

stral Coefficients and then to validate the application of cointegration to remove environmental trends from these DSFs.

In **Chapter 5** the integrity assessment of a RC-masonry tower equipped with a Non-Conventional Tuned Mass Damper (NC TMD) located in Rieti (Italy) is carried on. Some of the DSFs described in the previous chapters, modal parameters in **Chapter 2** and Cepstral Coefficients in **Chapter 3**, are computed starting from the data collected during the three-years long monitoring campaigns conducted on the historic tower. Initially, an historical and geometrical description of the structure is given, with a report on the passive control system installed on the tower. Subsequently, the monitoring campaigns are described, with detailed information about the monitoring system placed for the long-term monitoring campaign.

The fourth and last part of the dissertation sums up the findings and contributions of the research while identifying possible streams of future research.

Part I
Modal Parameters as Damage Sensitive Features

Chapter 2

Unsupervised Extraction Process of Modal Parameters

This chapter introduces an automated alternative extraction process to derive modal parameters from the vibration response of structural systems. This methodology offers a powerful tool to compute frequencies, damping ratios, and mode shapes within a framework that is built over user-independent parameters.

Firstly, an overview is given about the automated procedures available in the literature, followed by the theoretical background of Stochastic Subspace Identification, which is the system identification technique at the core of the proposed methodology. Later the procedure itself is presented in theory, step by step, highlighting the parameters driving the extraction process. The proposed automated methodology is tested on the experimental monitoring data collected on the Civic Tower of Rieti.

2.1 Introduction to Automated System Identification Procedure

The accuracy of vibration-based SHM approaches, performed within a SPR framework, stands with their capability of describing the structural dynamic behavior and tell when it diverges from the observed normal patterns. Within this aim, novelty detection approaches based on *feature tracking* are the most established and popular methodologies to spot anomalies. They consist of constructing a sta-

tistical model that knows and learns the normal behavior of the structure. This model is built starting from the observation over time of particular features which best represent and sum the health condition of the monitored system. The main assumption is obviously that the chosen features are the most robust to tell if something is deviating from the regular behavior.

In civil engineering, we mentioned that the most common features adopted to represent the reference dynamics of a structure are the modal parameters: frequencies, damping ratios, and mode shapes. The pro and cons of using modal parameters as DSFs were exhaustively presented in the previous chapter. Modal information, particularly frequencies, are susceptible to variation in stiffness, and this means that theoretically, they represent one of the best choices for performing damage detection. However, two main disadvantages have been pointed out in using modal parameters as DSFs: the uncertainty hidden behind their extraction process and their extreme sensitivity to environmental and operational changes. This chapter accounts for the first problem, addressing a methodology to reduce the uncertainties carried on with the computation of modal parameters.

The feature extraction process, which is the third step in the SPR paradigm, is a very significant step. The signal processing tool used to extract modal features needs to be carefully chosen. Indeed, it establishes the accuracy in the definition of the healthy structural state and, the ability to track this information.

System identification is the process which aims to characterize the behavior of an unknown system assuming it is describable by a specific mathematical representation. The chosen model is then used to estimate the system's physical parameters (i.e., mass, stiffness, and damping) starting from measured experimental data. Structural identification starts from the measured response of the system and the external excitations and tries to determine a mathematical relation between them. Three different representation of the same model can be built depending on the level of details about what is happening inside the system. They depend on the complexity level of the model and on the parameters that are used to represent the system: white, gray, and black-box models (Kim and Lynch 2012a,b).

The so-called *white-box models* are physics-based model derived from the first principles of Newton equations and, they have a powerful and direct physical meaning. However, such models will be too complicated and sometimes impossible to find in reasonable time due to the complex nature of processes involved.

In the *gray-box model*, also known as semi-physical models, the details of what is going on inside the system are not totally explicit. Therefore, a specific model based on both insight into the system and experimental data is constructed. This model does, however, still have some unknown free parameters which can be estimated using system identification.

Black-box model are data-driven mathematical models derived by subspace system identification. Most system identification algorithms are of this type.

Ljung 1987 proved that subspace identification could be a powerful tool for control engineers. Unfortunately, they have been introduced later in the civil engineering area because of the absence of a direct and easy way to derive the physical meaning and its complex mathematical derivation. In the last twenty years, subspace system identification has made significant inroads in the civil engineering field. Nowadays, black-box models are the most commonly adopted tools for extracting information about structural systems. Indeed, despite the lack of mathematical mapping the state-space parameters to the physical ones, it is possible to directly derive from it the *modal model*, which provides modal parameters for a measured structure (Kim and Lynch 2012b). Both models can be obtained using either input (excitation) and output (response) measurements (I/O identification) or the single output (O/O identification).

O/O structural identification is the process which provides structural parameters and the mathematical model starting only from the measured response of the system. This approach implemented in Operational Modal Analysis (OMA) methodologies has received growing interest in the civil engineering community due to several benefits compared to I/O identification and the related experimental modal analysis. In OMA approaches, the structure is operative during the monitoring, as only the responses to ambient vibrations are utilized. Moreover, using O/O algorithms, there is neither the necessity to measure the input during operative conditions nor to excite the structure with artificial excitations of sufficient intensity to overcome the unavoidable ambient noise. Experimental Modal Analysis (EMA) techniques, instead, are more challenging, especially in the presence of large-scale structures, because installing a controlled and measurable exciter on large scale structure (e.g., bridge, dam, etc.) is complex and sometimes unfeasible. Over the years, OMA has gradually developed as an autonomous technique, even though most OMA methods have been derived from EMA procedures. OMA differentiate from EMA in the type of input, which is a known quantity in

EMA, while it is a random process in OMA. Therefore, while EMA procedures are developed in a deterministic framework, OMA methods can be seen as their stochastic counterpart.

The application of O/O system identification techniques comes with disadvantages as well. A single run of a system identification technique, which is associated with a specific set of parameters, leads to the computation of a single set of modal estimates. It consequently brings with itself a certain uncertainty level. It is has been observed that the identification results are highly sensitive to the selections of these parameters, and this could often affect the accuracy of the techniques themselves. As reported in Peeters and Ventura 2003, even when applying the same methodology to the same data, different users end up with different results. Even if for most of these techniques, there are general guidelines for correctly choosing the parameters, the accuracy of the final identification is highly dependent on the user's expertise. Reynders et al. 2016 offers a methodology to quantify this uncertainty admitting that the identified modal parameters present a certain level of inaccuracy and that that level needs to be computed. They define a method for estimating the covariance of modal characteristics that are identified with the stochastic subspace identification approaches and validate the methodology for two civil engineering structures.

There is one parameter which needs to be chosen by the analyst in all parametric system identification techniques: the model order of the system n. Unfortunately, the model order is usually an unknown in the identification problems, and even when it is known, it does not guarantee the best identification of the structural modes. Several proposals have been made for model validation techniques in order to automatically choose n, so that the prediction capacity of the identified model is maximized Ljung 1987. Van der Auweraer and Peeters 2004 proposed an alternative approach, based on the empirical observation that often in modal identification investigations, the structural physical modes appear at nearly the same eigenfrequency when the model order is over-specified, while spurious modes do not. In this approach, parametric models are performed for a wide range of model orders and, the identified modes are plotted in a model order vs.eigenfrequency chart, known as *stabilization diagram*. The physical modes should then display as vertical lines in this diagram. Although the stabilization diagram has become a vital tool in modal testing, its interpretation, i.e., the selection of physical modes from the diagram, is often not straightforward. The results may depend on the

judgment of the analyst, and possible additional validation criteria may be needed.

In addition to the model order, all parametric system identification techniques imply the definition by the user of a set of parameters characterizing the algorithm itself. Even when the best fitting of these parameters is found for a specific record, rarely it is possible to keep these values fixed along with a continuous and long monitoring campaign. This instability and uncertainty in the accuracy of the final identification are more evident for real complex structures, for which the fundamental assumptions, under which these algorithms live, are not always valid.

However, in SHM applications, the main concern is about correctly identifying the structural modes instead of ranking the prediction capacity of an identified model. On the wave of this through an incredible research effort has been spent on automating the identification of structural modal parameters using parametric algorithms. The focus has been mainly on three complementary aspects. The first is the conception of identification algorithms that can deliver more clear stabilization diagrams. Then there is the study of additional parameters to characterize the modes estimates to make a more well-founded selection of the stable modes. The last point is the development of methodologies to perform an automatic analysis of the information usually presented in stabilization diagrams.

Verboven et al. 2002 and Vanlanduit et al. 2003 are among the first ones to give additional criteria to distinguish the physical modes estimates from the spurious ones, that is suitable for all system identification methods. They use fuzzy C-means clustering for classifying the modes, estimated with frequency-domain Maximum Likelihood Estimation for a single model order n, into two categories: physical and spurious modes. From that moment on increasing attention has been paid to this topic, with the formulation of methodologies for automated identification Brincker et al. 2007; Deraemaeker et al. 2008 relying on OMA methods based both on control theory and on conventional signal processing.

After the elimination of all or at least part of the spurious mode estimates, it is still necessary looking for a procedure to group all the values related to the same physical mode. The most simplistic approaches overcome this step with the selection of conservative model order. However, this is not very correct, because it can happen that the selected model does not contain estimates for all the modes. Additionally, even when all estimates are present, there is no guarantee that those provided by that model order are the best ones. A straightforward way for the automatic interpretation of stabilization diagrams is to develop algorithms to mimic

the decisions that an experienced modal analyst takes during the examination of a stabilization diagram.

Pappa et al. 1998 were perhaps the first to report a methodology based on hierarchical clustering for separating structural modes with similar properties, using the eigenfrequency difference and the MAC value as distance measures. They successfully applied it to automate the Eigensystem Realization Algorithm (Juang and Pappa 1985) for an EMA analysis of the Space Shuttle tail rudder. Chauhan and Tcherniak 2008 present slight variations on the original approach of Pappa et al. 1998. Goethals and Moor 2004 propose an alternative distance measure, incorporating the eigenfrequency and damping ratio difference. Closely spaced modes are detected through the presence of modes with the same model order in the same cluster; they are then separated using the MAC value. Allemang et al. 2010 use yet another distance measure, namely the MAC value between extended, pole-weighted mode shape vectors that are identified for each mode. Verboven et al. 2004 present quite a different approach, where it is assumed that the number of modes in one cluster is a priori known; this is, however, rarely the case. A successful application of hierarchical clustering is reported by Magalhaes et al. 2009, who analyzed more than 2500 high-quality datasets collected on a 280 m span concrete arch bridge.

Alternatively, Scionti and Lanslots 2005 use fuzzy C-means clustering to group the modes, present in a stabilization diagram, directly into a user-defined number of C clusters. The clustering is performed in the eigenfrequencydamping ratio plane. The main drawback of this approach is that the number of clusters is a user-defined quantity. Additionally, several non-intuitive enhancements to the basic C-means clustering algorithm and a combination with genetic algorithms are needed to provide reasonable results.

Reynders et al. 2012 propose one of the most complete fully automated technique to derive modal parameters from measured vibration data. The motivations driving this research are not only related to an improvement in terms of time-coast approach. They recognize the importance of implementing this kind of information to reduce as much as possible the user interaction and to apply these procedures easily to different kind of health monitoring problems. They implement a three-stage clustering strategy to interpret stabilization diagrams easily. The three stages cover the stages that every user should be supervising when carrying the analysis manually: defining the thresholds for clearing out the stabilization

diagram, identifying the columns associated with stable modes, and choosing a representative mode from each column. The methodology proposed in Reynders et al. 2012 is widely validated using the monitoring data of the Z-24 bridge in Switzerland.

Recently Ubertini et al. 2013 combined in a single methodology different approaches derived from previously proposed automated system identification methodologies (Magalhaes et al. 2009; Reynders et al. 2012). The methodology is validated in several works. It happens to provide very consistent results, even for complex historic structures that often do not stick with the theoretical assumptions that need to be assured when applying O/O extraction techniques (Ubertini et al. 2017).

In this chapter, an alternative automated procedure to derive modal parameters is proposed. The following methodology depends on the application of the well established Data-Driven Stochastic Subspace Identification (DD-SSI) algorithm. In Section 2.2, the problem background is defined in the subspace domain, and then the theoretical steps to implement DD-SSI are laid down with the parameters governing this algorithm (Section 2.3). Finally, in Section 2.4, the proposed automated procedure to derive modal parameters is presented in detail in all his steps.

2.2 Problem Statement

The system identification technique explored in this work, DD-SSI, belongs to the family of subspace methods. Their background theory is widely explained by Van Overschee and De Moor 2012, together with a historical survey of the concepts involving subspace identification. This algorithm aims to completely identify a linear dynamic system through the extraction of the structural matrices representing the system itself in the state space domain.

A finite-dimensional linear time-invariant dynamic system is commonly represented by a set of N second-order differential equations. Using the matrix notation, the equation of motion can be expressed as

$$\mathcal{M}\ddot{\mathbf{z}}(t) + \mathcal{L}\dot{\mathbf{z}}(t) + \mathcal{K}\mathbf{z}(t) = \mathbf{f}(t) \tag{2.1}$$

where $\ddot{\mathbf{z}}(t), \dot{\mathbf{z}}(t), \mathbf{z}(t) \in \mathbb{R}^{N\times 1}$ are respectively the acceleration, velocity and

displacement vectors and $\mathbf{f}(t)$ is the forcing function. Instead $\mathcal{M}, \mathcal{L}, \mathcal{K} \in \mathbb{R}^{N \times N}$ are the mass, damping and stiffness matrices.

Nevertheless among all the possible mathematical representations of dynamic systems, state-space models have become very popular in particular because they are well suited for system analysis, numerical simulation and controller design via established and robust techniques. In this case the dynamic system is represented by a set of $2N$ second-order differential equations. The transition from the set of second-order differential equations to the first-order set is possible by introducing a new vector: the state vector $\mathbf{x}(t)$, which recollect the displacement and velocity vectors

$$\mathbf{x}(t) = \begin{bmatrix} \mathbf{z}(t) \\ \dot{\mathbf{z}}(t) \end{bmatrix} \tag{2.2}$$

The introduction of the state vector leads to the reformulation of the dynamic system described in Equation 2.1 considering the consequent new arrangements of matrices. Therefore a discrete-time linear-time-invariant state-space model is defined as

$$\mathbf{x}(k+1) = \mathbf{A}\mathbf{x}(k) + \mathbf{B}\mathbf{u}(k) + \mathbf{w}_p(k) \tag{2.3a}$$

$$\mathbf{y}(k) = \mathbf{C}\mathbf{x}(k) + \mathbf{D}\mathbf{u}(k) + \mathbf{w}_m(k) \tag{2.3b}$$

where $\mathbf{x} \in \mathbb{R}^{n \times 1}$ is the state vector, $\mathbf{u} \in \mathbb{R}^{p \times 1}$ is the input vector, $\mathbf{y} \in \mathbb{R}^{m \times 1}$ is the output vector, $\mathbf{A} \in \mathbb{R}^{n \times n}$ is the system matrix, $\mathbf{B} \in \mathbb{R}^{n \times p}$ is the input matrix, $\mathbf{C} \in \mathbb{R}^{m \times n}$ is the output matrix, and $\mathbf{D} \in \mathbb{R}^{m \times p}$ is the direct influence matrix, with p indicating the number of input time-histories and m indicating the number of output time-histories and n indicating the system order in the subspace ($n = 2N$). Equation 2.3a is the *State Equation* and Equation 2.3b is the *Observation Equation*. Such a model is linear since the variables $\mathbf{u}$, $\mathbf{x}$ and $\mathbf{y}$ appear linearly in Equation 2.3, and it is time-invariant since the matrices $\mathbf{A}$, $\mathbf{B}$, $\mathbf{C}$ and $\mathbf{D}$ are constant over time. The system in Equation 2.3 is supposed to completely state controllable and observable. The vectors $\mathbf{w}_p \in \mathbb{R}^{n \times 1}$ and $\mathbf{w}_m \in \mathbb{R}^{m \times 1}$ take into account the noise in the process and in the measurement, respectively. The standard assumption is that the process and measurement noises are zero-mean white stationary processes, uncorrelated with the input vector $\mathbf{u}$ and the output vector $\mathbf{y}$. It is important to underline that switching to this state-space model the physical meaning of the identification is completely lost and the matrices in

Equation 2.3 define a black box, hiding the system physical information. DD-SSI has shown to be extremely effective in identifying the matrices of structural models when both input and output measurements are available.

When the input measurements are not available but can be assumed to be white and stationary, the system in Equation 2.3 can be rewritten as

$$\mathbf{x}(k+1) = \mathbf{A}\mathbf{x}(k) + \mathbf{w}'_p(k) \tag{2.4a}$$

$$\mathbf{y}(k) = \mathbf{C}\mathbf{x}(k) + \mathbf{w}'_m(k) \tag{2.4b}$$

where $\mathbf{w}'_p \in \mathbb{R}^{n\times 1}$ and $\mathbf{w}'_m \in \mathbb{R}^{m\times 1}$ are zero-mean white stationary processes including the original process and measurement noises and the effect of the unknown input on the state equation ($\mathbf{Bu}(k)$) and on the measurement equation ($\mathbf{Du}(k)$). As a result $\mathbf{w}'_p$ and $\mathbf{w}'_m$ satisfy the same assumptions as the original process and measurement noise.

In the Output Only approach, the input measurements are not available and the system information are collected in the single output data set $\mathbf{y}(k)$,available for s temporal steps.

$$\{\mathbf{y}(k)\} = \{\mathbf{y}(0), \mathbf{y}(1), \mathbf{y}(2) \dots \mathbf{y}(s-1)\} \tag{2.5}$$

The state space system itself, described by Equation 2.3 occurs with a substantial new face, where matrices $\mathbf{B}$ and $\mathbf{D}$ are no longer taken into account, because directly linked to the input data set. The ultimate goal remains the same of input-output approach: the system identification through the available system matrices and the determination of the system order n, given the system measurements. In this case, only $\mathbf{A}$,$\mathbf{C}$ are computed, but they present enough information to extract the system modal parameters Luş et al. 2003.

2.3 DD-SSI

Among all the existing system identification procedures defined in the state space, DD-SSI is one of the most popular and commonly used (Pridham and Wilson 2003, Kim and Lynch 2012a). DD-SSI directly starts from the response measurement data of the system without any previous manipulation, unlike the covariance version of SSI, where an initial correlation calculus is expected. Indeed, in DD-SSI, the output covariance is computed through matrix projections. Therefore,

it has become an attractive alternative to Covariance-SSI (Cov-SSI), because the computational cost is highly reduced.

DD-SSI is a straightforward algorithm which is built over well-established linear algebra tools, such as orthogonal projection, SVD, and QR factorization and is driven by a small finite number of user-defined parameters.

The DD-SSI algorithm addressed in this work follows the version presented by Priori et al. 2018, which also give specific guidelines for properly choosing the parameters governing the algorithm. The structure of DD-SSI consists of five main steps:

(i) The construction of the Hankel matrix;

(ii) The orthogonal projection of the future outputs onto the past outputs;

(iii) The choice of weighting matrices;

(iv) The extraction of the observability range space;

(v) The derivation of the system matrices.

Such steps are developed in the following section.

2.3.1 The Algorithm

The input to an output only DD-SSI algorithms is the sequence of measured system output $\{\mathbf{y}(k)\}$ of length s (Equation 2.5). The outcome of the algorithm is the set of matrices $\mathbf{A}$ and $\mathbf{C}$. The main steps are:

(i) *The construction of the Hankel matrix.*

The output data are directly arranged in a block Hankel matrix $\mathbf{H} \in \mathbb{R}^{m \cdot i \times j}$, split into two partitions:

$$\mathbf{H} = \begin{pmatrix} \mathbf{Y}_p \\ \mathbf{Y}_f \end{pmatrix} = \left(\begin{array}{ccc} \mathbf{y}(0) & \dots & \mathbf{y}(j-1) \\ \mathbf{y}(1) & \dots & \mathbf{y}(j) \\ \vdots & \ddots & \vdots \\ \mathbf{y}(i-h-1) & \dots & \mathbf{y}(i-h+j-2) \\ \hline \mathbf{y}(i-h) & \dots & \mathbf{y}(i-h+j-1) \\ \mathbf{y}(i-h+1) & \dots & \mathbf{y}(i-h+j) \\ \vdots & \ddots & \vdots \\ \mathbf{y}(i-1) & \dots & \mathbf{y}(i+j-2) \end{array}\right) \tag{2.6}$$

where $\mathbf{Y}_p \in \mathbb{R}^{m \cdot g \times j}$ and $\mathbf{Y}_f \in \mathbb{R}^{m \cdot h \times j}$ are called respectively past outputs and future outputs Van Overschee and De Moor 2012. The dimensions of the partitioned Hankel matrix depend on four parameters (i, j, g, h) Priori et al. 2018. The number of block rows i, the number of columns j and h (or g) are independent and can be fixed by the user, while the parameter g (or h) can be selected respecting:

$$g + h = i$$

In order to reduce the computational effort of the subsequent steps of the algorithm, the block Hankel matrix $\mathbf{H}$ is decomposed by means of LQ decomposition:

$$\mathbf{H} = \mathbf{L}\mathbf{Q}^T = \begin{pmatrix} \mathbf{L}_{11} & \mathbf{0} \\ \mathbf{L}_{21} & \mathbf{L}_{22} \end{pmatrix} \begin{pmatrix} \mathbf{Q}_1^T \\ \mathbf{Q}_2^T \end{pmatrix} \tag{2.7}$$

Therefore The matrices $\mathbf{Y}_p$ and $\mathbf{Y}_f$ can be also expressed using $\mathbf{L}$ and $\mathbf{Q}$ matrices:

$$\mathbf{Y}_p = \mathbf{L}_{11}\mathbf{Q}_1^T \tag{2.8a}$$

$$\mathbf{Y}_f = \mathbf{L}_{21}\mathbf{Q}_1^T + \mathbf{L}_{22}\mathbf{Q}_2^T \tag{2.8b}$$

(ii) *The orthogonal projection of the future outputs onto the past outputs.*

The orthogonal projection of the row space of $\mathbf{Y}_f$ onto the row space of $\mathbf{Y}_p$, which is denoted by $\mathbf{Y}_f/\mathbf{Y}_p$, can be directly calculated:

$$\mathbf{\Pi} = \mathbf{Y}_f/\mathbf{Y}_p = \mathbf{Y}_f\mathbf{Y}_p^T(\mathbf{Y}_p\mathbf{Y}_p^T)^\dagger\mathbf{Y}_p \tag{2.9}$$

The computation of Equation 2.9 can be efficiently made using LQ decomposition (Equation 2.8):

$$\mathbf{\Pi} = \mathbf{L}_{21}\mathbf{Q}_1^T \tag{2.10}$$

(iii) *The choice of the weighting matrices and extraction of the observability range space.*

In the third step the user needs to choose the weighting matrices. Indeed,

the matrix $\mathbf{\Pi}$ is generally multiplied by two matrices $\mathbf{W}_1$ and $\mathbf{W}_2$:

$$\mathbf{P} = \mathbf{W}_1 \mathbf{\Pi} \mathbf{W}_2 \tag{2.11}$$

where $\mathbf{P} \in \mathbb{R}^{m \cdot h \times m \cdot g}, \mathbf{W}_1 \in \mathbb{R}^{m \cdot h \times m \cdot h}, \mathbf{W}_2 \in \mathbb{R}^{j \times m \cdot g}$. There are several options for the wighting matrices (Hong 2010), such as Partial Least Squares (PLS), Canonical Correlation Analysis (CCA), Multiple Linear Regression (MLR) and Enhanced CCA (ECCA), which coming out from multivariate analysis methods.

(iv) *The extraction of the observability range space.*

The observability range space can be extracted by means of the SVD of the matrix $\mathbf{P}$:

$$\mathbf{P} = \mathbf{U}\mathbf{S}\mathbf{V}^T = \begin{pmatrix} \mathbf{U}_1 & \mathbf{U}_2 \end{pmatrix} \begin{pmatrix} \mathbf{S}_1 & \mathbf{0} \\ \mathbf{0} & \mathbf{S}_2 \end{pmatrix} \begin{pmatrix} \mathbf{V}_1^T \\ \mathbf{V}_2^T \end{pmatrix} \tag{2.12}$$

From Equation 2.12 the order n of the system can be theoretically determined by considering the non-zero singular values of $\mathbf{P}$, since n is represented by the dimensions of $\mathbf{S}_1$. According to the main theorem of subspace identification Priori et al. 2018, the observability matrix $\mathbf{O} \in \mathbb{R}^{m \cdot h \times n}$ can be extracted from the singular values and vectors of $\mathbf{P}$. Using the right singular vector matrix $\mathbf{V}_1$ corresponding to the first n singular values in $\mathbf{S}_1$ and the orthogonal projection in Equation 2.10, the extended observability matrix can be extracted:

$$\mathbf{O} = \mathbf{L}_{21} \mathbf{V}_1 \tag{2.13}$$

(v) *The derivation of the system matrices.*

From the observability matrix,$\mathbf{O}$, using its shift invariance property, the matrices $\mathbf{A}$ and $\mathbf{C}$ can be obtained:

$$\mathbf{C} = \mathbf{O}(1 : m, :) \tag{2.14}$$

$$\mathbf{A} = \overline{\mathbf{O}}^{\dagger} \mathbf{O}(m + 1 : m \cdot h, :) \tag{2.15}$$

where $\overline{\mathbf{O}}$ is the matrix $\mathbf{O}$ without the last block of q rows (where $\dagger$ represents

the MoorePenrose inverse).. Once the system matrices are identified, the extraction of the modal parameters of the system is straightforward.

2.3.2 Modal Model

The identification algorithms presented in the previous section permit to form a black-box model for the studied system; obviously, I/O techniques provide a realization with the matrices $\mathbf{A}$, $\mathbf{B}$, $\mathbf{C}$, $\mathbf{D}$, while O/O procedures only $\mathbf{A}$ and $\mathbf{C}_d$. From an identified black-box model without physical meaning, a modal model can be obtained in a further step. The knowledge of frequencies, damping ratios, and eigenvectors (mode shapes) is advantageous in many application within SHM (e.g., model updating, damage detection). As previously said, when the objective of structural identification is the sole estimation of the modal parameters of a system, it is referred to as EMA in the case of knowledge of both input and output, and OMA when only output is available. Modal parameters can be estimated from the identified system and output matrices $\mathbf{A}$ and $\mathbf{C}$. The decomposition of the matrix $\mathbf{A}$:

$$\mathbf{A} = \Psi \Lambda \Psi^{-1} \tag{2.16}$$

gives the n discrete eigenvalues $\lambda_1, \ldots, \lambda_n$ on the diagonal of the matrix $\Lambda \in \mathbb{C}^{n \times n}$. Therefore, the natural frequencies ω_n and the damping ratios ξ_n can be obtained firstly transforming the identified discrete eigenvalues into the complex conjugate pairs of eigenvalues of the continuous state matrix $\mathbf{A}_c$ according to:

$$\lambda_n = \frac{1}{\Delta t} \ln(\mu_n) \tag{2.17}$$

Referring to systems with viscous proportional damping, From the eigenvalues it is possible to extract the pseudo-frequencies $\omega_{pk} = \sqrt{\lambda_k \lambda_k^*}$ and the pseudo-damping ratios $\xi_{pk} = -\frac{Re(\lambda_k)}{\omega_{pk}}$. The mode shapes in correspondence of the measurement points (the columns of $\Phi \in \mathbb{C}^{m \times n}$) are extracted from the system eigenvectors Ψ, which are the same for the discrete and for the continuous representations, by means of the output matrix $\mathbf{C}$:

$$\Phi = \mathbf{C}\Psi \tag{2.18}$$

2.3.3 Algorithm Parameters

There are four parameters in the DD-SSI algorithm that are chosen by the user, and they influence the effectiveness of the algorithm itself, leading to unreliable identifications if they are not correctly selected. These parameters are linked to the dimensions of the Hankel matrix built with the measurements of the output response and its subpartitions (namely, the past output submatrix and the future output submatrix): i, h, j and g.

- The parameter i: The number of block rows of the Hankel matrix;
- The parameter j: The number of columns of the Hankel matrix;
- The parameter h: The number of block rows, h, of future output subpartition $\mathbf{Y}_f$;
- The parameter g: The number of block rows of the past output subpartition $\mathbf{Y}_p$.

These four parameters can be fixed by the user, keeping in mind that they must satisfy certain conditions such as $g + h = i$, and according to Cayley-Hamilton theorem:

$$m \cdot g \geq n \tag{2.19a}$$

$$m \cdot h \geq n \tag{2.19b}$$

$$\tag{2.19c}$$

The number of columns j is typically chosen on the basis of i and the number of samples s in the time-history (Van Overschee and De Moor 2012):

$$i + j - 1 \leq s \tag{2.20}$$

In this section, the effects of each parameter on the identification results are discussed and some rules for their selection are presented.

Parameter i

The parameter i is highly dependent on the structure to identify, particularly from its frequency content and its damping properties. Moreover, the length of the output structural measurements and the sampling frequency should be taken into account as well in choosing the parameter i.

The parameter i defines the number of correlation points in Equation 2.9 and therefore establish the amount of information of the system taken into account for the identification. This makes the parameter i the primary feature strongly affecting the Data-SSI performance.

Since the parameter i depends on the frequency content of the structure, its choice depends on whether the lower frequency f_1 of the studied system, or at least a first estimate, is known or not considering the amount of information carried by the specific chosen value. When an estimate of the frequency content is available, it is possible to use a simple relation to determine the minimum value of i (Magalhaes et al. 2009):

$$\frac{i}{f_s} f_1 > n_c \tag{2.21}$$

where n_c is the number of cycles of the lower frequency. Thus, fixing a value for $n_c \geq 1$, the number of block rows is determined. Therefore a minimum value of i, which ensures at least n_c cycles of the lower frequency f_1 can be determined as follows:

$$i_{min} = n_c \frac{f_s}{f_1} \tag{2.22}$$

Having a value of $i < i_{min}$ if n_c is set equal to 1 will imply that there is not even one full cycle of the lowest structural frequency in the segment of the time histories considered in the identification and will make difficult, if not impossible, to provide an accurate estimation of the lower frequencies.

It is worth pointing out that large values of i will allow us to handle the information about the system better but, at the same time, will increase the computational effort. Besides, especially in the presence of measurement noise, having large values of i will introduce some inaccuracies such as fictitious numerical modes (Rainieri and Fabbrocino 2014) which have nothing to do with the structure under consideration.

Parameter h

In terms of algorithm, h represents the number of block rows of future output sub-partition $\mathbf{Y}_f$ which is, respectively, the part of the entire output measurements used by DD-SSI to extract the observability range space (the signal subspace). Therefore, the parameter h, defining the number of rows of $\mathbf{Y}_f$, represents the length of the prediction horizon and determines the number of rows of the observability matrix.

In order to extract that matrix, the algorithm retains the information of the system contained in the past outputs $\mathbf{Y}_p$ through the orthogonal projection.

In Literature (Peeters and De Roeck 1999; Ubertini et al. 2013) the size of both past and output matrices is usually fixed and considered equal, according to a symmetric partitioning, i.e $h = g = 0.5i$.

To consider the effects of h (and g) on the identification, three different situations need to be considered:

- (a) $h = 0.5i$: the number of block rows of the matrices $\mathbf{Y}_p$ and $\mathbf{Y}_f$ are equal, the matrix $\mathbf{P}$ is square, and the problem presents only one solution as the number of unknowns equals the number of independent equations (determined problem);

- (b) $h < 0.5i$: the past output matrix $\mathbf{Y}_p$ is taller (i.e., has more rows) than the future output matrix $\mathbf{Y}_f$ and the number of block rows of the matrix $\mathbf{P}$, as well as that of the observability matrix, are reduced. The number of rows of the matrix $\mathbf{P}$ is less than the number of columns, corresponding to an undetermined problem for which the number of unknowns is greater than the number of independent equations. In this case, there is not enough information to obtain a unique solution: among the possible solutions, it is of interest the one that minimizes the norm of the unknown vector;

- (c) $h > 0.5i$: contrary to the previous case, the future output matrix, and consequently the observability matrix, is taller. The matrix $\mathbf{P}$ becomes a tall rectangular matrix, corresponding to an overdetermined problem for which the number of independent equations is greater than the number of unknowns; in this case, the least square method provides a solution that minimizes the sum of squared errors of the individual equations (Juang 1994). This situation is preferred because in an ideal free noise problem provides

the exact solution, as the case (a), while in the presence of noise, involves the minimization of a squared error.

Since h is linked to the identification horizon and affects the amount of information, DD-SSI uses to identify the model of the system, larger values of h may result in an improvement of the performance of the algorithm. For this reason, it may be convenient to partition the Hankel matrix in an asymmetric way choosing $h > 0.5i$. On the other end, since g is related to the amount of information needed to determine the observability range space, h cannot exceed a certain limit; otherwise, the algorithm does not retain sufficient information to identify the system. Thus, the selection of the value of h is strictly related to the chosen value of i and should consider all the aspects taken into account for this parameter, above all modal characteristics and sampling frequency.

The value of h, which ensures that, in the data, there are at least n_c cycles of the lowest frequency f_1 is:

$$h \geq n_c \beta \tag{2.23}$$

Finally, the minimum value of h can be expressed as:

$$h_{min} = \max(n_c \beta; 0.5i) \tag{2.24}$$

Parameter g

The user can obviously choose a greater value of h but keeping in mind that the corresponding value of g should ensure that the information about the system contained in the g block rows of the past output matrix be sufficient to allow the extraction of the observability matrix and the identification of the system matrices through the orthogonal projections and the SVD. On such note, the minimum theoretical value of g is determined following one of the conditions imposed in Equation 2.19. Such a theoretical value of g is generally lower than the effective minimum value, mainly because of the presence of noise in the measurements. In practical cases, on the basis of Equation 2.19 it is suggested to use the following rule:

$$g \geq 10 \frac{n}{m} \tag{2.25}$$

in which it is easy to define the minimum value of g:

$$g_{min} = 10\frac{n}{m} \tag{2.26}$$

Parameter j

In Literature the problem of the selection of j is addressed (Chauhan and Tcherniak 2003; Pridham and Wilson 2003). The parameter is typically chosen according to Equation 2.20, once the values of i are fixed. The purpose behind this relation is to select the maximum available value for j because it can aid to reduce the measurement noise and more temporal information of the signal is considered. These benefits go with an increase of the computational effort due to the enlargement of the Hankel matrix. Thus, a good choice of j is a trade-off between all these aspects.

It is worth to underline the connection between j and the number of block rows of $\mathbf{Y}_p$. The Hankel matrix has j columns, each of which contains $m \cdot g$ samples used to identify the system through the remaining $m \cdot h$ samples; thus, in a generic column and for a measurement point, only a signal of g samples is considered. Thus, it is necessary to verify whether the number j of signals of length g is sufficient to contain enough information of the system; a minimum value of j can be defined similarly to that found for i:

$$j =\geq i\frac{h}{g} \tag{2.27}$$

therefore the minimum value of j can be expressed as:

$$j_{min} = i\frac{h_{min}}{i_{min} - h_{min}} \tag{2.28}$$

2.4 Automated Extraction Methodology

In this paper, an automated model identification strategy based on DD-SSI and unsupervised tools is proposed: this strategy allows to extract the modal characteristics of a structure without relying on a single set of selected parameters.

Several automated methodologies have been implemented over the years based on the canonical formulation of DD-SSI, where the main goal is to mimic the abil-

ity of an expert user to perform the identification process successfully. Almost all the proposed methodologies rely on three basic steps: the application of the identification algorithms considering a set of different combinations of the parameters driving the algorithm itself; the removal of noise modes and the collection of the structural ones; a grouping methodology to separate similar structural modes.

All the automated procedures available in literature do not take into account the possibility of adopting an asymmetric partition of the Hankel matrix in the DD-SSI formulation reducing substantially the computational effort. However, it has been proved (Priori et al. 2018) that the structural identification could change consistently with the asymmetric partitioning, often leading to more robust outputs.

Another critical point of the automated methodologies is that, usually, there are some parameters that the users need to set according to their expertise.

The automated methodology presented in this chapter addresses the importance of considering an asymmetric partition of the Hankel matrix in the application of the DD-SSI algorithm and introduces alternatives to the classic, adopted clustering approaches.

The procedure results from an improvement of the one introduced by Ubertini et al. 2013 which, in turn, resulted from an additional upgrade of the automated methodology previously proposed in Hong et al. 2010; Reynders et al. 2012. Ubertini et al. 2013 addressed a procedure consisting in four steps: (a) run of DD-SSI analysis for different values of n and i; (b) elimination of noise modes; (c) clustering of remaining modes; (d) extraction of mean values of modal parameters estimates and their 95% confidence intervals under variations of n and i. Here the first three steps are extended and improved.

The methodology proposed here consists of the following steps:

1. (a) Run of the DD-SSI algorithm for different values of user's defined parameters;
2. (b) Hard validation criteria for certainly mathematical modes;
3. (c) Elimination of noise modes;
4. (d) Clustering of remaining modes & Outliers Removal
5. (e) Selection of the Representative Modal Quantity.

The main steps of the procedure are detailed in the following. Afterward, the methodology will be validated on the dynamic characterization of a real structure, the Civic Tower of Rieti. The sensitivity of the procedure to certain parameters will be discussed within possible tuning strategies of the numerical parameters involved.

2.4.1 DD-SSI runs and parameters selection

A single run of DD-SSI consists in the extraction of the eigenvalues and eigenvectors estimates using the set of identified matrices **A** and **C**; such matrices have been obtained from the measured data using prefixed values of the parameters involved in the algorithm: the system's order n, the number of rows i, the number of block rows of the future outputs h and the number of columns j. As previously mentioned, the model's order which allows the best fitting of the experimental data and the algorithm parameters, i, j, h which provide the best identification results are unknown a priori. In this paper, hence, it is convenient to estimate these eigenvalues/eigenvectors using values of n, i, j, h that vary within defined intervals: ($[n_{min}, n_{max}]$ for n; $[i_{min}, i_{max}]$ for i; $[h_{min}, h_{max}]$ for h; $[j_{min}, j_{max}]$ for j).

About the order model, the lower limit n_{min} should not be less than twice the expected number of physical modes N_m that contributes to the structural response, while the upper limit, n_{max}, should be chosen to be safely greater than n_{min}. The selection of n_{max} must be carefully determined: in fact, while on one hand a large n_{max} is necessary to account for weakly excited modes, on the other hand it will cause the appearance of a large number of numerical modes Magalhaes et al. 2009, which reproduce the noise content of measurement data, usually referred to as noise modes. These spurious modes must then be eliminated in subsequent steps.

Regarding the parameters governing the DD-SSI algorithm, i, j, h, it is possible to choose a reasonable variability range for all of them following some simple guidelines given in Section 2.3.3. The list of the suggested rules for tuning these parameters range is presented in Table 2.1.

Table 2.1: Variability range of DD-SSI Parameters

Parameter	**Description**	**Suggested Value**
n_{min}	Minimum value of n	$2N_m$
n_{max}	Maximum value of n	$5n$
g_{min}	Minimum value of g	$10\frac{n}{m}$
h_{min}	Minimum value of h	$3\frac{f_s}{f_1}$
i_{min}	Minimum value of i	$g_{min} + h_{min}$
i_{max}	Maximum value of i	$3i_{min}$
$j_{min}(i)$	Minimum value of j	$i\frac{h_{min}}{i_{min} - h_{min}}$
$h_{max}(i)$	Maximum value of h	$i - g_{min}$
$j_{max}(i)$	Maximum value of j	$s - i{+}1$

The definition of these parameters comes in a very specific order. This selection starts by defining: the sampling frequency f_s, the number of recording channels m, an estimate of the number of modes excited in the response (hence the model order) and an estimate of the first structural frequency f_1. The first two quantities directly come from the specifications of the monitoring system while the estimates of the model order and of the first structural frequency can be obtained after a preliminary investigation in the frequency domain of the recorded measurement data or from a Finite Element model of the structure if available. Once this information is known, then n_{min}, n_{max}, g_{min}, h_{min}, i_{min} and i_{max} can be immediately computed. For each value of i, within the i_{min}-i_{max} range, it is then possible to define the related values of $j_{min}(i)$, $h_{max}(i)$ and $j_{max}(i)$, which depend on the chosen value for the number of rows in the Hankel matrix. Once these minimum and maximum values are computed for each i it is possible to identify the allowable ones, valid for all the combinations of parameters. The allowable final j_{min} is going to be the maximum one among all the possible ones derived for each choice of i, while the allowable h_{max} and j_{max} are going to be the minimum ones respectively.

Once the maximum-minimum ranges have been set for the four parameters, four corresponding step amplitudes are defined (Δi, Δn, Δh, Δj). Then, the DD-SSI procedure is performed for each possible combination of parameters which lies in those allowable ranges.

Let $\bar{N}$ be the number of DD-SSI analyses and $2W$ the number of complex identified modes and the associated complex conjugates, the outputs of this first

step are the vector that consists of the $2W$ identified complex eigenvalues $\mathbf{\Lambda} = [\lambda_1 \lambda_2 \ldots \lambda_{2W-1} \lambda_{2W}]^T$ and the matrix $\underline{\mathbf{\Psi}} = [\mathbf{\Psi}_1 \mathbf{\Psi}_2 \ldots : \mathbf{\Phi}_{2W-1} \mathbf{\Psi}_{2W}]^T$ that collects the $2W$ associated complex eigenvectors.

2.4.2 Hard validation criteria for certainly mathematical modes

The goal of this methodology is to derive a reliable and robust set of modal information from the computed eigenvalues and eigenvectors. Before extracting them, as described in Section 2.3.2, it is essential to previously separate physical or structural modes (those that are related to the structure) from those, instead, that are associated with mathematical operations. Whether a mode represents a physical mode or a mathematical mode can usually not be deduced from its isolated modal properties. However, there are certain indicators for mathematical modes. Stable systems do not have negative damping. Poles without imaginary part do not represent a system capable of oscillation. Physical poles always occur in complex conjugate pairs at a single model order n. These three criteria, which test whether a mode is certainly mathematical, are sometimes called hard validation criteria (HVC) (Reynders et al. 2012) and can be expressed using the following formulas:

$$Re(\lambda_i) \geq 0 \qquad Im(\lambda_i) = 0 \qquad \lambda_i \overset{n_{\lambda_i}=n_{\lambda_j}}{\neq} \lambda_j^* \tag{2.29}$$

Poles that meet these criteria are removed immediately. The application of the HVC (and the a priori removal of the negative frequency range) as a first step reduces the computational effort of the algorithm.

2.4.3 Noise Modes Elimination

However, not all the noisy mathematical modes will be removed using the HVC, and therefore, an additional effort should be made so to remove as many non-structural modes as possible. In this step, the primary assumption is that physical modes tend to share some similarities with their siblings associated with a different set of DD-SSI parameters or system's order. This task is achieved using the properties of similarity check usually adopted in the construction of the stabilization diagram. For a fixed value of n, a mode can be considered stable when

it appears, with similar frequency, damping and mode shape, also in the model with order $n+2$. The stability property of the modes is then assumed to be an indicator of their physical nature under the assumption that noise modes do not appear with consistent values of frequency, damping and mode shapes when varying the order of the model. This step can be considered an extension of what is the stabilization diagram to the model order. This procedure offers the possibility to take into account the variation of both the model order n but also the possible combinations of the algorithm parameters within an acceptable range.

To explain this mode selection process let the following vectors be constructed:

$$\begin{aligned} \mathbf{f} &= [f_1\ f_2\ \dots\ f_{W-1}\ f_W]^T \\ \boldsymbol{\xi} &= [\xi_1\ \xi_2\ \dots\ \xi_{W-1}\ \xi_W]^T \\ \underline{\boldsymbol{\Phi}} &= [\boldsymbol{\Phi}_1\ \boldsymbol{\Phi}_2\ \dots : \boldsymbol{\Phi}_{W-1}\ \boldsymbol{\Phi}_W]^T \end{aligned} \tag{2.30}$$

where f_w, ξ_w and $\boldsymbol{\Phi}_w$ denote the frequency, damping ratio and mode shape vector of the w^{th} identified mode, for $w = 1, 2, ..., W$. To discern between noise modes and structural ones, the following vector is computed:

$$\mathbf{c} = [c_1\ c_2\ \dots\ c_{W-1}\ c_W]^T \tag{2.31}$$

where the generic w^{th} component c_w, for $w = 1, 2, ..., W$, represents the number of modes, among all the W identified ones, which have frequency, damping and mode shape that are similar to those of the w^{th} mode. These quantities can be calculated as:

$$\mathbf{c}_w = \begin{cases} -1 + \sum_{l=1}^{W} \delta_{l,w}, & \text{if } \xi_w \in [0,\ \xi_{max}] \\ 0, & \text{if } \xi_w \notin [0,\ \xi_{max}] \end{cases} \tag{2.32}$$

with:

$$\delta_{l,w} = \begin{cases} 1, & \text{if } \Delta f_{l,w} \leqslant \epsilon_f, \Delta\xi_{l,w} \leqslant \epsilon_\xi, 1 - MAC_{l,w} \leqslant \epsilon_{MAC} \\ 0, & \text{otherwise} \end{cases} \tag{2.33}$$

$$\Delta f_{l,w} = \frac{|f_l - f_w|}{f_w}\ ;\quad \Delta\xi_{l,w} = \frac{|\xi_l - \xi_w|}{\xi_w}\ ;\quad MAC_{l,w} = MAC(\boldsymbol{\Phi}_l, \boldsymbol{\Phi}_w)$$

where ξ_{max} is an estimated maximum value for the damping ratio of the physical modes (which must be chosen according to the structural characteristics),

$MAC(\boldsymbol{\Phi}_l, \boldsymbol{\Phi}_w)$ is the Modal Assurance Criterion between $\boldsymbol{\Phi}_l$ and $\boldsymbol{\Phi}_w$, while ϵ_f, ϵ_ξ and ϵ_{MAC} are user-defined tolerances that are equivalent to those often adopted to build stabilization diagrams. There are several options for choosing the values of these tolerances: in the current literature, the following values-ranges are suggested: ϵ_f=0.01, ϵ_ξ=0.03-0.04 and ϵ_{MAC}=0.01-0.05. However, it is important to investigate these values for the specific system under investigation and check the sensitivity of the identification results with respect to these tolerances.

The *wth* mode is said to be stable when it is "similar", in terms of frequency, damping ratio and mode shape, to a reasonable and acceptable number of other modes. Consequently the user needs to set a minimum number $\bar{C}_{min}$ of similar modes that has to be reached in order to declare that that group of modes represents a structural mode and not a spurious one. Choosing large values for $\bar{C}_{min}$ increases the severity of the stability check and is not recommended as it would increase the risk of eliminating physical modes. On the contrary, to keep relatively small value of $\bar{C}_{min}$ would allow to eliminate most of the noise modes without removing structural ones. Residual noise modes will then be eliminated by the subsequent clustering analysis.

To evaluate the number of stable poles, the vector $\mathbf{S}$ is computed:

$$\mathbf{c} = [S_1 \; S_2 \; \ldots \; S_{W-1} \; S_W]^T \tag{2.34}$$

$$S_w = \begin{cases} 1, & \text{if } c_w \geqslant \bar{C}_{min} \\ 0, & \text{otherwise} \end{cases} \tag{2.35}$$

where 0 and 1 indicate unstable and stable modes, respectively. Hence, the total number of stable modes, P, turns out to be:

$$P = \sum_{l=1}^{W} S_l \tag{2.36}$$

The vectors of stable frequencies, damping ratios and mode shapes (where stability is denoted by the superscript s) can be extracted as:

$$\begin{aligned} \mathbf{f}^s &= \mathbf{HE} \times \mathbf{f} \\ \boldsymbol{\xi}^s &= \mathbf{HE} \times \boldsymbol{\xi} \\ \underline{\boldsymbol{\Phi}}^s &= (\mathbf{HE} \times \boldsymbol{\Phi}^T)^T \end{aligned} \tag{2.37}$$

where **HE** is a $P \times W$ matrix whose non-zero components are:

$$HE_{p,\pi_p} = 1 \text{ for } p = 1, 2, \ldots, P \tag{2.38}$$

where π_1, π_2, ..., π_P are the positions of the non-zero terms contained in vector **S**.

2.4.4 Clustering & Outliers Removal

Each stable mode is identified by its position p in vectors $\mathbf{f}^s$ and $\boldsymbol{\xi}^s$, whereas the corresponding eigenvector is the p^{th} column of matrix $\underline{\boldsymbol{\Phi}}^s$, indicated as $\boldsymbol{\Phi}_p^s$. The clustering analysis aims at grouping the P stable modes into homogeneous sets (clusters). The final aim is that each cluster contains only the modal parameters estimates of the same structural mode.

Here two different clustering solutions are given. The first one comes from the application of a particular application of the k-Means clustering technique, and the second consists in the introduction of the Density-Based Spatial Clustering of Applications with Noise (DBSCAN) procedure. The generic version of k-Means (Lloyd 1982) is probably the most well-known clustering algorithm of all times; however, it presents several disadvantages. First of all, this algorithm requires the definition of a priori number of clusters and, additionally, is extremely sensitive to the starting point. Here a slightly different version of the k-Means algorithm is adopted, proposed by Ubertini et al. 2013: this algorithm is based on the random generation of the cluster seeds without any specific requirement on the number of clusters. However, this methodology is here improved, introducing a final outlier cleaning procedure which was missing in the original proposal Ubertini et al. 2013. Furthermore, the MSD is here considered as an alternative metric distance to the one initially used by Ubertini et al. 2013. The MSD presents several advantages, and mainly, it takes into account the variance carried on by each feature, and that could be efficiently used within the blind k-Means procedure.

DBSCAN (Ester et al. 1996) is here proposed as an optimal substitute of the blind k-Means search previously cited and has several significant advantages. This algorithm is born without the specific requirement regarding the number of clusters, as opposed to k-Means, it can find arbitrarily shaped clusters and presents the advantage of reducing the single-link effect that affects several clustering tech-

niques is reduced. Only two parameters are governing the algorithm which are mostly insensitive to the ordering of the points in the dataset and for that can be easily set following defined guidelines. More importantly, this algorithm has a notion of noise and is robust to outliers.

The ultimate definition of a generic r^{th} cluster (C_r) is the same for both these approaches, and it is given by a set of integer numbers representing the positions of its elements within the vectors $\mathbf{f}^s$, $\boldsymbol{\xi}^s$, $\underline{\boldsymbol{\Phi}}^s$. As an example, the following cluster:

$$C_r = \{a_1, a_2, \ldots, a_{g_r}\} \tag{2.39}$$

has dimension $D_{C_r} = g_r$, and is composed by all the modes having the following frequencies, damping ratios and mode shapes:

$$\begin{aligned} C_{r,f} &= \{f^s_{a_1}, f^s_{a_2}, \ldots, f^s_{a_{g_r}}\} \\ C_{r,\xi} &= \{\xi^s_{a_1}, \xi^s_{a_2}, \ldots, \xi^s_{a_{g_r}}\} \\ C_{r,\boldsymbol{\Phi}} &= \{\boldsymbol{\Phi}^s_{a_1}, \boldsymbol{\Phi}^s_{a_2}, \ldots, \boldsymbol{\Phi}^s_{a_{g_r}}\} \end{aligned} \tag{2.40}$$

The mean values of the sets defined in Equation 2.44 represent the coordinates of the centroid of cluster C_r and are denoted as $\bar{f}_{C_r}$; $\bar{\xi}_{C_r}$ and $\bar{\boldsymbol{\Phi}}_{C_r}$, respectively.

Blind k-Means

Letting the vector $\mathbf{p}$ be defined as $\mathbf{p} = [1, 2, ..., P]^T$, a random permutation is introduced, which yields a new vector v containing the elements of $\mathbf{p}$ sorted in random order. At this point a P step procedure is performed.

At the first step, the v_1^{th} mode is considered as the first cluster seed, v_1 being the value of the first component of vector $\mathbf{v}$. The first cluster C_1 is thus initiated as:

$$C_1^1 = \{v_1\} \tag{2.41}$$

where C_1^1 represents the cluster C_1 evaluated at step number 1 (superscript 1).

The second step starts considering the v_2^{th} mode and computing a distance measure of this mode from the available clusters $d_{v_2-C_1}$ (in the second step the only available cluster is C_1). This distance quantifies the degree of similarity between the v_2^{th} mode and the existing cluster C_1. Once this distance is available, it is possible to decide if the v_2^{th} mode belongs to the already available clusters or if it is something different, once a reasonable threshold, d_{max}, is set for the distance

level. Then, the assignment can follow this rule

$$\begin{aligned} \text{if } d_{v_2-C_1} \leqslant d_{max} \Rightarrow C_1^2 = C_1^1 \cup \{v_2\} \\ \text{if } d_{v_2-C_1} > d_{max} \Rightarrow C_1^2 = C_1^1, C_2^2 = \{v_2\} \end{aligned} \tag{2.42}$$

Therefore mode v_2 is assigned to cluster C_1 if it is similar to it in terms of frequency and mode shape, otherwise v_2 is taken as a new cluster seed and cluster C_2 is initiated.

At the generic q^{th} step, a certain number r of clusters will exist, each of them containing a different number of modes. At this step, the v_q^{th} mode is considered and the following vector, $\mathbf{d}_q$, containing the distances from this mode to all the available clusters at the q^{th} step, is calculated:

$$\mathbf{d}_q = [d_{v_q-C_1}\ d_{v_q-C_2}\ \dots d_{v_q-C_r}]^T \tag{2.43}$$

Then, the following rule is applied:

$$\begin{aligned} \text{if } d_{q,h} = \min(\mathbf{d}_q) \leq d_{max} \Rightarrow C_1^q = C_1^{q-1}, \cdots, C_h^q = C_h^{q-1} \cup \{v_q\}, \cdots, C_r^q = C_r^{q-1} \\ \text{if } d_{q,h} > d_{max} \Rightarrow C_1^q = C_1^{q-1}, \cdots, C_r^q = C_r^{q-1}, C_{r+1}^q = \{v_q\} \end{aligned} \tag{2.44}$$

Once this vector is available, it is possible to decide if the v_q^{th} mode belongs to one of the already available clusters or if a new cluster needs to be initiated. This goal is achieved, looking for the minimum distance, $d_{q,h}$, collected in the distance vector, $\mathbf{d}_q$, which represents the distance of the v_q^{th} mode from a cluster C_h available at q^{th} step. If this relative distance is less or equal to the defined threshold, d_{max}, mode v_q is assigned to cluster C_h (which is the closest one in terms of mean frequency and mode shape); otherwise mode v_q is taken as a new cluster seed and cluster C_{r+1} is created.

The procedure stops at step number P. At this stage a certain number of clusters will exist and only N_{cl} of those clusters are retained. A criterion for the user to choose N_{cl} might be that of disregarding those clusters that are so small that cannot be considered as representative samples.

Ubertini et al. 2013 in their automated methodology propose the following physical-distance to evaluate the similarity level of each mode with respect the

available clusters

$$d_{v_q - C_h} = \frac{|f^s_{v_q} - \bar{f}_{C^q_h}|}{\bar{f}_{C^q_h}} + 1 - MAC(\boldsymbol{\Phi}^s_{v_q}, \bar{\boldsymbol{\Phi}}_{C_h}) \tag{2.45}$$

which represents a combined, dimensionless measure of the distance between the considered mode and the centroid of the clusters, in terms of frequency and mode shapes.

Here an alternative distance measure is proposed: the Mahalanobis Square Distance (Mahalanobis 1936).

Let us denote by $\mathbf{x}_q \in \mathbb{R}^{b\times 1}$ the feature vector, obtained collecting once the frequencies and once the mode shapes identified for the q^{th} mode, where b specify the dimensionality of the feature vector, and it will be equal to the number of structural modes, N, for the frequency vector and equal to m for the mode shapes. Then $\boldsymbol{\mu}_{C_r}$ and $\boldsymbol{\Sigma}_{C_r}$ represent the mean vector and covariance matrix of the r^{th} cluster. The Mahalanobis Squared Distance of $\mathbf{x}_q$ from the r^{th} cluster is defined as:

$$D^2_{\mathbf{x}_q - C_h} = (\mathbf{x}_q - \boldsymbol{\mu}_{C_r})^T \boldsymbol{\Sigma}^{-1}_{C_r} (\mathbf{x}_q - \boldsymbol{\mu}_{C_r}) \tag{2.46}$$

where the superscripts ^{T} and $^{-1}$ denote transpose and inverse of a matrix, respectively.

The Mahalanobis Squared Distance may be thought of as a weighted squared Euclidean distance of $\mathbf{x}_q$ from $\boldsymbol{\mu}_{C_r}$, where the weighting matrix is the covariance matrix. The MSD provides a measure of how distant a feature vector is from the training population in a statistical sense, as the Mahalanobis distance takes into account the correlations among variables.

In other words, two feature vectors having the same Mahalanobis distance from the mean of the training population have the same probability of having been generated from that training population. The downside in using the MSD is that it relies on the assumption that the data are drawn from an underlying normal distribution. Therefore before performing this step with MSD, it is important to assure that the data are normally distributed.

The driving parameter in both the distance options for the blind k-Means approach is the threshold distance d_{max}. This is the indicator to define the criterion for constructing the clusters of modes. Indeed, a relatively small value of d_{max} might lead to the appearance of clouds of clusters representing the same physical

mode, while a relatively large number of d_{max} might lead to erroneous attributions of estimated modes to clusters. The knowledge of the data distribution is crucial for defining a threshold, able to robustly distinguish different clusters. The definition of this parameter in the case of the physical distance depends on the sensitivity of the user, introducing uncertainty in the identification that should be avoided. The Mahalanobis Squared Distance of normally distributed instances is asymptotically χ^2-distributed with b degrees of freedom, where b is the dimension of the feature vector. However, the asymptotic convergence is very slow, and defining the threshold based on the χ^2 percentiles may be too conservative, even for large samples (Hardin and Rocke 2005). Also, the χ^2 b-distribution of MSD is true when the true mean and covariance matrix of the feature population are employed, while in the present application, the sample estimators of said statistics are used. Ververidis and Kotropoulos 2009 proved that the distribution of the MSD of a b-variate point $\mathbf{x}$, when $\mathbf{x}$ is not involved in the estimation of the sample mean and the sample covariance matrix, follows a scaled F-distribution with degrees of freedom b and $n_{obs} - b$, where b is the dimension of $\mathbf{x}$, and n_{obs} is the number of observations used to construct the sample statistic estimators. This property can be used to set the threshold value.

Regardless of the distance, the user is willing to use; it is important to introduce an additional step before moving to the selection of the representative modal quantity: the outlier removal. Outlier deletion is controversial, especially when the underlying probability distribution is unknown or small sets are investigated. There is very small literature investigating whether modal properties from different model orders, which are associated with the same physical system mode, tend to be normally distributed or not. Physical poles often follow trends with increasing system order, which sometimes are suddenly disrupted. Empirical evidence also shows that sometimes obvious outliers are present in a cluster and that the identification variance from large numbers of measurements can be improved when outlier rejection is applied to the identifications from the individual measurements. Outliers are individual values that fall outside of the overall pattern of the rest of the data. This definition is somewhat vague and subjective, so it is helpful to have the rule to help in considering if a data point truly is an outlier.

Here the interquartile range rule is used for detecting the presence of outliers and remove them.

The starting point is that any set of data can be described by five number:

the *minimum*, or lowest value of the dataset; the *first quartile* Q_1 - this represents a quarter of the way through the list of all the data; the *median* of the data set - this represents the midpoint of the list of all of the data; the *third quartile* Q_3 - this represents three quarters of the way through the list of all the data; the *maximum*, or highest value of the data set.

These five numbers can be used to tell us quite a bit about our data. The interquartile range shows how the data is spread about the median, and it is less susceptible than the range (the minimum subtracted from the maximum) to outliers. The interquartile range is calculated in much the same way as the range. All that we do is subtract the first quartile from the third quartile:

$$IQR = Q_3 - Q_1. \tag{2.47}$$

The interquartile range can be used to help detect outliers. A commonly used rule says that a data point is an outlier if it is more than 1.5 IQR above the third quartile or below the first quartile. Said differently, low outliers are below Q_1-1.5IQR and high outliers are above Q_3+1.5IQR.

Let us denote by $Q_{1_{C_{r,f}}}$, $Q_{3_{C_{r,f}}}$, $Q_{1_{C_{r,\xi}}}$ and $Q_{3_{C_{r,\xi}}}$, the first and third quartiles of rth frequency cluster and of the rth damping cluster. Accordingly, $IQR_{C_{r,f}}$ and $IQR_{C_{r,\xi}}$ are the IQRs of the rth frequency cluster and of the rth damping cluster respectively. The interquartile rule is then applied separately on the frequency and damping ratio dimension of the cluster.

$$\mathbf{v}_q = \begin{cases} \text{stable pole ,} & \text{if } Q_{1_{C_{r,f}}} - 1.5 \cdot IQR_{C_{r,f}} \leq f_q \leq Q_{3_{C_{r,f}}} + 1.5 \cdot IQR_{C_{r,f}} \\ \text{outlier ,} & \text{otherwise} \end{cases} \tag{2.48}$$

$$\mathbf{v}_q = \begin{cases} \text{stable pole ,} & \text{if } Q_{1_{C_{r,\xi}}} - 1.5 \cdot IQR_{C_{r,\xi}} \leq \xi_q \leq Q_{3_{C_{r,\xi}}} + 1.5 \cdot IQR_{C_{r,\xi}} \\ \text{outlier ,} & \text{otherwise} \end{cases} \tag{2.49}$$

DBSCAN

Ester et al. 1996 proposed a clustering approach which quickly has become the most established density-based clustering algorithm, *DBSCAN* (Density-Based Spatial Clustering of Applications with Noise).

Unlike several clustering algorithms, like k-Means, DBSCAN does not require the number of clusters as a parameter. It infers the number of clusters just working on the data, and it can discover clusters of arbitrary shape (for comparison, k-Means usually discovers spherical clusters).

DBSCAN tries to mimic the capacity of humans to identify clusters when looking at sample sets of points easily. The main reason why humans are able to tell the clusters is that within each cluster, there is a density of points, which is considerably greater than that outside of the cluster. Moreover, the density within the regions of noise is lower than the density in each cluster.

The principal idea is that for each point of a cluster the neighborhood of a given radius ϵ has to contain at least a minimum number of points (MP), i.e., the density in the neighborhood has to surpass some threshold. The shape of a neighborhood is given by the choice of a distance function for two points p and q, denoted by *dist(p,q)*.

Before explaining the step of the DBSCAN algorithm, let us give some definitions which lay at the core of this procedure.

Definition 1 (ϵ-neighborhood of a point): The ϵ-neighborhood of a point p, denoted by N$\epsilon(p)$, is defined N$\epsilon(p) = \{q \in D | dist(p,q) \leq \epsilon\}$. A naive method could require for each point in a cluster that there are at least a minimum number (MP) of points in an ϵ-neighborhood of that point.

However, this strategy fails because there are two different types of points in a cluster, the ones inside of the cluster (core points) and the ones on the edge of the cluster (border points). In general, an ϵ-neighborhood of a border point contains significantly fewer points than an ϵ-neighborhood of a core point. Accordingly, the minimum number of points needs to be set to a relatively low value for including all points belonging to the same cluster. However, this parameter will not be characteristic for the respective cluster, especially in noisy applications. Therefore, we require that for every point p in a cluster C there is a point q in C so that p is inside of the ϵ-neighborhood of q and N$\epsilon(q)$ contains at least MP points. This definition is elaborated in the following

Definition 2 (directly density-reachable): A point p is directly density-reachable from a point q with respect to ϵ and MP if

1) $p \in N\epsilon(q)$

2) $|N\epsilon(q)| > MP$ (core point condition).

Directly density-reachable is symmetric for couples of core points. Despite of

this definition, it is not symmetric if one core point and one border point are involved.

Definition 3 (density-reachable): A point p is density-reachable from a point q with regard to ϵ and MP if there is a chain of points $p_1, ..., p_n$, $p_1 = q$, $p_n = p$ such that p_{i+1} is directly density-reachable from p_i.

Density-reachability is a canonical expansion of direct density-reachability. This relation is transitive, and it is not symmetric in general; however, it is symmetric for core points.

There is the possibility that two border points belonging to the same cluster C are not density reachable from each other because the core point condition might not true for both of them. Nevertheless, there must exist a core point in C from which both border points of C are density-reachable. Therefore, the definition of density-connectivity is defined, which covers this relation of border points.

Definition 4 (density-connected): A point p is density-connected to a point q with respect to ϵ and MP if there is a point o such that both, p and q are density-reachable from o with respect to ϵ and MP. Density-connectivity is a symmetric relation.

For reachable density points, the relation of density-connectivity is also reflexive. A cluster can be defined as a set of density-connected points, which is maximal with regard to density-reachability. The definition of noise is given in relation to a given set of clusters. Noise is the collection of points in D not belonging to any o fits clusters.

Definition 5 (cluster): Let D be a database of points. A cluster C with respect to ϵ and MP is a non-empty subset of D satisfying the following conditions:

1) $\forall$ p, q: if $p \in C$ and q is density-reachable from p with regard to ϵ and MP, then $q \in C$. (Maximality)

2) $\forall$ p, $q \in C$: p is density-connected to q with respect to ϵ and MP. (Connectivity)

Definition 6 (noise): Let C_1 ..... C_k be the clusters of the database D with respect to parameters ϵ and MP_i, $i = 1.....k$. The noise is defined as the set of points in the database D not belonging to any cluster C_i, i.e. noise = $\{p \in D | \forall i : p \notin C_i\}$.

DBSCAN starts from a randomly chosen data point that has not been visited. The neighborhood of this point is computed using a distance ϵ (All points which are within the ϵ radius are considered to be neighborhood points). If the number

of points within that radius is sufficient (MP), then the data point is the first point in the new cluster, and the clustering process starts. Otherwise, the point is classified as noise. In any case, that point is marked as visited.

Then, all the points within the ϵ distance neighborhood of this first point in the new cluster, also are assumed to belong to the same cluster. This procedure is then iteratively replicated for all of the new points that have been just added to the cluster.

This process is repeated until all points in the cluster are determined i.e., all points within the ϵ neighborhood of the cluster have been visited and labeled.

Once the current cluster is completed, a new point, labeled as unvisited, is retrieved and processed, leading to the creation of a new cluster or noise. This process is repeated until all points are marked as visited, and each point has been assigned to a cluster or being noisy.

The DBSCAN algorithm basically requires two parameters: ϵ and MP. ϵ is the minimum distance between two points. Consequently, if the distance between two points is lower or equal to this value (ϵ), these points are considered neighbors. MP is the minimum number of points to form a dense region.

As a general rule, a minimum (MP) can be derived from a number of dimensions (b) in the data set, as $MP \geq b+1$. When dealing with a noisy dataset, larger values are usually more suitable, leading to more significant clusters. The minimum value for the MP must be three, but the larger the data set, the larger the MP value that should be chosen and an empirical rule usually adopted is to pick MP at least equal to $\log(n_{obs})$, where n_{obs} is the number of available observations in the dataset.

If the ϵ value chosen is too small, a large part of the data will not be clustered. It will be considered outliers because it does not match the number of points to create a dense region. However, if the chosen value is too large, clusters will merge, and most of the objects will be in the same cluster. The ϵ should be chosen based on the distance of the dataset, but in general small ϵ values are preferable. In a clustering with $MP = k$, we expect that core pints and border points k-distance are in a certain range, while noise points can have much larger k-distance; thus we can observe a knee point in the k-distance plot. This heuristic rule is based on the following observation. Let d be the distance of a point p to its k-th nearest neighbor, then the d-neighborhood of p contains exactly $k + 1$ points for almost all points p. The d-neighborhood of p includes more than $k + 1$ points only if

many points have precisely the same distance d from p, which is quite unlikely. Moreover, changing k for a point in a cluster does not reflect in large changes of d. This only happens if the k-th nearest neighbors of p for $k = 1, 2, 3....$ are placed around a straight line which is commonly not true for a point in a cluster.

For a given k it is possible to define a distance function k-dist, starting from the database D, mapping each point to the distance from its k-th nearest neighbor. Information about the density distribution of the dataset can be derived by sorting ordering the points of the database in decreasing order of their k-dist values. This graph is known as the sorted k-dist plot. Choosing an arbitrary point p, the parameter ϵ can be set equal to k-dist(p) and the parameter MP equal to k, all points with an equal or smaller k-dist value will be core points. If a threshold point is found with the maximal k-dist value in the thinnest cluster of D, then the desired parameter values are defined. The threshold point is the first point in the first valley of the sorted k-dist graph. All points with a higher k-dist value (left of the threshold) are considered to be noise, all other points (right of the threshold) are assigned to some cluster.

2.4.5 Selection of the Representative Modal Quantity

Each cluster obtained from the clustering step contains a large number of modes. Hence, the question arises on how to choose a single representation of the individual modal properties. Magalhaes et al. 2009 used the average natural frequency, damping ratio and mode shape calculated from all observations in each physical cluster while Ubertini et al. 2013 gave the modal parameters estimates in terms of their mean values and corresponding 95% confidence. All the aforementioned methods have their advantages and disadvantages, which depend on the planned application of the algorithm, and can be used with the proposed AOMA methodology. In this work, the approach described by Ubertini et al. 2013. The N_{cl} clusters obtained after completing the previous step are conveniently sorted in increasing order of their average natural frequencies. Then, the identified modal parameters estimates (superscript id) are finally given in terms of their mean values and corresponding 95% confidence intervals as:

$$f^{id} = \left[\bar{f}_{C_1} \pm \frac{1.96 \cdot \sigma_{f,C_1}}{\sqrt{D_{C_1}}} \quad \bar{f}_{C_2} \pm \frac{1.96 \cdot \sigma_{f,C_2}}{\sqrt{D_{C_2}}} \quad ... \quad \bar{f}_{C_{\bar{N}_{cl}}} \pm \frac{1.96 \cdot \sigma_{f,C_{\bar{N}_{cl}}}}{\sqrt{C_{\bar{N}_{cl}}}} \right] \tag{2.50}$$

$$\xi^{id} = \left[\bar{\xi}_{C_1} \pm \frac{1.96 \cdot \sigma_{\xi,C_1}}{\sqrt{D_{C_1}}} \quad \bar{\xi}_{C_2} \pm \frac{1.96 \cdot \sigma_{\xi,C_2}}{\sqrt{D_{C_2}}} \quad ... \quad \bar{\xi}_{C_{\bar{N}_{cl}}} \pm \frac{1.96 \cdot \sigma_{\xi,C_{\bar{N}_{cl}}}}{\sqrt{C_{\bar{N}_{cl}}}} \right] \tag{2.51}$$

$$\underline{\mathbf{\Phi}}^{id} = \left[\bar{\mathbf{\Phi}}_{C_1} \pm \frac{1.96 \cdot \sigma_{\mathbf{\Phi},C_1}}{\sqrt{D_{C_1}}} \quad \bar{\mathbf{\Phi}}_{C_2} \pm \frac{1.96 \cdot \sigma_{\mathbf{\Phi},C_2}}{\sqrt{D_{C_2}}} \quad ... \quad \bar{\mathbf{\Phi}}_{C_{\bar{N}_{cl}}} \pm \frac{1.96 \cdot \sigma_{\mathbf{\Phi},C_{\bar{N}_{cl}}}}{\sqrt{C_{\bar{N}_{cl}}}} \right] \tag{2.52}$$

where σ_{f,C_r} and σ_{ξ,C_r} are the standard deviations of the frequencies and damping ratios of the generic rth cluster C_r, while $\sigma_{\mathbf{\Phi},C_r}$ is a vector containing the standard deviations of the single components of $\bar{\mathbf{\Phi}}_{C_r}$.

The 95% confidence intervals for the mean values, in Equations 2.50, 2.51 and 2.52 are calculated under the hypotheses of Gaussian populations and large samples (dimensions larger than 1015). Though such confidence intervals are not directly related to the overall uncertainties of the modal parameters estimates (for details on this topic the reader is referred to Carden and Mita 2011), they are related to the uncertainties arising from different selections of n, h, j and i and allow to check the appropriateness of the chosen intervals for those parameters. For instance, relatively small confidence intervals confirm, to some extent, the adequateness of the chosen values, while large confidence intervals may indicate that convergence of the modal parameters estimates with those choices of the algorithm's parameters has not been achieved.

2.5 Conclusions

An unsupervised multi-stage approach to perform Automated Operational Modal Analysis was proposed. This approach improves the ones existing in literature in multiple aspects, offering a is fully automated methodology. No parameters or thresholds have to be provided depending on the user's expertise and sensitivity. Neither the damping ratios nor the complexities of the to-be-identified modes are limited in any way. The methodology is validated in Chapter 5, where it is applied to the ambient vibration data recorded during a long-term monitoring campaign on a historical civic tower located in Italy.

Part II
New Damage Indicators

Chapter 3

Audio Indicators as Damage Sensitive Features

In the previous part of the dissertation, an automated procedure is addressed to derive modal parameters from the vibration response of a structural system using almost none parameters depending on the user's sensitivity to the problem, in order to confidently use them as damage sensitive features. However, the proposed framework consists of several steps and presents a complex structure with medium computational requirements involved.

The computational requirements of an optimal DSF should be minimal, as the feature extraction process is repeated many times, in order to get a feature population with a number of individuals large enough to be statistically meaningful. Moreover, the feature extraction process should be as simple as possible, to guarantee consistency of the results, irrespective of the user's expertise level.

The type of feature proposed herein, Cepstral Coefficients is an adaptation of the Mel-Frequency Cepstral Coefficients (MFCCs), which are the features conventionally used in the fields of speech and speaker recognition.

The procedure apt to extract such information from the structural response time histories is presented in Section 3.1.1, stressing how well the CCs meet the characteristics of compactness, minimal computational expense and damage sensitivity required to damage sensitive features. In particular, it will be shown how the extraction modalities of the Cepstral features are quite different from those commonly used in the field of structural health monitoring. On the contrary, Cepstral features are extracted directly from the structural response only by means of

digital signal processing operations.

3.1 Cepstral Coefficients

Recently, Balsamo et al. 2014 proposed an adaptation of Mel Frequency Cepstral Coefficients as damage sensitive features for damage detection problems in civic structures. MFCCs are features widely used in the field of speaker and speech recognition, and they differ from the other common DSFs, such as modal frequencies, as they allow for consideration of the response property in both the frequency and time domain simultaneously. These MFCCs are defined as the inverse discrete cosine transform of the log-modified-spectrum of the system response.

Originally the cepstrum was born with the aim of finding a procedure able to filter the effects of echoes from time series, and it was first introduced by Bogart 1963 and his colleagues at Bell Laboratories in 1963. The discrete-time formulation of the cepstrum and of its complex counterpart, the complex cepstrum, was lately addressed by Oppenheim and Schafer 2004; Oppenheim et al. 2001. They also gave an analytical expression for the cepstrum for minimum phase signals, from which it results that the cepstrum is an explicit function of the poles and zeros of the transfer function of the analyzed system.

The potential of cepstrum as monitoring features has increased with time, and these indicators were used in a lot of different fields, from geophysics to mechanical engineering. Because of its nature, Cepstral Coefficients resulted in being particularly suitable as damage sensitive features for pursuing damage detection in rotating machinery (Farrar and Duffey 1999). Their ability to display the presence of echoes in a signal turns out to be particularly helpful when dealing with malfunctioning rotating machines, where the effect of a broken element produces periodic peaks in the cepstrum representation of the machine response (Farrar and Duffey 1999).

Gao and Randall 1996 exploited the explicit relation of cepstrum coefficients to the poles and zeros of the transfer function to retrieve the frequency response function from the measured response of a mechanical system.

Davis and Mermelstein 1980 proposed a compact version of cepstrum and suggested the use of the Mel-spectrum, named after the Melody scale, to get the Cepstral representation of speech signals. The discrete set of coefficients extracted

from the sampled speech signal were called Mel-Frequency Cepstral Coefficients. It is noteworthy that such representation of the Cepstral features is a compact version of the real cepstrum, which preserves only information on the magnitude of the log-spectrum, while the information on the phase is lost.

The first application of these coefficients for civil engineering applications was given by Zhang et al. 2011, who used MFCCs to detect concrete delamination on a bridge deck by analyzing the MFCCs extracted from records of the impact sound produced by impacting the surface of the concrete slab with a steel bar. A more robust application of MFCCs as damage sensitive features was given in Balsamo et al. 2014, where these features were implemented in a statistical pattern recognition framework to carry on damage detection in civil structures.

These coefficients present explicit relations to poles and zeros of the system transfer function leading to the speculation that a strong relationship must exist between such coefficients and structural properties. Finally, these features require very low user expertise to be extracted and analyzed, making them particularly convenient for implementation into automatic structural health monitoring procedures.

In this section, the Cepstral Coefficients (CCs) are investigated. They are the results of the adaptation of MFCCs, proposed by Balsamo et al. 2013, implemented to make these features suitable for civil structures. These features are extracted directly from the time histories of the structural response and were successfully used in a statistical pattern recognition approach to infer damage occurrence (Balsamo et al. 2014 Balsamo et al. 2013).

3.1.1 Features Extraction Procedure

The Cepstral Coefficients can be extracted from a sampled signal $x[n]$ applying the procedure defined in the flow chart in Figure 3.1; the reader is referred to Beigi 2011 for a detailed treatment of the subject.

In the preliminary step, each one of the time histories N_{th} is framed into segments (N_{frames}), which must be long enough to be considered stationary (Figure 3.2a). $N_{samples}$ is the number of samples for each frame. Then, in order to reduce the riddle effects on the frame spectra due to the segmentation procedure, non-rectangular windows (usually Hamming windows) are applied to each frame (Figure 3.2b).

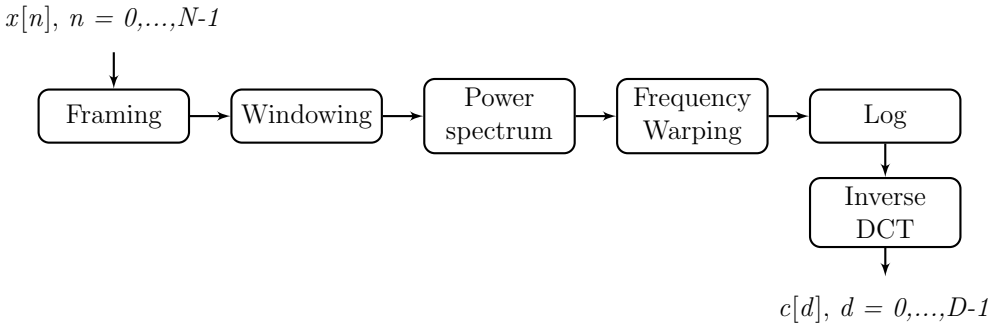

Figure 3.1: CCs Extraction Process.

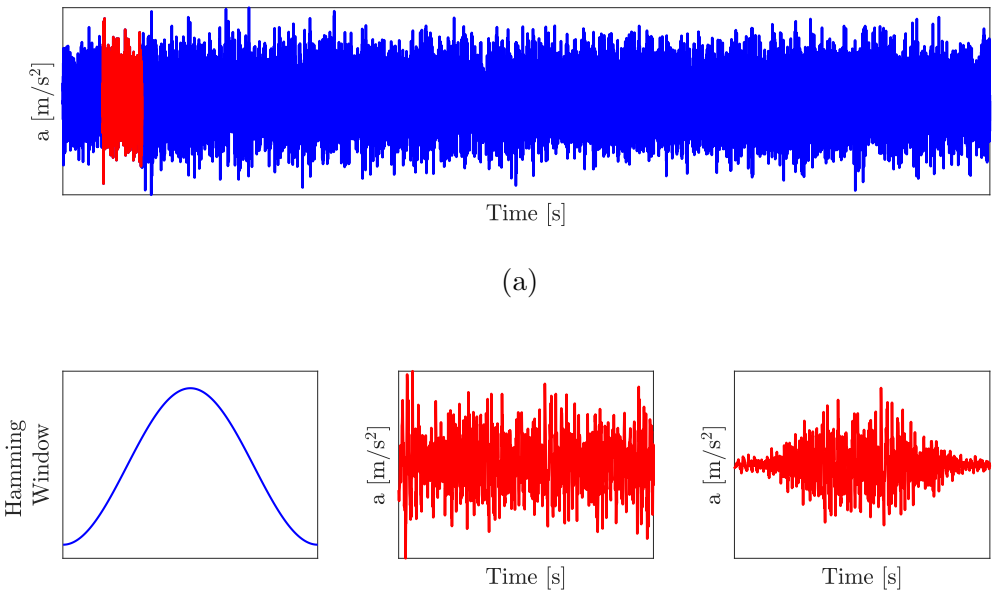

Figure 3.2: Framing and Windowing: (a) frame selection in the acceleration time history, (b) application of the Hamming window to the i^{th} frame.

Subsequently, applying the Discrete Fourier Transform (DFT), the power spectrum is evaluated for each frame. To emphasize the parts of the spectrum that are more likely to be expressing the structural behavior a *frequency warping* procedure is performed. It allows to modify and scale the linear frequency scale with the objective of weighing more the area of the spectrum with the greatest energy content. The new modified frequency scale and the linear frequency scale are almost equivalent up to a cutoff frequency f_c, after which their relation becomes

logarithmic. This cutoff parameter is defined by the user. If N_{frames} is the number of frames obtainable from one time history, at the end of this first framing stage for each realization N_{th} there will be $N_{samples} \times N_{frames}$ response windowed segments. Averaging the spectra of all such segments results in the generation of what will be referred to as an *average spectrum* (Figure 3.3a). The average spectrum highlights the frequency range within which the greatest frequency content is observable. The cutoff frequency is then chosen as the upper bound of the portion of the averaged spectrum. This new scale mimics the trend of the Mel-scale, working on a frequency range compatible with structural problems, according to the following expression

$$\tilde{f} = f_c \log_2(1 + \frac{f}{f_c}) \tag{3.1}$$

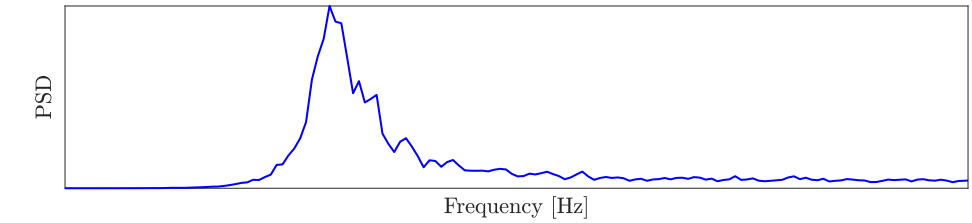

(a)

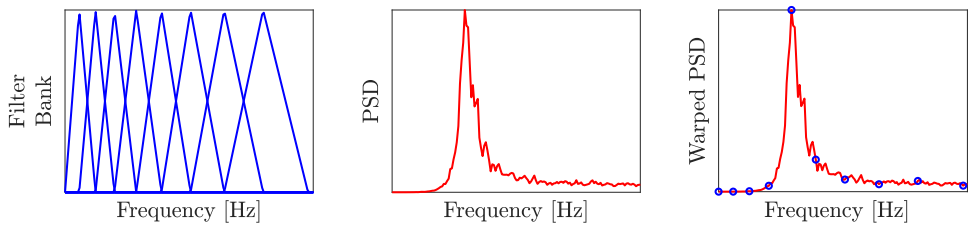

(b)

Figure 3.3: (a) average PS and (b) frequency warping procedure.

The frequency warping step is performed by grouping together the PS values into M frequency bands and weighting each group by a triangular weighting function. According to the Fraile et al. criterion (Fraile Muñoz et al. 2008), M can be set equal to $3ln(f_s)$, where ln() represents the natural logarithm operation, while f_s is the sampling frequency, which is a quite common relationship in the speaker recognition research field and that can also be adopted for structural problems.

The triangular filters are constructed such that their centers are equally spaced on the frequency scale ($\tilde{f}$) given in Equation 3.1, with each filter being symmetric with respect to its center (Figure 3.3b).

The power spectrum of each frame is weighted multiplying it by the triangular filter corresponding to each m^{th} frequency band (Figure 3.3b). After that, each contribute coming from this multiplication is summed along with the frequency range leading to the matrix H of dimensions $M \times N_{frames}$ (Figure 3.4a).

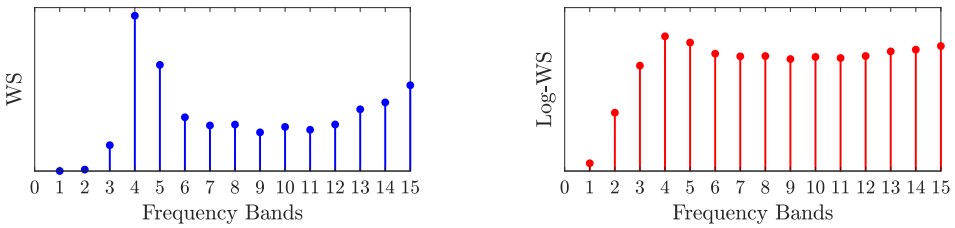

(a) (b)

Figure 3.4: (a) Warped Spectrum and (b) Log-Warped Spectrum for the i^{th} frame.

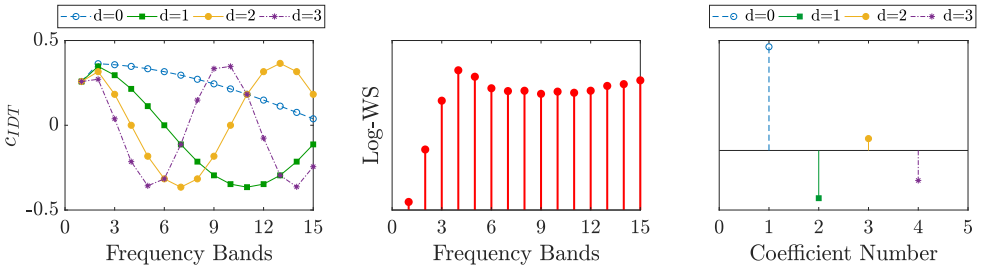

(a)

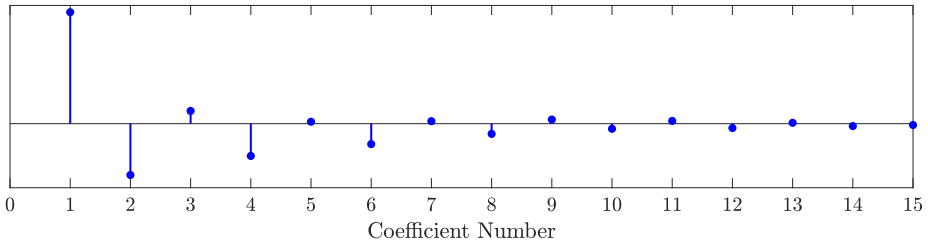

(b)

Figure 3.5: (a) Application of the first six coefficients of the IDCT; (b) Cepstral Coefficients for the i^{th} frame.

The Cepstral Coefficients extraction procedure is completed applying to the logarithm of the modified spectra (Figure 3.4b) a D-points Inverse Discrete Cosine

Transform (IDCT) (Figure 3.5a):

$$c[d,k] = \sum_{m=0}^{M-1} a_m \ln(H[m,k]) cos[\frac{\pi(2d+1)m}{2M}] \quad \begin{matrix} \text{for } d = 0, ..., D-1 \\ \text{for } k = 1, ..., N_{frames} \end{matrix} \tag{3.2}$$

where a_m is equal to $\frac{1}{M}$, for $m = 0$, and to $\frac{2}{M}$ otherwise. $H[m]$ represents the m^{th} point of the modified spectrum, where $m = 0, ..., M-1$ while $c[d]$ is the d^{th} Cepstral Coefficient, which could be collected in a coefficient vector for each k^{th} frame $\mathbf{c}(k) \in \mathbb{R}^{D \times 1}$. The number of of CCs is chosen arbitrarily, but commonly is selected equal to the number of M frequency bands already defined.

Computing the coefficients of IDCT independently for each Cepstral Coefficients (Figure 3.5a), it is possible to appreciate better how these coefficients modify the different frequency contribute of the new modified log spectrum.

$$c_{IDCT}[d] = \sum_{m=0}^{M-1} a_m cos[\frac{\pi(2d+1)m}{2M}] \quad \text{for } d = 0, ..., D-1 \tag{3.3}$$

CCs are always real and convey information about the physical aspects of the signal. When $d = 0$, the cosine term of the DCT becomes 1. Then the first Cepstral Coefficient c_0 is then the average power of the signal. A negative coefficient relates to the local minimum of the cosine in the DCT, noting that the higher frequency indexes in the summation of the DCT are contributing more. On the other hand, a positive peak means that there must be more power in the lower frequency range. As the CCs dimension d becomes larger, the number of alternating partitions in the frequency range increases.

It is precisely this characteristic that makes CCs valuable for discriminating the trends in data due to the environmental and operational variation from the alterations caused by damage. The application of the DCT coefficients of higher orders allows to naturally detrend some of the CCs, because the contributes of the frequency bands carrying the environmental information, cross out with each other in the summation. This characteristic will be highlighted in the following section.

Here the IDCT is used in place of Inverse Discrete Fourier Transform (IDFT). Defined by Ahmed et al. 1974, DCT was shown to perform better than DFT in transforming the original data into more compact and almost uncorrelated representations, and was proved to compare closely to the Karhunen-Loeve Transform

(KLT) (Vranic et al. 2001), which is optimal for compressing data dimensionality. However, despite its optimality, there is no efficient algorithm able to implement KLT, while DCT may be implemented exploiting Fast Fourier Transform (FFT), i.e., in a highly computationally efficient fashion. KLT is the most basic approach to perform Principal Component Analysis (PCA), which is concerned with transforming the original data by projecting them into a reduced dimension space, whose basis vectors are represented by the data covariance eigenvectors associated with the largest eigenvalues, which, in turn, represent data components characterized by the greatest variance and are the most useful for recognition purposes.

3.2 MPEG7-NASE

The MPEG-7 low-level descriptors (LLDs) form the foundation layer of the standard (Manjunath et al. 2002). It consists of a collection of simple, low complexity audio features that can be used to characterize any type of sound. The LLDs offer flexibility to the standard, allowing new applications to be built in addition to the ones that can be designed based on the MPEG-7 high-level tools. The foundation layer comprises a series of 18 generic LLDs consisting of a normative part (the syntax and semantics of the descriptor) and an optional, nonnormative part which recommends possible extraction and/or similarity matching methods. The temporal and spectral LLDs can be classified into the following groups:

- Basic descriptors: audio waveform (AWF), audio power (AP).
- Basic spectral descriptors: audio spectrum envelope (ASE), audio spectrum centroid (ASC), audio spectrum spread (ASS), audio spectrum flatness (ASF).
- Basic signal parameters: audio harmonicity (AH), fundamental audio frequency (AFF).
- Temporal timbral descriptors: log attack time (LAT) and temporal centroid (TC).
- Spectral timbral descriptors: harmonic spectral centroid (HSC), harmonic spectral deviation (HSD), harmonic spectral spread (HSS), harmonic spectral variation (HSV) and spectral centroid (SC).

- Spectral basis representations: audio spectrum basis (ASB) and audio spectrum projection (ASP).

An additional silence descriptor completes the MPEG-7 foundation layer. The four basic spectral LLDs provide time series of logarithmic frequency descriptions of the short-term audio power spectrum. The use of logarithmic frequency scales is supposed to approximate the response of the human ear. All these descriptors are based on the estimation of short-term power spectra within overlapping time frames. This section describes the descriptors, based on the notations and definitions introduced in Section 2.2. For reasons of clarity, the frame index l will be discarded in the following formulae.

3.2.1 Features Extraction Procedure

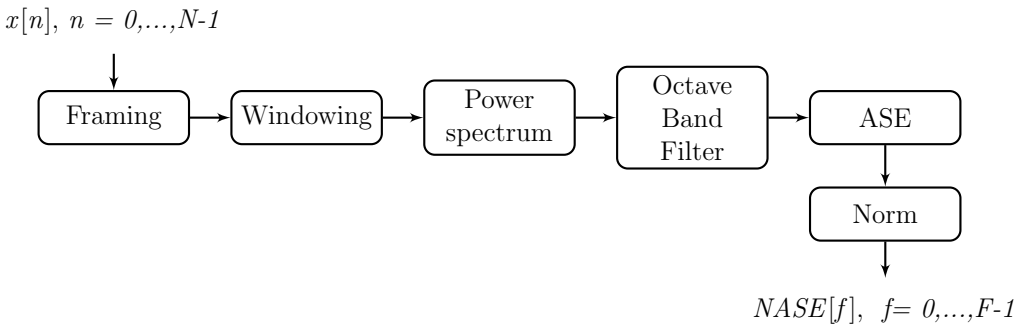

Figure 3.6: NASE Extraction Process.

The audio spectrum envelope (ASE) is a log-frequency power spectrum that can be used to generate a reduced spectrogram of the original audio signal. It is obtained by summing the energy of the original power spectrum within a series of frequency bands.

The initial step is the same described for the Cepstral Coefficients in the previous section. Each one of the time histories N_{th} is framed into overlapping segments (N_{frames}). Subsequently, applying the DFT, the power spectrum, $P(k)$, is evaluated for each frame.

To extract reduced rank spectral features, the spectral coefficients are grouped in logarithmic sub-bands. The output of the logarithmic frequency range is the sum of the power spectrum in each logarithmic sub-band.

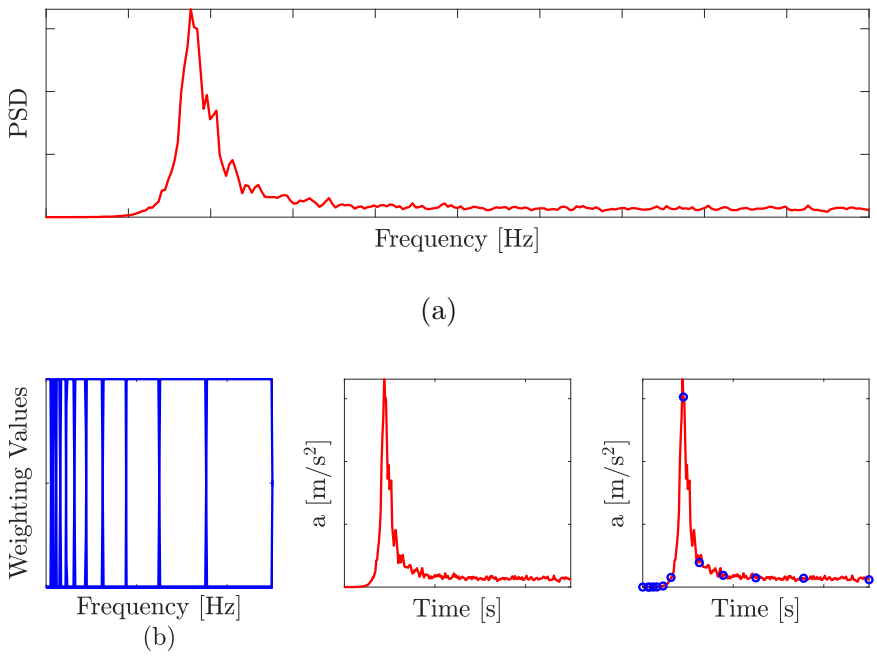

Figure 3.7: (a) Average Power Spectrum and (b) Frequency Warping procedure

The bands are logarithmically distributed (base 2 logarithms) between two frequency edges lo_{Edge} (lower edge) and hi_{Edge} (higher edge). The spectral resolution r of the frequency bands within the $[lo_{Edge},hi_{Edge}]$ interval can be chosen from eight possible values, ranging from 1/16 of an octave to 8 octaves:

$$r = 2^{j} octaves(4 \leq j \leq +3) \tag{3.4}$$

lo_{Edge} and hi_{Edge} represents the frequency range of the study case. Within the default $[lo_{Edge},hi_{Edge}]$ range, the number of logarithmic bands that corresponds to r is $B_{in} = 8/r$. The low (lo_{F_b}) and high (hi_{F_b}) frequency edges of each band are given by:

$$\begin{aligned} lo_{F_b} &= lo_{Edge} \times 2^{(b-1)r} \\ hi_{F_b} &= lo_{Edge} \times 2^{br} \end{aligned} \tag{3.5}$$

The sum of power coefficients in band b $[lo_{F_b},hi_{F_b}]$ gives the ASE coefficient for

this frequency range. The coefficient for the band b is:

$$ASE(b) = \sum_{k=loK_b}^{hiK_b} P(k)(1 \leq b \leq B_{in}) \tag{3.6}$$

where $P(k)$ are the power spectrum coefficients, and loK_b (respectively hiK_b) is the integer frequency bin corresponding to the lower edge of the band lo_{F_b} (the higher edge of the band hi_{F_b}) obtained from Equation 3.5.

However, the repartition of the power spectrum coefficients $P(k)$ among the different frequency bands can be a problem, particularly for the narrower lowfrequency bands when the resolution r is high. It is reasonable to assume that a power spectrum coefficient whose distance to a band edge is less than half the FFT resolution (i.e., less than F/2) contributes to the ASE coefficients of both neighboring bands. How such a coefficient should be shared by the two bands is not specified by the standard. The bin within-band band power coefficients are completed by two additional values: the powers of the spectrum between 0 Hz and lo_{Edge} and between hi_{Edge} and the Nyquist frequency $f_s/2$ (provided that hi_{Edge} < Nyquist frequency). These two values represent the *out-of-band* energy.

The summation of all ASE coefficients equals the power in the analysis window, according to Parsevals theorem. More generally, this descriptor has useful scaling properties: the power spectrum over an interval is equal to the sum of power spectra over subintervals. The ASE provides a compact representation of the spectrogram of the input signal.

The resulting log-frequency power spectrum is converted to the decibel scale.

$$D(b,k) = 10log(ASE(b,k)) \tag{3.7}$$

where f is the logarithmic frequency range. Finally, each decibel-scale spectral vector is normalized with the RMS (root mean square) energy envelope, thus yielding a normalized log-power version of the ASE (NASE). The full rank features for each frame k consist of both the RMS-norm gain value R_k and the normalized ASE (NASE) vector.

$$R_k = \sqrt{\sum_{b=1}^{B}(D(b,k))^2} \tag{3.8}$$

$$NASE(b,k) = \frac{D(b,k)}{R_k} for b = 0, ..., B-1, for k = 1, ..., N_{frames} \tag{3.9}$$

where B is the number of ASE spectral coefficients and N_{frames} is the total number of frames.

3.3 Numerical Application

In this section, a numerical study case is carried on to present the application of the Cepstral Coefficients and the MPEG-7 features. The parameters governing their extraction process are initially highlighted, and then the coefficients are tested within a damage detection framework. The performance of these parameters as damage sensitive features is compared with the results obtained, replacing them with the modal parameters (frequencies and damping ratios).

3.3.1 System's description

The simulated system is an 8-story shear-type frame (Figure 3.8). It is built up according to the mass-spring-viscous damper structure. It is a classically damped system, and the damping matrix is defined following the Rayleigh damping mechanism. The nodes are numbered in ascending order starting from the one closest to the constraint.

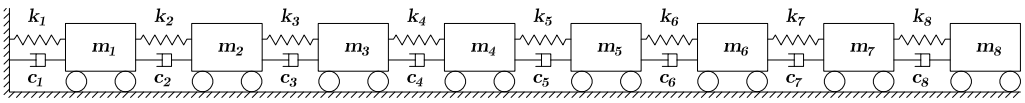

Figure 3.8: 8 Degrees of Freedom Shear Type System

The reference system is characterized by inter-story stiffness $k_i^0 = 6 \times 10^6$ N/m and mass $m_i^0 = 2 \times 10^3$ Kg for $i = 1, ..., 8$. The undamaged and damaged scenarios considered for this structure are defined in Table 3.1. In order to take into account the operational and environmental variability conditions 9 undamaged states are defined, while, on the other hand, 8 different damaged scenarios are planned to simulate different occurring damages. The system is excited by a white Gaussian noise input applied at each DOF. The input time histories, of mean 0 and standard

Table 3.1: Damaged and Undamaged states considered for the 8-story frame.

State	**Label**	**Description**
1	Undamaged (U1)	baseline
2	Undamaged (U2)	$m_1 = 1.05\, m_1^0$
3	Undamaged (U3)	$m_8 = 1.05\, m_8^0$
4	Undamaged (U4)	$k_i = 0.98\, k_i^0\ ,\ i = 1, ..., 5$
5	Undamaged (U5)	$k_i = 0.98\, k_i^0\ ,\ i = 6, 7, 8$
6	Undamaged (U6)	$k_i = 0.99\, k_i^0\ ,\ i = 1, ..., 5$
7	Undamaged (U7)	$k_i = 0.99\, k_i^0\ ,\ i = 6, 7, 8$
8	Undamaged (U8)	$k_i = 1.03\, k_i^0\ ,\ i = 1, ..., 5$
9	Undamaged (U9)	$k_i = 1.03\, k_i^0\ ,\ i = 6, 7, 8$
10	Damaged (D1)	$k_5 = 0.85\, k_5^0$
11	Damaged (D2)	$k_7 = 0.85\, k_7^0$
12	Damaged (D3)	$k_8 = 0.85\, k_8^0$
13	Damaged (D4)	$k_1 = 0.90\, k_1^0$
14	Damaged (D5)	$k_3 = 0.90\, k_3^0$
15	Damaged (D6)	$k_5 = 0.90\, k_5^0$
16	Damaged (D7)	$k_7 = 0.90\, k_7^0$
17	Damaged (D8)	$k_8 = 0.90\, k_8^0$

deviation 1, last 2 minutes, with a sampling time of 0.01 seconds. The effect of the measurement noise is taken into account adding 10% RMS white Gaussian noise to the system response. Moreover to reproduce the operational variability, for each data set realization, the values of structural masses and stiffnesses for both damaged and undamaged states reported in Table 3.1, are perturbed by a small amount, randomly picked from a set of values, uniformly distributed between -0.01 and 0.01. For each undamaged scenario, 50 realizations are simulated.

The system simulated response data have to be normalized before extracting the structural sensitive features:

$$x_{normalized}[n] = \frac{x[n] - \overline{x}}{\sigma_x} \tag{3.10}$$

where $x[n]$ is the original signal, $\overline{x}$ its mean and σ_x its standard deviation. This standardization is performed on each frame, when Cepstral features and audio spectrum envelope features are extracted while it is applied on the whole signal when frequencies are identified through the system identification techniques.

3.3.2 Feature extraction & User's defined parameters

The extraction procedure of CCs and NASE features previously exploited in Sections 3.1 and 3.2 presents a straightforward implementation procedure, a very low computational burden, and a few user's defined parameters.

The parameters driving the extraction process of the Cepstral Coefficients are three: the cutoff frequency f_c; the sampling frequency f_s and the number of triangular filters. The cutoff frequency f_c is an entire user's defined parameters, and it indicates the separating boundary between the area of the spectrum which is treated linearly and the one in which the content is weighted logarithmically. Therefore, the cutoff frequency plays an important role in how the filters are stretched in the frequency domain. The sampling frequency f_s, on the other hand, it is a quantity that rarely can be specified by the user, who usually received the data already sampled and recorded. Indeed, who is in charge of the monitoring system installed on the structure is the one setting the value of the sampling frequency. This parameter, even if not specified by the user, gives important information about how many filters should be considered to carry on the necessary information about the frequency energy content of the signal. As mentioned in

Section 3.1. Fraile Muñoz et al. 2008 suggested an empirical expression to derive the number of filters M, knowing the sampling frequency. However, the user is free to set the desired number of filters, and consequently of Cepstral Coefficients, where the aim is to find the right balance between a good resolution in reading the energy content optimizing the number of coefficients.

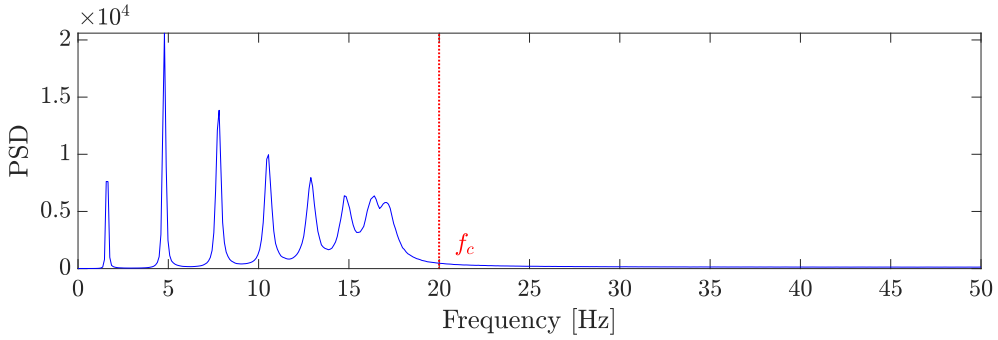

Figure 3.9: Average Spectrum

In the extraction process of the NASE features, the number of rectangular filters is the only parameter that needs to be set and is entirely in the hands of the user. The assumptions made for the identification of the number of triangular filters are valid also for the definition of the rectangular ones; therefore, the empirical expression given by Fraile Muñoz et al. 2008 can be used as well. There is no need for defining a cutoff frequency because the octave scale, used for these coefficients is logarithmic all over the frequency spectra.

Here, the number of triangular filters can be set according to the Fraile et al. criterion presented in Section 3.1. Since the sampling frequency adopted to simulate the system response is equal to 100 Hz, M is set to 13. The resolution for the octave scale is here chosen (1/2 octave) in order to have the same number of frequency bins derived for the Cepstral Coefficients.

To form the average spectrum, 50 realizations of the response of the system, under the baseline state 1 of Table, are employed, and the most reasonable cutoff frequency f_c is set equal to 20 Hz since the entire frequency content is concentrated in the lower part of the spectrum (Figure 3.9). Figure 3.10 and Figure 3.11 show the distribution of the triangular filter and of the rectangular filters, respectively, in the frequency domain.

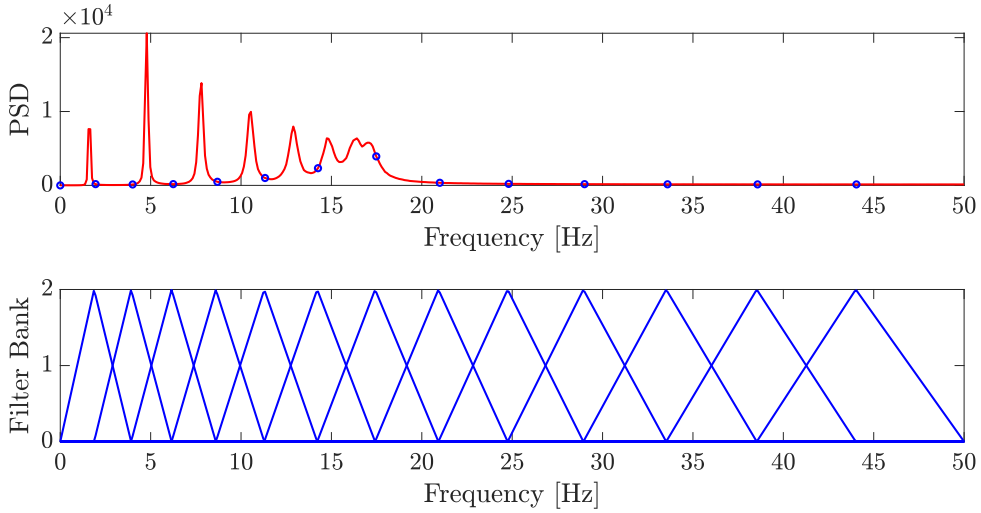

Figure 3.10: Frequency Warping with Cepstral Coefficients.

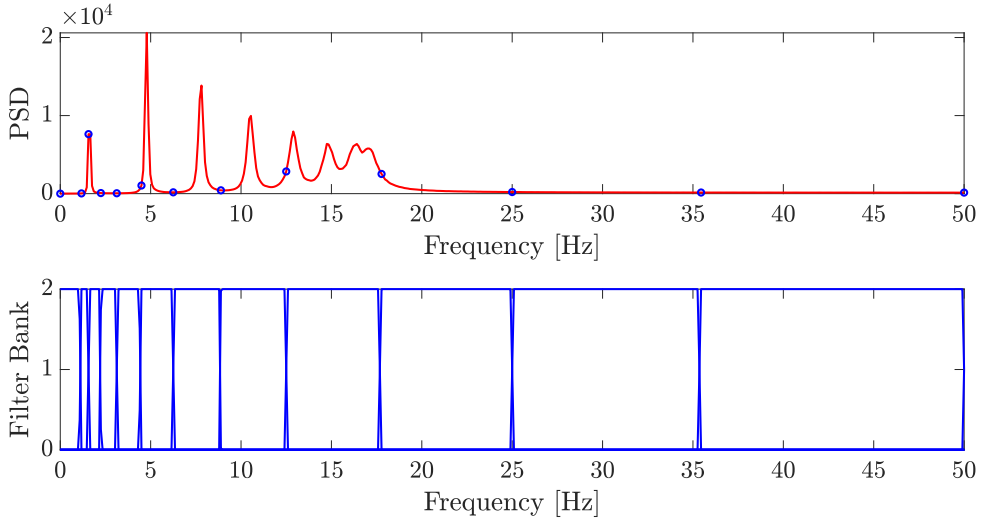

Figure 3.11: Frequency Warping with MPEG7.

3.3.3 Damage Detection Algorithm

The research in the field of statistical pattern recognition based damage detection has been quite active in the last ten years, leading to the proposal of numerous damage detection algorithms. The typical scheme is that of constructing a model of the damage sensitive features representative of the healthy states and then comparing new instances of features extracted from the response of the system

under unknown conditions against those representatives of the original trained model to determine whether these new instances are novel, i.e. deviating from the reference model, or are instead new realizations of the healthy system. The training model is usually represented by a probability density function estimated using the trained features. In this work, CCs, MPEG-7, and modal parameters are assumed to be multivariate and normally distributed. This assumption is not far from reality, especially when the number of training data is large.

In fact, for what concerns Cepstral Coefficients normality, due to the optimal decorrelation properties of inverse DCT, the Cepstral Coefficients may be considered to be almost uncorrelated, as far as allowed by the use of noisy data.

In addition, since the vectors are obtained through the same operations, it is reasonable to assume that they are identically distributed. It is well known that a set of n independent identically distributed (i.i.d.) vectors will approach a normal distribution as the limit of n approaches large values. Therefore, estimating the mean vector and the covariance matrix of the ensemble of training feature vectors is enough to characterize the distribution of all these three features.

The structural damage detection strategy proposed in this chapter makes use of the Mahalanobis Squared Distance as the damage index. The Mahalanobis Squared Distance of a d-dimensional point, $\mathbf{x}$, from a population characterized by mean, μ, and covariance matrix, Σ, is a scalar given by:

$$D_{\mu}^{2}(\mathbf{x}) = (\mathbf{x} - \mu)^{T} \Sigma^{-1} (\mathbf{x} - \mu) \tag{3.11}$$

The advantage of employing MSD is twofold: firstly, the use of the sample covariance matrix, estimated using samples measured under different external conditions, e.g., temperature, traffic, wind in a bridge structure, allows to account for the feature variability produced by such factors' influence; furthermore, MSD is the preferred metric in the field of outlier detection, such that a substantial body of work is available on the subject. As mentioned in Section 2.4.4, the knowledge of the damage index distribution is crucial for defining a threshold to use for the outlier analysis. It is known that the Mahalanobis Squared Distance of normally distributed instances is asymptotically χ^2-distributed. However, it is proved that the distribution of the MSD of a d-variate point $\mathbf{x}$, when $\mathbf{x}$ is not involved in the estimation of the sample mean and the sample covariance matrix, follows a scaled F-distribution with degrees of freedom d and $n - d$, where d is the dimension of

$\mathbf{x}$, and $\mathfrak{n}$ is the number of observations used to construct the sample statistics' estimators.

The steps involved in the following damage sensitive features are divided into two macro-phases: the training phase and the testing phase. Let us assume that, for the training phase, $\mathfrak{n}_{tr}$ sets of structural response time histories are available from each of the s sensors located on the monitored system. Before engaging into the feature extraction process, a subset of the $\mathfrak{n}_{tr}$ realizations, previously referred to as $\mathfrak{n}$, is selected to construct the filter bank. Then, the desired coefficients are extracted from each of the $\mathfrak{n}_{tr} \cdot \mathfrak{s}$ time histories. Each response time series of the ith data set realization is divided into N_{frames} frames, and from each frame a $V \times 1$ feature vector is derived, where V is the generic dimension of the damage sensitive feature vector (it is equal to D for the Cepstral Coefficients, equal to B for the MPEG-7 and equal to the number of identified structural modes for the frequencies). The sample mean of the N_{frames} feature vectors is stored and concatenated to the other $\mathfrak{s}-1$ mean feature vectors, generating a feature vector $f_d^{(i)} \in \mathbb{R}^{\mathfrak{s}\cdot(V-1)\times 1}$, for $i = 1, ..., \mathfrak{n}_{tr}$. The training model is then constituted by the set of $\mathfrak{n}_{tr}$ feature vectors $f_d^{(i)}$, for $i = 1, ..., \mathfrak{n}_{tr}$ whose sample mean $\mathfrak{m}_{tr}$:

$$\mathfrak{m}_{tr} = \frac{1}{\mathfrak{n}_{tr}} \sum_{i=1}^{\mathfrak{n}_{tr}} f_d^{(i)} \tag{3.12}$$

and unbiased sample covariance matrix $\mathbf{S}_{tr}$:

$$\mathbf{S}_{tr} = \frac{1}{\mathfrak{n}_{tr}-1} \sum_{i=1}^{\mathfrak{n}_{tr}} (f_d^{(i)} - \mathfrak{m}_{tr})(f_d^{(i)} - \mathfrak{m}_{tr})^T \tag{3.13}$$

can be evaluated, forming what can be defined as the training model.

Let us now assume that a set of $\mathfrak{n}_{te}$ data sets are available for testing. These are data sets for which the condition of the structure is unknown and will be used to assess whether or not changes have occurred in the structure. In the case of short-term applications, $\mathfrak{n}_{te}$ can be equal 1 but, in general, let us assume that $\mathfrak{n}_{te} \geqslant 1$. From each testing data set, a feature vector $\tilde{f}_d^{(j)} \in \mathbb{R}^{\mathfrak{s}\cdot(V-1)\times 1}$, for $i = 1, ..., \mathfrak{n}_{te}$, is extracted, in order to get a population of $\mathfrak{n}_{te}$ feature vectors. The Mahalanobis Squared Distance between training and testing models is estimated according to Equation 3.11:

$$D^2_{\mathfrak{m}_{tr}}(\mathfrak{m}_{te}) = (\mathfrak{m}_{te} - \mathfrak{m}_{tr})^T \Sigma_{tr}^{-1} (\mathfrak{m}_{te} - \mathfrak{m}_{tr}) \tag{3.14}$$

where $\mathfrak{m}_{te}$ represents the sample mean of the $\mathfrak{n}_{te}$ feature realizations computed from the testing data set, if $\mathfrak{n}_{te} > 1$:

$$\mathfrak{m}_{te} = \frac{1}{\mathfrak{n}_{te}} \sum_{j=1}^{\mathfrak{n}_{te}} \tilde{f}_d^{(j)} \tag{3.15}$$

while it is simply equal to $\tilde{f}_d^{(1)}$ if $\mathfrak{n}_{te}$ is equal to 1. The damage index $D^2_{\mathfrak{m}_{tr}}(\mathfrak{m}_{te})$ must then be compared against a threshold, Γ,in order to assess the occurrence of damage. As previously stated, the Mahalanobis Squared Distance of the testing point $\mathfrak{m}_{te} \in \mathbb{R}^{\mathfrak{s}\cdot(V-1)\times 1}$ from the training population, whose sample mean vector, $\mathfrak{m}_{tr}$, and the sample covariance matrix, $\mathbf{S}_{tr}$, have been estimated using $\mathfrak{n}_{tr}$ data points, but without using the point $\mathfrak{m}_{te}$, is distributed according to a scaled F-distribution with degrees of freedom $s \cdot (V-1)$ and $\mathfrak{n}_{tr} - s \cdot (V-1)$:

$$\frac{\mathfrak{n}_{tr}(\mathfrak{n}_{tr} - d)}{(\mathfrak{n}_{tr}^2 - 1)d} D^2_{\mathfrak{m}_{tr}}(\mathfrak{m}_{te}) \sim F_{d,\mathfrak{n}_{tr}-d} \tag{3.16}$$

where d is equal to $s \cdot (V-1)$. The threshold, Γ, is then set to the value of the 1-α percentile of $F_{d,\mathfrak{n}_{tr}-d}$. For each test, the value of $D^2_{\mathfrak{m}_{tr}}(\mathfrak{m}_{te})$, scaled by $\frac{\mathfrak{n}_{tr}(\mathfrak{n}_{tr}-d)}{(\mathfrak{n}_{tr}^2-1)d}$ can then be compared to Γ: if it exceeds the threshold value the structure is declared damaged. In this work, $\alpha$is set equal to 1%.

3.3.4 DSF performance

Training: For the present example, $\mathfrak{n}_{tr}$ is equal to 450 (50 realizations of each of the nine undamaged scenarios). Therefore, the training data-set is constituted by 450 $\times$ $\mathfrak{s}$ time histories, where $\mathfrak{s}$ is the number of accelerometers available for a specific sensor setup. The construction of the training model requires only the evaluation of sample mean and sample variance-covariance matrix of the features extracted from the training data.

The threshold value is found to be 1.4235 when Cepstral Coefficients and NASE indicators are used, while, when using frequencies and frequencies-damping ratios, the thresholds become 2.5516 and 2.0417, respectively. The Mahalanobis Squared Distance evaluated for the Cepstral Coefficients is scaled by a factor of 0.0074, like when NASE coefficients are involved, the damage index is scaled by a factor of, in the case of frequencies it becomes 0.1228 and 0.0603.

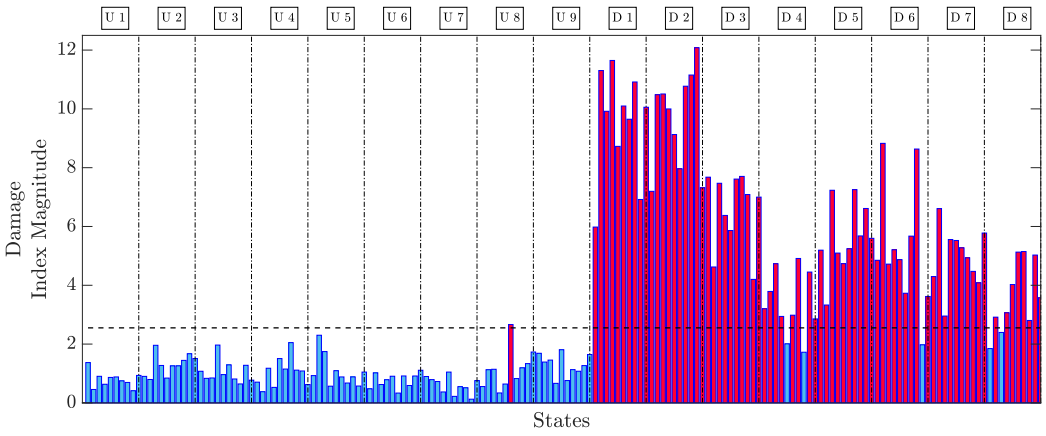

Figure 3.12: Mahalanobis Squared Distance for Tests of Case Study using frequencies as features.

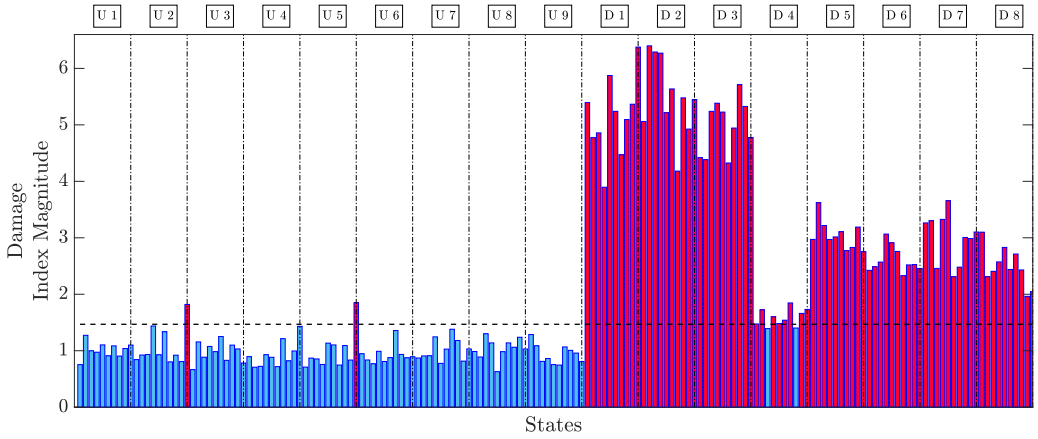

Figure 3.13: Mahalanobis Squared Distance for Tests of Case Study using NASE as features.

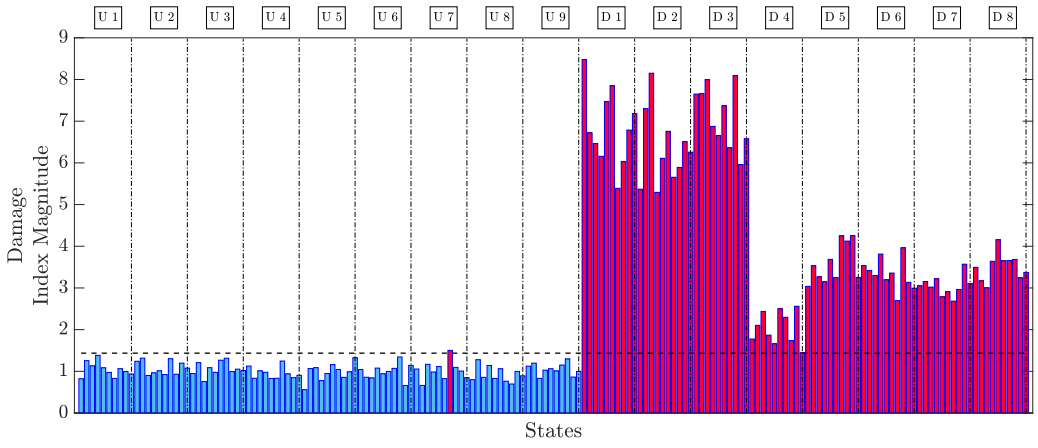

Figure 3.14: Mahalanobis Squared Distance for Tests of Case Study using Cepstral Coefficients as features.

Table 3.2: Results

DSF	**No. Features**	**Type I error**	**Type II error**
CCs (f_c=20)	13	1.11	1.25
MPEG-7	13	2.22	2.50
DD-SSI (f)	8	1.11	6.25
DD-SSI (f+ξ)	16	1.11	12.5

Testing: To test whether the algorithm is capable of identifying the presence of structural damage, ten realizations of the response of the system for each of the 17 states of Table 3.1 are simulated. Each resulting dataset is treated individually as a single test, in order to simulate the short-term SHM modus operandi. The results of the tests are given in Table 3.2 in terms of Type I and Type II errors, in Figure 3.12, Figure 3.13, Figure 3.14 the performance of Cepstral Coefficients, NASE indicators, and modal parameters are compared.

Observation of Table 3.2 clarifies that the performances of Cepstral Coefficients and NASE indicators are comparable, although the Cepstral Coefficients perform slightly better than the NASE coefficients.

Modal parameters show to be the less effective DSFs. Even if they keep a small error rate towards type I error, they fail the identification of damage in the states where the damage is present, leading to high Type II error, which is not

acceptable. The type II error rate gets worse when the structural frequencies are combined with the damping ratios, which confirm to be an unstable indicator and not as efficient as damage sensitive features.

It is worth noticing how the Mahalanobis distance, when frequencies are used as DSFs (Figure 3.12), shows a high variability between every realization belonging to the same state, damaged or undamaged state. When using Cepstral Coefficients and MPEG-7 this variability is less pronounced, and the MSD is more compact in every state. This finding demonstrates the less sensitivity of the audio features towards operational and environmental variability, which is simulated, introducing a small perturbation for each realization.

It is also interesting to note that the damage index magnitude, for all the study cases, is higher for damage cases from 1 to 3, which are characterized by a 15% decrease of interstory stiffness, while decreases for the remaining cases (10% reduction), indicating proportionality between the amplitude of all the adopted damage sensitive features and the damage severity.

An additional investigation is carried on varying the number of coefficients for Cepstral features and MPEG-7 and the number of identified frequencies, to check the sensitivity of the damage detection methodology towards the parameters driving the extraction of these features. As already mentioned, for Cepstral Coefficients, the only two variables the user can define are the cutoff frequency and the number of frequency bands, which also corresponds to the number of features; while for the MPEG-7 features, the user needs to set only the number of actual coefficients. The results in terms of type error I and type error II are shown in Table 3.3. It is evident that the cutoff frequency for CCs is not a highly influencing parameter since the value of both type error I and type error II is slightly changing. On the other hand, the number of coefficients, used in the damage detection strategy, strongly affects the performance of the framework. Increasing the number of frequency bands and consequently, the number of coefficients leads to a less effective.

It is also interesting to analyze the performance of the damage detection strategy, varying the number of frequencies used as features. This test aims to simulate the condition in which not all the frequencies are correctly identified, which commonly happens in the identification of complex structures. In the three cases, it is assumed that the eight structural modes, the first six modes and finally only the first four modes are respectively identified. It is clear how missing some frequencies

can cause an important failure in the identification of the damage states.

Table 3.3: Results.

DSF	**No. Features**	**Type I error**	**Type II error**
CCs (f_c=10)	13	3.33	0.00
CCs (f_c=15)	13	2.22	0.00
CCs (f_c=20)	13	1.11	0.00
CCs (f_c=50)	13	2.22	0.00
CCs (f_c=80)	13	2.22	0.00
CCs (f_c=20)	8	2.22	0.00
CCs (f_c=20)	13	1.11	0.00
CCs (f_c=20)	15	1.11	1.25
CCs (f_c=20)	20	1.11	2.50
CCs (f_c=20)	30	2.22	3.75
MPEG-7	8	2.22	2.50
MPEG-7	13	2.22	2.50
MPEG-7	15	3.33	6.25
MPEG-7	20	3.33	6.25
MPEG-7	30	2.22	7.50
DD-SSI (f)	8	1.11	6.25
DD-SSI (f)	6	0.00	17.5
DD-SSI (f)	4	0.00	33.75

3.4 Conclusions

new family of DSFs was investigated. The proposed indicators come from the speech and speaker recognition research field and are audio features: the Cepstral Coefficients and the MPEG-7 NASE indicators. An extensive treatment of the extraction modality of such features was described, explaining in detail the approach used to define the filter bank and the number of coefficients necessary to perform the extraction.

Both these features are then implemented in a damage detection technique

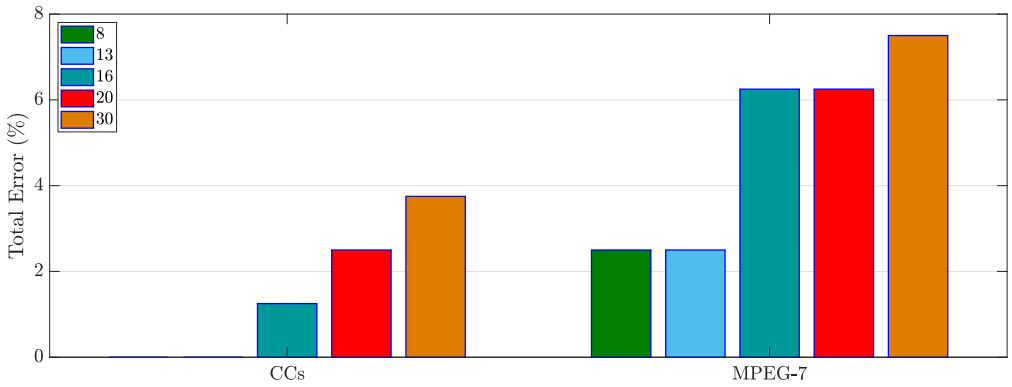

Figure 3.15: Total error for the two audio features varying the number of coefficients.

which is based on Mahalanobis Squared Distance. The definition of the threshold has been performed taking into account the fact the Mahalanobis Squared Distance of a d-dimensional point, $\mathbf{x}$, is F-distributed with degrees of freedom d and $n - d$, when $\mathbf{x}$ has not been used to estimate the sample mean and the sample covariance matrix, and when n samples from a d-variate normal distribution are available to construct the sample statistics estimators. The algorithm was tested on a frame structure, comparing the performance of the novel damage sensitive features with the one given by the use of frequencies and damping ratios as damage indicators. The test adopted a set of simulated data from an 8 DOFs shear-type system.

The performance of the algorithm under operational and environmental variability, as well as considering different damage scenarios, was investigated.

Comparing the properties of Cepstral features and MPEG with those of the modal parameters, the proposed indicators are generally more compact and require lower computational effort than the modal parameters, making the model more robust to environmental factors. More importantly, the results show that CCs and MPEG are less sensitive to environmental and operational variability in the training data than modal parameters. Moreover, the false acceptance rate of CCs is quite low, never exceeding 5%, for the considered case studies.

Chapter 4

Temperature Sensitivity of Cepstral Coefficients and Cointegration-based Removal Approach

TThis chapter introduces the cointegration technique, a tool usually used in the econometric field to remove trend from data. Here, the cointegration is applied to deal with nonstationary time series of DSFs, which present long-term dependency from environmental variation. If two or more monitored variables from an SHM system are cointegrated, then it is possible to find some combination of them that will be stationary. The stationary residual created from the cointegration procedure can be used as a DSF that is independent of the normal environmental and operational conditions. The cointegration is addressed in its linear and nonlinear formulation, to take into account the possible nonlinear relations between DSFs and temperature that usually occur in SHM problems for civil structures. The object of this chapter is to examine the temperature dependency of Cepstral Coefficients from environmental fluctuations, like temperature, and, then apply the cointegration technique to remove the environmental dependencies if present. Two applications are addressed: a numerical simulation of a cantilever beam subjected to damage and temperature variation and an experimental case on the data available from the benchmark Z-24 study case.

The Z24 data have been collected within the Brite EuRam Programme BE-3157

SIMCES with a financial contribution of the European Commission. The data have been kindly provided by the project coordinator, the Structural Mechanics Section of KU Leuven.

4.1 Introduction to cointegration

In the Introduction, SPR approaches have been stresses to be suitable for implementing efficient damage detection strategies in civil structures. SPR methodologies start from the response measurement of a structure and build a statistical model which represents and knows the behavior of the monitored system. Consequently, this model is able to say when the structures behavior deviates from the normal learned trend. Particularly, novelty detection methodologies proved to be extremely effective in spotting anomalies in structural behavior, being able to deal with a major downside of SHM problems, the lack of damage data reference.

Novelty detection approaches are based on the assumption that some monitored DSFs will remain stationary as long as a structure keeps behaving in its normal condition. The occurrence of damage is then suggested by any meaningful shift happening in those features.

Unfortunately, several studies have been carried on, that proved that changes in DSFs could often be caused by variations in the environmental or operational conditions. Moreover, it has been observed that, changes caused by environmental fluctuations can sometimes be of the very degree of magnitude or even more significant than the ones due to damage. This dependency can cause several problems if not well managed. An efficient and reliable SHM strategy should be able to distinguish damage-based changes from the operational-based ones, without leading to any false-positive or false-negative detections. These problems are the major reasons for the slow uptake of SPR-based damage detection methodologies outside the world of academic research.

There are two different ways of facing the problem. One approach is to look for DSFs that are insensitive by nature as much as possible to environmental and operational changes. Unfortunately, the DSFs commonly adopted in SHM problems are highly dependent on environmental variations.

Modal parameters represent a safe and common choice for civil engineers aiming to solve SHM problems. Indeed, frequencies, damping ratios, and mode shapes

have the unique characteristic of having a direct and readable correlation to the structures mechanical parameters. Features like Cepstral Coefficients, instead, do not have the same direct connection to physical parameters. This advantage makes modal parameters extremely feasible in theory for damage detection problems. However, hundreds of studies showed that they are extremely sensitive to environmental/operational fluctuations, being, consequently, pretty unreliable as DSFs. Therefore, if natural frequencies want to be used in a damage detection strategy, it is mandatory to account for or remove environmental/operational variability in damage-sensitive features (Sohn 2006).

Cepstral Coefficients, on the other hand, showed to have all the characteristics a good DSF should have. They present a very easy and fast extraction process with almost no user-defined parameters to be set. The dependency of CCs from the environmental changes has never been investigated before, and it will be addressed in this chapter. It is shown that, because of their extraction procedure, some of the extracted CCs tend to be less sensitive to environmental fluctuations.

In the research literature, several approaches have been proposed for dealing with the dependency of DSFs from environmental and operational changes. These methodologies can be classified according to the kinds of data obtained in a monitoring campaign. One way of approaching to the problem, appropriate despite the direct measurement of the changing environment may or may not be available, is to directly define the normal condition with data collected over a long period from an undamaged structure. The observed regular behavior will encompass feature deviations influenced by alternative benign conditions if a large bank of data is available. This dataset should include measurements occurring under the influence of a wide range of environmental and operational conditions. One obvious disadvantage is the lack of ability to guarantee that the dataset does include data from a full range of environmental/operational conditions. An additional limitation is that within a wide normal condition, any sensitivity to damage a detector has may well be lost. When measurements of the relevant environmental conditions are available, an alternative that may restore sensitivity to damage could be to work with subsets of normal condition data. In this case, a novelty detector is constructed for a subset that relates to a specific environmental condition. Then, new data could be tested by the novelty detector relevant to the environmental condition at the time. Although this approach should improve damage sensitivity, it would still require a large amount of data to be acquired and stored before

any meaningful SHM could be carried out. Most commonly, where comprehensive measurements of the relevant operational and environmental conditions are available, regression techniques have been used.

Churchward and Sokal 1981 attempted to predict the temperature distribution within bridge sections and to determine longitudinal expansion, and vertical deflection based on three-year monitoring of a post-stressed concrete section of a bridge. The measured environmental parameters include ambient air temperature, solar radiation, hours of sunshine, and the temperature on the top surface of the section. It is found that the temperature profile can be reasonably represented through only two design variables, namely maximum differential temperature and base temperature. Sohn et al. 1998 investigate a linear adaptive model that may discriminate the variations of modal parameters related to temperature changes from those caused by structural damage or other effects. They validate the procedure using the data from the Alamosa Canyon Bridge in the state of New Mexico. Results indicate that a linear four-input filter of temperature can reproduce the natural variability of the frequencies for different time of day. Using this simple model, they try to build a confidence interval of the fundamental frequency for a new temperature profile to distinguish the natural change due to temperature. Recently Ubertini et al. 2017, investigated in detail the correlations between natural frequencies and environmental parameters in the study case of the masonry San Pietro bell tower in Perugia. They validated the application of a linear statistical regressive model based on the use of several environmental continuous monitoring sensors to predict frequencies and create a more informed statistical model representing the dynamic behavior of the structure.

A suitable regression efficiently works as a filter to eliminate the influence of the favorable conditions from the model error, which can then be used as a damage-sensitive, environmentally insensitive feature (Peeters et al. 2001; Sohn et al. 1998; Worden et al. 2000). The approaches examined in this study are intended to be applicable in situations where measurement of external conditions is not necessarily available. For a good review of previous approaches to the data normalization problem, readers are referred to Sohn 2006.

The current chapter intends to introduce the concept of *cointegration*. The cointegration idea comes from the econometric realm, where it is used to project out components of data that correspond to nonstationary long-term trends. Its theoretical background draws from several key texts from the econometrics liter-

ature, like Johansen 1995, Fuller 1996, Maddala and Kim 1998 and Juselius 2006, which the reader may refer to for a more mathematically rigorous treatment of the material.

Cointegration technique could be very useful in the data normalization phase of SHM, as it would remove the environmental and operational effects that generally appear on a longer time scale compared to the dynamics of the structure that is sensitive to damage. In general, in econometrics, it is considered more interesting to know if a relationship among different time series exists and to estimate its parameters. In contrast, for SHM purposes, engineers are interested in finding a relationship between the dynamic variables of a system. This connection should be sensitive to damage presence but insensitive to environmental and operational variations (Chen et al. 2009).

Cross et al. 2011 have proved the effectiveness of linear cointegration in SHM. They introduce the concept of cointegration as a tool for the analysis of nonstationary DSFs' time series. They showed that, if two or more monitored variables from an SHM system are *cointegrated*, then some linear combination of them will be a stationary residual purged of the common trends in the original dataset. The stationary residual created from the cointegration procedure can be used as a DSFs that is independent of the normal environmental and operational conditions. Shi et al. 2016 also explored nonlinear cointegration by fitting a nonlinear multiple regression model on one of the time series, recognizing that the linear nature of cointegration might limit its application to SHM problems. Coletta 2017; Coletta et al. 2019, as well, proposed an alternative nonlinear cointegration, where the nonlinearity relationship between the variables is taken into account using nonlinear regression models like Support Vector Machine and Relevance Vector Machine with nonlinear kernels.

Here, the application of cointegration is extended on two different levels: features and regression tools. Until now, the cointegration technique has been applied to common DSFs like frequencies. Here, it is applied to CCs to remove the dependency of some of these coefficients from long-term environmental trends like temperature. Additionally, the nonlinear regression techniques addressed by Coletta et al. 2019 are here considered as well and used to carry on the nonlinear cointegration approach.

4.2 Cointegration Technique

Starting from a set of nonstationary time series, that represents the evolution of the dynamic response over time, the aim behind the application of the cointegration technique is to define a combination of them which is stationary and that can be used as a damage index or control parameter. Here, to begin with, a simple definition of cointegration is given

Definition *Two or more nonstationary time series are cointegrated if a linear combination of them is stationary. If this stationary combination exists, the initial time series are defined cointegrated.*

In the following equation, where the nonstationary time series are modeled as a Vector Autoregression (VAR) process $\mathbf{y}_i$, the series are cointegrated if a vector $\boldsymbol{\beta}$ exists such that $\mathbf{z}_i$ is stationary, where

$$\mathbf{z}_i = \boldsymbol{\beta}^T \mathbf{y}_i \tag{4.1}$$

If this is the case, $\boldsymbol{\beta}^T$ is called a *cointegrating* vector. If $\mathbf{y}_i$ includes a total of n variables, there may be as many as $n-1$ linearly independent cointegrating vectors. Clearly, for the time series to be cointegrated, to begin with, they must have shared/common trends. There is one further restriction, which is that all times series must be integrated of the same order.

Definition *If a nonstationary process variable y becomes stationary after differencing d times, it is said to be integrated of order d, which is denoted $y \sim I(d)$.*

In other words, the time series must have the same 'degree of nonstationarity' if they are cointegrated.

For the purposes of SHM, the intent would be to use monitored variables that are cointegrated and find the cointegrating vector to create a stationary residual sequence for damage detection. From an engineering point of view, monitored variables from the same process or system are more than likely to share common trends on account that each process variable will be driven by the same latent influences. This cannot be said, however, of the order of integration of each monitored variable, this must be ascertained before any attempt is made to find the cointegrating vector. The order of integration of a time series is ascertained in econometrics by employing a stationarity test, which is often analogous to testing for a unit root in a time series model. The stationarity test employed here is

called the Augmented Dickey Fuller (ADF) test, the reader is referred to Dickey and Fuller 1979, 1981 for a detailed treatment of the subject. Once it has been ascertained to what order all process variables of interest are integrated to, it remains to find the cointegrating vector that will result in the most stationary combination of the variables.

4.3 Nonlinear Cointegration

In the context of SHM usually the reference time series are simply the dynamic features of monitored structures (eg. accelerations, frequencies, etc); thus, if it exists, the cointegration relationship will possibly be nonlinear.

Intuitively, nonlinear cointegration relates to a set of nonstationary variables that require a nonlinear combination to reduce the nonstationarity of the resultant. In the following, a set of nonstationary variables $\mathbf{y}_i$ are nonlinearly cointegrated if $\mathbf{z}_i$ is integrated to a lower order than $\mathbf{y}_i$ (or ideally stationary), where f represents a nonlinear function.

$$\mathbf{z}_i = f(\mathbf{y}_{i-1}) \tag{4.2}$$

In this case $f()$ will be referred to as the *cointegrating function*.

When reviewing progress of research into nonlinear cointegration, it is useful to bear in mind that for SHM applications, the aims in using nonlinear cointegration are probably very different to those of the econometric field. The approach in this thesis seeks to exploit the cointegration property of variables and create a stationary combination of them purged of environmentally or operationally induced (nonlinear) trends, and then use this stationary residual as a diagnostic tool to determine whether a structure continues to respond in a normal way. In the field of econometrics, the behaviour and influences to a process/variable are more uncertain, and in general the aim of studying cointegration is to establish if potentially spuriously related variables are truly related, and to predict how they will move together in the long run even after shocks and unforeseen events. Really the concern is to very accurately model the structure of these stochastic variables in relation to each other. For these reasons, a lot of attention is given to the nature of the variables under consideration, and statistical tests are needed to determine whether a variable should be modeled as linear and stationary, linear and

nonstationary, nonlinear and stationary, or finally nonlinear and nonstationary. Nonlinear cointegration analysis is necessary for the nonlinear and nonstationary variables. In econometrics, the property of nonlinear cointegration is often discussed and expressed through the ideas of stability, attractors and mixing; the property of cointegration generalizes to whether or not variables have attractors with similar topological properties (these include entropies, Lyapunov exponents and topological dimension), or to whether the nonlinear combination of variables is mixing or not.

The concept of mixing is quite an abstract one, but for the purposes of SHM, it can simply be regarded as a somewhat stronger condition than stationarity i.e. mixing in a time series implies ergodicity of that series, which in turn implies stationarity. For the purposes of this work a definition of nonlinear cointegration that will suffice applies to nonstationary variables that become stationary after some form of nonlinear combination, and it is finding this nonlinear combination that is most likely of interest to SHM practitioners more than anything else.

4.4 Cointegration within a Damage Detection Approach

The cointegration technique is a powerful tool that can be used to remove the dependency of damage sensitive features from environmental variations, making them more robust, insensitive to long-term trend and therefore more suitable for damage detection problems. The cointegration approach can be easily implemented in damage detection approaches and here it is considered in an outlier-based methodology.

Step 1: Initially the nature of the monitored damage sensitive features need to be checked to establish if the are suitable to be normalized using the cointegration approach. Each variables should be integrated of the same order, in other words they should have the same degree of nonstationarity.

Furthermore, for applying the Johansen procedure, each monitored variable should be integrated order one $I(1)$, i.e. a nonstationary variable with first difference stationary. To determine the integration order, the ADF test is initially run on each variable.

Step 2: Once the suitable variables are identified, it is necessary to split the

dataset into training and test set. The training one, represents the portion of the dataset on which the regression model is build. Therefore, it is necessary that the selected range of training data collects all the possible fluctuations due to environmental variations, in order to create a reliable and accurate regression model, able to mimic the behavior of the structure during all the common operational conditions.

Step 3: Considering the training data, the relationships between the variables matching the ADF requirements are investigated. Indeed, the construction of the regression model depends on how the different variables are correlated; particularly if these relationships are linear or nonlinear. Once this information is derived, it is possible to choose the most suitable regression model for the study case. Moreover, to build the regression model itself, it is necessary to select one of the variables as regression target and use the other ones to fit the model on that target.

Then, the performance of the model is tested on the training data, applying the ADF tests to the residuals obtained from the predicted data and the measured ones. If the model residual series is integrated to a lower order than the original variables, one can say that the cointegrating relationship is established successfully; the common trends are purged, therefore, the model residual series may be a potentially good indicator of damage induced variations.

Step 4: Once a suitable regression model has been found, new data from the monitored variables should be projected on to it. If the cointegrating vector was established on data from the normal condition of the structure, the residual sequence from the linear combination will continue to be stationary all the time the structure continues to operate in its normal condition. The residual sequence should therefore be continually monitored and deviations from stationarity taken to indicate a deviation from the normal condition of the structure.

4.5 The Augmented DickeyFuller test

The ADF test is a statistical test used to determine if a time series is stationary or not and, in this last case, how many times one has to difference a time series to make it stationary (Fuller 1996). Like many econometric stationarity tests, the ADF test is based on a unit root test for a time series model. If a time series model has a unit root, it will be inherently nonstationary.

The idea is perhaps best illustrated by looking at a first-order AR model (AR(1)), which takes the form

$$y_i = a_1 y_{i-1} + \epsilon_i \tag{4.3}$$

where ϵ_i can be considered to be a Gaussian white noise process. In this case,the value of a_1 defines the root of the characteristic equation of the process. The roots of the characteristic equation of any process determine its stability and, therefore, its stationarity. In this example, the process y_i will be stationary if a_1 is less than one in magnitude, and nonstationary, if it is larger or equal to one in magnitude. In the case that a_1 is equal to one, the process will have a unit root, and Equation 4.3 becomes

$$y_i = a_1 y_{i-1} + \epsilon_i \Rightarrow \Delta y_i = \epsilon_i \tag{4.4}$$

The process will be nonstationary but its first difference will be stationary; in econometrics terminology, it will be integrated order one, denoted $y_i \sim I(1)$.

When fitting a process to an AR(1) model then, information on the stationarity of the process is obtained from the parameters defining the characteristic root. This is normally achieved by testing a null hypothesis of $a_1 = 1$. The most obvious way of going about this would be to carry out a t-test on the parameter a_1; however, under the assumption of nonstationarity, the least-squares estimate of the parameter will not be distributed around unity. Rather than carrying out a traditional t-test, the t-test statistic will normally be compared with critical values constructed by and found in Dickey and Fuller 1979.

The ADF test follows the same premise as described above, but involves fitting the data to a more complex time series model as described in

$$\Delta y_i = \rho y_{i-1} + \sum_{j=1}^{p-1} b_j \Delta y_{i_j} + \epsilon_i \tag{4.5}$$

Here, the difference operator Δ is defined as $\Delta y_{i_j} = y_{i-j} - y_{i-j-1}$. A suitable number of lags p should be included to insure that ϵ_i becomes a white noise process. To convert from the more traditional AR(p) model to the model form (Equation 4.5), the following substitutions should be made: let $a_1 = 1 + \rho + b_1$, $a_n = -b_{n-1} + b_n$, for $n = 2...p-1$, and $a_p = b_{p-1}$, where a_j are the AR model coefficients. Using these substitutions, the characteristic Equation 4.5 can readily

be obtained from the characteristic equation of an AR(p) process as

$$1 - \lambda^{-1} - \rho\lambda^{-1} - \sum_{j=1}^{p-1} b_j(1 - \lambda^{-1})\lambda^{-j} = 0 \tag{4.6}$$

where λ are the roots of the characteristic equation. With this more complex form of time series model, there could be as many as p independent roots. As an explosive process would be obvious to the analyst from the outset, the scenarios that remain of interest here are those where all roots are smaller than or equal to unity. If at least one root of the characteristic equation is unity, it follows from Equation 4.6 that ρ must equal zero. Assume for the moment that there is a single unit root and consider the remaining $(p-1)$ roots of the characteristic equation. With $\rho = 0$, Equation 4.6 becomes

$$(1 - \lambda^{-1})\left\{1 - \sum_{j=1}^{p-1} b_j\lambda^{-j}\right\} = 0 \Rightarrow 1 - \sum_{j=1}^{p-1} b_j\lambda^{-j} = 0 \tag{4.7}$$

It is clear that if y_i has one unit root, all remaining roots are smaller in magnitude than one. Furthermore, on closer inspection, Equation 4.7 is the characteristic equation of the AR process of the differenced time series,

$$\Delta y_i = \sum_{j=1}^{p-1} b_j \Delta y_{i_j} + \epsilon_i \tag{4.8}$$

As Equation 4.7 must have all roots smaller than one in magnitude, the first difference Δy_i must be stationary. If y_i is nonstationary, but its first difference is stationary, as in the case above, the process is integrated order one. To summarize, for y_i to be integrated of order one, it is necessary that $\rho = 0$ in Equation 4.5. The ADF test procedure is, therefore, to estimate the parameters in Equation 4.5 by the least-squares methods and then test the null hypothesis $\rho = 0$. (Once the regression model parameters are found, a value t for the ADF test statistic is computed. The unit root test is then carried out under the null hypothesis $\hat{\rho} = 0$ (unit root exists; series is nonstationary) against the alternative hypothesis of $\hat{\rho} < 0$).

The test statistic

$$t_p = \frac{\hat{\rho}}{\sigma_\rho} \tag{4.9}$$

where $\hat{\rho}$ is the estimate of parameter ρ and σ_ρ the standard deviation of the estimate. The ADF statistics t_p can be compared to the relevant critical value for the DickeyFuller Test (see table in Fuller 1996). If the test statistic is more than the critical value ($t_p > t_\alpha$), he null hypothesis can be rejected in favor of the alternative hypothesis, the time series has a unit root and is $I(1)$ (the time series is stationary).

If the test statistic is less than the critical value ($t_p < t_\alpha$), then the null hypothesis of $\hat{\rho} = 0$ is rejected and no unit root is present at level *alpha*. If the hypothesis is rejected, the test is repeated for Δy_i,if the hypothesis is then accepted y_i is an $I(2)$ nonstationary sequence. The test can be repeated until the rejection of the null hypothesis is obtained and in this way the integration order is determined.

Additional hypotheses and test statistics are needed if the model form used is extended to include shifts or deterministic trends (or both). For the extended time series model form,

$$\Delta y_i = \rho y_{i-1} + \sum_{j=1}^{p-1} b_j \Delta y_{i-j} + c_2 + c_1 t + \epsilon_i \tag{4.10}$$

where $c_1 t$ is a deterministic trend term and c_2 is a constant. (The latter two terms are both optional choices which are dependent on the complexity of the real model). The null hypothesis for the time series to be integrated of order one should be extended to include $c_1, c_2 = 0$. More details for these specific cases can be found in Dickey and Fuller 1981 and Fuller 1996. Having ascertained the degree of nonstationarity of each process variable of interest, an attempt to create a stationary residual through combination of those variables integrated to the same order can be made. The phase of ADF testing is fundamental for the analysis, for the purpose of knowing if among variables a cointegration relationship exists. It is necessary to repeat the ADF test primarily on the time series and then, after fitting the regression models, on the model residual.

4.6 Regression Models

4.6.1 Johansen Procedure

Johansen 1995 proposed a maximum-likelihood-based procedure to find the cointegrating vectors of a dataset. The methodology is designed for nonstationary variables whose first difference is stationary. The Johansen procedure is built to estimate the parameters of a vector error-correction model (VECM) of the variables under consideration. A VECM takes the form

$$\Delta y_i = \Pi y_{i-1} + \sum_{j=1}^{p-1} B_j \Delta y_{i-j} + \phi D(t) + \epsilon_i \tag{4.11}$$

where y_i is an n-vector including all n variables to be analyzed, with the subscript i relating to time, $i = 1, ..., N$, p represents the model order, or the number of lags to be included and ϵ_i is a noise process. It is also possible to take into account a deterministic trend including the $D(t)$ term.

The hypothesis behind the Johansen procedure is that, for the VEC model, if the y_i are cointegrated, parameters can be found such that the noise process is normally distributed; $\epsilon_i \sim N(0, [\Sigma])$.

Equation 4.11 is the multi-variate analogue of Equation 4.10 and in these circumstances, a VECM can simply be viewed as a reformulation of a vector autoregressive (AR) model. Therefore, to find the best model order p, the variables in question are fit to a VAR model,

$$y_i = A_1 y_{i-1} + A_2 y_{i-2} + ... + A_p y_{i-p} + \epsilon_i \tag{4.12}$$

and the most suitable model order p for those variables can be found using the Akaike information criterion (AIC) or similar.

Error-correction models are common in econometrics and are closely linked with the idea of cointegration. In fact, the existence of an error-correction model implies that the included variables are cointegrated and vice versa, this is called the Granger representation theorem (Engle and Granger 1987). If a true error-correction model exists (i.e. where $\epsilon_i \sim N(0, [\Sigma])$), the parameters in Π would describe the long-run equilibrium between variables, and the parameters B_j would account for short-run adjustments needed to return the process to equilibrium after

any drifts.

The Johansen procedure uses the maximum likelihood of observing the correction ϵ_i to estimate the parameter matrix Π.

Under the assumption that Equation 4.13 is a true error-correction model and that the variables under consideration are $I(1)$ (which implies that Δy_i and Δy_{i-j} are stationary), the parameter matrix Π must be rank-deficient, say of rank r, and can therefore be decomposed into two matrices

$$\Pi = \alpha\beta^T \tag{4.13}$$

where α and β are both $n \times r$ matrices. From basic linear algebra theory, the r rows of β^T will span the row space of Π. Now as the original matrix Π described the long-run equilibrium relations between the variables, β can be taken as the desired cointegrating vector to be found.

As previously indicated, parameter estimation is achieved by maximizing the likelihood of observing the correct ϵ_i. If $\epsilon_i \sim N(0, [\Sigma]))$, its probability density function will be

$$p(\epsilon_i) = \frac{1}{\sqrt{((2\pi)^n|\Sigma|)}} \exp\left(\frac{1}{2}\epsilon_i^T\Sigma^{-1}\epsilon\right) \tag{4.14}$$

where $|\Sigma|$ is the determinant of the estimated covariance of ϵ_i. It follows that the likelihood of observing the entire correct sequence of ϵ_i will equal $\Pi_{i=1}^N = p(\epsilon_i)$. On closer inspection of Equation 4.14, each individual term is bounded above by the fractional term preceding the exponent, therefore the likelihood function is bounded above by $((2\pi)^n|\Sigma|)^{N/2}$, and so

$$\mathcal{L}_{MAX} = ((2\pi)^n|\Sigma|)^{-N/2} \tag{4.15}$$

Therefore, the maximum-likelihood parameter estimates will correspond to the parameters that maximize $|\Sigma|$.

This point will be returned to later; however,for now, the effort will be focused on manipulating the maximized-likelihood function in order to express all parameter estimates in terms of β. Before going any further, however, following Johansen 1995, some new notation will be introduced to simplify the VECM expression (Equation 4.11).

The best linear combination of the variables, or cointegrating vector, is found as the parameter β in the VECM simplified model of the variable set that takes

the form

$$z_{0i} = \alpha\beta^T z_{1i} + \Psi z_{2i} + \epsilon_i \tag{4.16}$$

where $z_{0i} = \Delta y_i$, $z_{1i} = y_{i-1}$, $z_{2i} = [\Delta y_{i-1}^T, \Delta y_{i-2}^T, ..., \Delta y_{i-p}^T, D^T]^T$, and $\Psi = [B_1, B_2, ..., B_{p-1}, \phi]$ and p is model order previously found.

Referring to this simplified form the log-likelihood function L, where $L() = \ln \mathcal{L}()$, is first used to estimate Ψ by calculating

$$\frac{\partial L}{\partial \Psi} = 0 \tag{4.17}$$

After the necessary matrix calculus and some careful rearrangement, the estimate for Ψ can expressed as

$$\hat{\Psi} = M_{02}M_{22}^{-1} - \alpha\beta^T M_{12}M_{22}^{-1} \tag{4.18}$$

where are M_{mn} product moment matrices defined by

$$M_{mn} = \frac{1}{N}\sum_{i=1}^{N} z_{mi}z_{ni}^T \qquad m, n = 0, 1 \tag{4.19}$$

Substituting Equation 4.19 back into Equation 4.17, ϵ may now be expressed as

$$\epsilon_i = z_{0i} - \alpha\beta^T z_{1i} - M_{02}M_{22}^{-1}z_{2i} - \alpha\beta^T M_{12}M_{22}^{-1}z_{2i} \tag{4.20}$$

This expression can be further simplified by defining the residualsR_{0i} and R_{1i} from the following regressions:

$$\begin{aligned} z_{0i} &= C_1 z_{2i} + R_{0i} \\ z_{1i} &= C_2 z_{2i} + R_{1i} \end{aligned} \tag{4.21}$$

where the coefficient matrices are found by ordinary least squares:$C_1 = M_{02}M_{22}^{-1}$ and $C_2 = M_{12}M_{22}^{-1}$. Finally, Equation 4.20 becomes

$$\epsilon_i = R_{0i} - \alpha\beta^T R_{1i} \tag{4.22}$$

ϵ_i has now been expressed in terms of the residuals of regressions of z_{0i} and z_{1i} on z_{2i} and α, β, which are still to be found. It now remains to find the maximum-likelihood estimates of α and Σ in terms of β. Assuming a fixed β, these are found

to be

$$\hat{\alpha} = S_{01}\beta(\beta^T S_{11}\beta)^{-1} \tag{4.23}$$

and

$$\hat{\Sigma} = S_{00} - S_{01}\beta(\beta^T S_{11}\beta)^{-1}\beta^T S_{10} \tag{4.24}$$

where S_{mn} are product moment matrices

$$S_{mn} = \frac{1}{N}\sum_{i=1}^{N} R_{mi}R_{ni}^T \qquad m, n = 0, 1 \tag{4.25}$$

The estimation of β is achieved using the previously ascertained fact that the maximum-likelihood parameter estimates will correspond to the parameters that maximize $|\Sigma|$ (Equation 4.15). From Equation 4.24 then, the maximum-likelihood estimate of β corresponds to the β that maximizes

$$|\Sigma| = |S_{00} - S_{01}\beta(\beta^T S_{11}\beta)^{-1}\beta^T S_{10}| \tag{4.26}$$

Applying different Lemmas from Johansen 1995 transform looking for the β that maximizes$|\Sigma|$ into looking for the solution of the following eigenvalue-eigenvector problem (the reader is sent back to Johansen 1995, Cross et al. 2011 for further details)

$$(\lambda_i' S_{11} - S_{10}S_{00}^{-1}S_{01})v_i = 0 \tag{4.27}$$

The relevant cointegrating vectors β are found solving the problem in the previous equation and it the best choice for the cointegrating vector (i.e. the one giving the more stationary combination) corresponds to the largest eigenvalue of Equation 4.27. The eigenvalues λ_i can be seen as the squared canonical correlations between R_{0i} and R_{1i}, so between the cointegrated combinations $\hat{\beta}y_{i-1}$ and a linear combination of the (stationary) differences $w_i\Delta y_{i-1}$. In other words, the eigenvalues λ_i measure how strongly the cointegrated relation correlates with the stationary part of the process. The larger the eigenvalue the 'more stationary' the cointegrated relation.

4.6.2 Support Vector Regression

Support Vector Machines (SVMs) are among the best "off-the-shelf" discriminative classifiers known in the Machine Learning community. Given a set of training

data, each labeled as belonging to a specific category (supervised learning), an SVM training algorithm outputs a model that assigns new examples to one of the categories, making it a non-probabilistic linear classifier. SVMs models work on the geometric representation of points in an N-dimensional space, trying to find the optimal hyperplane in that same space that distinctly classifies the data points. These models can efficiently perform both linear and nonlinear classification using what is called the kernel trick, implicitly mapping their inputs into high-dimensional feature spaces.

SVMs solve binary classification problems by formulating them as convex optimization problems (Vapnik 1998). The optimization problem consists of finding the maximum margin separating the hyperplane, while correctly classifying as many training points as possible. Relying on the solution of a quadratic optimization problem allows avoiding 'local minimum' issues. Therefore the resulting learning model is an optimization algorithm rather than a greedy search.

The sparse solution and good generalization of the SVM make these model extremely suitable for regression problems. In 1997 a version of SVM for regression was presented by Drucker et al. 1997; This method is called Support Vector Regression (SVR). The generalization of SVM to regression problems is achieved by introducing the ϵ-tube, an ϵ-insensitive region around the function. Accordingly, the objective of the training is to find the tube that best approximates the continuous-valued function while looking at the same time for a balanced agreement between the model complexity and prediction error.

Exactly as for the SVM problem, the SVR is formulated as an optimization problem. As first step, a convex loss function is defined and minimized to find the narrowest tube that contains most of the training instances. Hence, a multiobjective function is constructed from the loss function and the geometrical properties of the tube. Then, the convex optimization, which has a unique solution, is solved, using appropriate numerical optimization algorithms. The hyperplane is represented in terms of support vectors, which are training samples that lie outside the boundary of the tube and that are the most influential instances that affect the shape of the tube.

An N-dimensional dataset of inputs x_i and outputs y_i related by some function f such that $y = f(x)$ is given. The data are assumed to be independent and identically distributed (iid), drawn from the same unknown probability distribution function. It can be stated that the continuous-valued function f can be

approximated by a linear superposition as follows

$$f(\mathbf{x}, \mathbf{w}) = \mathbf{w}^T\mathbf{x} + \mathbf{b} \tag{4.28}$$

where the vector $\mathbf{w}$ collects the set of weights, one for each feature, whose linear combination predicts the value of labels $\mathbf{y}$.

This function approximation problem is treated as an optimization problem that tries to find the flattest tube centered around the hyperplane, minimizing at the same time the error between the predicted value of the function for a given input and the actual output (prediction error). This aim is summarized by the objective function in Equation 4.29

$$\min_{w} \frac{1}{2}||\mathbf{w}||^2 \tag{4.29}$$

where $||\mathbf{w}||$ represents the magnitude of the vector perpendicular to the hyperplane that is being approximated. The adopted loss function is ϵ-insensitive and tends to penalize the predictions that are farther than ϵ from the desired output. The sparsity of the solution is affected by the chosen ϵ since it represents the width of the tube and consequently the tolerance level. Smaller value indicates a lower tolerance for error and determines the numbers of support vectors in the problem. If ϵ decreases, the boundary of the tube is shifted inward. Therefore, more datapoints are around the boundary, which indicates more support vectors. Similarly, increasing ϵ will result in fewer points around the boundary. Because it is less sensitive to noisy inputs, the ϵ-insensitive region makes the model more robust.

There is no unique loss function that could be adopted. Linear (Equations 4.30), quadratic (Equations 4.31), and Huber (Equations 4.31) ϵ are all reasonable choices. The Huber loss function is smoother than the linear and quadratic functions, but it penalizes all deviations from the desired output, with greater penalty as the error increases. The information that drive the user towards the correct choice of loss function are: the noise distribution affecting the data samples, the model sparsity sought, and the training computational complexity. Even if, both symmetrical and asymmetrical loss functions can be adopted, the loss functions should be convex (like the tree example presented) to ensure that the optimization problem has a unique solution that can be found in a finite number

of steps.

$$L_\epsilon(\mathbf{y}, f(\mathbf{x}, \mathbf{w})) = \begin{cases} 0 & \text{if } |\mathbf{y} - f(\mathbf{x}, \mathbf{w})| \leq \epsilon \\ |\mathbf{y} - f(\mathbf{x}, \mathbf{w})| - \epsilon, & \text{else} \end{cases} \tag{4.30}$$

$$L_\epsilon(\mathbf{y}, f(\mathbf{x}, \mathbf{w})) = \begin{cases} 0 & \text{if } |\mathbf{y} - f(\mathbf{x}, \mathbf{w})| \leq \epsilon \\ (|\mathbf{y} - f(\mathbf{x}, \mathbf{w})| - \epsilon)^2, & \text{else} \end{cases} \tag{4.31}$$

$$L(\mathbf{y}, f(\mathbf{x}, \mathbf{w})) = \begin{cases} c|\mathbf{y} - f(\mathbf{x}, \mathbf{w})| - \frac{c^2}{2} & \text{if } |\mathbf{y} - f(\mathbf{x}, \mathbf{w})| > c \\ \frac{1}{2}|\mathbf{y} - f(\mathbf{x}, \mathbf{w})|^2, & \text{if } |\mathbf{y} - f(\mathbf{x}, \mathbf{w})| \leq c \end{cases} \tag{4.32}$$

Adopting a soft-margin approach similar to that employed in SVM, slack variables $\{\xi_i^*\}$,$\{\xi_i\}$ can be added to guard against outliers. These variables determine how many points can be tolerated outside the tube.

Considering a linear loss function (Equation 4.30) the optimization problem assumes the expression in Equation 4.33; where C is a regularization term, a tunable parameter that gives more weight to minimizing the flatness, or the error. Larger values of C give more weight to minimizing the error. This constrained quadratic optimization problem can be solved by finding the Lagrangian (Equation 4.36). The Lagrange multipliers, or dual variables, are λ, λ^*, α, α^* and are nonnegative real numbers.

$$min\frac{1}{2}||w||^2 + C\sum_{i=1}^{N} \xi_i^* + \xi_i, \tag{4.33}$$

Subject to the following constraints:

$$\xi_i, \xi_i^* \geq 0 \quad i = 1, \cdots, N \tag{4.34}$$

$$\begin{aligned} y_i - w^T x_i &\leq \epsilon + \xi_i^* \quad i = 1, \cdots, N \\ w^T x_i - y_i &\leq \epsilon + \xi_i \quad i = 1, \cdots, N \end{aligned} \tag{4.35}$$

$$\begin{aligned} \mathcal{L}(w, \xi^*, \xi, \alpha^*, \alpha, C^*, \gamma^*, \gamma) = \tfrac{1}{2}||w||^2 + \textstyle\sum_{i=1}^{N}(\xi_i^* + \xi_i) + \sum_{i=1}^{N} \alpha_i^*[y_i - w^T x_i - \epsilon - \xi_i^*] \\ + \textstyle\sum_{i=1}^{N} \alpha_i[-y_i + w^T x_i - \epsilon - \xi_i] - \sum_{i=1}^{N}(\gamma_i^* \xi_i^* + \gamma_i \xi_i) \end{aligned} \tag{4.36}$$

The minimum of Equation 4.36 is found by taking its partial derivatives with respect to the variables and setting them equal to zero (Equation 4.37). The

partial derivatives with respect to the Lagrange multipliers return the constraints (Equation 4.37).

$$\begin{aligned}
\frac{\delta\mathcal{L}}{\delta w} &= w - \sum_{i=1}^{N}(\alpha_i^* - \alpha_i)x_i = 0 \\
\frac{\delta\mathcal{L}}{\delta\xi_i^*} &= C - \gamma_i^* - \alpha_i^* = 0 \\
\frac{\delta\mathcal{L}}{\delta\xi_i} &= C - \gamma_i - \alpha_i = 0 \\
\frac{\delta\mathcal{L}}{\delta\gamma_i^*} &= \sum_{i=1}^{N}\xi_i^* \leq 0 \\
\frac{\delta\mathcal{L}}{\delta\gamma_i} &= \sum_{i=1}^{N}\xi_i \leq 0 \\
\frac{\delta\mathcal{L}}{\delta\alpha_i^*} &= y_i - w^T x_i - \epsilon - \xi_i^* \leq 0 \\
\frac{\delta\mathcal{L}}{\delta\alpha_i} &= y_i - w^T x_i - \epsilon - \xi_i \leq 0
\end{aligned} \tag{4.37}$$

$$\begin{aligned}
\alpha_i^*(y_i - w^T x_i - \epsilon - \xi_i^*) &= 0 \\
\alpha_i(y_i - w^T x_i - \epsilon - \xi_i) &= 0 \\
\gamma_i^*\xi_i^* &= 0 \qquad \forall i \\
\gamma_i\xi_i &= 0
\end{aligned} \tag{4.38}$$

$$w = \sum_{i=1}^{N_{SV}}(\alpha_i^* - \alpha_i)x_i \tag{4.39}$$

The product of the Lagrange multipliers and the constraints is equal to zero (Equation 4.38). The Lagrange multipliers that are equal to zero correspond to data inside the tube, whereas the support vectors have nonzero-valued Lagrange multipliers. The solution is written in terms of the support vector onlyhence, the solution sparsity. The function approximation is represented in (Equation 4.40). By replacing Equation 4.37 in Equation 4.36, the dual form of the optimization problem can be written as shown in Equation 4.41.

$$f(x) = \sum_{i=1}^{N_{SV}}(\alpha_i^* - \alpha_i)x_i^T x, \alpha_i, \alpha_i^* \in [0, C] \tag{4.40}$$

$$max_{\alpha,\alpha^*} - \epsilon\sum_{i=1}^{N_{SV}}(\alpha_i^* - \alpha_i)y_i - \frac{1}{2}\sum_{j=1}^{N_{SV}}\sum_{i=1}^{N_{SV}}(\alpha_i^* - \alpha_i)(\alpha_j^* - \alpha_j)x_i x_j, \tag{4.41}$$

subject to

$$\sum_{i=1}^{N_{SV}}(\alpha_i^* - \alpha_i) = 0, \alpha_i, \alpha_i^* \in [0, C] \tag{4.42}$$

At the beginning of this section, the weights vector **w** was augmented with the

scalar b, and the derivation of the SVRs mathematical formulation was carried out, disregarding the explicit computation of b (Equation 4.28). However, b could have been calculated from the KKT conditions, as shown next. Training data that belong to the outside of the boundary of the tube will have nonzero α_i or a α_i^*; they cannot both be zero, because that would mean that the instance (x_i, y_i) belongs to the lower and upper boundary, which is not possible. Therefore, the corresponding constraints will be satisfied with equality, as demonstrated in Equation 4.43. Furthermore, because the point is not outside the tube, $x_i = 0$, leading to the result in Equation 4.44 when $\alpha \in (0, C)$. Equation 4.45 computes b. Performing the same analysis for α_i^* ,one gets Equations 4.46 and 4.47.

$$y_i - w^T x_i - b - \epsilon - \xi_i = 0 \tag{4.43}$$

$$y_i - w^T x_i - b - \epsilon = 0 \tag{4.44}$$

$$b = y_i - w^T x_i - \epsilon = 0 \tag{4.45}$$

$$-y_i + w^T x_i - b - \epsilon = 0 \tag{4.46}$$

$$b = -y_i + w^T x_i - \epsilon = 0 \tag{4.47}$$

The previous section dealt with data in the feature space, assuming $f(x)$ is linear. For non linear functions, the data can be mapped into a higher dimensional space, called kernel space, to achieve a higher accuracy, using kernels that satisfy Mercers condition.

Therefore, replacing all instances of x in Equations 4.28−4.47 with $k(x_i, x_j)$ yields the primal formulation shown in Equation 4.48, where $\phi(.)$ is the transformation from feature to kernel space. Equation 4.50 describes the new weight vector in terms of the transformed input. The dual problem is represented in Equation 4.50, and the function approximation $f(x)$ is in Equation 4.51, where $k(.,.)$, the kernel, is as illustrated in Equation 4.52.

$$min \frac{1}{2}||w||^2 + C \sum_{i=1}^{N} \xi_i^* + \xi_i, \tag{4.48}$$

Subject to the following constraints:

$$\begin{aligned} \xi_i, \xi_i^* \geq 0 \qquad & i = 1, \cdots, N \\ y_i - w^T \phi(x_i) \leq \epsilon + \xi_i^* \quad & i = 1, \cdots, N \\ w^T \phi(x_i) - y_i \leq \epsilon + \xi_i \quad & i = 1, \cdots, N \end{aligned} \tag{4.49}$$

$$w = \sum_{i=1}^{N_{SV}} (\alpha_i^* - \alpha_i) \phi(x_i) \tag{4.50}$$

$$\begin{gathered} max_{\alpha,\alpha^*} - \epsilon \sum_{i=1}^{N_{SV}} (\alpha_i^* - \alpha_i) y_i - \frac{1}{2} \sum_{j=1}^{N_{SV}} \sum_{i=1}^{N_{SV}} (\alpha_i^* - \alpha_i)(\alpha_j^* - \alpha_j) k(x_i, x_j), \\ \alpha_i, \alpha_i^* \in [0, C], i = 1, ..., N_{SV}, \sum_{i=1}^{N_{SV}} (\alpha_i^* - \alpha_i) = 0 \end{gathered} \tag{4.51}$$

$$f(x) = \sum_{i=1}^{N_{SV}} (\alpha_i^* - \alpha_i) k(x_i, x) \tag{4.52}$$

4.6.3 Relevance Vector Machine

Relevance Vector Machine (RVM) is a kernel-based approach for classification and regression formulated by Tipping 2001. The SVM combines an excellent generalization property with a sparse kernel representation, but it suffers from several disadvantages: the predictions are not probabilistic; there is a requirement to estimate hyperparameters (a trade-off parameter, insensitive parameter et al.); there is a need to use "Mercer" kernel functions.

The RVM conserves the sparseness capacity and retains the excellent predictive performance of the SVM but it does not suffer from any of above limitations. The RVM adopts a Bayesian approach to learning, where a prior over the weights is introduced (governed by a set of hyperparameters), that is the most probable resulting from iterative process on the set of data. In this way, sparsity is achieved since the posterior distribution of many of the weights are peaked around zero. The remained non-zero weights are the so called "relevance vectors", in deference to the principle of automatic relevance determination which motivates the presented approach. However RVMs use an expectation maximization (EM)-like learning method and are therefore at risk of local minima. This is unlike the standard sequential minimal optimization (SMO)-based algorithms employed by SVMs, which are guaranteed to find a global optimum (of the convex problem).

Given again a data set of predictor variables and targets, x_i and y_i respectively, we follow the standard probabilistic formulation and assume $p(\mathbf{y}|\mathbf{x})$ is Gaussian $\mathcal{N}(\mathbf{y}|f(x), \sigma^2)$.

For the Relevance Vector Machine the mean of this distribution, is modeled for a given x by the following equation,

$$f(\mathbf{x}, \mathbf{w}) = \mathbf{w}^T k(\mathbf{x}, \mathbf{x}_i) + \mathbf{w}_0 \tag{4.53}$$

while the likelihood is calculated as,

$$p(\mathbf{y}|\mathbf{w}, \sigma^2) = (2\pi\sigma^2)^{-N/2} \exp\{-\frac{1}{2\sigma^2}||\mathbf{y} - \Phi\mathbf{w}||^2\} \tag{4.54}$$

where $\mathbf{y}$ is the vector of the N target, $\mathbf{w}$ is the weight vector and Φ is a matrix of dimension $N \times (N+1)$ called "design matrix" where each terms is defined as $\Phi_{ij} = k(x_i, x_j)$ and $\Phi_{n1} = 1$. In general the estimate of w and σ^2 from the previous equation leads to strong overfitting, so it is preferred to use smoother and less complex functions by defining an automatic relevance determination Gaussian prior over the weights,

$$p(\mathbf{w}|\boldsymbol{\alpha}) = \prod_{i=0}^{N} N(w_i|0, \alpha_i^{-1}) \tag{4.55}$$

where $\boldsymbol{\alpha}$ is a vector with $N+1$ hyperparameters. So it is important to notice that there is an individual hyperparameter for every weight: this is the fundamental feature of the model and is responsible for the model sparsity properties. The posterior over the weights is given by Bayess rule,

$$p(\mathbf{w}|\mathbf{y}, \boldsymbol{\alpha}, \sigma^2) = (2\pi)^{-(N+1)/2}|\boldsymbol{\Sigma}|^{-1/2} \exp\{-\frac{1}{2}(\mathbf{w} - \boldsymbol{\mu})^T\boldsymbol{\Sigma}^{-1}(\mathbf{w} - \boldsymbol{\mu})\} \tag{4.56}$$

where the posterior covariance and mean are respectively:

$$\boldsymbol{\Sigma} = (\boldsymbol{\Phi}^T\mathbf{B}\boldsymbol{\Phi} + \mathbf{A})^{-1} \tag{4.57}$$

$$\boldsymbol{\mu} = \boldsymbol{\Sigma}\boldsymbol{\Phi}^T\mathbf{B}\mathbf{y} \tag{4.58}$$

$\mathbf{A}$ is a matrix which has the N α on the diagonal and $\mathbf{B} = s\sigma^{-2}\mathbf{I}_N$. Also σ^2 is considered an hyperparameter which must be estimated from the data set. By integrating out the weights, one can achieve the marginal likelihood, or evidence

for the hyperparameters:

$$p(\mathbf{y}|\alpha,\sigma^2) = (2\pi)^{-(N)/2}|\mathbf{B}^{-1} + \Phi A^{-1}\Phi^T|^{-1/2}e^{-\frac{1}{2}(t(B^{-1}+\Phi A^{-1}\Phi^T)t)} \tag{4.59}$$

The key feature of this approach is that as well as offering good generalization performance, the inferred predictors are exceedingly sparse in that they contain relatively few non-zero w_i parameters. The majority of parameters are automatically set to zero during the learning process, giving a procedure that is extremely effective at discerning those basis functions which are 'relevant' for making good predictions.

4.7 Numerical Application Cantilever Beam

Model: The simulated system tested in this section is a steel cantilever beam (Figure 4.1), modeled according to the common Euler-Bernoulli's theory of the beam. In the analysis the system is framed in n_e subelements (Figure 4.2) and the nodes are numbered in ascending order, so that the node closest to the constraint is labeled as 1. The energy dissipation properties of the system are modeled through the Rayleigh damping mechanism. The material chosen for the beam is steel and the mechanical and geometric properties assigned to the beam are reported in Table (4.1)

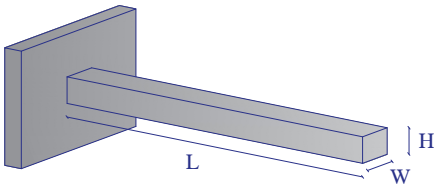

Figure 4.1: 3D view of the cantilever beam.

Table 4.1: Mechanical and geometric properties of the beam.

Mechanical Property	Symbol	Value
Length	L[m]	5
Section Height	H[m]	0.3
Section Base	W[m]	0.3
Young's Modulus	E[GPa]	210
Volume Density	$\rho[\frac{kg}{m^3}]$	8000

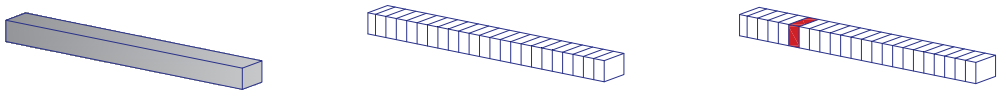

(a) (b) (c)

Figure 4.2: cantilever beam:(a) continuous model, (b) discretized model and (c) view of the damaged element

Temperature influence: The mechanical parameters are considered to be temperature-dependent and it is well known that thermal expansion and Young's modulus vary linearly within the range of normal ambient temperature (Yuen and Kuok 2010). Let α and β be the thermal coefficients for expansion and Young's modulus, respectively. In the normal range of temperature, the length and Young's modulus of the beam at temperature T can be expressed as

$$L = L_0(1 + \alpha\Delta T) \tag{4.60}$$

$$E = E_0(1 + \beta\Delta T) \tag{4.61}$$

where L_0 and E_0 are the length and Young's modulus, respectively, at 0 . Therefore, the area and the second moment of inertia follow similar relationships:

$$A = A_0(1 + \alpha\Delta T)^2 \tag{4.62}$$

$$I = I_0(1 + \alpha\Delta T)^4 \tag{4.63}$$

where A_0 and I_0 are the corresponding beam and material properties at 0 . Typical values of α and β for steel are $1.2\times10^{-5}/C$ and $-3.2\times10^{-4}/C$ respectively.

Signal processing: Two different analysis are carried on. An initial group of realizations is generated to compare the level of sensitivity of CCs towards temperature with the one related to the damage. Next a second group of tests is conducted, in which the temperature varies almost continuously for each realization, affecting the beam initially in undamaged conditions and then in damaged ones.

In each realization the acceleration response to a white Gaussian noise input is simulated. The input time history, of mean 0 and standard deviation 1, is 2 minutes long with sampling frequency of 200 Hz and it is applied at the ending node of the beam. The acceleration response of the system is simulated applying the Newmark integration approach.

The simulated response data are further standardized and normalized prior to being used for feature extraction:

$$x_{normalized}[n] = \frac{x[n] - \bar{x}}{\sigma_x} \tag{4.64}$$

where $x[n]$ is the original signal, $\bar{x}$ its mean and σ_x its standard deviation. The normalization procedure is performed on each frame.

Feature Extraction: Before applying the extraction procedure discussed in Section 3.1.1, the number of triangular filters must be selected with the value for the cutoff frequency. The number of filters can be set according to the Fraile et al. criterion presented in the Section 3.1.1 (Fraile Muñoz et al. 2008), since the sampling frequency adopted to simulate the system response is equal to 200 Hz, M is set to 15 for both the set of analysis. Consequently, as mentioned in Section 3.1.1, the number of selected CCs $(D-1)$ is chosen equal to the number of frequency bands M.

Then the cutoff frequency is set looking at the average spectrum (Figure 4.3); in both the analysis conducted the value is set to 80 Hz, since the entire energy content is between 0 Hz and 80 Hz. However in the sensitivity analysis the results are compared with the ones obtained setting the cutoff frequency equal to 8 Hz, in order to observe the results in two different spatial configuration of the triangular filters (Figure 4.4).

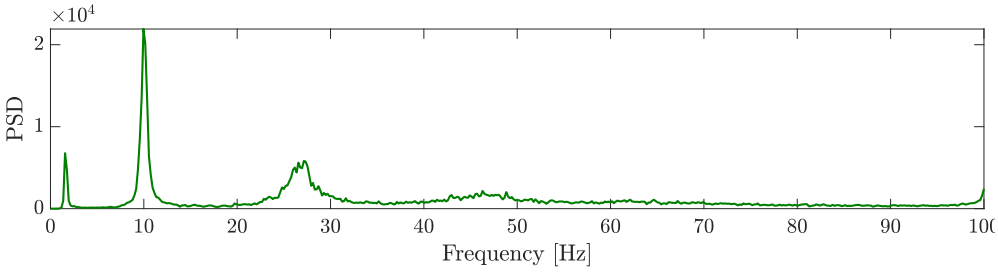

Figure 4.3: Average Spectrum.

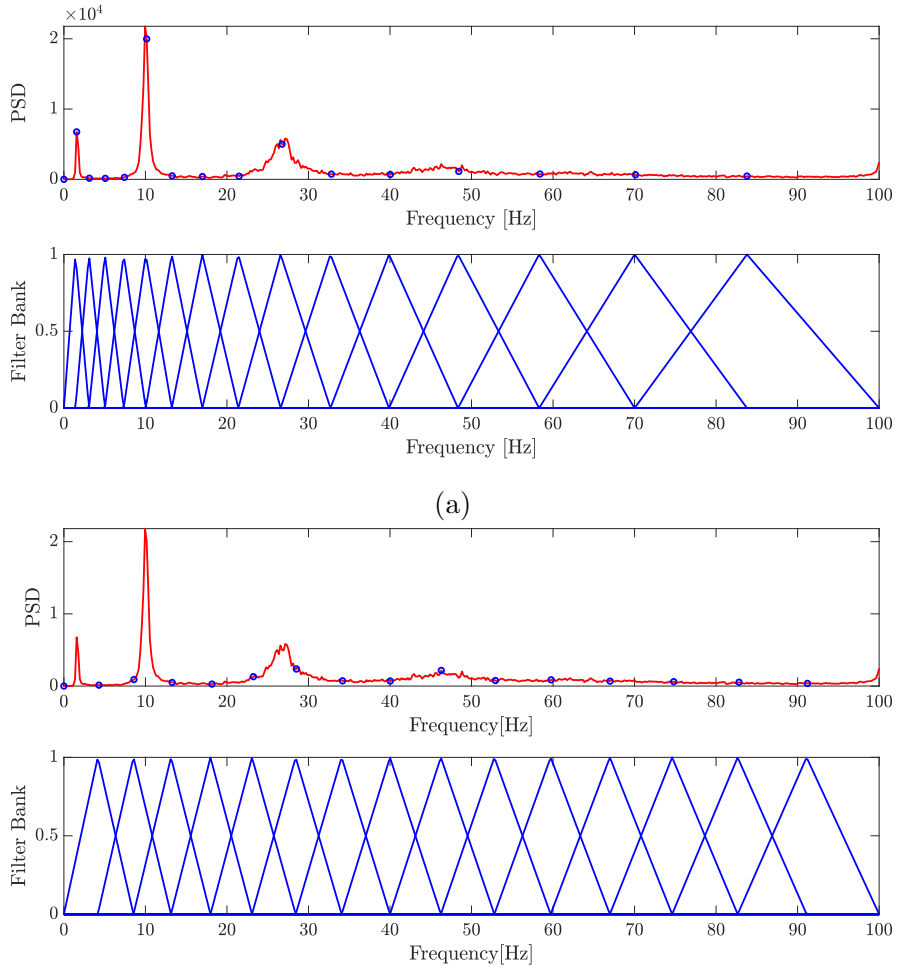

Figure 4.4: Frequency Warping: (a) $f_c = 8Hz$, (b) $f_c = 80Hz$

At the end of the extraction process, for each sensor and each realization, a matrix C of dimension $D \times N_{frames}$ is computed, which collects the vectors of CCs

for each frame. Then, in order to have only one vector of CCs for each realization coming from the single sensor, the extracted matrix is averaged over the frames.

4.7.1 Sensitivity of Cepstral Coefficients

In this test the beam is discretized in 10 subelements and about the system vibration response, no additional noise is taken into account to simulate measurement noise. Seven different scenario are performed considering temperature variation with the beam in undamaged conditions (Table 4.2), while for the damage status, four damage conditions are simulated introducing an increasing reduction of the stiffness of the 5^{th} subelement (Table 4.2).

Table 4.2: Damage and Undamage scenarios.

Condition	**Temperature**	**Damaged Element**	**Damage**
	℃	n	%
Undamaged(U1)	-30 (T_1)	-	-
Undamaged(U2)	-20 (T_2)	-	-
Undamaged(U3)	-10 (T_3)	-	-
Undamaged(Reference)	0 (T_4)	-	-
Undamaged(U5)	10 (T_5)	-	-
Undamaged(U6)	20 T_6)	-	-
Undamaged(U7)	30 (T_7)	-	-
Damaged(D1)	0 (T_4)	5	5
Damaged(D2)	0 (T_4)	5	10
Damaged(D3)	0 (T_4)	5	15
Damaged(D4)	0 (T_4)	5	20

Figure 4.5 shows the percentage variation of the first six CCs with respect to the corresponding parameters in the reference condition for each sensor, in the undamaged conditions. The behavior of the CCs is perfectly symmetric with respect to the temperature variation from -30°C up to +30°C in both choices of cutoff frequency, showing a robustly linear behavior of CCs with respect to temperature when the structure is linear. The magnitude of these variations, instead, changes within the choice of the cutoff frequency. There is no common trend within the

variations of the different coefficients in the two cases; this happens because changing the cutoff frequency, the spatial configuration of the filters changes and the frequency bands happen to work on different areas of the spectra in the two configurations. However it is possible to compare the first Cepstral Coefficient in the two cases, because it is the only coefficient proportional to the energy content of the all spectrum. For this coefficient can be noticed, then, that the magnitude of the variations decreases choosing 80 Hz as cutoff frequency, for all the sensors, because in this configuration the filters are not catching properly the frequency content corresponding to the structural frequencies (Figure 4.4b). On the other hand the configuration related to the cutoff frequency equal to 8 Hz presents the vertex of three filters matching exactly the structural frequencies (Figure 4.4a) and then the energy frequency content of the system is entirely taken into account.

In Figure 4.6 the same results are presented considering also the addition of the four damage scenarios. In the D3 and D4 cases, the variations due to damage are consistently higher than the variations due to the temperature changes, in all sensors and for all CCs. This happens to be true for both the choices of cutoff frequency, meaning that, even in the worst warped spectrum scenario, these coefficients are able to clearly distinguish damage from temperature effects, when the damage scenario starts to be important. Setting the cutoff frequency equal to 80 Hz, instead, leads to uncertainties in some sensors and for some coefficients regarding the D2 condition. The first D1 scenario is always not well discriminated in both cases.

4.7.2 Novelty detection

In this section, two different set of simulations are run for the cantilever beam: a set of 4500 simulations considering the system in its healthy state and another set of 3600 tests in which the beam is damaged. The damage condition is simulated introducing a reduction of 10 % of the stiffness of the 6^{th} subelement (Figure 4.2). Each realization, both in the undamaged or damaged conditions, corresponds to a specific value of temperature in between -5 C and +30 C. In these group of analysis the beam is discretized in 20 elements. The system is subjected to a white Gaussian noise input, which in this case is applied in order to suppress the first structural frequency (about 1.5 Hz) of the beam and create a scenario in which not all the structural frequency information are visible in the spectrum.

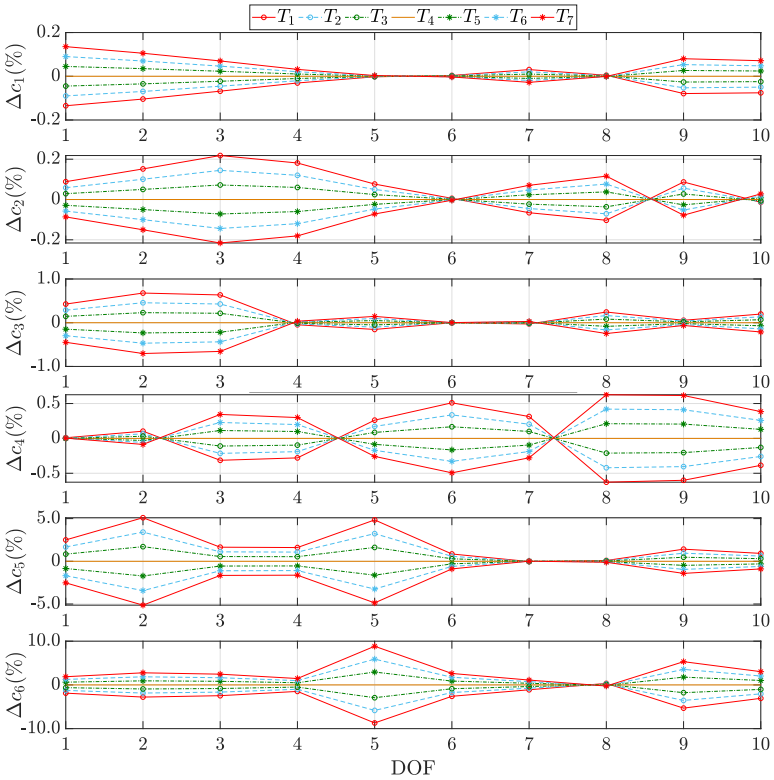

(a) $f_c = 8Hz$

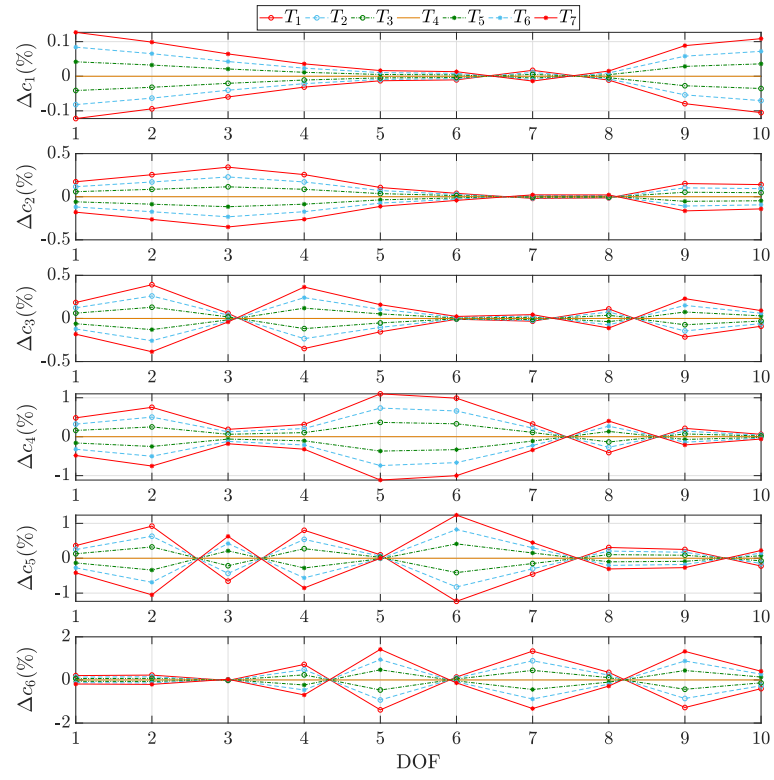

(b) $f_c = 80Hz$

Figure 4.5: Variation of CCs in undamaged conditions with respect to the reference scenario

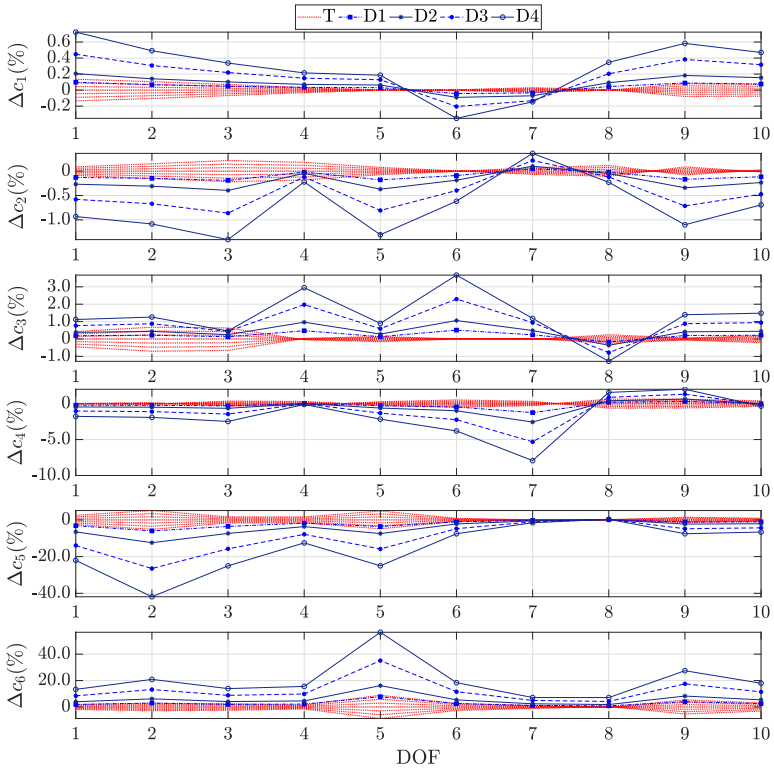

(a) $f_c = 8Hz$

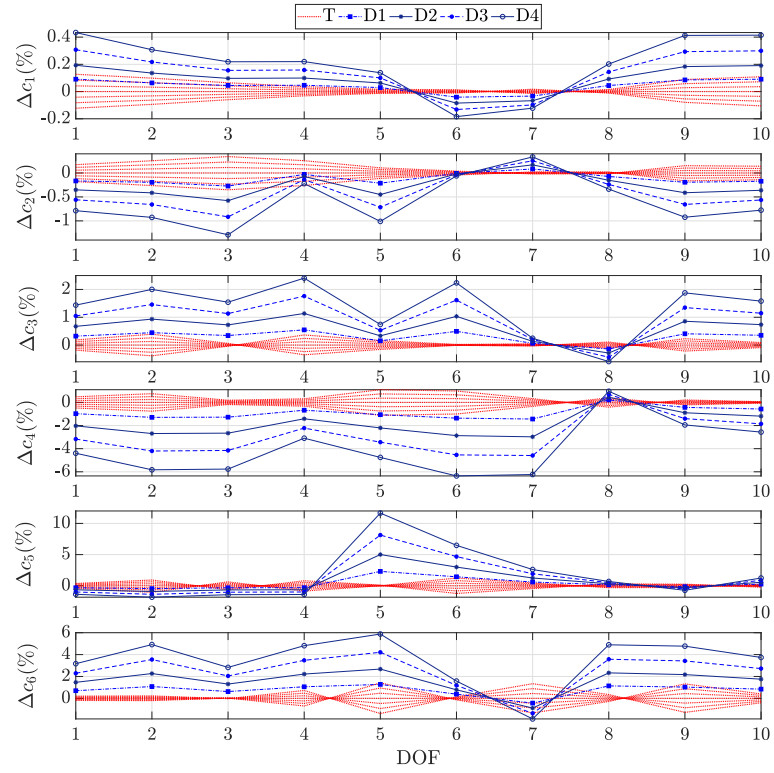

(b) $f_c = 80Hz$

Figure 4.6: Variation of CCs in damaged conditions with respect to the reference scenario

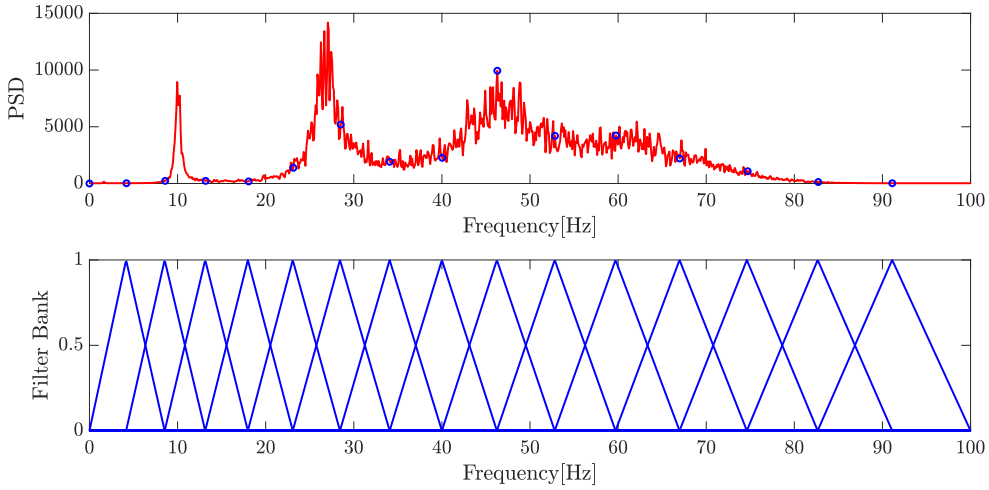

Figure 4.7: Average Spectrum for the first frame

To simulate the effects of measurement noise, 10 % RMS white Gaussian noise is added to the simulated response.

As previously mentioned the cutoff frequency is set looking at the frequency energy content of the average spectrum (Figure 4.7), and in this case is set equal to 80 Hz.

A matrix collecting the CCs time history for each sensor is extracted following the procedure presented in Section 3.1.1. The 15 Cepstral Coefficients extracted for the first sensor in the undamaged condition are presented in Figure 4.11. Looking at the trend of the CCs (Figure 4.11) and comparing it with the simulated variation of temperature, it can be noticed how some of the coefficients results to be influenced by the environmental fluctuations (c_1, c_2, c_3), while others remain mainly stationary (c_4, c_6, c_7). The same behavior can be observed for the coefficients computed from the time histories measured with the other 19 sensors. This distinction arises from the nature itself of the CCs and their extraction process. The frequency warping step, presented in Section 3.1.1, consists in the application of a set of triangular filters to the PS of each frame and each filter is going to weights and collects different areas of the spectra.

Looking at the log-contribute of each filter along the observations in time (Figure 4.8), it can be inferred that only some filters, related to different frequency areas of the spectrum, carry the environmental effects, presenting a trend that matches the temperature variation. In this study case the 5^{th} and 8^{th} triangular filters collect the frequency area mainly dependent from the environmental varia-

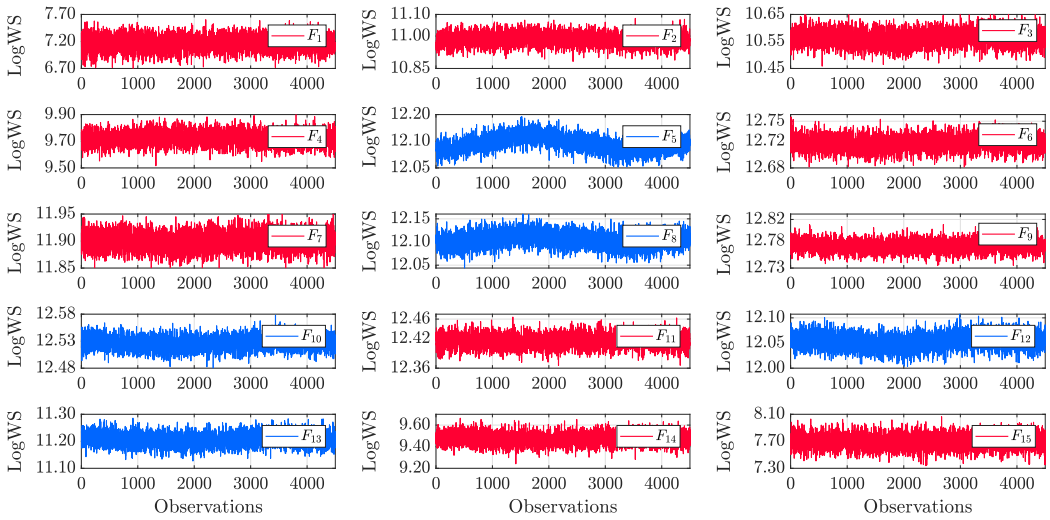

Figure 4.8: Terms of the log-warped spectrum over time

tion; the 10^{th}, 12^{th} and 13^{th} filters are also slightly varying, while the remaining filters are almost stationary.

The final step of the extraction process, involves the application of the Inverse Discrete Cosine Transform to the log-warped power spectrum according to Equation 3.3. Each CC results from the multiplication of each coefficient of the IDCT (Figure 4.9) by the terms of the log-warped spectrum. This implies that, because of the shape itself of the IDCT coefficients, this multiplication of contributes can highlight or delete the trend trapped in the log-warped spectrum terms. In this study case the second coefficient of the IDCT brings up the trend carried by the higher filters (10^{th}, 12^{th} and 13^{th}) while the contributes brought by the 5^{th} and 8^{th} filters cancel each other in the sum (Figure 4.10). In the sixth coefficient of the IDCT, instead, all the contributes from these filters cancel in the sum and the resulting CC is stationary (Figure 4.10).

The CCs computed for the damaged conditions are presented in Figure 4.12 where the damage start is indicated by the vertical black line. The jump due to the stiffness variation, even if it is only a change of 10 % in the stiffness of one element over twenty, is clearly visible up to the coefficient c_9, while it tends to fade in the last features. In the time histories of CCs affected by the variation of temperature, this little gap presents the same magnitude order of the fluctuations due to temperature and because of that the damage could be hidden and not detected. In the stationary coefficients, instead, the presence of damage clearly

shows up.

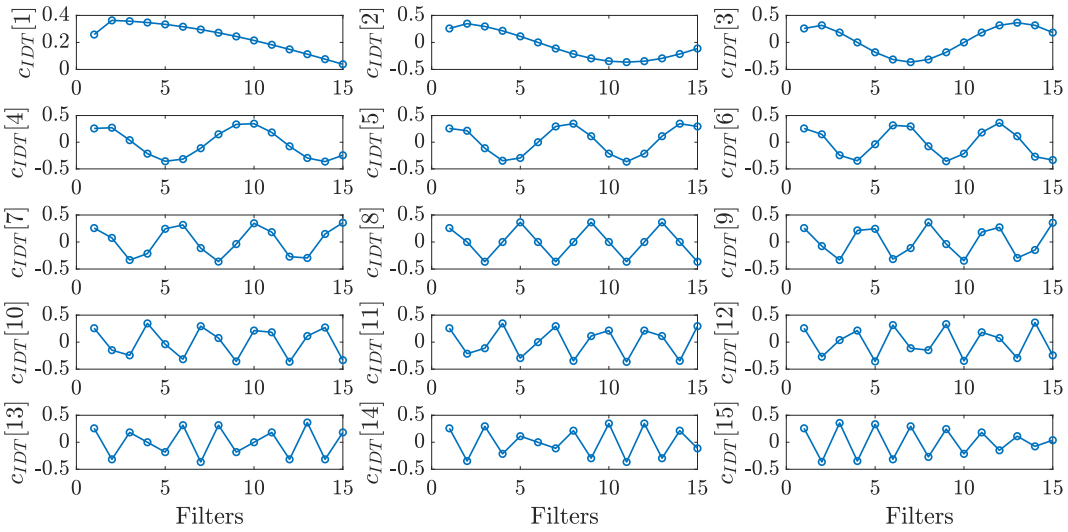

Figure 4.9: Coefficients of the inverse discrete cosine transform (IDCT)

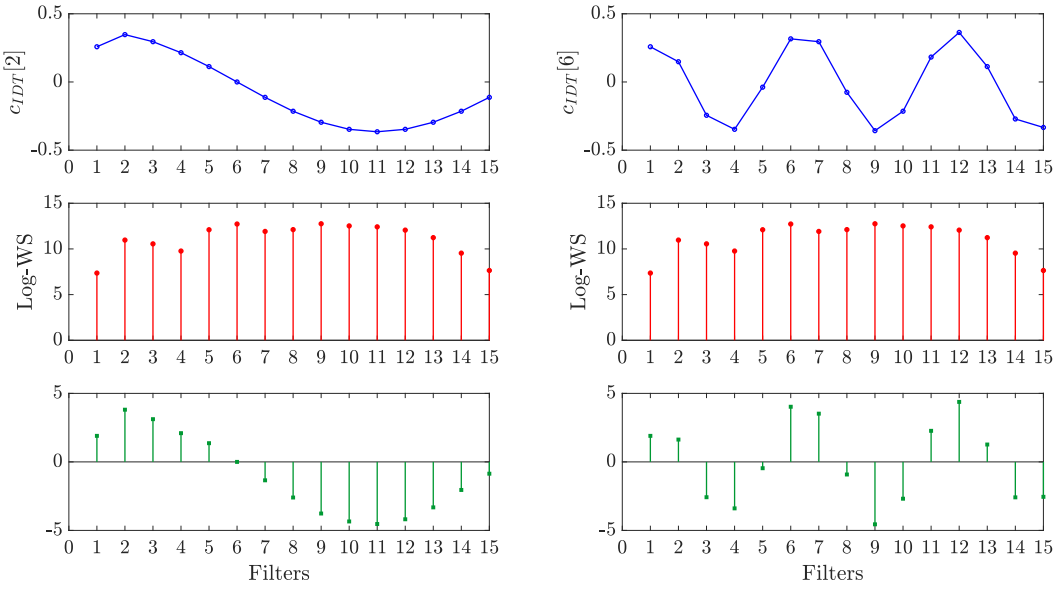

Figure 4.10: Application of the second and sixth coefficients of the IDCT to the log-warped spectrum

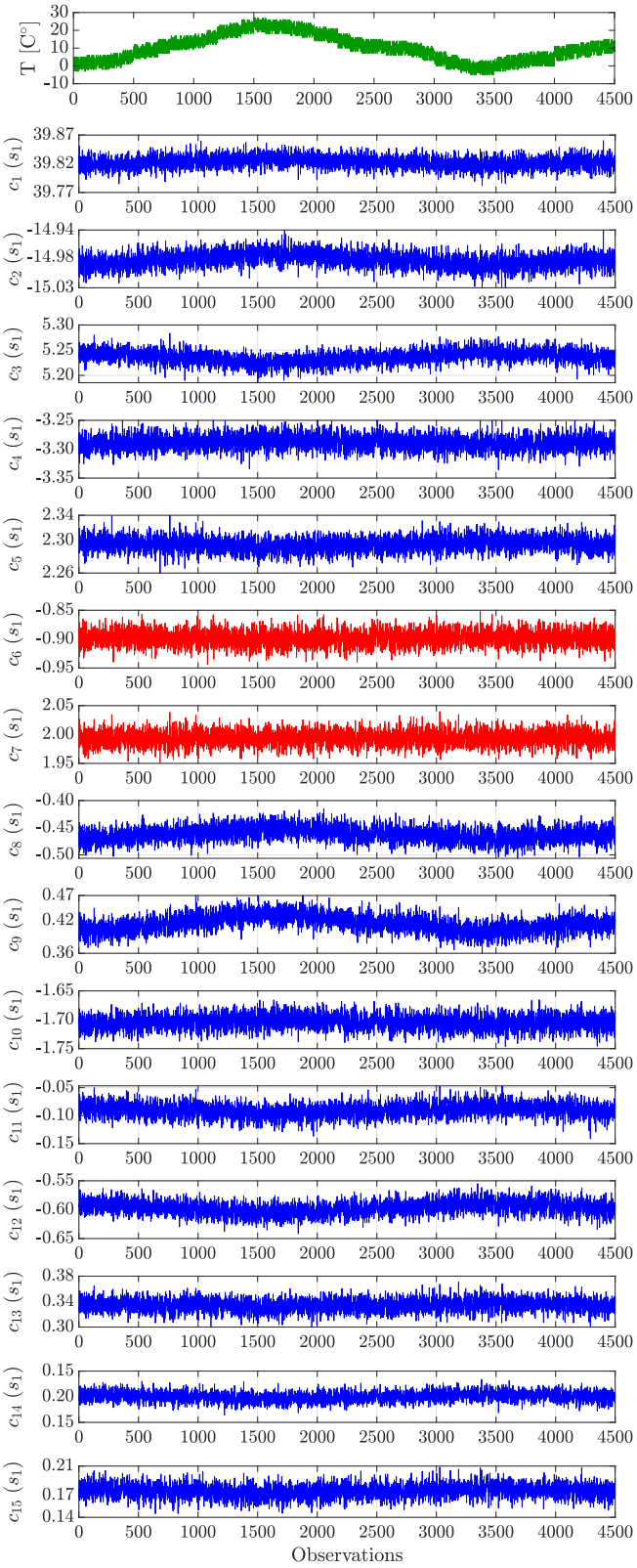

Figure 4.11: Time histories of Cepstral Coefficients: Undamaged Scenarios

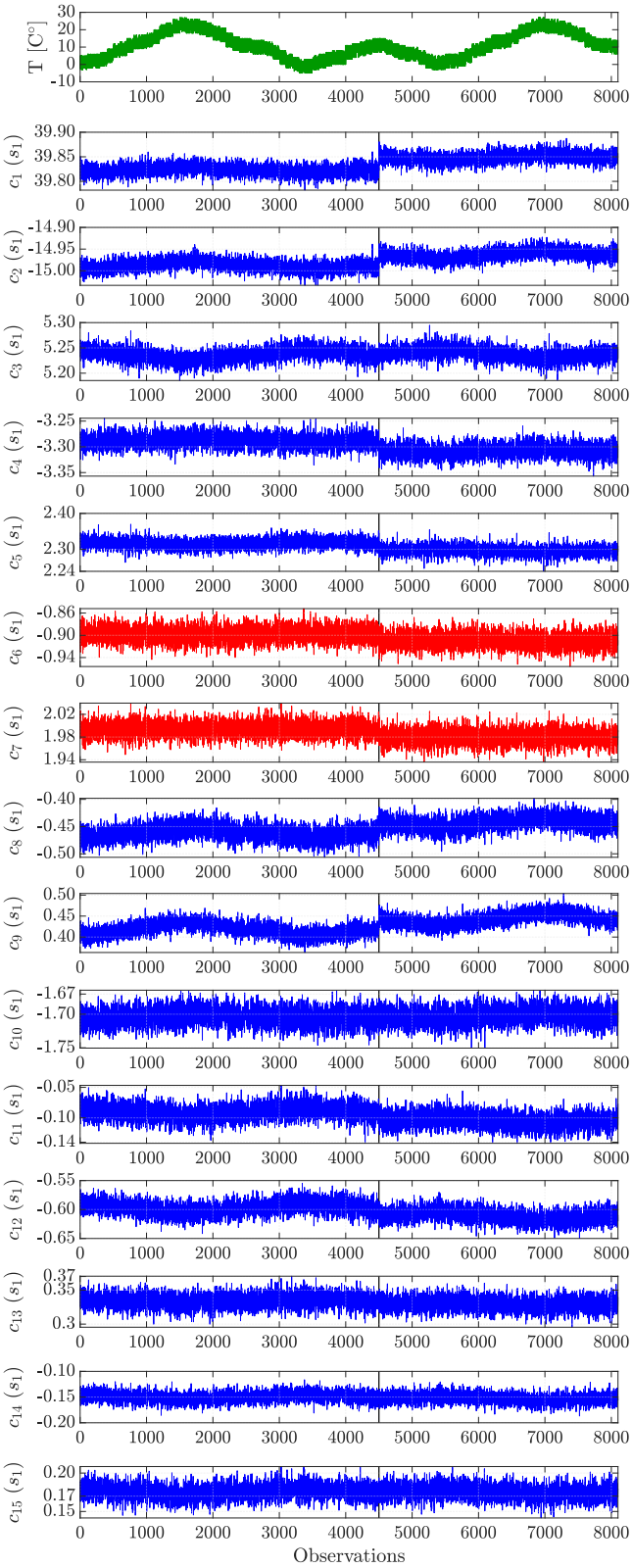

Figure 4.12: Time histories of Cepstral Coefficients: Damaged Scenarios

4.7.3 Cointegration

In this section the cointegration technique is applied to remove the dependency of Cepstral Coefficients from the environmental fluctuations, building damage sensitive features that are strictly dependent only on the occurrence of damage. The monitored variables analyzed are the CCs computed in the previous section for the cantilever beam at sensor 1 (s_1).

Before computing the cointegrating vectors, it is necessary to check which variables, presenting the same integration order, can be cointegrated. To determine the integration order, the ADF test is initially run on the variables derived from the single sensor. The results are given in Table 4.3, and show that almost all the coefficient series are nonstationary at the 95% confidence level and integrated of order one, i.e. they are $I(1)$ series.

At this point the data set is divided into two parts: a training and test data set. Training data are used to train the regression model, the test data set is employed for the aim of monitoring potential system variation. The training data should not contain any data corresponding to damage, but should as far as possible span the range of environmental and operational variability anticipated. Considering the behavior of CCs with temperature, data points from $1200 \sim 1800$ are selected as training data, because this part of the data contains both large peaks and small fluctuations caused by environmental conditions.

The selected training data are used to build the regression model and to check its performance, the ADF test is applied again to the residuals for establishing whether the model residual series is integrated to a lower order than the original variables. Once this goal is achieved, one can say that the nonlinear cointegrating relationship is established successfully, the common trends are purged, therefore, the model residual series may be a potentially good indicator of damage induced variations. The rest of the data set is later used for testing.

To build the regression model it is necessary to select one of the CCs as regression target and use the other coefficients to fit the model on that target. It is possible to choose among the 15 possible coefficients (coefficients c_{11}, c_{14}, c_{15} are not considered being already stationary). It is worth pointing out that it is not obvious that, once the target coefficient is chosen c_t, fitting the regression model with all the remaining coefficients is the best choice. Here the first Cepstral Coefficient is chosen as the target and the $c_4, c_6, c_8, c_9, c_{10}$ are chosen as variables

(Model 1).

Table 4.3: ADF Test on Cepstral Coefficients for sensor 1

CCs	t_p	t_α	Stationarity	Integration Order
c_1	0.0190	-1.94	NS	1
Δc_1	-155.11	-1.94	S	-
c_2	-0.0746	-1.94	NS	1
Δc_2	-153.34	-1.94	S	-
c_3	-0.1459	-1.94	NS	1
Δc_3	-154.93	-1.94	S	-
c_4	-0.2307	-1.94	NS	1
Δc_4	-151.97	-1.94	S	-
c_5	-0.3658	-1.94	NS	1
Δc_5	-157.66	-1.94	S	-
c_6	-0.8930	-1.94	NS	1
Δc_6	-150.04	-1.94	S	-
c_7	-0.4021	-1.94	NS	1
Δc_7	-157.76	-1.94	S	-
c_8	-1.7486	-1.94	NS	1
Δc_8	-150.40	-1.94	S	-
c_9	-1.8129	-1.94	NS	1
Δc_9	-154.34	-1.94	S	-
c_{10}	-0.4646	-1.94	NS	1
Δc_{10}	-153.38	-1.94	S	-
c_{11}	-7.652	-1.94	S	0
c_{12}	-1.121	-1.94	NS	1
Δc_{12}	-153.68	-1.94	S	-
c_{13}	-1.835	-1.94	NS	1
Δc_{13}	-155.15	-1.94	S	-
c_{14}	-3.840	-1.94	S	0
c_{15}	-3.247	-1.94	S	0

In this section the regression algorithms tested are the SVR and the RVM, which having the kernel-based formulation allow to consider the nonlinear rela-

tionship between variables. The choice between the linear solution and the nonlinear kernel-based one, highly depends on the relationship between the variables; i.e. if they are linearly correlated, there is no need of considering the nonlinear cointegration, while if they are nonlinearly correlated the linear formulation of cointegration is not accurate for building the regression model. Here, the Pearson product-moment correlation coefficients are derived to determine the level of linear dependency between the variables and the values are presented in Table 4.4. Looking at the correlations coefficients, it is evident that the relationship between the target coefficient and the ones that are supposed to be used to build the regression model, is weakly linear. This finding can be appreciated also looking at the plot of the target coefficient with respect to the ones used for the regression (Figure 4.13); where it can also be appreciated, that even if nonlinearly correlated, there is a consistent positive relation between the target coefficient and c_8, c_9, c_{10} that can be taken into account to built a linear regression model.

Therefore, it is necessary to build a nonlinear regression model to derive stationary residual. The results from these two formulations are compared with the residuals obtained from the Johansen procedure which consider only linear relations between the cointegrated variables.

Table 4.4: ADF Test.

Target Coefficient	Correlated Coefficients				
c_1	c_4	c_6	c_8	c_9	c_{10}
	0.46	0.32	0.44	0.53	0.57

Once the regression model is trained, the ADF test is performed on the training residuals to check the robustness of the computed cointegration. The results are listed in Table 4.5, since all ADF test statistics are smaller than the critical value at 5% level, the residuals are considered stationary and both the linear and the nonlinear cointegrating relationships are successfully established.

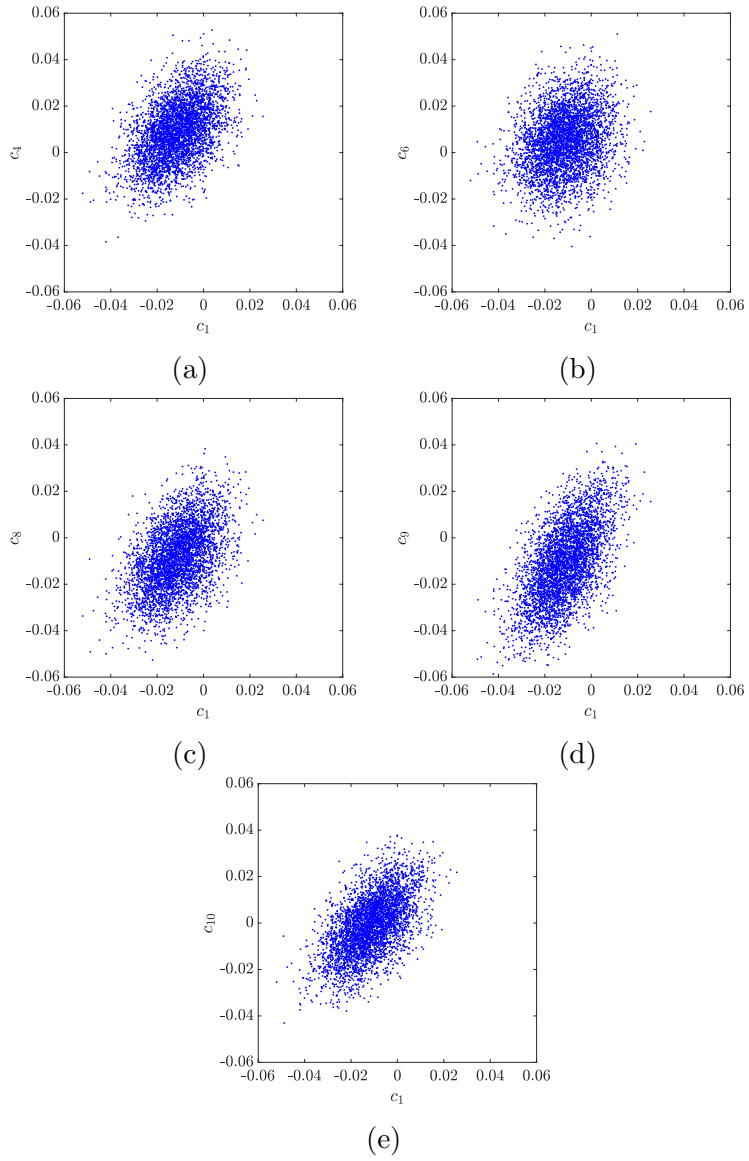

Figure 4.13: Mutual relationships of the target coefficient with the related coefficients.

Table 4.5: ADF Test.

Regression Model	Model	t_p	t_α	Stationarity
Johansen	Model 1	-22.64	-1.9416	S
SVM (GK)	Model 1	-23.78	-1.9416	S
RVM (GK)	Model 1	-23.79	-1.9416	S

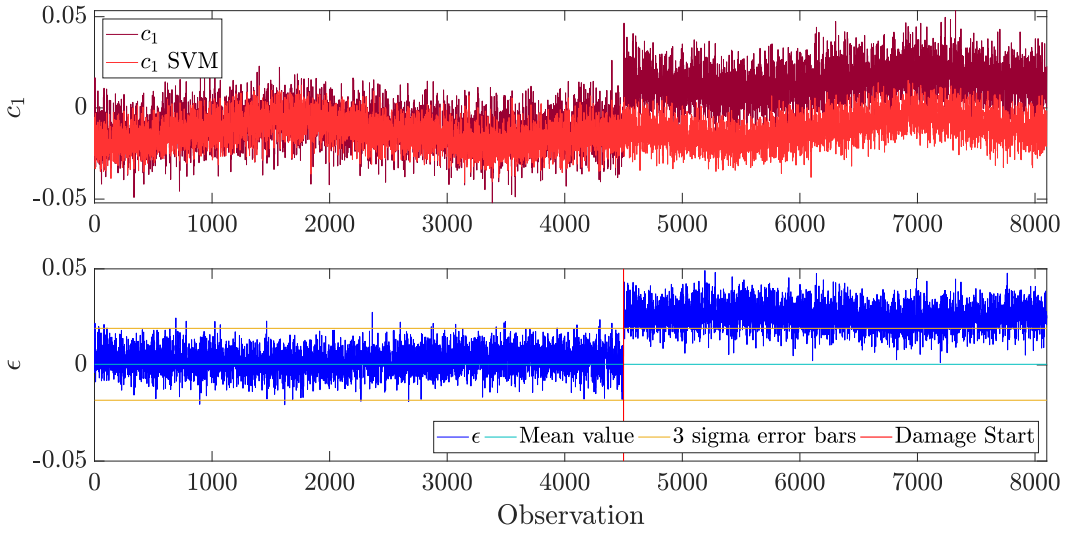

Figure 4.14: Regression of the first Cepstral Coefficient using a SVM model with Gaussian Kernel and residuals.

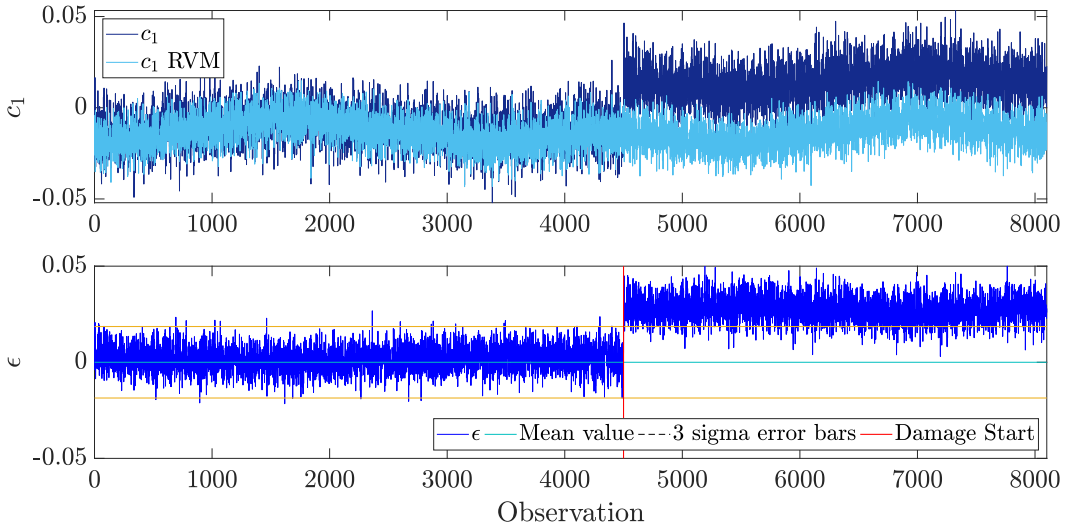

Figure 4.15: Regression of the first Cepstral Coefficient using a RVM model with Gaussian Kernel and residuals.

The prediction behaviors of the three possible models are quite similar, they all tend to have a good fit to the data. Figure 4.14 and Figure 4.15 show the prediction performance of the SVM and RVM regression models considering a nonlinear kernel and the model residuals. Both the SVM and RVM models follow the trend of the measurement data very well, predicting accurately the environmentally induced variations in the CCs. Observing closely the residuals it can be noticed

that they become nonstationary after the damage is introduced. The upper and lower yellow lines represent the training residual mean plus or minus three times the standard deviations.

Applying the Johansen procedure with the coefficients selected to build the regression SVM and RVM model, result in a less pronounced alarm output, because of the nonlinear relationship that is established between them. Although each frequency is related nonlinearly to temperature and between them, which drives the Cepstral fluctuations, some of the coefficients (although not all) are related to each other in a more linear way, which means that the Johansen procedure can successfully combine them to remove their common trends. (Figure 4.16) presents the residuals obtained using the Johansen procedure; the temperature dependency has been correctly cleaned up, where the residuals predominantly results from a combination of the eighth, ninth and tenth coefficient. However, even if the residuals are correctly stationary in the undamaged scenario, their deviation from the mean once the damage occurs is less clear with respect to the one obtained adopting the nonlinear regression model.

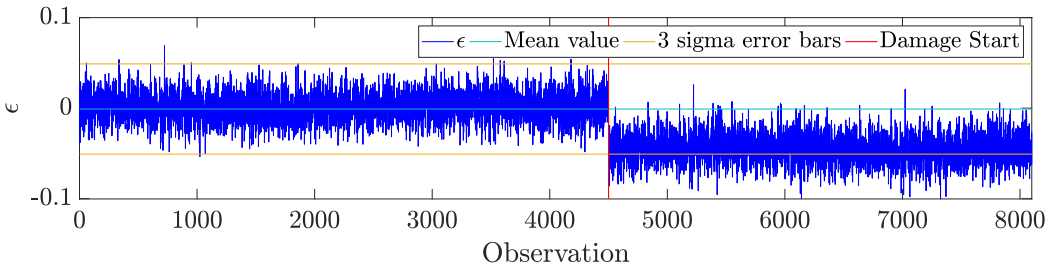

Figure 4.16: Cointegrated residuals obtained from the Johansen procedure.

4.8 Experimental Application Z24 Bridge

The Z24 bridge tests herein presented, have been performed in the framework of the European Brite EuRam research project BE-3157, System Identification to Monitor Civil Engineering Structures (SIMCES) (Roeck 2003).

The SIMCES project was born with the aim of giving a proof of feasibility for vibration-based structural health monitoring of civil engineering structures by full-scale, long-term tests and progressive failure tests of a representative structure,

the Z24 Bridge. The project was coordinated by KU Leuven (Department of Civil Engineering, Structural Mechanics Section). The other partners in the project were: Aalborg University (Institut for Bybninbsteknik); EMPA (Swiss Federal Laboratories for Materials Testing and Research, Concrete Structures Section); LMS (Leuven Measurement and Systems International N.V.; Engineering and Modeling); WS Atkins Consultants Ltd (Science and Technology); Sineco Spa (Ufficio Promozione e Sviluppo); Technische Universitt Graz (Structural Concrete Institute).

4.8.1 Bridge Description

Figure 4.17: Views of the Z24 bridge.

The Z24 bridge was a post-tensioned concrete two-cell box-girder bridge located in Switzerland, in the canton Bern near Solothurn. It was built in 1963 and it connected the villages of Koppigen and Utzenstorf, over-passing the A1 highway between Bern and Zrich. The bridge presented a main span of 30 m and two side spans of 14 m (Figure 4.18).The bridge was built as a freestanding frame with the approaches backfilled later. Both abutments consisted of triple concrete columns connected with concrete hinges to the girder. Both intermediate supports were concrete piers clamped into the girder. An extension of the bridge girder at the approaches provided a sliding slab. The bridge was slightly skew because all supports were rotated with respect to the longitudinal axis. The bridge was demolished at the end of 1998, because a new railway next to the highway required a bridge with a larger side span.(Reynders and Roeck 2009)

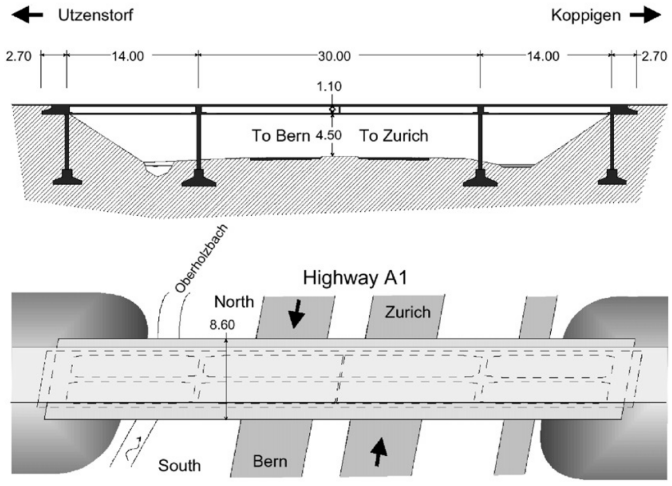

Figure 4.18: Bridge section and plan view.

A year before the demolition, a long-term environmental monitoring system (EMS) was installed and the bridge was monitored from 11 November 1997 till 11 September 1998. The final goal of this monitoring test was to provide both environmental and the response vibration data of the bridge, in order to subsequently quantify the contribution of the environmental fluctuations in the bridge dynamics.

The EMS consists in the installation of different sensors to measure different environmental parameters: air temperature, air humidity, rain true or false, wind speed, and wind direction. Also a sensor consisting of two inductive loops was installed to detect the presence of vehicles on the bridge. Particular attention was given to the temperature measurements. At the middle of the three spans, the temperature was measured at eight points on the girder: at the center of the north (TWN), central (TWC), and south (TWS) web; below the north (TSWN) and south (TSWS) sidewalk; at the top (TDT) and soffit (TDS) of the deck, and at the soffit (TS) of the girder (Figure 4.20). The soil temperature near each of the concrete columns at the approaches was monitored, as well as that near the north, central, and south parts of the intermediate piers (12 sensors in total). Although the original blueprints of the Z24 bridge indicated that the asphalt layer should have a thickness of 5 cm, the drilling of access holes for the installation of the temperature sensors on the girder revealed a cover of 1618 cm of asphalt. Therefore, the temperature of the pavement (TP) was measured at the middle of

the three spans (Figure 4.20).

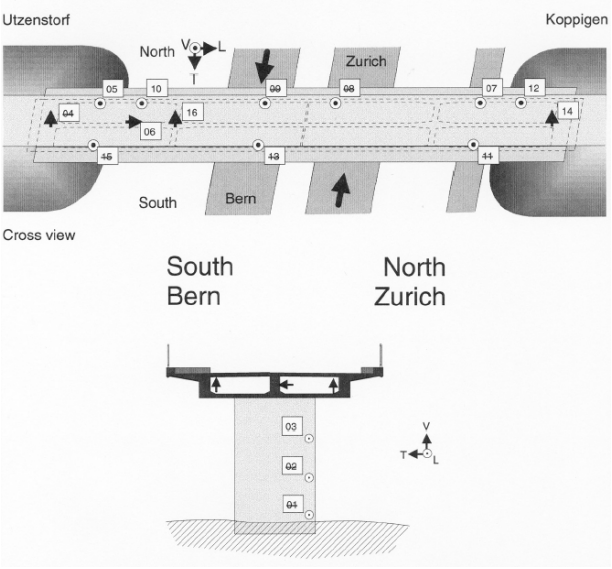

Figure 4.19: Sensors location.

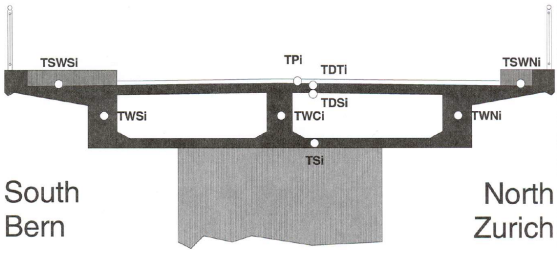

Figure 4.20: Position of the temperature sensors.

To monitor the bridge dynamics, 16 accelerations have been measured on the bridge at different points and in different directions. Every hour, 10 scans of environmental data, sampled at 48 sensors, and 8 averages of 8192 acceleration samples, taken at 16 sensors, were collected and stored to a hard disk after compression.

A series of progressive damage tests have been carried out during the summer of 1998, shortly before complete demolition of the bridge. For a full description of all damage scenarios, instrumentation and safety considerations, refer Krämer et al. 1999. The first 17 scenarios are summarized in Table (4.6). The practical significance of these tests was ensured by checking that they were relevant for the safety of the bridge and that the simulated damage occurred frequently.

Before and after each applied damage scenario, the bridge was subjected to a forced and an ambient operational vibration test. With a measurement grid consisting of a regular 3×45 grid on top of the bridge deck and a 2×8 grid on each of the two pillars, 291 degrees of freedom have been measured: all displacements on the pillars, and mainly vertical and lateral displacements on the bridge deck. Because the number of degrees of freedom to be measured exceeded the number of available accelerometers and acquisition channels, the data were collected in nine setups using five reference channels. The forced excitation was applied by two vertical shakers, placed on the bridge deck. A 1 kN shaker was placed on the middle span and a 0.5 kN shaker was placed at the Koppigen side span. The shaker input signals were generated using an inverse fast Fourier transform (FFT) algorithm, resulting in a fairly flat force spectrum between 3 and 30 Hz. After scenario 8, a drop weight test was also performed, using a device that allowed to drop a mass of up to 120 kg from a height of up to 1 m in a controlled way. The applied shaker and drop weight forces were periodic with eight periods.

Figure 4.21: Damage scenarios.

Table 4.6: Damage Scenarios on Z24.

♯	Date	Scenario
1	04/08/1998	Undamaged condition
2	09/08/1998	Installation of pier settlement system
3	10/08/1998	Lowering of pier, 20 mm
4	12/08/1998	Lowering of pier, 40 mm
5	17/08/1998	Lowering of pier, 80 mm
6	18/08/1998	Lowering of pier, 95 mm
7	19/08/1998	Lifting of pier, tilt of foundation
8	20/08/1998	New reference condition
9	25/08/1998	Spalling of concrete at soffit, 12 m^2
10	26/08/1998	Spalling of concrete at soffit, 24 m^2
11	27/08/1998	Landslide of 1 m at abutment
12	31/08/1998	Failure of concrete hinge
13	02/09/1998	Failure of 2 anchor heads
14	03/09/1998	Failure of 4 anchor heads
15	07/09/1998	Rupture of 2 out of 16 tendons
16	08/09/1998	Rupture of 4 out of 16 tendons
17	09/09/1998	Rupture of 6 out of 16 tendons

Signal processing: A total of 65536 samples was collected at a sampling rate of 100 Hz, using an antialiasing filter with a 30-Hz cutoff frequency. The simulated response data are standardized and normalized prior to being used for feature extraction:

$$x_{normalized}[n] = \frac{x[n] - \bar{x}}{\sigma_x} \tag{4.65}$$

where $x[n]$ is the original signal, $\bar{x}$ its mean and σ_x its standard deviation. The normalization procedure is performed on each frame.

Feature Extraction: Before applying the extraction procedure discussed in Section 3.1.1, the number of triangular filters must be selected with the value for the cutoff frequency. The number of filters can be set according to the Fraile et al. criterion presented in the Section 3.1.1, since the sampling frequency adopted to simulate the system response is equal to 100 Hz, M is set to 13. Then the cutoff frequency is set equal to 20 Hz.

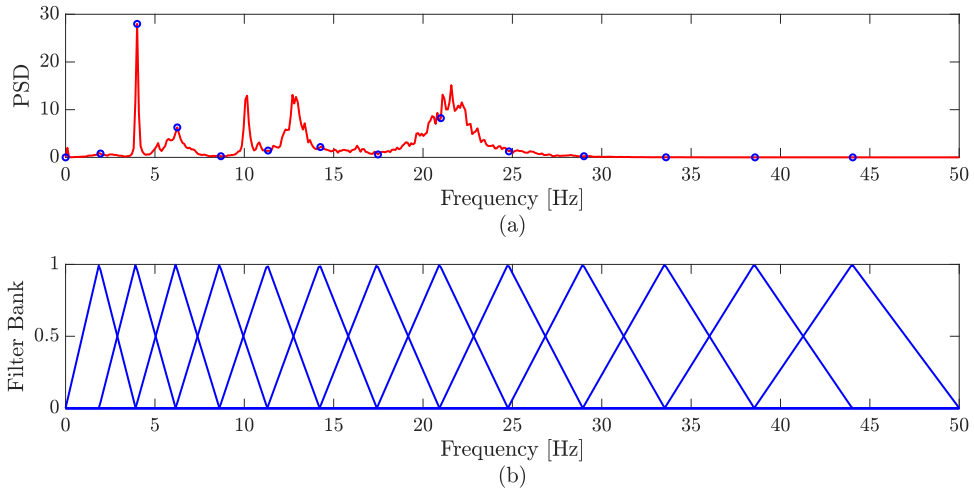

Figure 4.22: Frequency Warping.

At the end of the extraction process, for each sensor and each realization, a matrix C of dimension $D \times N_{frames}$ is computed, which collects the vectors of CCs for each frame. Then, in order to have only one vector of CCs for each realization coming from the single sensor, the extracted matrix is averaged over the frames.

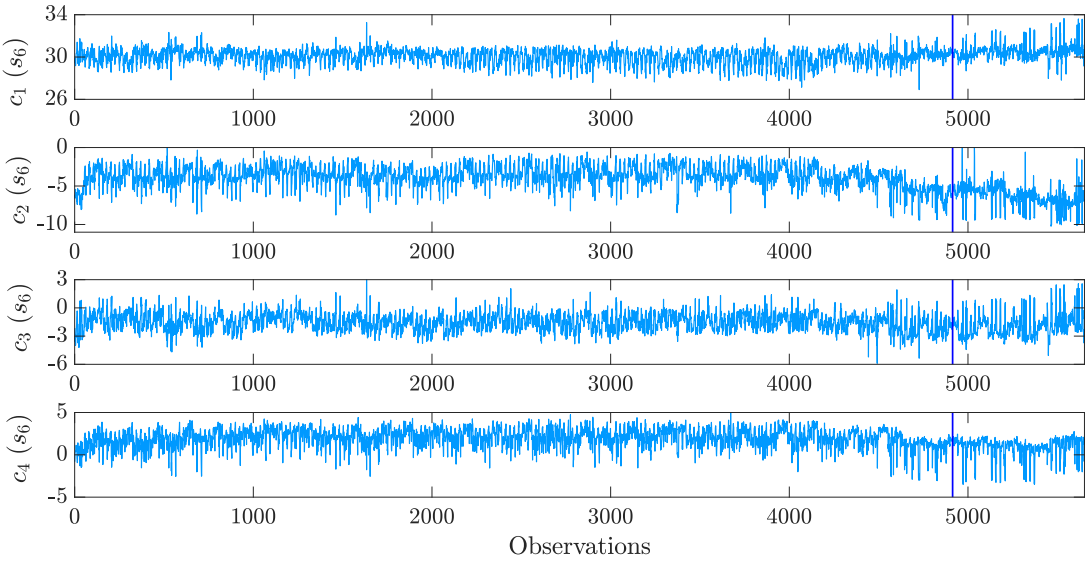

Figure 4.23: First three CCs extracted for sensor 5.

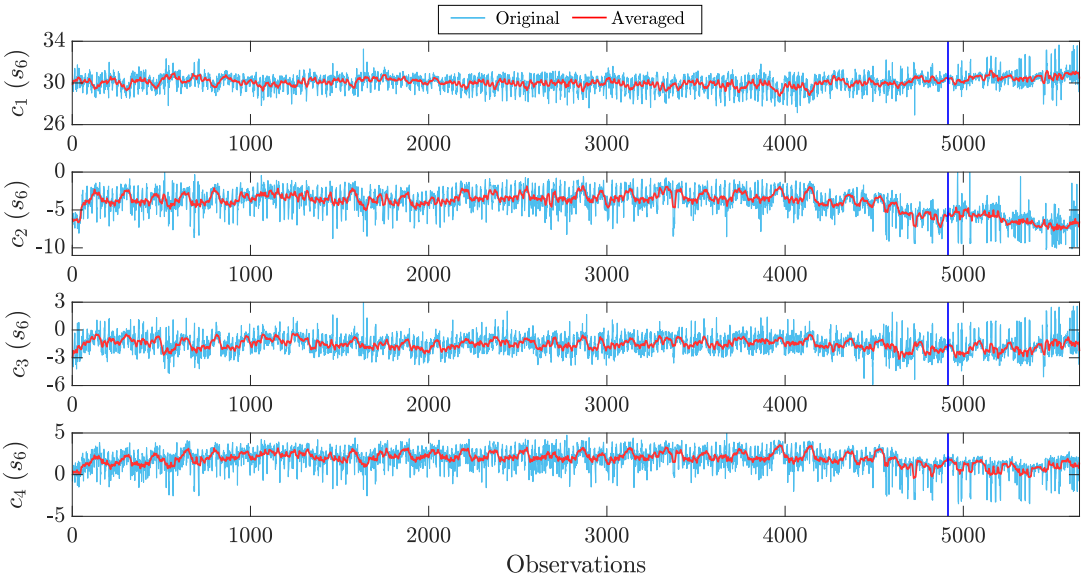

Figure 4.24: Cepstral Coefficients with and without moving average.

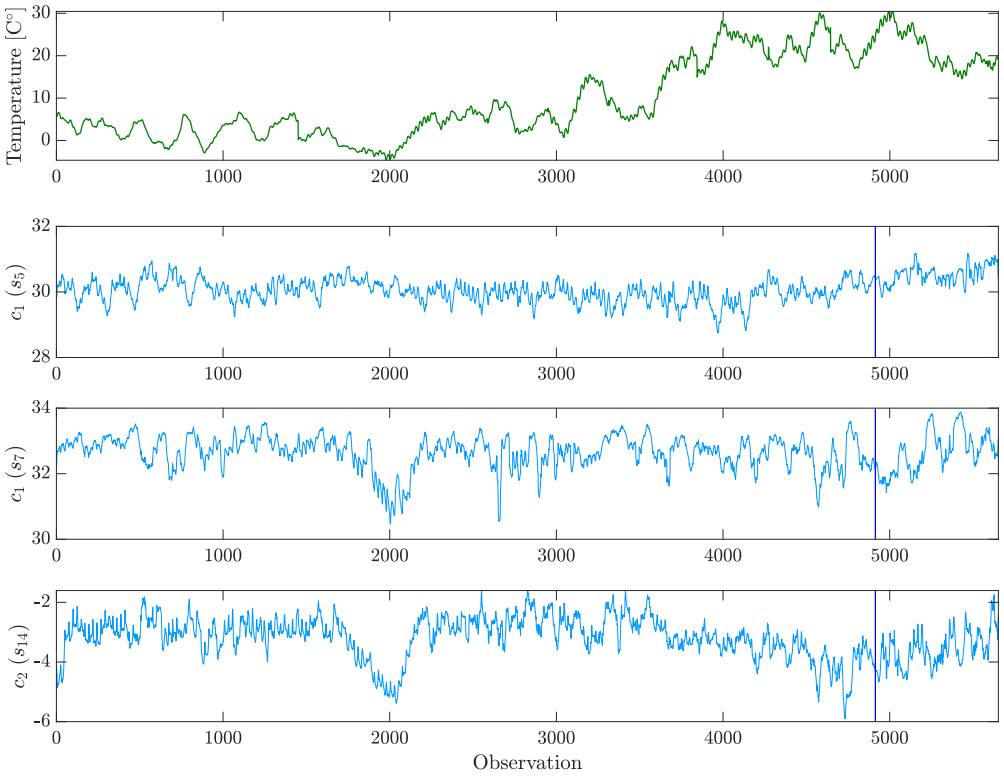

Figure 4.25: Temperature observations and examples of Cepstral Coefficients for different sensors.

The coefficients extracted from the Z-24 bridge acceleration measurements are noisy and their variability is quite high (Figure 4.23), nevertheless it is possible to underline some trends in the data. In order to overcome this variability a simple moving average is introduced (Figure 4.24) and the averaged coefficients are adopted as the new features. This procedure is implemented considering 20 samples as the number of previous data points to be used in conjunction with the current data point when calculating the moving average. Then the features processed adopting this technique are used as damage sensitive features.

4.8.2 Cointegration

In this section the cointegration technique is applied to remove the dependency of Cepstral Coefficients from the environmental fluctuations, building damage sensitive features that are strictly dependent only on the occurrence of damage. The monitored variables analyzed are the CCs computed in the previous section for the Z-24 bridge, considering each sensor separately.

Before computing the cointegrating vectors, it is necessary to check which variables, presenting the same integration order, can be cointegrated. To determine the integration order, the ADF test is initially run on the variables derived from the single sensor. The results are given in Table (4.7), and show that almost all the coefficient series are nonstationary at the 95% confidence level and integrated of order one, i.e. they are $I(1)$ series.

At this point the data set is divided into two parts: a training and test data set. Training data are used to train the regression model, the test data set is employed for the aim of monitoring potential system variation. The training data should not contain any data corresponding to damage, but should as far as possible span the range of environmental and operational variability anticipated. Considering the behaviour of CCs with temperature, data points from data point $1700 \sim 2500$ are selected as training data, for the reason that this part of the data contains both large peaks and small fluctuations caused by environmental conditions.

The selected training data are used to build the regression model and to check its performance, the ADF test is applied again to the residuals for establishing whether the model residual series is integrated to a lower order than the original variables. Once this goal is achieved, one can say that the nonlinear cointegrating relationship is established successfully, the common trends are purged, therefore,

the model residual series may be a potentially good indicator of damage induced variations. The rest of the data set is later used for testing.

Table 4.7: ADF Test (Sensor 5&7).

CCs	t_p		t_α	Stationarity		I ()	
	s_5	s_7		s_5	s_7	s_5	s_7
c_1	-1.84	-1.32	-1.94	NS	NS		
Δc_1	-9.59	-10.92	-1.94	S	S	1	1
c_2	-1.62	-1.23	-1.94	NS	NS		
Δc_2	-9.67	-18.61	-1.94	S	S	1	1
c_3	-2.18	-1.32	-1.94	S	NS		
Δc_3	-	-10.56	-1.94	-	S	0	1
c_4	-2.73	-1.96	-1.94	S	S		
Δc_4	-	-	-1.94	-	-	0	0
c_5	-1.63	-1.24	-1.94	NS	NS		
Δc_5	-12.57	-12.33	-1.94	S	S	1	1
c_6	-1.72	-2.37	-1.94	NS	S		
Δc_6	-9.11	-	-1.94	S	-	1	0
c_7	-0.98	-1.27	-1.94	NS	NS		
Δc_7	-12.33	-12.87	-1.94	S	S	1	1
c_8	-1.07	-0.65	-1.94	NS	NS		
Δc_8	-9.76	-21.39	-1.94	S	S	1	1
c_9	-0.93	-2.16	-1.94	NS	S		
Δc_9	-11.80	-	-1.94	S	-	1	0
c_{10}	-1.67	-0.84	-1.94	NS	NS		
Δc_{10}	-8.17	-15.05	-1.94	S	S	1	1
c_{11}	-1.54	-0.76	-1.94	NS	NS		
Δc_{11}	-11.36	-12.08	-1.94	S	S	1	1
c_{12}	-1.17	-1.41	-1.94	NS	NS		
Δc_{12}	-10.06	-13.77	-1.94	S	S	1	1
c_{13}	-0.78	-0.98	-1.94	NS	NS		
Δc_{13}	-9.17	-10.82	-1.94	S	S	1	1

To build the regression model it is necessary to select one of the CCs as regression target and use the other coefficients to fit the model on that target. It

is possible to choose among the 13 possible coefficients (coefficients c_3, c_4 are not considered for sensor 5 and coefficients c_4, c_6 and c_9 are not considered for sensor 7 because they are stationary). It worths pointing out that it is not obvious that, once the target coefficient is chosen c_t, fitting the regression model with all the remaining coefficients is the best choice. Here the first Cepstral Coefficient is chosen as the target for both sensors, while the c_5, c_7, c_9, c_13 are chosen as variables for sensor 5 (Model 1) and c_3, c_5, c_9, c_11 are chosen as variables for sensor 7 (Model 2).

In this section the regression algorithms tested are the SVR and the RVM, which having the kernel-based formulation allow to consider the nonlinear relationship between variables. The choice between the linear solution and the nonlinear kernel-based one highly depends on the relationship between the variables; i.e. if they are linearly correlated, there is no need of considering the nonlinear cointegration, while if they are nonlinearly correlated the linear formulation of cointegration is not accurate for building the regression model. Studying the correlation coefficients derived for the variables involved in the two models (Table 4.8 and Table 4.9) it can be noticed that, while for the first model (sensor 7), there are some coefficients that can be considered linearly correlated with the target coefficient (c_3, c_9 and c_{10}), the same can't be stated for the second model, where almost all the coefficients (except for c_6) show a nonlinear correlation with the target coefficient. This finding allows to build for the first regression model, both a linear and nonlinear relationship, while for the second model, there is room only for the nonlinear option.

The results obtained with SVM and the RVM models are compared with the residuals obtained from the Johansen procedure which consider only linear relations between the cointegrated variables.

Table 4.8: Correlation Coefficients between the target coefficient and the regression ones for sensor 7.

Target Coefficient	Correlated Coefficients			
c_1	c_3	c_5	c_9	c_{11}
	0.95	0.36	0.74	0.70

Table 4.9: Correlation Coefficients between the target coefficient and the regression ones for sensor 5.

Target Coefficient	Correlated Coefficients				
c_1	c_5	c_6	c_7	c_9	c_{13}
	0.52	0.14	0.69	0.29	0.14

Once the regression model is trained, the ADF test is performed on the training residuals to check the robustness of the computed cointegration. The results are listed in Table 4.10, since all ADF test statistics are smaller than the critical value at 5% level, the residuals are considered stationary and the nonlinear cointegrating relationships are successfully established.

Table 4.10: ADF Test.

Regression Model	Model	ADF statistic(5% level)	5% critical value	Stationarity
SVM (LK)	Model 1	-3.32	-1.94	S
RVM (LK)	Model 1	-5.31	-1.94	S
SVM (GK)	Model 1	-4.00	-1.94	S
RVM (GK)	Model 1	-4.79	-1.94	S
SVM (GK)	Model 2	-5.42	-1.94	S
RVM (GK)	Model 2	-4.25	-1.94	S

The prediction behaviors of the four possible models are quite similar, they all tend to have a good fit to the data. Figure 4.26, Figure 4.27, Figure 4.28 and Figure 4.29 show, respectively, the prediction performance of the SVM and RVM regression models considering a linear and nonlinear kernel and the model residuals, for the Cepstral measured at the seventh sensor. Both the SVM and RVM models follow the trend of the measurement data very well; the environmentally induced variations are also well predicted. It can be noticed that, also the linear regression models built with SVM and RVM lead to very good results, comparable to the ones obtained using the nonlinear model. This outcomes is justified by the fact that the target coefficient is linearly related to the third coefficient and weakly

linearly related also to the ninth and eleventh indicators. This finding allows the Johansen procedure to successfully combine them to remove their common trends, even considering a linear regression model. The damage is correctly identified in all the plots; however, the 'damage' condition seems to be detected earlier with respect to the actual introduction of damage. Similar detection results can be found in Peeters and De Roeck 2001, the similar sudden frequency drop was interpreted in terms of a possible increase of mass of the bridge due to some heavy trucks standing on it. The residuals coming from the application of the Johansen procedure take advantage of the same linearly relations between the coefficients that helped building the linear regression model for SVM and RVM. Therefore, the damage is correctly identified and the dependency from temperature fluctuation efficiently removed.

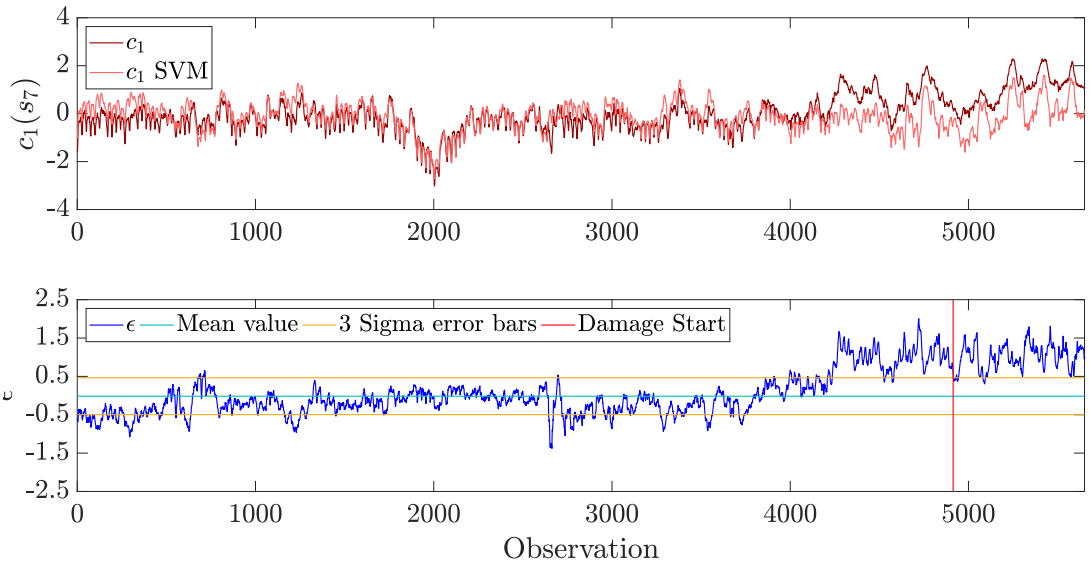

Figure 4.26: Regression of the first Cepstral Coefficient SVM model with Linear Kernel (sensor 7).

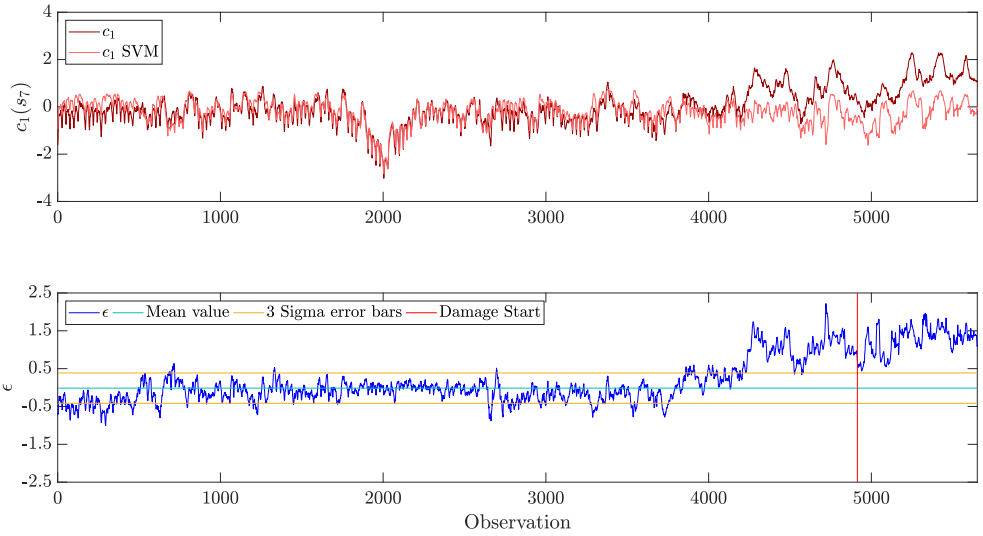

Figure 4.27: Regression of the first Cepstral Coefficient SVM model with Gaussian Kernel (sensor 7).

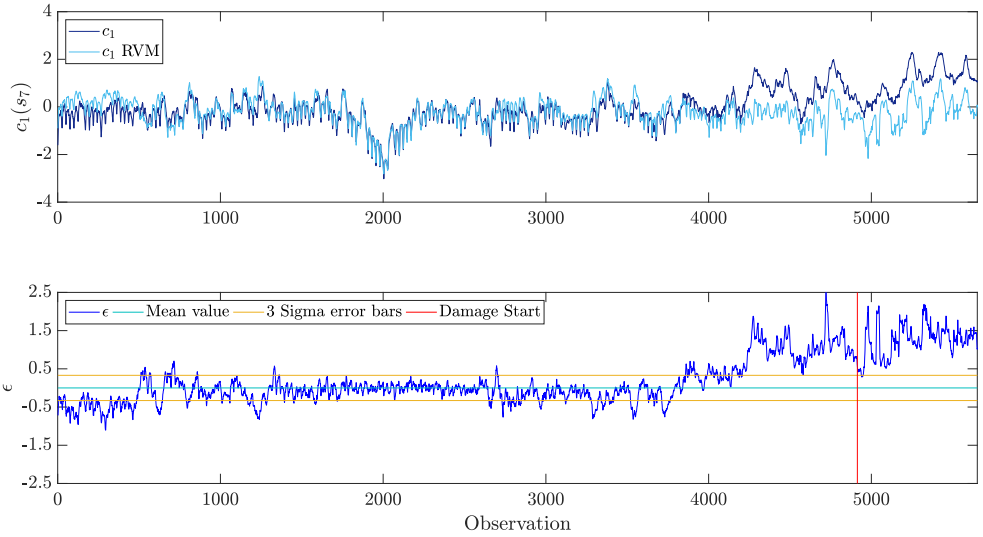

Figure 4.28: Regression of the first Cepstral Coefficient SVM model with Linear Kernel (sensor 7).

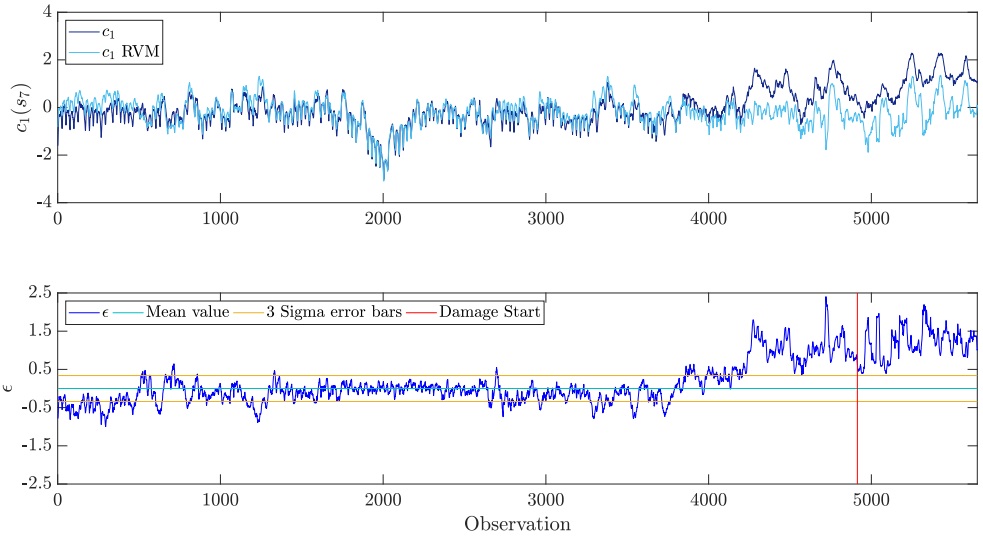

Figure 4.29: Regression of the first Cepstral Coefficient SVM model with Gaussian Kernel (sensor 7).

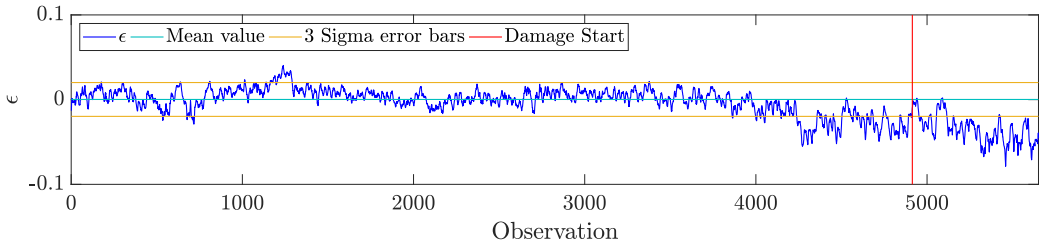

Figure 4.30: Cointegrated residual obtained from the Johansen procedure (sensor 7).

Figure 4.31 and Figure 4.32 show the results, for sensor 5, in terms of regression model and residuals obtained building a nonlinear model with SVM and RVM respectively. The chosen target coefficient, happens to be almost independent from the temperature fluctuation, which makes the application of the cointegration technique, unnecessary, at least for normalizing the coefficient with respect to the temperature fluctuation. Here the methodology is applied to keep the consistency in the computation of the residuals, which result to be correctly stationary in undamaged conditions and then deviate from the mean once the damage occurs. Even in this case, the damage conditions seems to appear earlier than expected and the cause can be identified as the same of the previous study case.

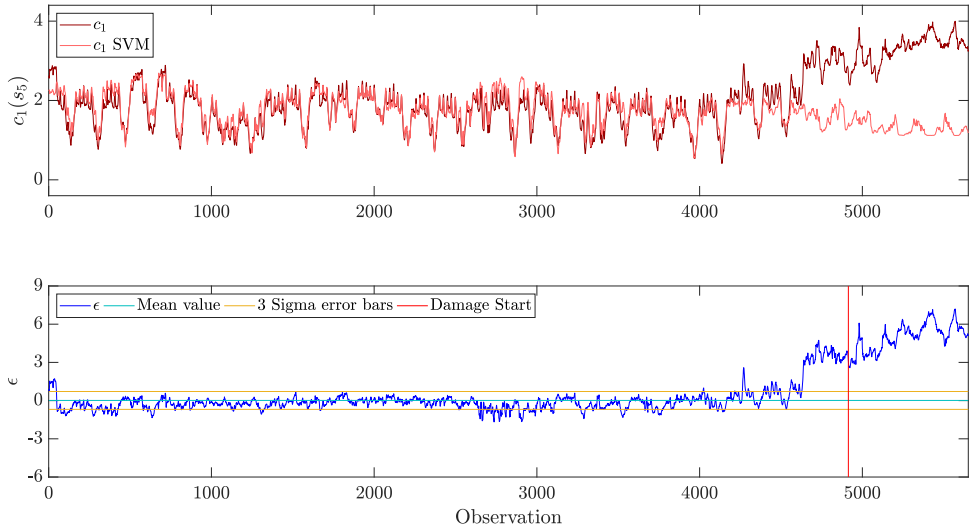

Figure 4.31: Regression of the first Cepstral Coefficient SVM model with Gaussian Kernel (sensor 5).

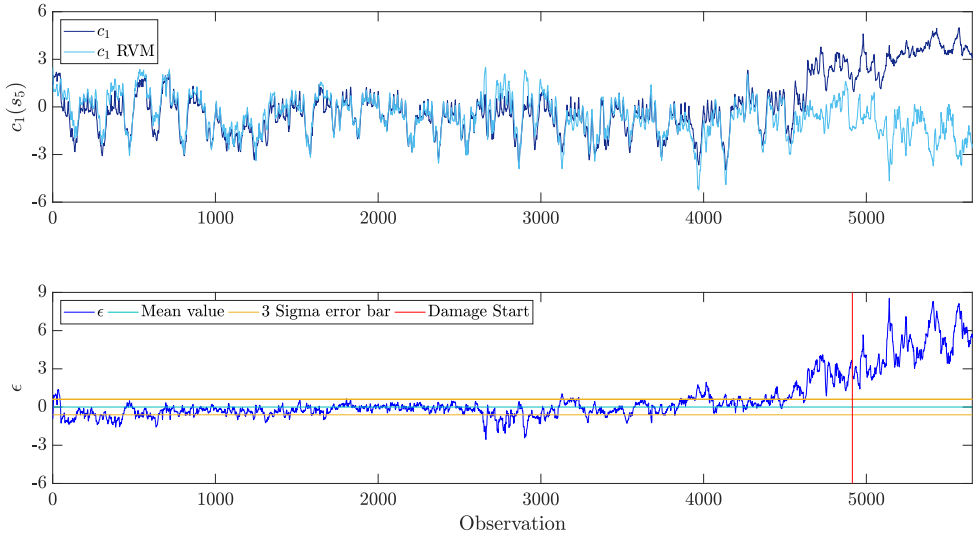

Figure 4.32: Regression of the first Cepstral Coefficient SVM model with Gaussian Kernel (sensor 5).

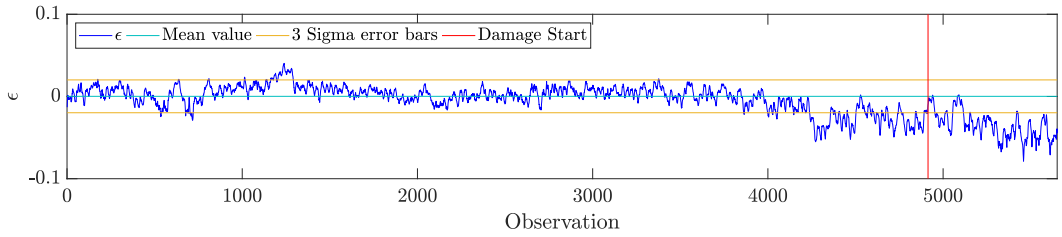

Figure 4.33: Cointegrated residual obtained from the Johansen procedure (sensor 5)

It is worth noticing that the simple monitoring of the target coefficient, when it does not depend from the temperature fluctuations, can lead to the identification of damage with a high degree of confidence, as shown in Figure 4.34, without any additional manipulation of the dataset. Here the values of mean and standard deviation are set considering the same training range adopted for building the regression model. The coefficient can be considered with a stationary behavior in the undamaged condition and then increases when the artificial deterioration is introduce.

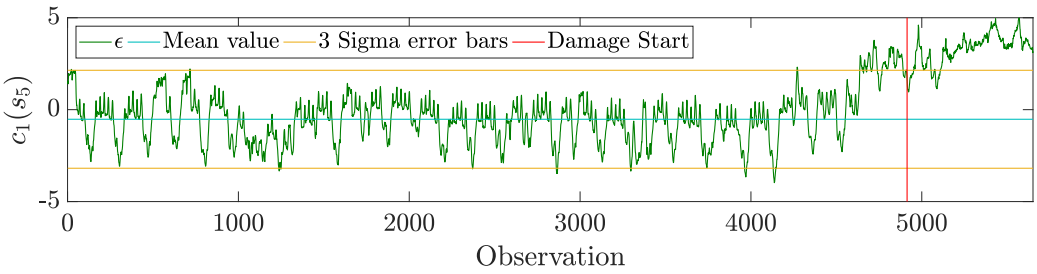

Figure 4.34: Time serie of the target coefficient.

4.9 Conclusions

Econometricians understand nonstationarity in terms of trends, stationary and difference stationary processes. This chapter argued that neither approach might be philosophically suited for SHM feature variables. However, these feature variables do mimic the behavior of difference stationary processes, for which the Johansen procedure was developed for. With this in mind, no problems should arise by applying the theory presented in the previous chapter to SHM data.

The environmental dependency of Cepstral Coefficients from temperature was investigated. Then, the possibility of using linear and nonlinear cointegration technique was explored in this chapter, to remove environmental trends from the Cepstral Coefficients and build robust DSFs.

Nonlinear cointegration is necessary when feature variables are nonlinearly related, as usually happen in SHM problems. This chapter explored how one might attempt to nonlinearly combine feature variables to create useful diagnostic tools in the face of changing environmental and operational conditions. The ideas followed are based on multinomial combinations of feature variables, and optimal combinations are attempted using SVR and RVM models.

The second half of the chapter consists of the application of the cointegration technique to data obtained from two study cases. Initially, a numerically simulated cantilever beam is addressed. In this case, CCs were extracted and investigated, showing their robustness towards environmental trends and also their ability to detect small damages. Later, the Z-24 bridge study case was examined. The proposed methodology was able to remove environmental and operational trends from Cepstral Coefficients. The environmentally insensitive features created were able to successfully detect damage scenarios both in the simulated and experimental study case.

Part III
SHM of the Civic Tower of Rieti

Chapter 5

SHM of the Civic Tower of Rieti

SHM approaches have been in constant evolution for decades since they need to face structures which evolve in turn. The necessity of having monitoring systems that efficiently suit the structures they are designed for, to identify their dynamic behavior, is currently a central topic in worldwide research. Indeed the recent structural collapses occurred in the world pointed out the importance of consciously control the health state of structures, particularly the ones that have strategic importance or historic meaning. Therefore an efficient monitoring system combined with an optimized vibration-based approach allows tracking the dynamic response of the structure, offering the possibility to check their integrity level continuously along with time, allowing to prevent severe damages and avoid condition-based maintenance which, especially for cultural heritage structures is extremely expensive.

Chapter 2 addressed an automated procedure to extract the modal parameters with an extremely low dependency from the user's expertise. This methodology has great potential and offers all the right characteristics to be easily implemented within a long-term monitoring system, providing robust modal information. On the other hand, in Chapter 3 the Cepstral Coefficients showed to be a robust alternative damage sensitive feature which can be implemented in an easy and user-friendly methodology. The unsupervised extraction process presented in Chapter 2 and the Cepstral features described in Chapter 3 are tested in this section, using them to carry on the structural health monitoring campaign on the Civic Tower

located in Rieti, a town in the central region of Italy. The tower is monitored by the research group supervised by professor Maurizio De Angelis, in the Department of Structural and Geotechnical Engineering at "Sapienza" University of Rome.

The current trend of collecting massive amounts of data in the name of SHM from civil structures cannot be constructive unless this data is used. At least three years of reliable monitoring data is now available from the Civic Tower monitoring system, which provides a unique opportunity for the development of a reliable SHM system. The tower represents a rare study case for SHM purposes, with a high degree of complexity, being the structure equipped with a Non-Conventional Tuned Mass Damper for the passive control of vibrations.

5.1 Description of the Tower

The Civic Tower of Rieti is located in Piazza Vittorio Emanuele, in the historical, civic center of Rieti and stands on the right side of the Town Hall of the city. While the Town Hall was built in the XIII century (Figure 5.1a) and subsequently consolidated in 1909 after the 1898 earthquake, the tower was erected in 1940 (Figure 5.1b). The tower was built along the north and east fronts of the old

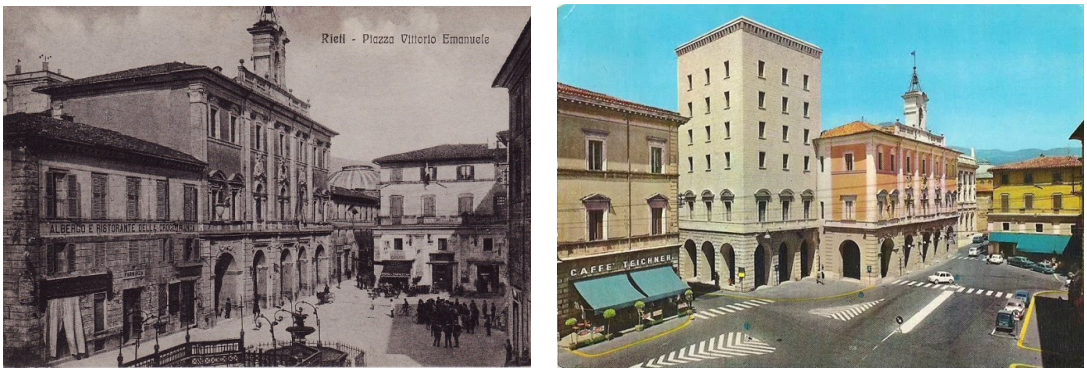

(a) (b)

Figure 5.1: View of Piazza Vittorio Emanuele in an historical postcard: (a) before the erection of the Civic Tower, (b) after the erection of the Civic Tower.

Town Hall building, while the sides facing south and west, respectively lookout on Piazza Vittorio Emanuele and Via Pennina. The tower was part of an expansion project of the Town Hall building assigned to the Arch. G. Battistrada and recall

the rationalist architecture style. Due to its institutional role and its historic value, the tower with the Town Hall unit is one of the most important buildings in Rieti. The solution found by Arch. G. Battistrada (Figure 5.2a) was that of

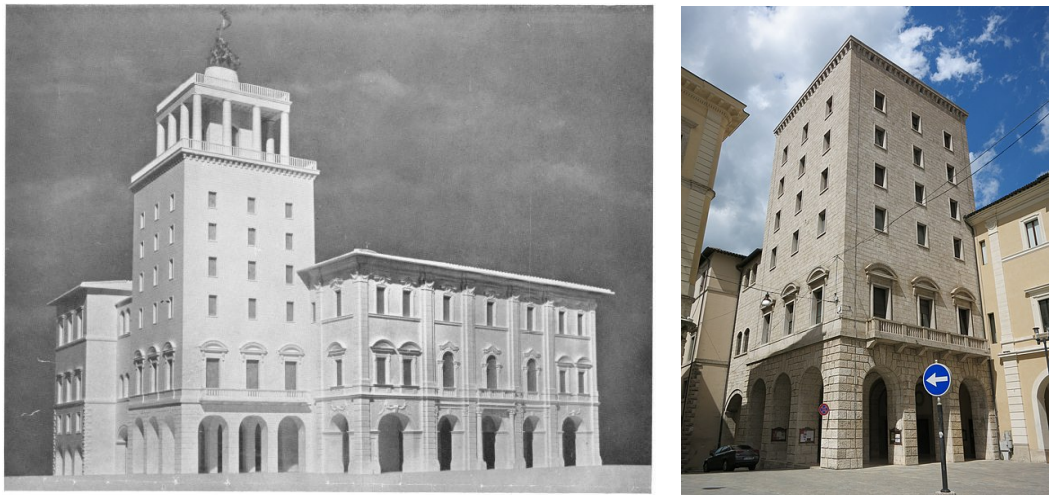

(a) (b)

Figure 5.2: Civic Tower view: (a) The model of the project presented by Battistrada, (b) view of the Civic Tower nowadays.

concentrating the rooms in a tower and in a lower secondary level, being able to integrate the architecture to the existing structure and to expand, at the same time, the use of public spaces adjacent to the municipal building.

The Civic Tower (Figure 5.2b) is included in the building of the Town Hall of Rieti, with two sides rigidly linked with it on the east and north side. The connection between the two buildings is obtained through the floor continuity at the second, fourth, and fifth floors and through the internal load-bearing walls. The overall structural complex can be divided into four different blocks (Figure 5.3b), according to the year of construction and to the different construction materials:

- block 1: it is the historic part of the Town Hall, built in the XIII century (1200-1300) and characterized by wooden floors and masonry walls with decreasing thickness along with the height of the structure (1.40 m at the basement up to 0.80 m at the last level);

- block 2: this section is realized after the demolition of a part of the building between 1930 and 1940, and it is characterized by a mixed masonry structure

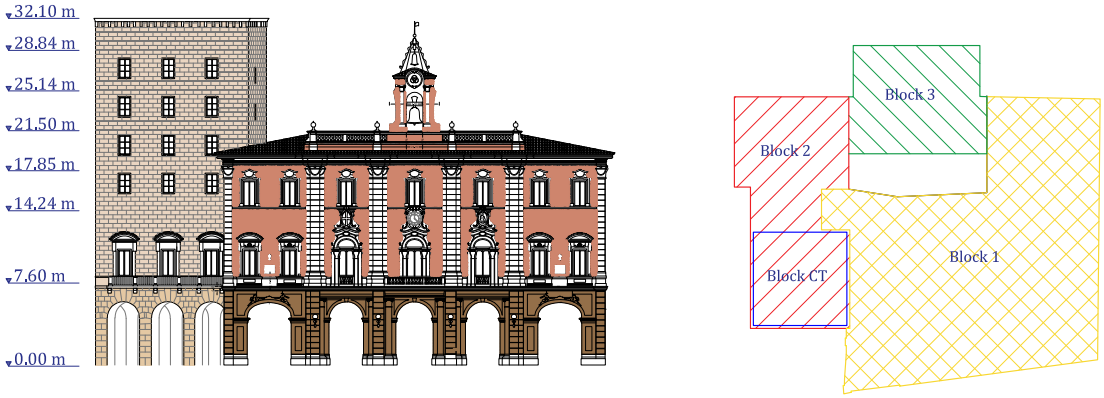

(a) (b)

Figure 5.3: Front (a) and plan (b) view of the building complex collecting the Town Hall and the Civic Tower.

in the perimeter area and reinforced concrete in the interior; it includes the Civic Tower;

- block 3: it is the most recent part of the Town Hall, built between 1960 and 1970, and it is entirely built with reinforced concrete columns and beams;
- block CT: it is an additional block that should be considered separately. It comprises the top floor of the tower, characterized by the presence of the NC TMD system, built between 2014 and 2015 as a seismic structural improvement.

The Town Hall, excluding the Civic Tower, has a total height of 17.70 m above ground. The first block is totally made up of masonry, with a thickness of the walls that decrease from 1.40 m (basement) to 0.80 m (last level). The second block is made up of masonry for the external structure with central columns in reinforced concrete. The columns have a square section characterized by dimensions that vary along the height from 0.85 m x 0.85 m to 0.45 m x 0.45 m. The thickness of masonry decreases from 1.10 m to 0.80 m at the last level. The third and last block (the most recent one) is entirely built with reinforced concrete columns and beams. Columns have dimensions of 0.4 m x 0.4 m in plant.

The Civic Tower (Figure 5.3a) has an approximately square plan of dimensions 14.00 m x 13.70 m and an overall height of 32 m, with seven floors above ground,

including the roof level, a level on the ground floor covered by a portico with vaulted ceilings and a basement level.

The porch located at the ground floor is made of blocks of solid travertine and concrete mortar within the blocks. The lofts at the underground level consist of alternate layers of concrete tiles and slabs, while the ones at the upper levels consist of cement rafter and hollow block slabs.

The external structure consists of masonry walls with coating blocks of travertine, which present a thickness comparable with the one of the masonry section. The thickness decreases starting from 1.00 m (first floor) up to 0.60 m (last floor). On the inside, there is a reinforced concrete frame with four columns. The dimensions of the columns vary along with the height (1.00 m x 1.00 m at the first floor and 0.40 m x 0.40 m at the penultimate one), while the section of the beams is fixed equal to 0.50 m x 0.50 m.

5.1.1 Non-Conventional TMD

In 2014, and a NC TMD system was installed on the Civic Tower in order to reduce its seismic vulnerability. Both conventional and non-conventional TMDs provide supplemental damping by inducing a vibration energy transfer from the structural portion below the isolation system to the structural portion above the isolation system. Unlike the conventional configuration of a TMD, which consists in a small auxiliary mass installed ex novo on the structure to be protected, NC TMDs, instead, are implemented by converting masses already present on the structure into tuned masses, retaining their structural function in addition to the control function De Angelis et al. 2012; Reggio and Angelis 2015. Not requiring additional weight, a NC TMD has the ability to reach larger values of the mass ratio, which has been proven to increase its seismic effectiveness and robustness against deviations in the design parameters De Angelis et al. 2012; Reggio and Angelis 2015. The introduction of this passive vibration control system improves the structural performance, avoiding at the same time invasive interventions on the bearing masonry structure and on the travertine covering.

The roof slab and the columns at the last floor (Figure 5.4a and Figure 5.5a) were demolished (Figure 5.4b and Figure 5.5b) and a steel structure was built up, constrained to the existing floor by four High Damping Rubber Bearing (HDRB) isolators, at the locations of the previous concrete columns (Figure 5.4c, Figure

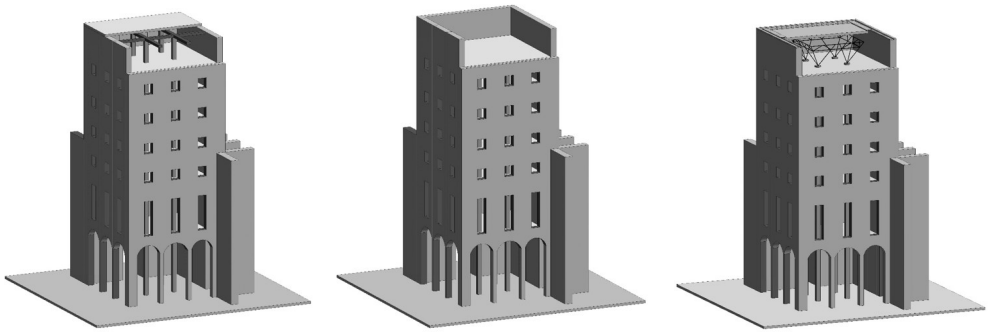

(a) (b) (c)

Figure 5.4: Last floor configuration during the constructions phases of the TMD (3D view): (a) before the intervention, (b) after the demolition of the slab, (c) erection of the TMD.

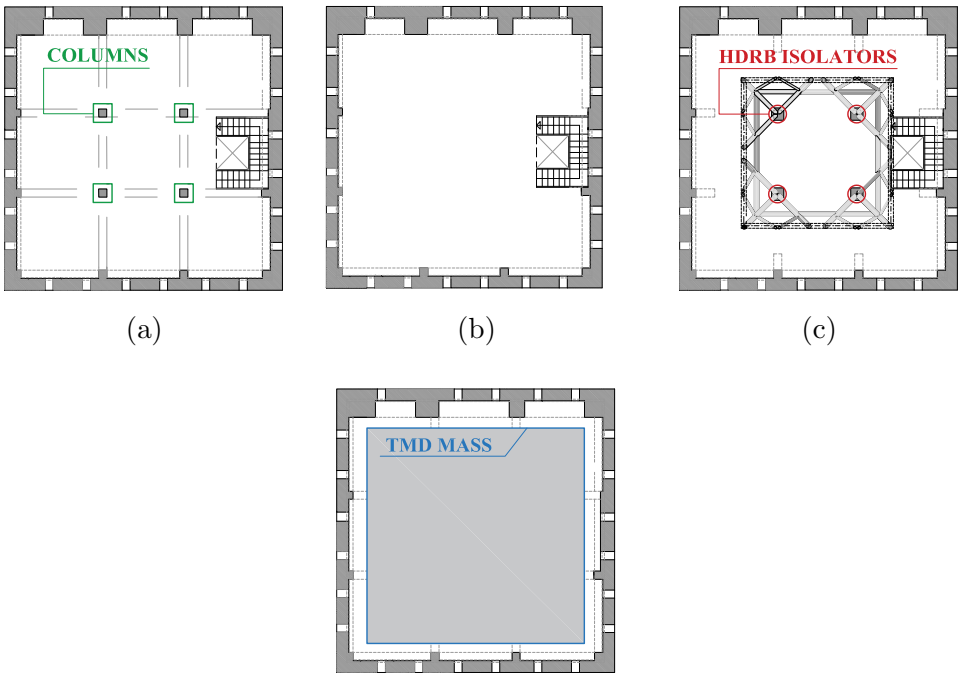

(a) (b) (c)

(d)

Figure 5.5: Last floor configuration during the constructions phases (plan view):(a) before the intervention, (b) after the demolition of the slab, (c) realization of the NC TMD (Support view), (d) mass of the NC TMD.

5.5c and Figure 5.5d). This steel frame aims to support also the old roof which plays now the role of the tuned mass in the NC TMD system, while the choice of the isolators defines the values of stiffness and damping coefficient of the TMD

control system. There is a 30 cm gap between the lateral walls and tuned mass which gives room for the system displacement (Figure 5.6b). The system consists of tubular steel beams (Figure 5.6c), with diameters of 219.1 mm and 101.6 mm and a thickness of 5 mm, and beams HEA200 (Figure 5.6a).

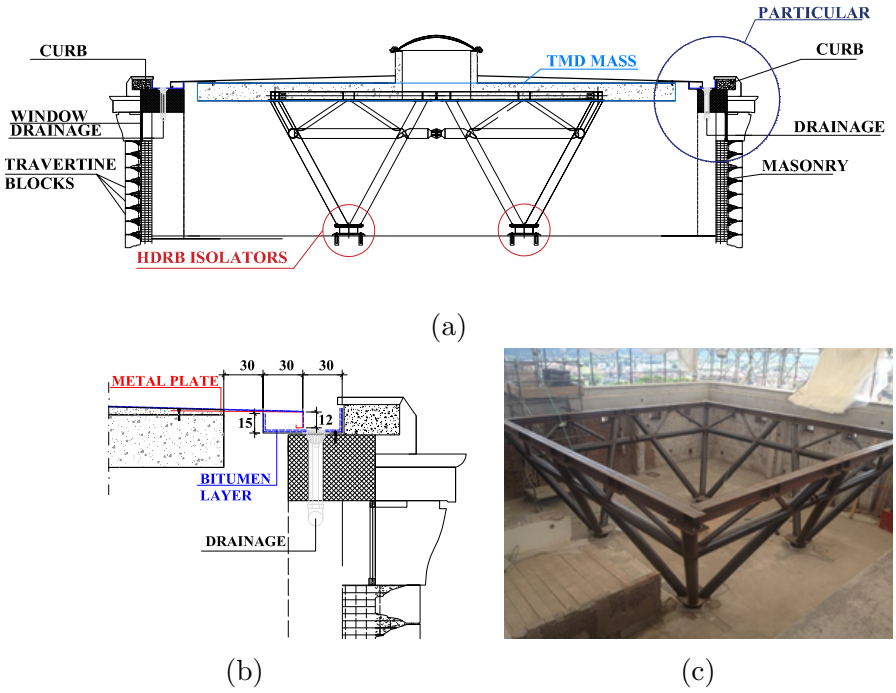

Figure 5.6: Non-Conventional TMD views: (a) front design view of the last floor of the civic tower, (b) particular of the connection, (c) picture of the steel frame at the base of the tuned mass during construction.

The rubber isolators are elastomeric seismic isolators SOMMA ISI S 400/100 and are made of alternating rubber layers and reinforcement steel plates (Figure 5.7). The rubber layers have high dissipative capacity on three levels, depending on the dynamic modulus of the material. They are completed by outer plates of adequate thickness for the connection with the structure (the columns). They have a non-linear response, characterized by values of stiffness and damping that can vary with the variation of the shearing deformation γ. For low levels of shear deformation (γ <10 %), the shear modulus G is higher (even one order in magnitude) than the one related to the seismic design conditions level of deformation (γ=100 $\div$ 150 %) and it allows to obtain a high design value of stiffness. Around γ=100 $\div$ 200 % (γ = 1.0 $\div$ 2.0), The shear modulus G is constant.

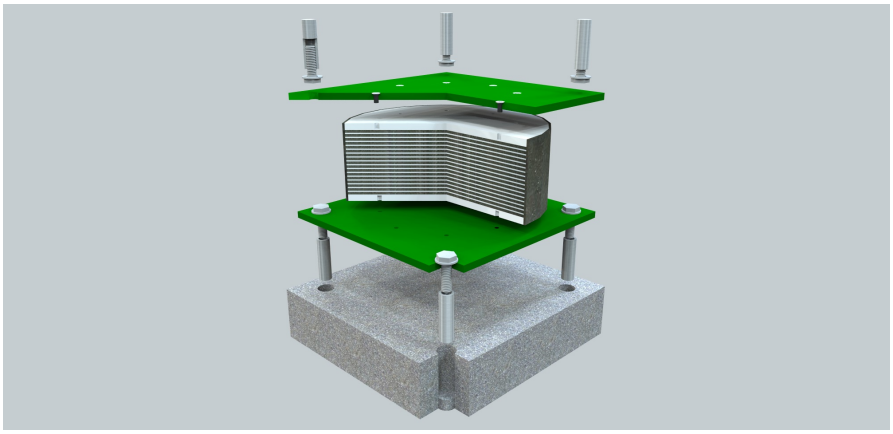

Figure 5.7: Elastomeric seismic isolators SOMMA ISI S 400/100.

5.2 FEM Model

A preliminary study of the dynamic characteristics of the Civic Tower of Rieti is conducted on the basis of a Finite Element Model (FEM) developed through the software SAP2000, version 19.0.0. The purpose is to define a geometric and mechanical model able to describe, with a sufficient degree of accuracy, the dynamic behavior of the structure.

An initial geometric model was constructed and implemented in the FE software and then, taking advantage of the available historic and design documentation about the building, the mechanical characteristics of the materials constituting the different structural components were selected. The constraints were defined and imposed on the elements, and both gravitational, as well as live loads were applied.

Table 5.1: Parameters assumed in the FE numerical model.

Material	**Blocks**	**Specific weight** γ N/m^3	**Density** ρ kg/m^3	**Young's modulus** E N/m^2	**Poisson's ratio** ν -
Concrete		2.45E+04	2500	1.79E+10	0.20
Travertine		2.20E+04	2240	1.98E+09	0.25
Mixed masonry	Block CT	2.00E+04	2040	1.94E+09	0.25
Masonry	Block 1	2.00E+04	2040	2.00E+09	0.25
Masonry	Block 2	2.00E+04	2040	1.95E+09	0.25

For the model, beams and columns were modeled with frame elements, while

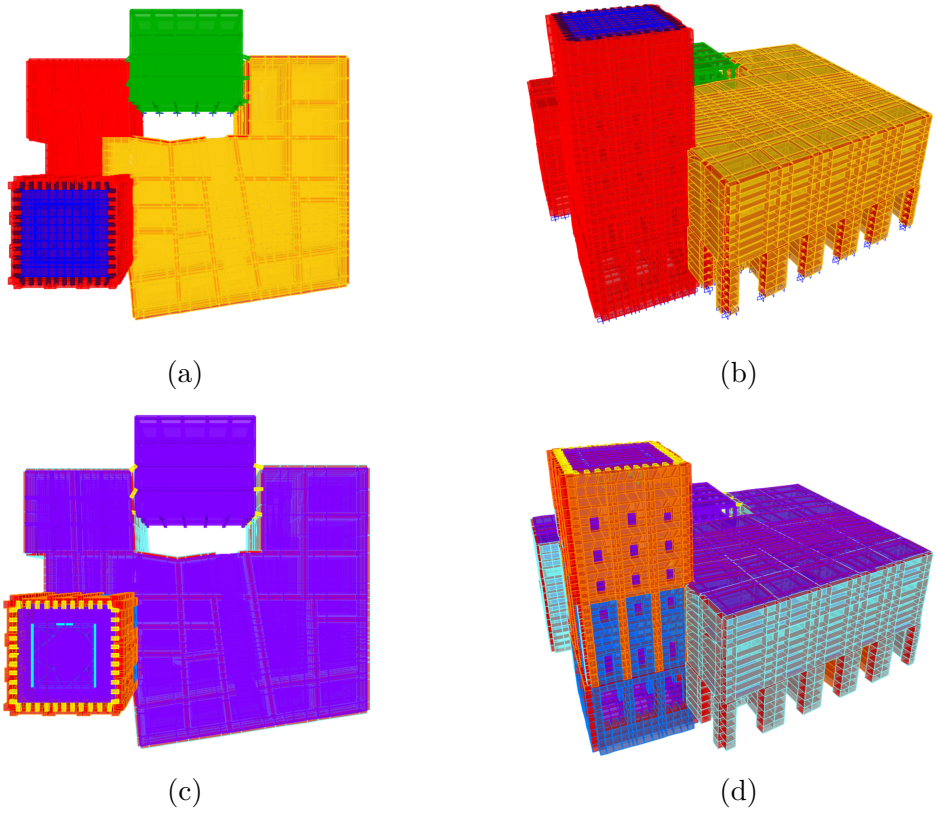

(a) (b)

(c) (d)

Figure 5.8: FE Model of the Civic Tower of Rieti: (a) plan view of the baseline model; (b) 3D view of the model with material distinction.

shell elements were used for walls, partitions, and slabs. The primary materials are concrete, travertine, and masonry with coating blocks of travertine. The characteristic mechanical parameters assumed in the FEM for the materials are summarized in Table 5.1.

Concrete was used to model beams and columns, and its mechanical characteristics were derived from the experimental strength values obtained from the in situ testing campaigns, carried out before the final restoration project of the Town Hall.

Travertine was used to model the building walls of the ground floor, entirely made of travertine blocks. Its mechanical characteristics were derived from the available technical documentation about the building (Table 5.1).

The masonry mixed with travertine was used to model the perimeter walls of the Civic Tower from the first level up to the roof. The structural interaction between the two materials is reflected in the material's mechanical parameters, which

results as a combination of the mechanical characteristics of the two materials, as also suggested by the available technical documentation.

The loads applied to the model are gravitational and live ones. The gravitational ones, also known as dead loads, are directly derived by the FE software during the analysis, considering the specific weight of the materials associated with the different structural elements. The variable loads represent the occupancy loads in the building. These loads, instead of being independently applied, are taken into account considering an equivalent additional thickness of the slab to which is assigned only the gravitational load. This choice does not influence the dynamic analysis because the floors are modeled as rigid floors. The additional thickness of the slabs varies to take into account the distinct occupancy level between the floors of the building. For the first level, given the uncertainty as well as the actual destination category of the building (offices open to the public), the thickness is computed to be equivalent to the whole variable load. For the 2nd to the 6th (attic) floors, the variable load has been considered at 30 %. For the last level, it was decided to consider the whole variable load, because of the presence of antennas and radio links.

Particular attention was paid to model the top floor of the tower, where the NC TMD is installed. The passive control system is composed of a mass which rests on elastomeric isolators, that should represent the only contact of the TMD with the rest of the building. The isolators were modeled through link elements (Figure

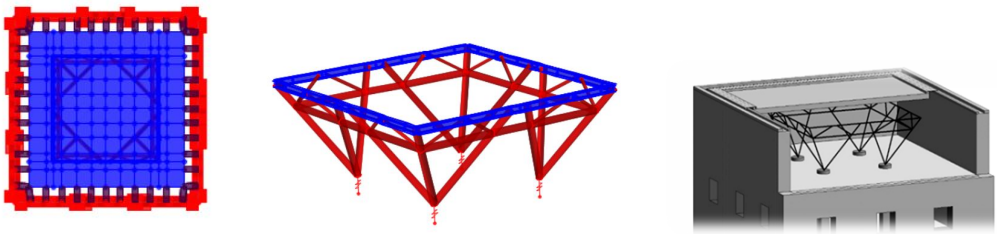

(a) (b) (c)

Figure 5.9: Particular of the NC TMD system on the FEM:(a) plan view, (b) 3D view, (c) NC TMD installed on the last floor of the tower model.

5.9b) with linear elastic behavior, with horizontal stiffness equal to 3000 N/mm. The roof slab, which represents the mass of the TMD, is made of lightweight concrete and it rests on a tubular steel structure forming a single body, connected through elastomeric isolators on the last floor to the four columns coming from

the lower level. The support of the mass of the TMD was modeled with frame steel elements of different dimensions (Figure 5.9). During the construction, the new TMD slab slowly settled on two sidewalls, and particular modeling had to be carried out because of this "unintended" connection between TMD and the upper side of the tower. In the current state, the TMD is supported by two sides of the tower, and it is not totally free to move, as it should be. In the model, this design detail is recreated by inserting rigid links (Figure 5.9a) between the TMD and the exterior wall of the tower were inserted to simulate the connection.

The modal analysis performed on the FEM gave preliminary information about the dynamic behavior of the structure, which was used to design a monitoring system, customized on the Civic Tower. Figure 5.10 shows the first five structural modes, whose frequencies are: 3.09 Hz, 3.42 Hz, 4.61 Hz, 5.01 Hz, and 5.62 Hz. The first two modes are mainly translational, with very little torsion ($f_1 = f_X$ and $f_2 = f_Y$), while the third and fourth mode result to be torsionally coupled ($f_3 = f_{XT}$ and $f_4 = f_{YT}$), exhibiting angular deviations from the principal directions; finally, the fifth mode is purely rotational ($f_5 = f_T$). This rotation of modal directions is conceivably attributable to the restraining effects of the low-rise adjacent Town Hall building to which the tower is connected. So, the shapes of the first two modes are primarily dictated by the tower, which is practically axial-symmetric, while the shapes of higher-order modes are affected by its boundary conditions. Notably, the dominant structural modes of the structure result to be aligned along principal directions rotated of 45 degrees with respect to the main horizontal and vertical axes. This behavior is then confirmed also by the results derived from the AVTs, as shown in the next sections. Therefore, in all the monitoring campaigns, the accelerometers have been accordingly rotated to optimize the reading of the structural dynamic behavior.

5.3 Description of the monitoring system

A long term monitoring system was planned and installed on the Civic Tower to continuously monitor its dynamic behavior and health condition during normal operations.

The adopted monitoring system is a multi-channel acquisition system by HBM and combines a data acquisition system MGCplus with an AB22A indication and

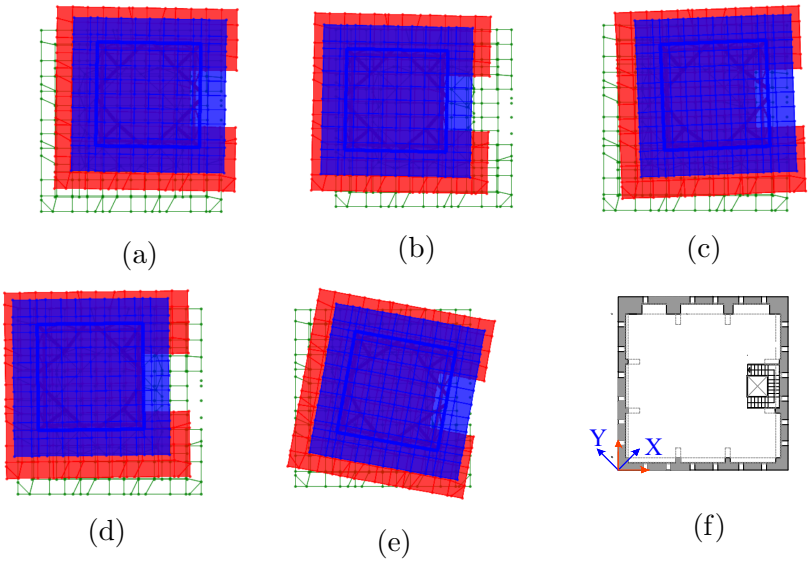

Figure 5.10: Real Eigenvectors of the FEM (TMD modal kinematics in blue and support modal kinematics in red): (a) Mode 1 ($f_1 = f_X$), (b) Mode 2 ($f_2 = f_Y$), (c) Mode 3 ($f_3 = f_{XT}$), (d) Mode 4 ($f_4 = f_{YT}$), (e) Mode 5 ($f_5 = f_T$), (f) principal axis.

control unit. The equipment consists of a communication processor (model CP42), two connection panels for multi-channel amplifiers (model AP418i) for piezoelectric transducers for a total of eight channels. The MGCplus system is interfaced with the software Catman Professional 5.0. The monitoring data are recorded using this same data acquisition system connected to a host personal computer (PC) located on the top floor of the tower.

The monitoring of the Civic Tower has been conducted in three separate phases (Table 5.2): phase 1 consists in the first five monitoring campaigns; phase 2 starts with the campaign VI and ends with campaign IX while the third one, corresponding to campaign X, starts from December 2017 and is currently ongoing. Structural accelerations are measured using a sensor setup that consists of piezoelectric model PCB 393A03 (Figure 5.11) uni-axial accelerometers (10 V/g sensitivity). The number of sensors and their spatial disposition varies within the monitoring phase conducted on the tower (Table 5.2).

Table 5.2: Monitoring Campaigns.

Campaign		Date		f_s(Hz)	AVT	FVT	No.Sensors
Phase 1	I	28/07/2015		100	Y	N	8
	II	03/11/2015		100	Y	N	8
	III	10/11/2015		100	Y	N	8
	IV	15/12/2015		200	Y	Y	8
	V	26/01/2016		200	Y	Y	8
Phase 2	VI	24/08/2016	04/10/2016	100	Y	N	6
	VII	04/10/2016	30/10/2016	100	Y	N	6
	VIII	01/11/2016	15/12/2016	100	Y	N	6
	IX	14/12/2016	20/03/2017	100	Y	N	6
Phase 3	X	18/12/2017	Present	100	Y	N	6

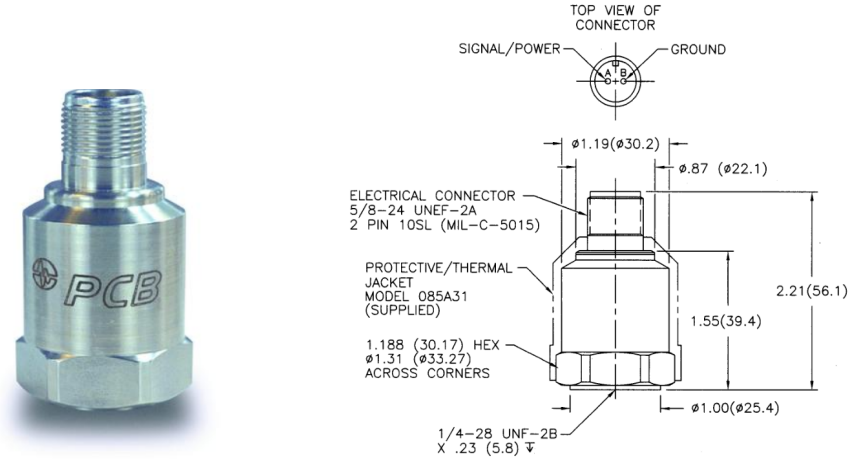

Figure 5.11: PCB Piezotronic accelerometer.

Phase 1 consists of daily monitoring campaigns, which result to be fundamental in the understanding of the dynamic reference behavior of the structure and in defining a baseline sensor setup for all the future campaigns. The attempts and choices made in this preliminary phase were driven by the information obtained from the preliminary guidelines given by the FEM of the building complex consisting in the Town Hall and the Civic Tower. The recorded data were collected testing different spatial configurations of the sensors and also considering different types of external excitation: ambient vibrations as well as forced sinusoidal accelerations. Mainly AVTs were carried on in all the campaigns (I-V) while FVTs

were designed and run in the IV and V campaigns. All the acceleration recordings were 5 minutes-long, and the sampling frequency varied from 100 Hz to 200 Hz (Table 5.2).

All the tests were carried out using eight high-sensitivity piezoelectric uniaxial accelerometers, positioned in different setup configurations: 10 different spatial scenarios were tested. For each configuration, the accelerometers were moved either between the fourth and seventh floor of the Civic Tower, either halfway between the tower and the Town Hall building at the fourth floor, where the two structures are linked. Especially this last case highlighted that the dynamic behavior observed considering the accelerometers placed on the tower was the same derived from the ones localized on the Town Hall. This finding demonstrated that the Civic Tower can be considered rigidly linked to the Town Hall and that it is reasonable to adopt only a small number of sensors placed on the tower to fully characterize its dynamic response. Consequently, two of the eight accelerometers were discarded, and the reference sensor setup, which better catches the dynamic behavior of the structure was identified. It consists of six accelerometers: three accelerometers (natural numbers in Figure 5.12a were placed on the support floor (height=28.84 m) and three corresponding sensors (natural numbers in Figure 5.12b) on the TMD level (height=31.24 m). The accelerometers have been rotated of 45 degrees with respect to the horizontal direction (Figure 5.12a) because the dynamic analysis performed on the FEM, confirmed the dominant modes to be along those directions. This configuration allows to completely describe the kinematics of the two rigid planes on the last floor of the tower (support and TMD). Once identified the reference configurations for the accelerometers, it was kept the same for all the future monitoring campaigns (VI-X).

The second monitoring phase, started on August 24^{th}, 2016, right after the earthquake that stroke the small town of Amatrice and the surrounding areas. At this time, the acquisition system was set alternatively in continuous mode (campaigns VI and VIII) or standby with trigger activation. Only AVTs were carried on in this phase adopting the optimal reference spatial configuration derived from phase 1. When the system was set in continuous mode, accelerations are measured every day, for 24 hours a day, in 5 minutes long record, while when it was set in standby with the trigger, accelerations were measured for 5 minutes, only when at least one value of acceleration within the recording overcame 0.005 m/s^2(campaigns VII and IX).

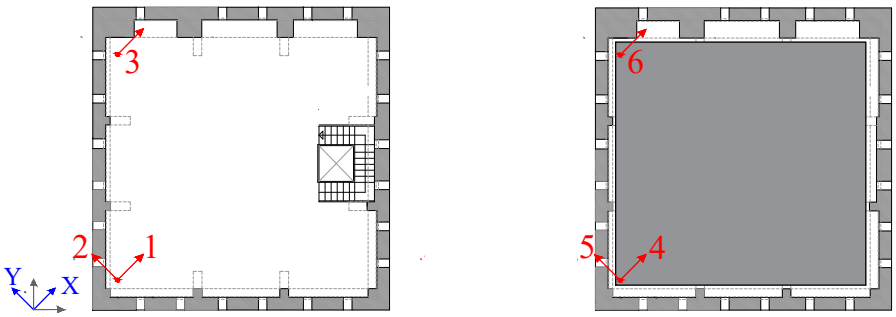

(a) (b)

Figure 5.12: Reference sensors setup: (a) support level, (b) TMD level.

Starting from December 2017, in phase 3, the monitoring system has collected eight ambient vibration recordings (5 minutes-long) per day at four different times of the day: 07:00 AM, 01:00 PM, 07:00 PM, and 01:00 AM. In addition, a trigger was additionally set on the acceleration level recorded by each channel, in order to collect all the possible seismic events in the Rieti area which could affect the structure and activate the passive control system.

Moreover, starting from July 13, 2018, a temperature data logger sensor from PCE Instruments has been installed on the last floor of the structure and included in the monitoring system to record temperature data. It can measure temperature within a measurement range of -40°C to +70°C (-40°F to 158°F). Users can easily set up the logging rate, high/low alarm and start-mode, and download the stored data by plugging the module into the PC's USB port and running the purposely designed software.

5.4 Applying the Unsupervised Procedure to the Civic Tower of Rieti

The unsupervised extraction procedure for modal parameters presented in Chapter 2 is built to give a not-user dependent framework to carry on structural health monitoring campaigns on real civil structures. Before applying the procedure on the data collected from the long-term monitoring system on the Civic Tower in Rieti, the procedure is here tested on the data collected on November, 3^{rd}, 2015,

that belongs to the second campaign, where the dynamic reference condition of the structure was identified. It is shown how the parameters at the core of the procedure are chosen and small sensitivity analysis are performed to display the way they affect the final identification results.

Step (a): DD-SSI&Parameter Selection

In the first step of the procedure, the user needs to select the values of the parameters used in the DD-SSI algorithm. In the present application, the allowable ranges of variation for the parameters governing the DD-SSI algorithm are set according to the guidelines given by Priori et al. 2018. Table 2.1, presented in Chapter 2, shows the suggested minimum and maximum values for these parameters which depend on the structural properties (f_1 first structural frequency of the system) of the structure and the monitoring sensor systems (m number of sensors, f_s sampling frequency) respectively.

Table 5.3: Variability range of DD-SSI Parameters.

Parameter	Description	Suggested Value
n_{min}	Minimum value of N	12
n_{max}	Maximum value of N	60
g_{min}	Minimum value of g	20
h_{min}	Minimum value of h	98
i_{min}	Minimum value of i	118
i_{max}	Maximum value of i	354
$j_{min}(i)$	Minimum value of j	$i \cdot 4.9$
$h_{max}(i)$	Maximum value of h	$i - 20$
$j_{max}(i)$	Maximum value of j	$30000 - i + 1$

For the application on the Civic Tower, it is possible to derive preliminary information about the system model order and the first structural mode just by looking at the dynamic response in the frequency domain. Figure 5.13 shows the Power Spectrum obtained from the acceleration time histories recorded by the six sensors during November 2015 campaign, which is used as reference for the dynamic characterization of the structure. Looking at the power spectrum, it can be observed that there are about 6 predominant modes, hence the system's order

n in the state space can be assumed equal to 12 and that the natural frequency of the first structural mode is about 3.08 Hz.

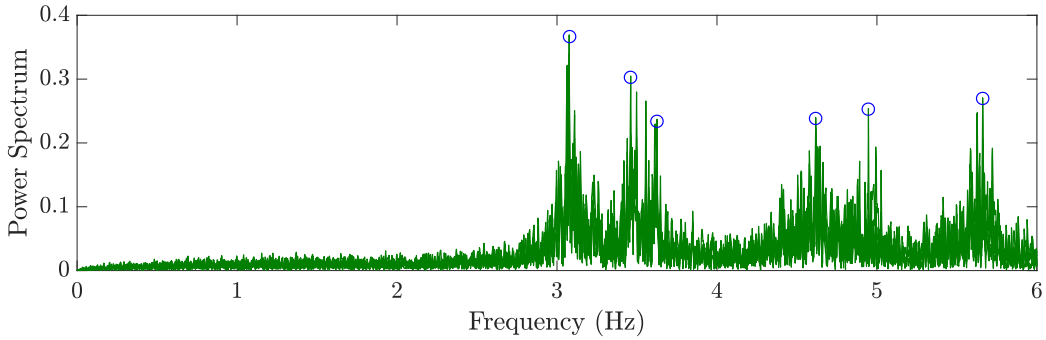

Figure 5.13: Power Spectrum of the acceleration response of the Civic Tower (monitoring campaign II).

At this point the variability range of the system order can be easily defined. The upper limit, n_{max}, of the order range should be chosen to be safely greater than twice the expected number of physical modes n, and the lower limit should not be less than the same number. In the current application, the order of the model has been varied from 2 to 50 with step increments of 2, considering also orders smaller than the effective system's order.

The initial definition of the system's dynamics and the monitoring system information lead to the definition of the g_{min} and h_{min} values which are equal to 20 and 98, respectively. Once set the minimum values of g and h, it is possible to derive the minimum and maximum value of i (Table 5.3), that in this case is 118. At this point all the other parameters can be accordingly derived. The last three values, j_{min}, h_{max} and j_{max}, as mentioned in Chapter 2, depend on the selected value of i, and it is necessary to define the final allowable range valid for all the combinations of parameters. The final j_{min} can be chosen equal to the largest value of j_{min} among all the possible ones derived for each value of i, while the final h_{max} and j_{max} are going to be the smaller ones, respectively.

In this paper the range for the parameter i has been chosen deliberately larger than what was needed to investigate how this parameter influences the final solution. The number of output block rows i in this case varies from 200 to 1000 with step increments of 20. Being the parameter that least affects the identification, only three values [17000, 20000, 23000] have been considered for the number of

output block columns j.

As previously mentioned, the partition of the Hankel matrix is an important step in the DD-SSI algorithms. Usually, a symmetric partition is chosen but recent studies have shown that this might not be the most appropriate partition. These considerations have never never been taken into account into these automated procedure. Here all the possible sets of partitions are considered, starting from a symmetric solution with $h = 0.5 \cdot i$ up to a highly asymmetric condition ($h = 0.9 \cdot i$), considering other three intermediate asymmetric conditions: $h = 0.6 \cdot i$, $h = 0.7 \cdot i$, $h = 0.8 \cdot i$.

Once all the allowable ranges of the parameters have been defined, the DD-SSI procedure can be performed repeatedly, choosing each time a set of values for i, j, h and n. For each repetition, a set of a system matrix $\boldsymbol{A}$ and of an output matrix $\boldsymbol{C}$ is obtained, from which the eigenvalues and the corresponding eigenvectors are derived.

Step (b)-(c): Hard Validation & Noise Modes Elimination

Let W be the total number of modes identified in all the $\bar{N}$ SSI-data analyses. Then, let the following vectors be constructed:

$$\begin{aligned} \boldsymbol{\Lambda} &= [\lambda_1 \, \lambda_2 \, \ldots \, \lambda_{2W-1} \, \lambda_{2W}]^T \\ \underline{\boldsymbol{\Psi}} &= [\boldsymbol{\Psi}_1 \, \boldsymbol{\Psi}_2 \, \ldots : \boldsymbol{\Phi}_{2W-1} \, \boldsymbol{\Psi}_{2W}]^T \end{aligned} \tag{5.1}$$

where λ_w, and $\boldsymbol{\Psi}_w$ denote the eigenvalue and eigenvector of the w^{th} identified mode, for w= 1, 2, . . ., $2W$. Here the second and third step of the unsupervised procedure are investigated.

Considering the parameters ranges cited in the previous section, the number of SSI analysis $\bar{N}$ is equal to 9600 and the number of structural identified modes $2W$ is equal to 319800, considering both complex and complex conjugates. Figure 5.14 shows the frequencies and damping ratios derived from the W complex eigenvalues collected in matrix Λ (the conjugates are discarded). It is evident that there are some areas in which the density of the identification is higher and they correspond to the zones in which there is the highest probability of having a structural mode. In Figure **??**, the area with the higher density results slightly shifted, because of a change in the dynamic behavior of the structure. It is also evident that there is a high number of noisy modes associated to unrealistic damping ratios values for

a civil structure, like negative damping or values higher than 20% (Figure 5.14b): these modes will be eliminated in the next step.

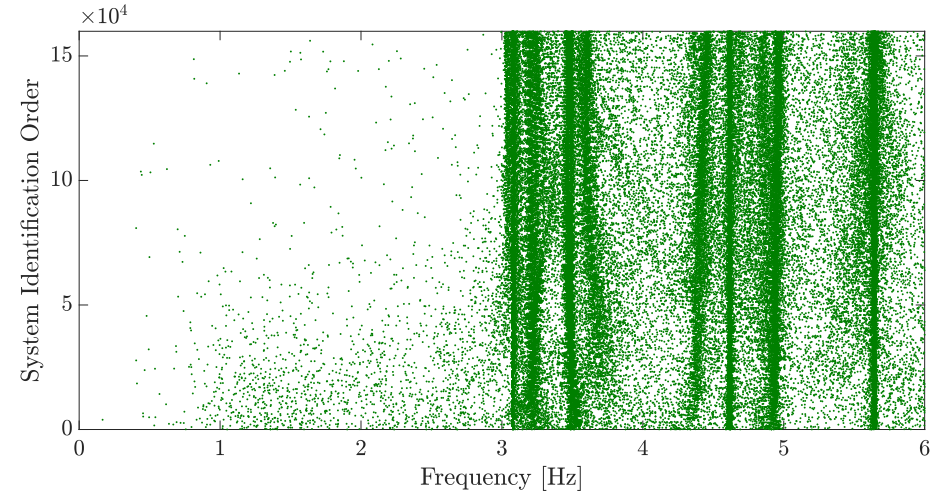

(a)

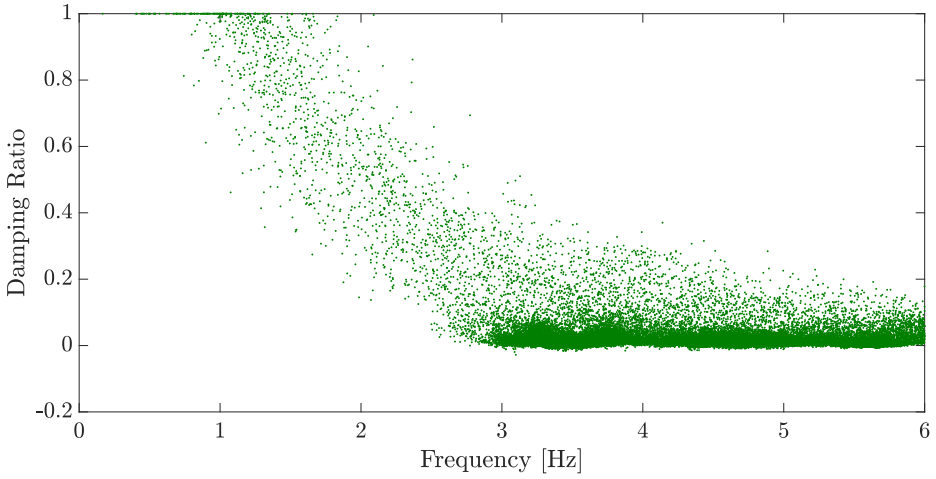

(b)

Figure 5.14: Modal frequencies and damping ratios identified in all SSI analyses. Frequency vs. Combination of parameters (November 2015).

The second and third step of the unsupervised methodology focus on differentiating the structural modes from the noisy ones, applying first the HVC and then checking the similarity level between all the identified modes. The third step starts from the assumption that the structural modes are those that are repeatedly identified, while the noisy modes are randomly identified. In the application of the HVC, first we remove those modes that are clearly linked to mathematical

artifacts, like the ones having negative damping or those complex conjugates pairs that do not match. However in this step, only a small number of non-structural modes were removed (310). It is the third step that actually makes the difference. In the noise modes elimination stage, the similarity within the modes is estimated comparing for each structural mode w, frequencies, damping ratios and mode shapes, according to the distance given in Chapter 2.

To carry on the elimination procedure, the user needs to decide which is the threshold of similarity for the structural modes. In civil engineering, these tolerances are usually set equal: 0.01 for relative changes in frequencies (ϵ_f), 0.05 for relative changes in modal damping ratios (ϵ_ξ), and 0.05 for differences between modal assurance criterion (MAC) values of two eigenvector estimates (ϵ_{MAC}). In this section, two of these tolerances are varied, ϵ_ξ, and ϵ_{MAC} to show how the final results can be affected by their variation.

There is an additional parameter that plays an important role in the noise elimination step, which is the minimum number $\bar{C}_{min}$ of similar modes that have to be reached in order to declare that a group of modes represents a structural mode and not a spurious one. Choosing large values for $\bar{C}_{min}$ increases the severity of the stability check and is not recommended as it would increase the risk of eliminating physical modes. While to keep a relatively small value of $\bar{C}_{min}$ would allow eliminating most of the noise modes without canceling physical ones. The influence of this parameter is addressed as well within a sensitivity analysis.

Figure 5.15 show how the identification is affected by varying the tolerance level over the damping ratio. It is well known that damping ratio is the more unstable among the modal parameters and its identification can be highly disperse sometimes, even within the same acceleration record. For small thresholds set on the damping ration (Figure 5.15a) it is not even possible to identify all the structural modes. Gradually relaxing the ϵ_ξ values the number of stable identified points increases and at least three structural modes are fully identified (Figure 5.15b and Figure 5.15c). For ϵ_ξ values of 0.04 and 0.05 other two frequencies start to be collected. These two frequencies are associated to structural modes that are not well defined for all the records.

Figure 5.16 shows a similar sensitivity analysis done on the threshold sets on the MAC values, which measure the similarity of structural modes in terms of eigenvectors. Complex mode shapes tend to be more robust in the identification with respect to damping ratios. This behavior is evident in Figure 5.16, where

also for low values of the ϵ_{MAC} more structural modes are identified. Therefore this parameter is affecting less the noise modes removal procedure. Because of the small dependency of the final results from this tolerance value, for the further analysis an ϵ_{MAC} equal to 0.05 is considered.

Finally, the influence of the minimum number $\bar{C}_{min}$ of similar modes is tested. Figure 5.17 present the results of the noise mode removal procedure considering five different values for the $\bar{C}_{min}$ parameter. The definition of these parameters highly affects the number of stable identified mode in the methodology. It can be noticed how increasing the value of the threshold, the number of identified modes drastically decreases, leading to the impossibility of identifying any structural mode.

In the light of the results obtained from the previous sensitivity analysis on the tolerance values on the parameters driving the noise mode removal step, four fixed values are set for all the identification procedures carried on further in this dissertation. In order to keep track of all the modes, without losing any important structural mode, the final thresholds are:ϵ_f=0.01, ϵ_ξ=0.05, ϵ_{MAC}=0.05 and $\bar{C}_{min}$=100.

The results in terms of frequency vs. system identified order and frequency vs. damping ration are presented in Figure 5.18. Comparing these results with the identification obtained right after the simple application of the DD-SSI procedure (Figure 5.14), it is evident how the removal approach consistently cleans the identification from the noisy modes. The distributed cloud of identified modes which was present in Figure 5.14a is sensibly reduced, leaving concentrated columns of identified stable points where the frequency content of the structure is. Figure 5.18b shows the clustered tendency of the identified points in terms of frequency and damping ratio.

Before moving to the cluster analysis, it is worthy it to investigate the relation between the identified stable modes and the parameters of DD-SSI. Additionally, to better appreciate the role played by the asymmetric partition into the identification of stable modes, the number of block rows of the future outputs h is normalized with respect to the total number of block rows i, giving the partition ratio $\hat{h}$ of the future outputs with respect to the past ones. Figure 5.19 shows four barplots, each referred to a parameter of SSI: the system order n, the number block rows i, the partition ratio $\hat{h}$, the number of block columns j of the Hankel matrix. Each barplot shows the ratio between the number of identified structural

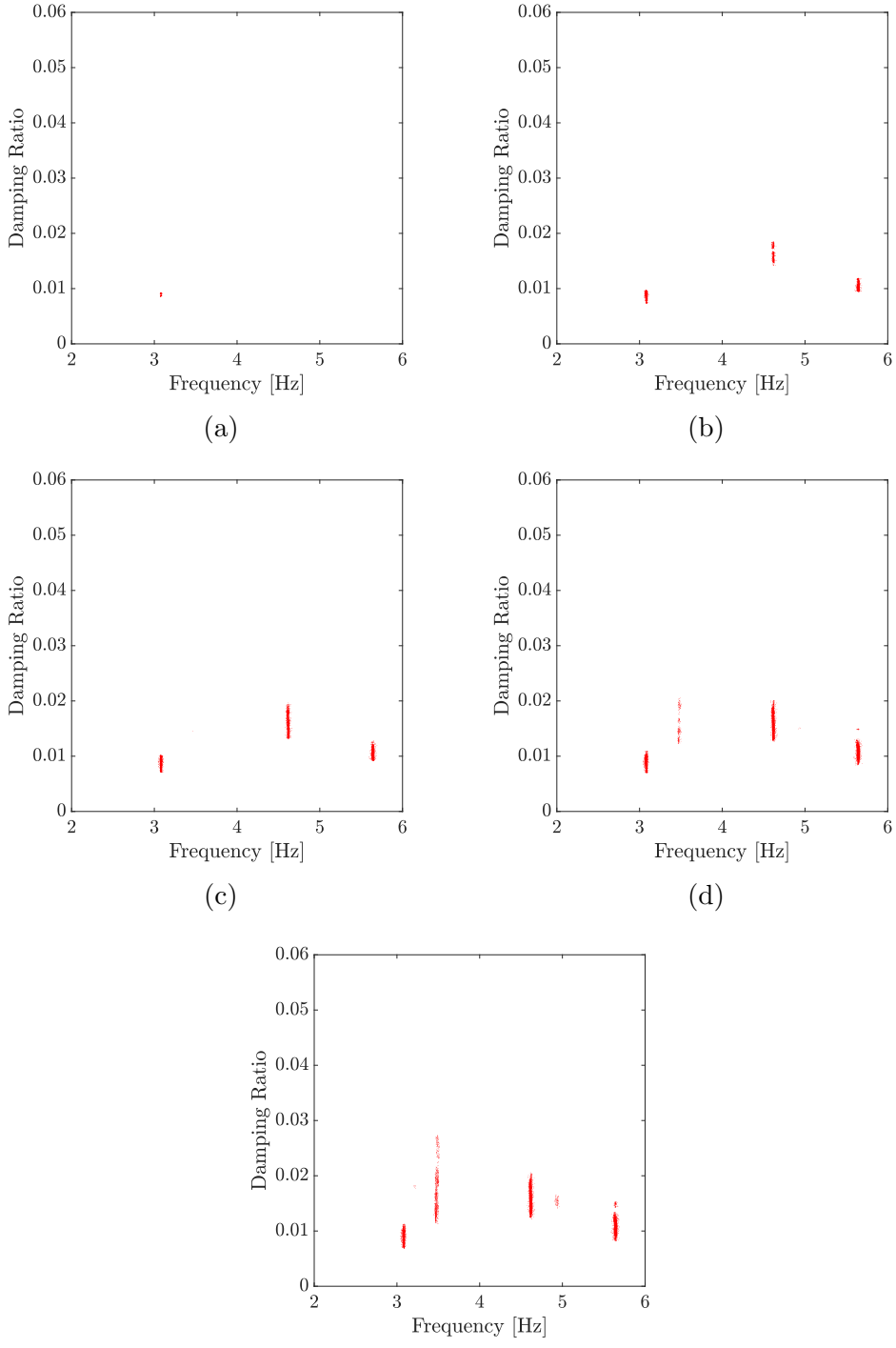

Figure 5.15: Noise modes removal considering ϵ_f=0.01, ϵ_{MAC}=0.05, $\bar{C}_{min}$=100 and varying ϵ_ξ:(a) ϵ_ξ=0.01,(b) ϵ_ξ=0.02, (c) ϵ_ξ=0.03, (d) ϵ_ξ=0.04, (e) ϵ_ξ=0.05.

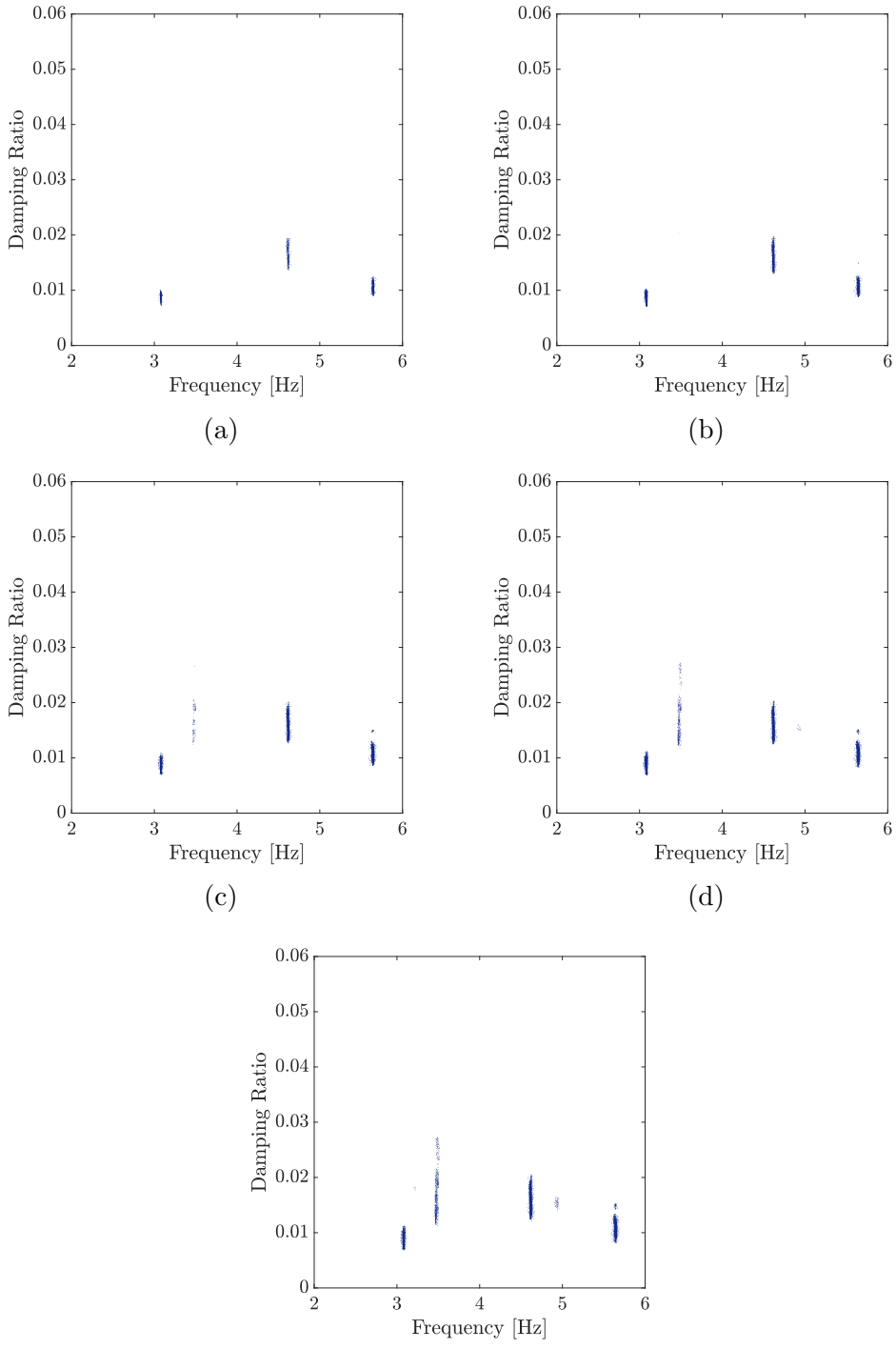

Figure 5.16: Noise modes removal considering ϵ_f=0.01, ϵ_ξ=0.05, $\bar{C}_{min}$=100 and varying ϵ_{MAC}:(a) ϵ_{MAC}=0.01,(b) ϵ_{MAC}=0.02, (c) ϵ_{MAC}=0.03, (d) ϵ_{MAC}=0.04, (e) ϵ_{MAC}=0.05.

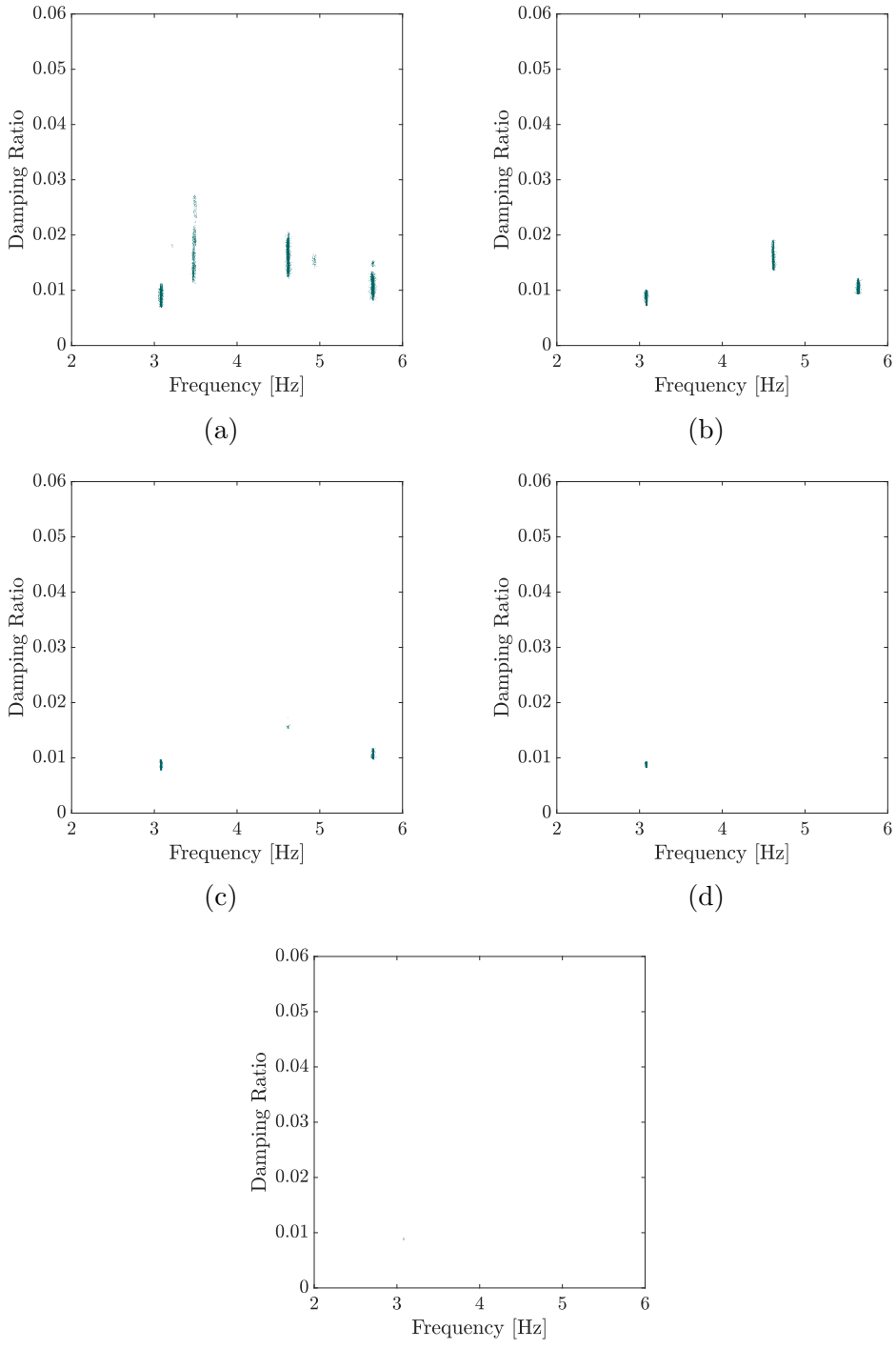

Figure 5.17: Noise modes removal considering ϵ_f=0.01, ϵ_ξ=0.05, ϵ_{MAC}=0.05 and varying $\bar{C}_{min}$:(a) $\bar{C}_{min}$=100,(b) $\bar{C}_{min}$=200, (c) $\bar{C}_{min}$=300, (d) $\bar{C}_{min}$=400, (e) $\bar{C}_{min}$=500.

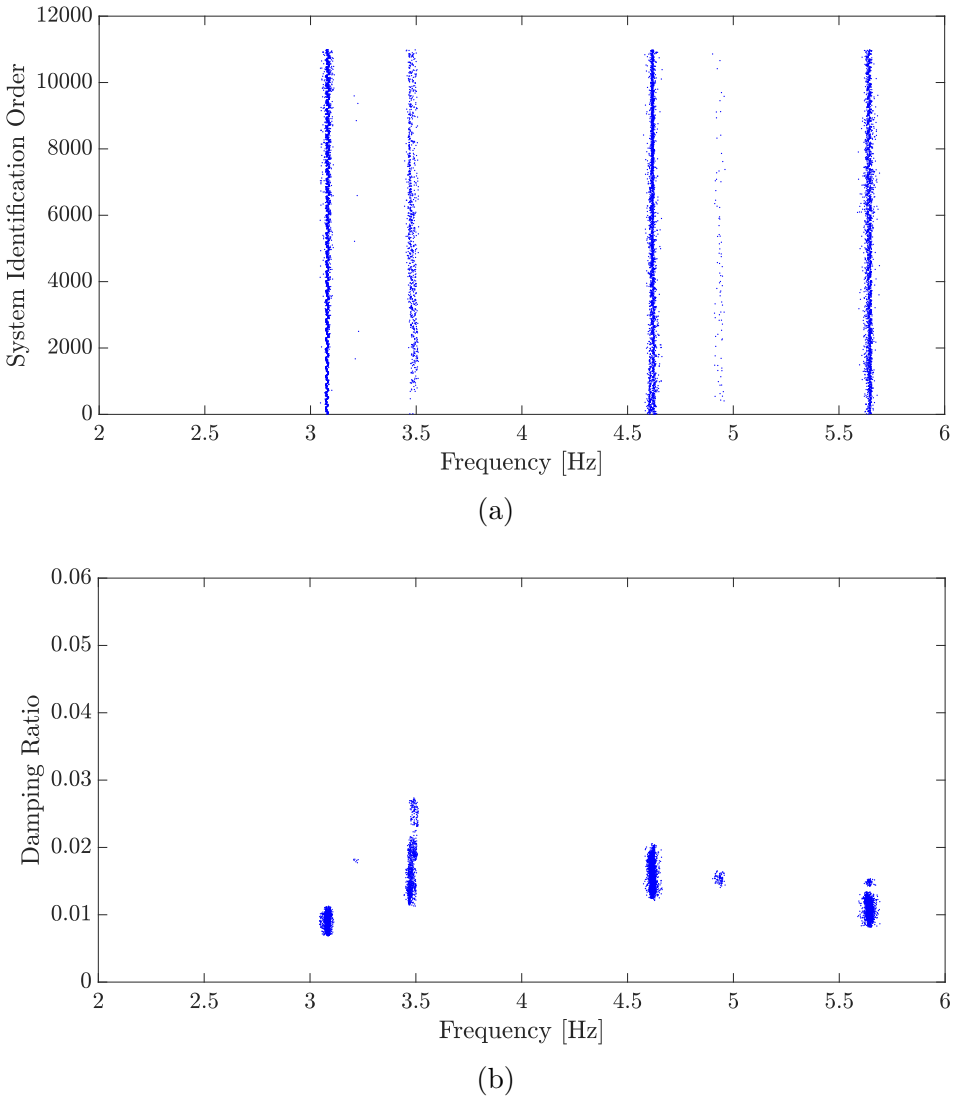

Figure 5.18: Stable identified modes. Frequency vs. Combination of parameters (November 2015).

modes for that specific parameter with respect to the maximum number of modes identified for the best case. Looking at the results, it can be immediately observed that the parameter j has minimal impact on the final identification of structural modes since the percentage of identified modes is high (>0.85) for all the three values considered.

All the considered values for the block rows of the Hankel matrix i lead to an identification ratio higher than 0.6; however above i=320, the ratio is consistently higher than 0.8, reaching the maximum around i=600. For i >600, the ratio

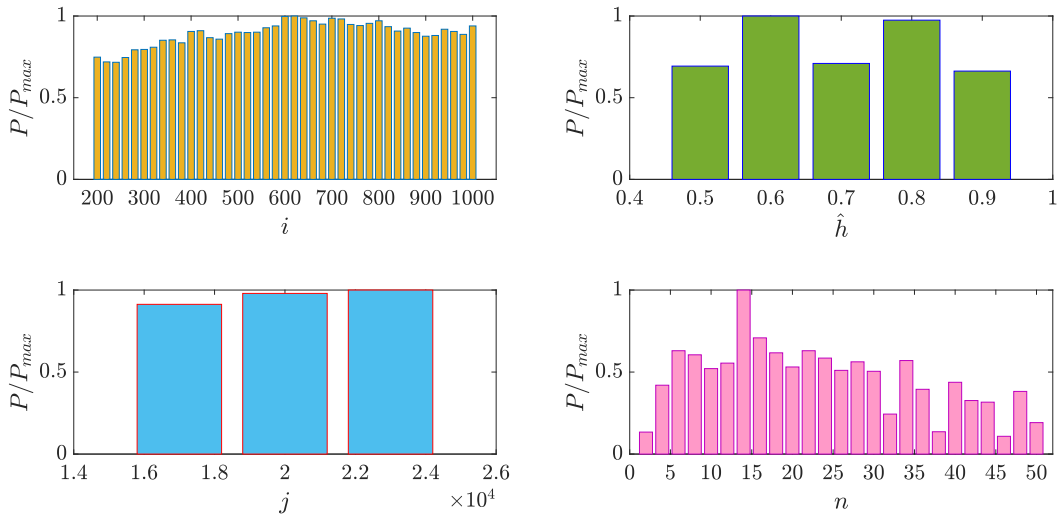

Figure 5.19: Percentage of stable identified structural modes (November 2015).

of identified modes tends to decrease. This can be explained by the fact that increasing the number of block rows in the Hankel matrix implies the introduction of more information about the system into the Hankel matrix. At the same time, working with larger matrices will introduce mathematical artifacts that will result in additional noise and, consequently in the identification of more noise modes. Hence it is important to keep the range of variations of i well confined, otherwise the computational cost of the analysis is increased without actually introducing any advantage in the identification. Regarding the system's order, $n = 14$ gives the highest identification ratio. For values of the system's order less than 6 and more than 30, the number of identified stable modes diminishes very rapidly. Finally it is important to highlight that, with regard to the partition coefficient, the highest identification ratio is not found for the most common symmetric partition ($\hat{h}$), but for the asymmetric conditions. Particularly $\hat{h}$=0.6 and $\hat{h}$=0.8 lead to the highest percentage of identified modes, pointing out how the symmetric partition, which is the solution used in almost all the applied DD-SSI procedures, could not be the best choice.

It is worthy it to investigate also the correlation between these four parameters. Figure 5.20 shows the number of stable identified modes associated with pairs of parameters. From Figure 5.20a, it is evident how the system's order n equal to 14 tends to be significant in terms of stable modes, when the parameter i assumes

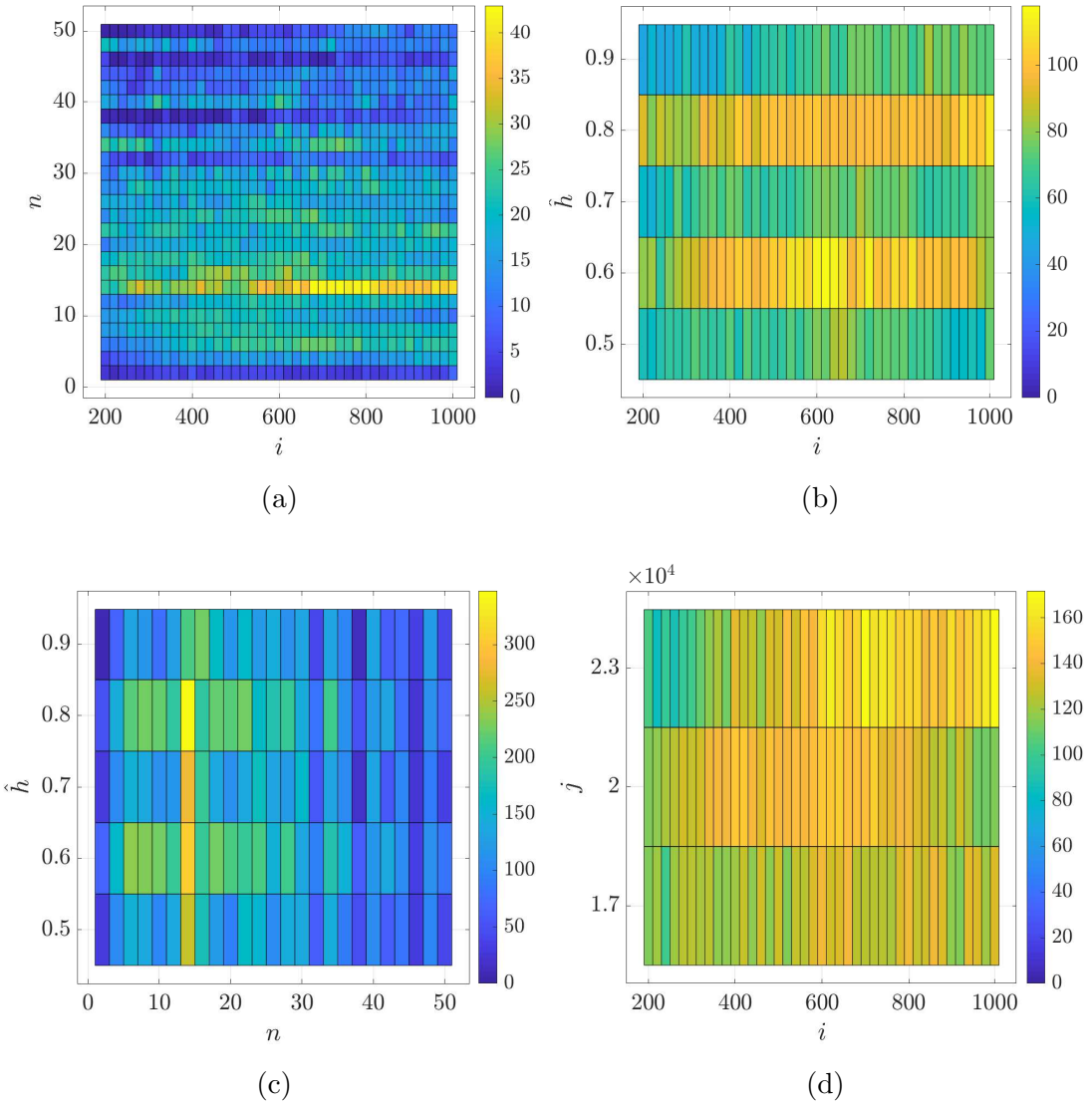

Figure 5.20: Stable identified modes with respect to the driving methodology's algorithm (November 2015): the number of block rows of the Hankel matrix i, the model system's order n, the partition ration on the past and future block rows $\hat{h}$ and the number of block columns of the Hankel matrix j.

values greater than 500. At the same time, the corresponding effective values of the partition $\hat{h}$ and of the number of block columns j are 0.6 (5.20b) and 23000 (5.20d) respectively, apparently narrowing down the variability range of these parameters.

Step (d): Clustering & Outlier Removal

The penultimate step of the procedure is the cluster analysis with the combined outlier removal procedure. In the proposed methodology two different approaches are given to carry achieve the separation of clusters: a blind k-Means approach and DBSCAN algorithm. These two procedures are both based on the computation of a similarity quantity which tells the distance between the identified stable poles. In the Blind k-Means methodology the similarity distance considered can be or a physical-distance or the MSD presented in Section 2.4.

Before starting the clustering step, the user needs to set the threshold for the maximum distance d_{max} which will be the separating threshold between clusters. This threshold happens to be empirically chosen for the Blind k-Means approach that relies on the physical distance. Indeed in this case the user needs to set this value according to his own expertise. For the study case of the Civic Tower in Rieti, the authors have defined a value of 0.04. On the other hand the blind k-Means version which is built over the MSD, allows to set the threshold taking advantage of the F-distribution assumed for the MSD. The threshold,d_{max} is then set to the value of the $1-\alpha$ percentile of $F_{d,b-d}$, where α is the confidence level, d is the dimensionality of the feature vector and b is the number of observations of the feature vector.

When choosing the clustering based on DBSCAN the user needs to set two parameters: the minimum number of points (MP) and the ϵ. The first parameter can be easily set considering that it needs to be bigger than the dimensionality of the feature vector d and in general is set at least equal to $\log(b)$ and in this case it is set equal to 10. The minimum number of points MP helps defining the value of the radius ϵ in the DBSCAN search. As previously mentioned in Section 2.4, it is possible to identify a reasonable value for ϵ defining a k-dist function from the database, mapping each point to the distance from its k-th nearest neighbor, where k is set equal to MP. Figure 5.21 shows the points of the dataset sorted in descending order of their k-dist values, considering 4 different possible values of MP and consequently of k. It can be noticed that for all the cases there is a "valley" around a k-dist of 0.0015 which separate the noisy points from the clusters. Accordingly the ϵ value is set euqal to the k-dist threshold with the higher value of minimum points MP (MP=10).

Figure 5.22, Figure 5.23 and Figure 5.24 respectively show the clustering pro-

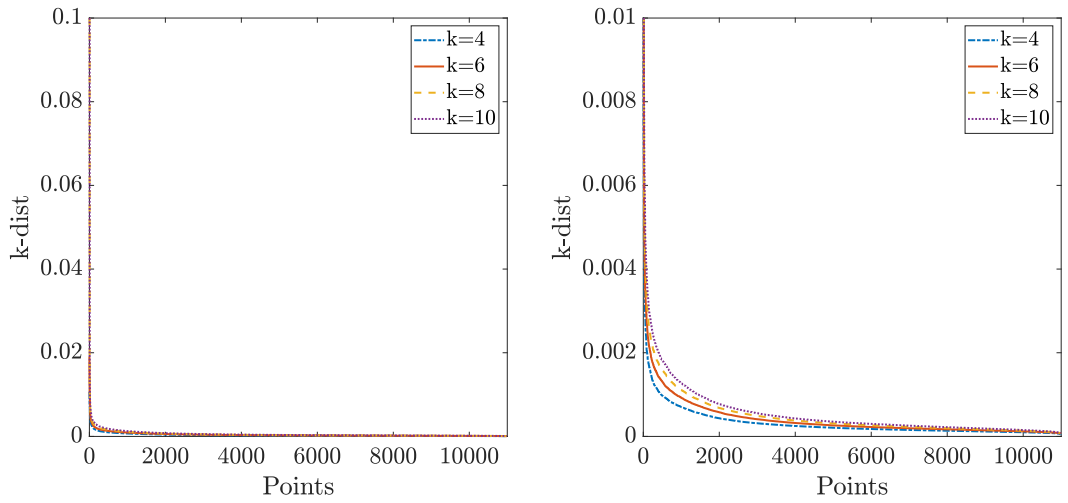

Figure 5.21: k-dist function.

cess considering the blind k-Means approach with the physical distance, then with the Mahalanobis Square Distance and then with the DBSCAN algorithm. In all three cases the feature vector collects both frequencies and mode shapes. In the two approached based on k-Means the clustering stage is carried on in two separate steps: the initial clustering (Figure 5.22b and Figure 5.23b) with the additional cancellation of the smaller clusters and then the outlier removal (Figure 5.22c and Figure 5.23c). The two methodologies based on k-Means leads to similar results, considering although that the introduction of the Mahalanobis Square Distance allows to set a threshold according to the F distribution of the distance itself, without any reference to the user's sensitivity.

DBSCAN algorithm allows to carry on the clustering process in a single step discriminating the clusters from the noisy points in one passage.

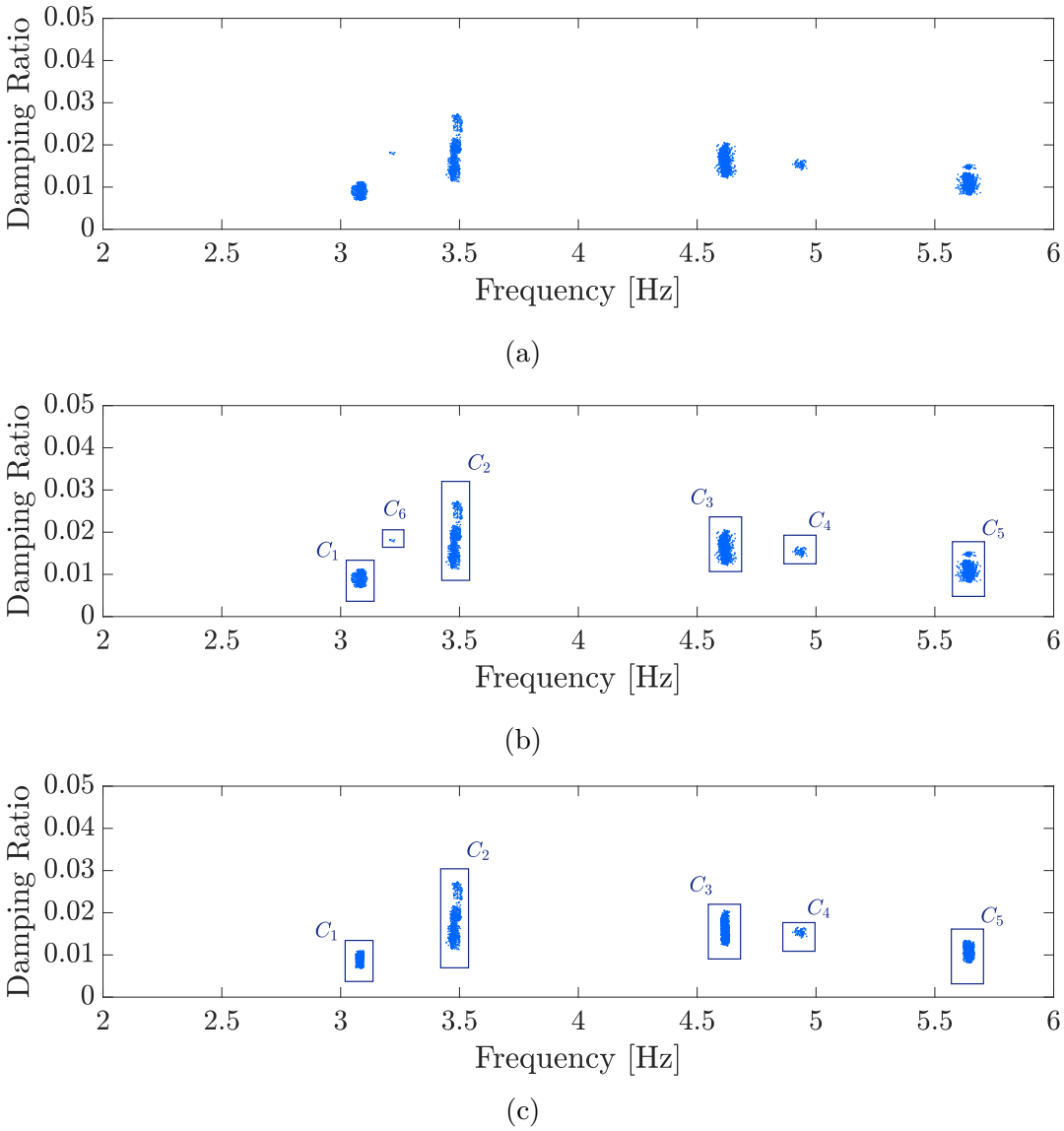

Figure 5.22: Clustering with blind k-Means with physical distance:(a) before clustering, (b) after clustering, (c) after removing noise and small clusters.

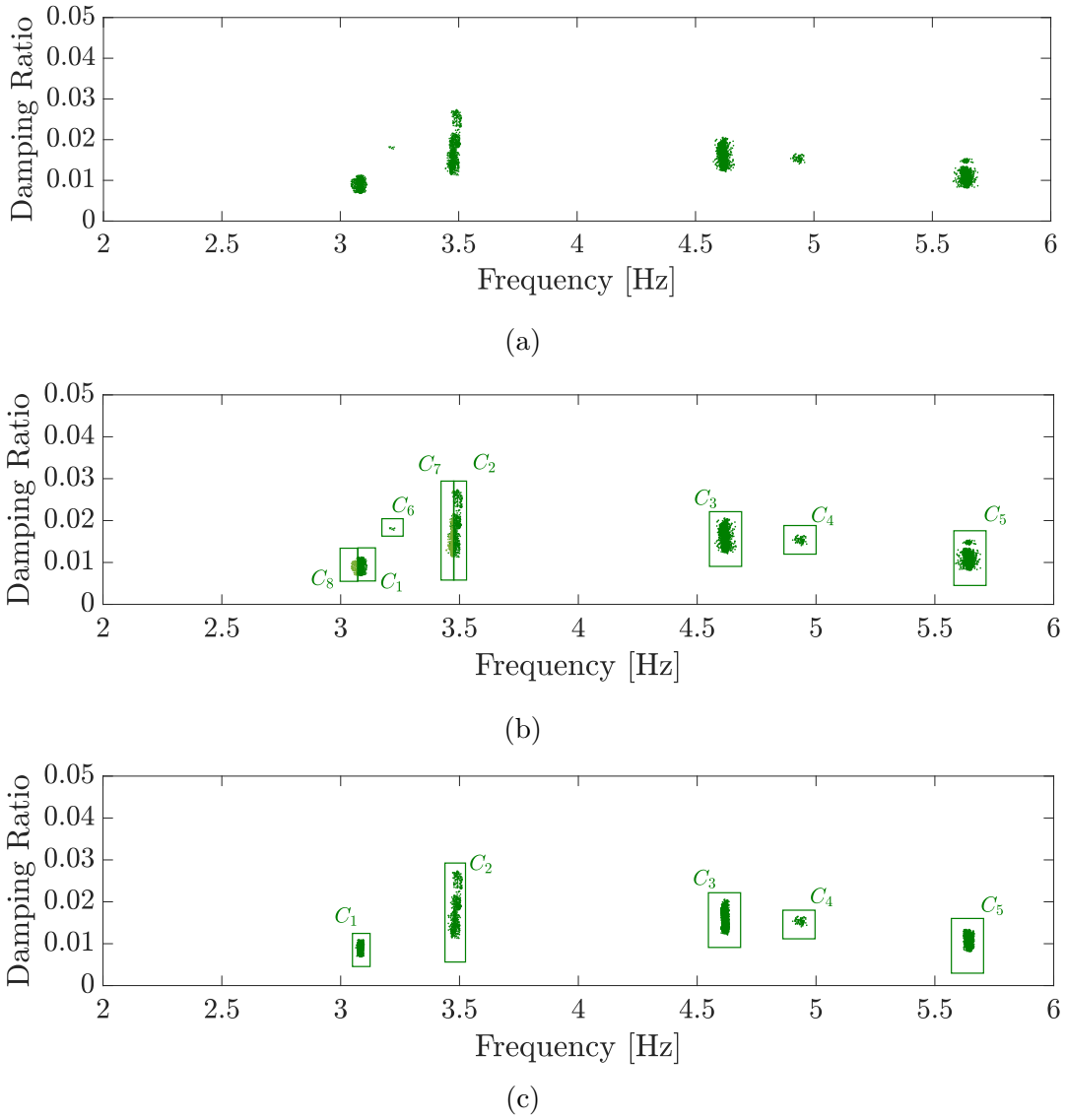

Figure 5.23: Clustering with blind k-Means with Mahalanobis Square Distance:(a) before clustering, (b) after clustering, (c) after removing noise and small clusters.

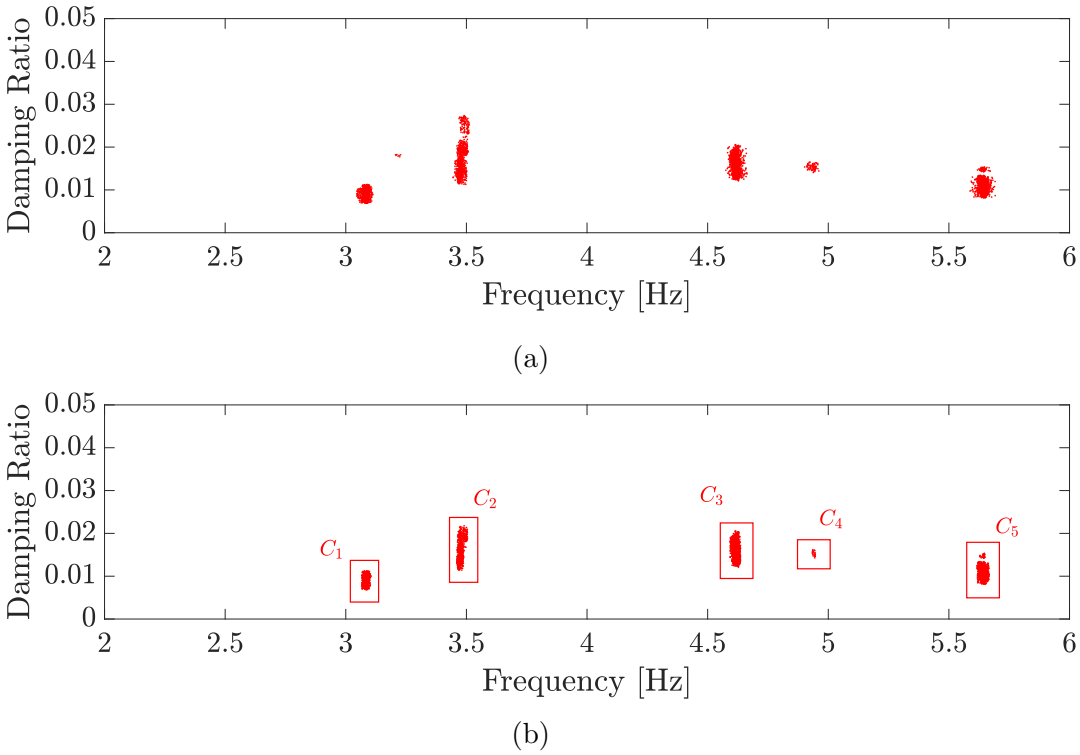

Figure 5.24: Clustering with DBSCAN:(a) before clustering, (b) after clustering and removing noise and small clusters.

Step (e): Selection of the Representative Modal Quantity

Figure 5.25 shows the final results obtained after the estimates of the mean values and the corresponding 95% confidence. It can be noticed how the two k-Means approaches lead to almost identical results. The methodology based on the MSD offers an improvement in terms of damping dispersion for the first structural mode, but at the same time leads to slightly more disperse damping ratio for the third mode. The approach based on DBSCAN clustering on the other hand, leads to the more stable and less disperse solution, both in terms of frequencies and damping ratios, which can be better appreciated looking at the values in Table 5.4 and Table 5.5.

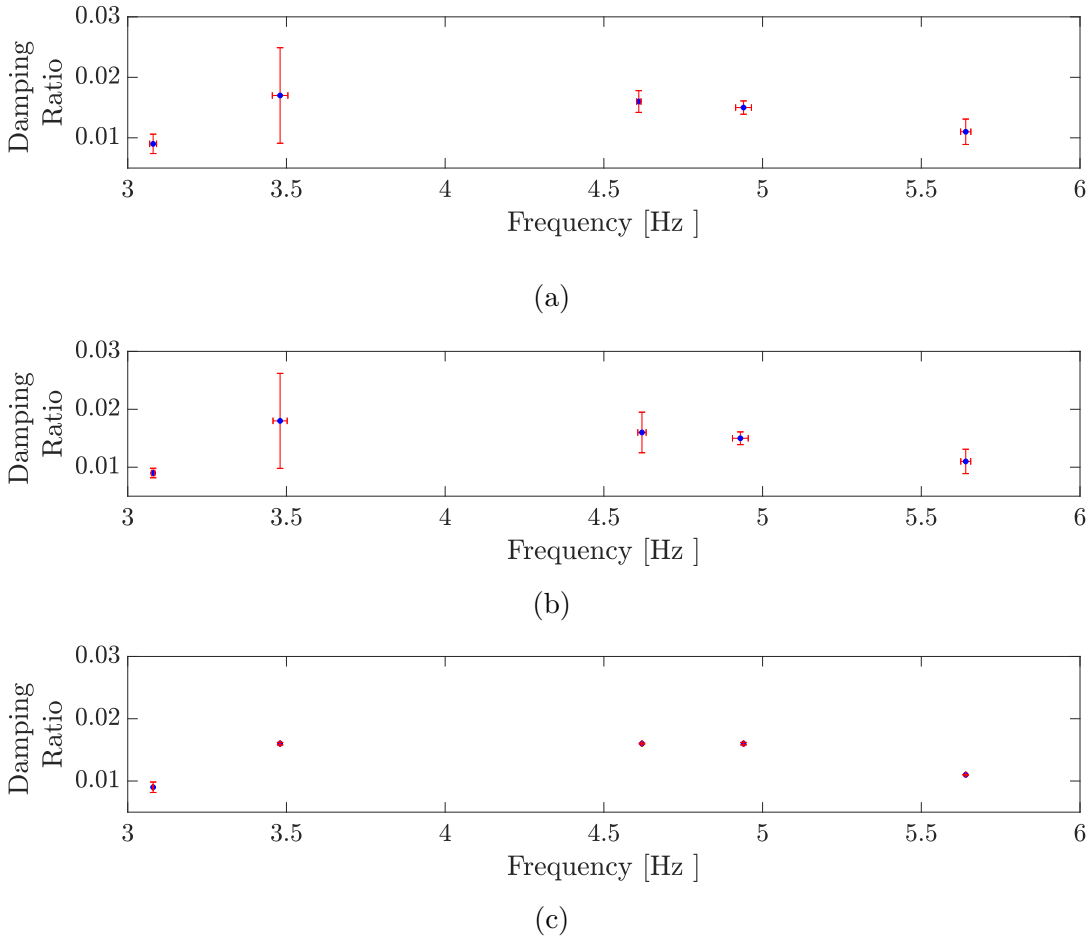

Figure 5.25: Bar plot of mean and standard deviation in terms of frequencies and damping ratios: (a) blind k-Means with physical distance; (b) blind k-Means with Mahalanobis Square Distance and (c) DBASCAN

Table 5.4: Mean and standard deviation in terms of frequencies for the three clustering approaches

Approach	**Blind-Kmeans**				**DBSCAN**	
Distance	**Physical dist**		**MSD**		**Eucledian**	
Mode	μ_f	σ_f	μ_f	σ_f	μ_f	σ_f
1	3.08	0.0108	3.08	0.0053	3.08	0.00018
2	3.48	0.0245	3.48	0.0223	3.48	0.00072
3	4.61	0.0069	4.62	0.0131	4.62	0.00027
4	4.94	0.0249	4.93	0.0248	4.94	0.00063
5	5.64	0.0161	5.64	0.0159	5.64	0.00031

Table 5.5: Mean and standard deviation in terms of damping ratios for the three clustering approaches

Approach	**Blind-Kmeans**				**DBSCAN**	
Distance	**Physical dist**		**MSD**		**Eucledian**	
Mode	μ_ξ	σ_ξ	μ_ξ	σ_ξ	μ_ξ	σ_ξ
1	0.009	0.0016	0.009	0.0008	0.009	0.00084
2	0.017	0.0079	0.018	0.0082	0.016	0.00020
3	0.016	0.0018	0.016	0.0035	0.016	0.00006
4	0.015	0.0011	0.015	0.0011	0.016	0.00020
5	0.011	0.0021	0.011	0.0021	0.011	0.00004

5.5 Dynamic Characterization of the Civic Tower

5.5.1 Preliminary AVTs

The dynamic response of the Civic Tower in operational conditions was recorded several times since July 2015. Especially the first experimental campaigns, collected in phase 1 (Table 5.2), from July 28^{th}, 2015, until January 26^{th}, 2016, were the ones giving the preliminary information on the dynamic behavior of the structure.

The modal information derived within the AVTs performed on November 3^{rd} 2015 are chosen as the baseline for the dynamic characterization of the structure and as the healthy reference state for all the future monitoring campaigns. This choice is driven by the fact that the identification results from the AVTs are identical to those obtained from the FVTs and the FEM.

The extraction of the modal parameters was carried out using the automated system identification procedure described in the previous section.

From a preliminary analysis through the Fourier Transform (FT), (Figure 5.26) five frequencies clearly emerge from a simple peak-picking analysis: the first one around 3 Hz, the second around 3.5 Hz, the last three are sufficiently spaced, and they are about 4.5 Hz, 5 Hz, and 5.6 Hz respectively. At the same time, the automated SSI procedure gives the identification of the same five frequencies with the corresponding damping ratios (Figure 5.26). Among the five identified modes, four (3 Hz, 4.5 Hz, 5 Hz, and 5.6 Hz) present distinct stability in terms of the frequency range, with associated damping ratios consistently clustered, confirming

the robustness in their identification. However, the second mode, even if stable in terms of frequency, shows high spread in the damping ratio's identification, caused by the uncertainty in the identification of the mode itself. Looking carefully at the FT in Figure 5.26, a sixth pick can be spotted around 3.5 Hz; however, there is no correspondence, in this preliminary phase, with the results derived from the AVTs. To further investigate the identification of the structural modes, FVTs were

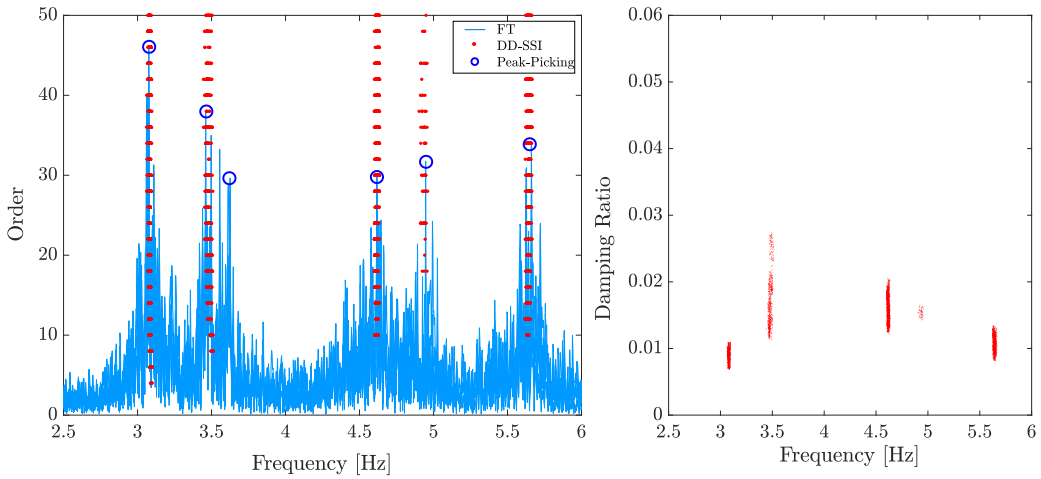

Figure 5.26: Fourier Transform and stable poles identified with the automated methodology for the AVT of 3rd November 2016.

performed during the IV and V monitoring campaigns. In the FVTs a vibrodyne, series VTE 40k by Valtronic Europe (Figure 5.27) was used with a sampling frequency equal to 200 Hz. The vibrodyne configuration adopted consists of two eccentric masses with a static moment of 0.896 kgm and a maximum force of approximately 32 kN at 30 Hz. Two kinds of tests were carried out: a sine sweep in which the force-frequency varies linearly and a second stepwise time-frequency test in which sinusoidal forces, characterized by different frequencies, are applied one at the time until the system reaches the stationary response. In the first test, the force-frequency linearly increases and decreases within the range 2-7 Hz in 240s (excluded time to reach the initial frequency). Figure 5.28 shows the Frequency Response Functions (FRFs) of the structural accelerations for the two FVTs and the identified frequencies from the automated SSI procedure, using the data from channel 3 (Figure 5.28a) and channel 6 (Figure 5.28b).

The values associated with the stepwise time-frequency test are higher than the ones coming from the sine sweep. This outcome is more evident for lower fre-

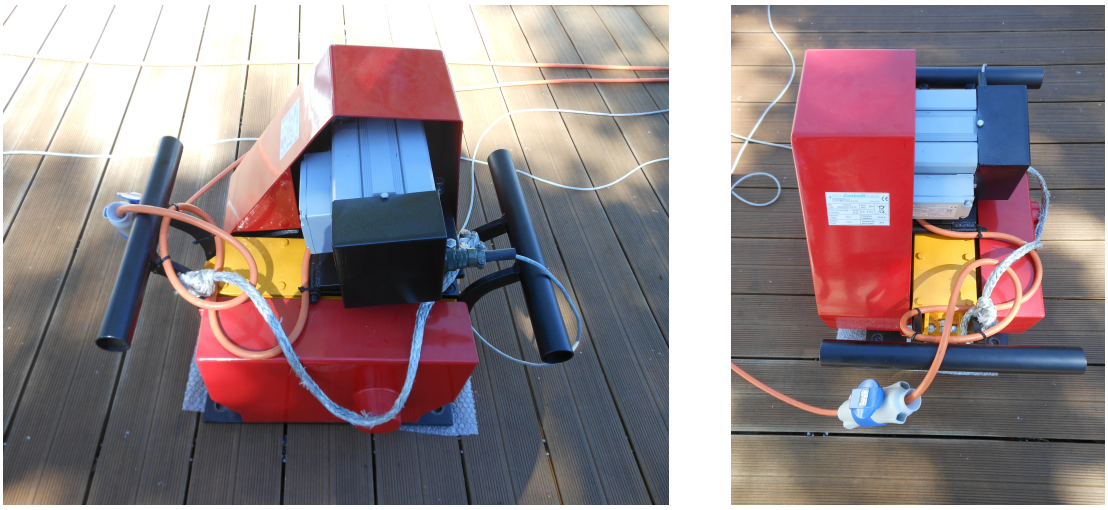

(a) (b)

Figure 5.27: Vibrodyne views: (a) side view, (b) back view.

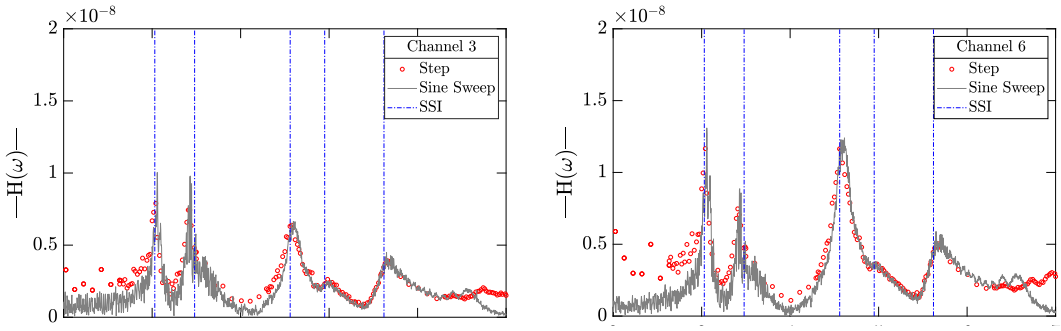

(a) (b)

Figure 5.28: Results of the FVTs: (a) channel 3, (b) channel 6.

quencies, while they are substantially coincident for higher frequencies. It could be due to the high speed of the stepwise test during which the structure did not have enough time to reach the stationary response in the lower frequency range, where the number of cycles is not adequate. Comparing the AVT results with those derived from the FVT, it is evident the agreement with the identified frequencies. Five frequencies are identified distinctly (Table 5.6), while around 3.5 Hz, the FRFs in Figure 5.28 shows that there could probably be another structural frequency that is difficult to identify. Looking at the identified frequencies along with the monitoring campaigns in this preliminary phase (Table 5.6), it distinctly emerges that the frequencies tend to vary along this period. Indeed all of them present higher values in July 2015 and then decrease during November 2015 and

Table 5.6: Modal results from AVT and FVT performed during experimental campaigns II-V and FE model.

Mode	**FEM**	**FT**	**FVT**	**AVT: Automated DD-SSI**				
		11/03 2015	11/03 2015	07/28 2015	11/03 2015	11/10 2015	12/15 2015	01/26 2016
	f (Hz)	f (Hz)	f (Hz)	f (Hz)	f (Hz)	f (Hz)	f (Hz)	f (Hz)
1	3.09	3.03	3.06	3.10	3.08	3.04	3.07	3.10
2	3.42	3.42	3.43	3.54	3.48	3.46	3.50	3.55
3	4.61	4.57	4.60	4.65	4.62	4.56	4.59	4.66
4	5.01	4.95	4.99	5.04	4.93	4.93	4.95	5.01
5	5.62	5.65	5.65	5.68	5.64	5.58	5.66	5.65

slowly increase again in January 2016. This behavior suggested a strong interaction of the structure with the environmental conditions and led to the introduction of a temperature sensor in the monitoring system so to track this behavior during a more extended monitoring period.

Besides frequencies and damping ratios, the automated identification methodology also provides the complex eigenvectors of the model of the tower (Figure 5.29). In the complex plane, all the components appear to be strongly aligned with each other, and they all lie along a line which passes through the origin. Accordingly, the imaginary part of the eigenvectors can be minimized, and the associated real mode shapes are plotted (Figure 5.30).

The results of the modal analysis derived from the experimental measurements of the AVTs, in terms of frequencies and modal kinematics show a consistent agreement with the corresponding modal characteristics obtained from the FEM (Table 5.6). The experimental frequencies differ from those of the FEM by extremely small percentages (Δf_1=0.3%, Δf_2=1.75%, Δf_3=0.2%, Δf_4=1.6% and Δf_5=0.35%). The real modal shapes confirm the alignment of the principal modes along the 45 degree principal directions, with the first two modes mainly translational, the third and fourth coupled on translation and torsion and finally the fifth mode is purely torsional (Figure 5.10).

It is worth noticing that both the FVTs and the preliminary peak picking analysis in the frequency domain highlighted that there could be an additional structural mode around 3.5 Hz. At the same time, the dynamic characteristics of the structure, as extracted by the FEM as well as by the AVTs, do not show any

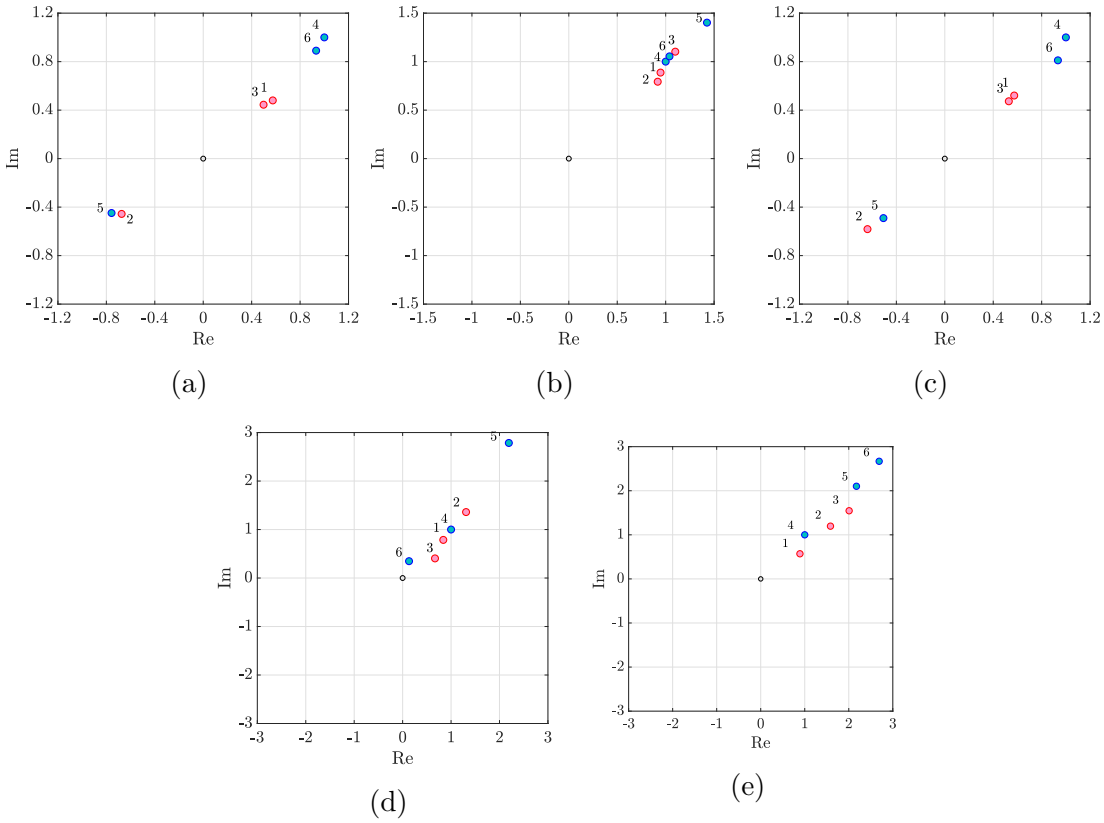

Figure 5.29: Complex Eigenvectors for the reference state (sensors on the TMD in blue and sensors on the support in red): (a) Mode 1 (f_X), (b) Mode 2 (f_Y), (c) Mode 3 (f_{XT}), (d) Mode 4 (f_{YT}), (e) Mode 5 (f_T).

mode in the vicinity of 3.5 Hz and so only five vibrational modes are considered at this stage. However, because system identification techniques founded on SSI are known to have difficulties in identifying close modes, and the FEM is in a preliminary stage, the region of the response spectrum around 3.5 Hz remains a region of interest in the following campaigns.

5.6 Structural Health Monitoring of the Civic Tower

The new 6-sensor monitoring system was installed on July 2015 and the acceleration response of the structure has been recorded since then. The dynamic response of the Civic Tower, during this monitoring period, resulted mainly from

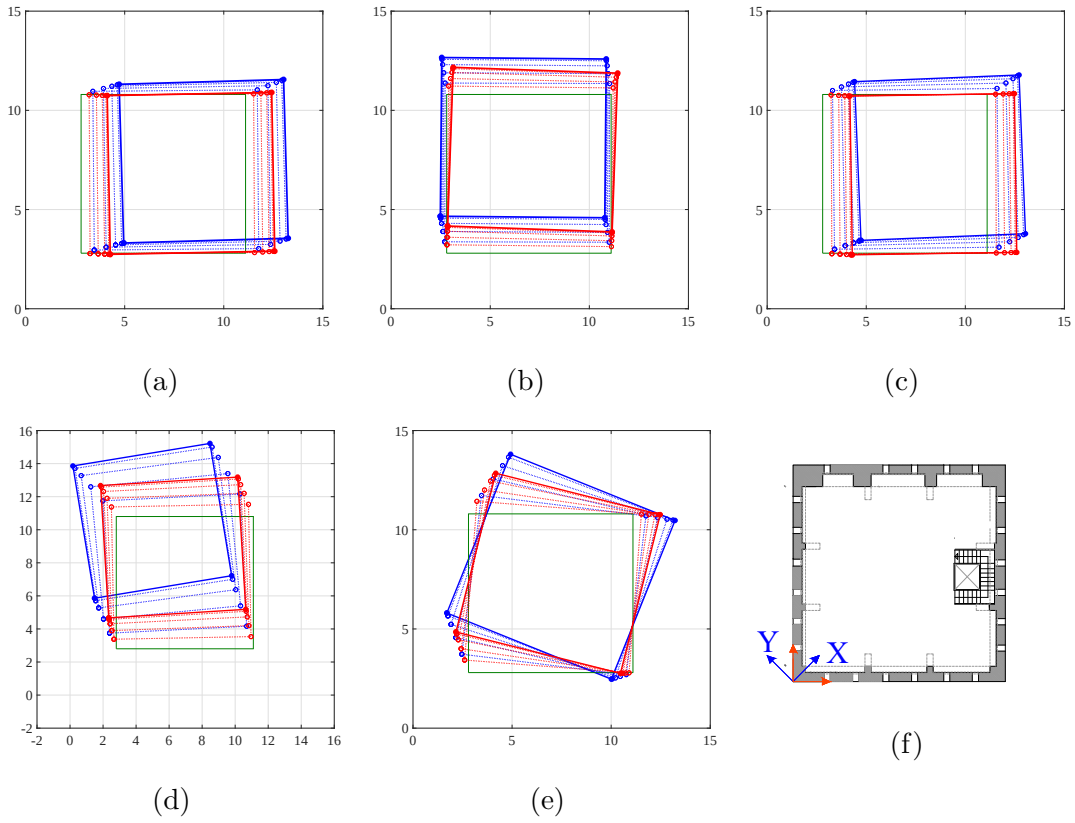

Figure 5.30: Real Eigenvectors for the reference state (TMD modal kinematics in blue, support modal kinematics in red, reference configuration in green): (a) Mode 1 (f_X), (b) Mode 2 (f_Y), (c) Mode 3 (f_{XT}), (d) Mode 4 (f_{YT}), (e) Mode 5 (f_T), (f) principal axis.

two excitation sources: (1) ambient vibrations and (2) earthquakes.

Starting from August 2016, the central regions of Italy were interested by a strong earthquake storm which lasted until February 2017. On August 24^{th}, 2016, and on October 26^{th} and 30^{th}, 2016, three severe earthquakes occurred, having magnitudes of 6, 5.4 and 6.5 on the moment magnitude scale respectively. The epicenter of the first earthquake in August was located near Accumoli, 47 km away from Rieti. The epicenters of the two earthquakes that occurred in October were located close to the city of Norcia, 62 and 54 Km away from Rieti (Figure 5.31).

Figure 5.31: Geographical location of the epicenters of the major seismic events with respect to Rieti.

These seismic events slightly affected the Rieti's area, even if their epicenters happen to be far from Rieti. They induced on the Civic Tower low amplitude accelerations because of the distance from the epicenter and the very stiff nature of the travertine basement on which the tower is erected, which led to no amplification of the base excitation.

5.6.1 Operational Vibration Monitoring

Figures 5.32 and 5.33 show the maximum accelerations (a_{max}) and maximum root mean square of the accelerations (RMS_a) recorded by the six sensors during the monitoring period (one record per day), where the distinction between the monitoring campaigns and the dates of the major earthquakes are marked with continuous and dashed vertical lines respectively.

In the preliminary five campaigns, from November 2015 up to August 2016, the maximum acceleration recorded at all the sensors and the RMS show higher values than those obtained in the subsequent campaigns, with a mean value of 0.0034 m/s^2 for the maximum acceleration, and a mean value of 0.0004 m/s^2 for the maximum RMS.

Right after the seismic event of August 2016 the maximum accelerations and the associated RMS tend to stabilize on smaller average values, 0.001 m/s^2 and 0.0002 m/s^2 respectively.

Moreover, from August 2016, the maximum acceleration and the RMS show a distinct gap between the sensors placed on the mass of the passive control system

(Channel 4, 5, 6) and the ones located on the tower support (Channel 1, 2, 3), with the former of lower value than the latter; this is because of the less rigid nature of the TMD with respect to the support level.

From December 2018 (Campaign X), the trends of a_{max} and RMS_a appear to be more regular and consistent. Sensor 5 and 6 show higher values of maximum acceleration and RMS than the sensors placed on the support, but also higher than the values measured on sensor 4 which is also on the mass of the TMD. To explain the differences, let's recall that sensor 4 is placed on the TMD's mass on the side which settled on the lateral wall; therefore, because of this boundary restraint, that sensor is going to be subjected to accelerations which are smaller compared to the ones recorded from the other sensors on the mass, but still higher than the acceleration measured on the support. The variations in the acceleration

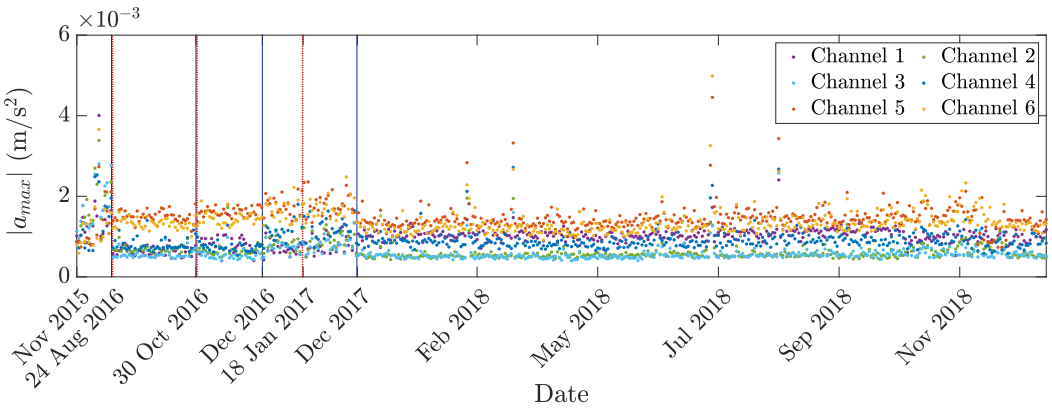

Figure 5.32: Maximum acceleration ($|a_{max}|$) recorded by the six sensors.

response of the structure right after the seismic events suggest that the concrete mass of the TMD system slightly moved with respect to the original configuration during the earthquake in August 2016. The original configuration had the concrete mass resting on one side of the tower, not being free to move. However, the accelerations induced on the structure by the earthquake, even if low, activated the passive control system, overcoming the friction resistance given by the mass lying on the lateral wall. After the event the TMD settled again on the same lateral wall, restoring the initial configuration before the earthquake. A similar analysis has been conducted on the displacements, which are derived from the measured accelerations applying a double integration procedure. The relative displacement between the sensors on the TMD and the ones on the support is computed along

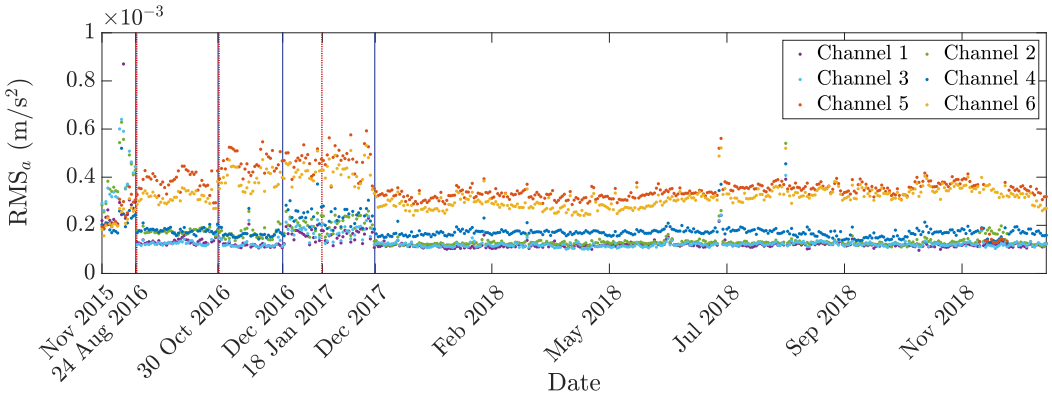

Figure 5.33: RMS of acceleration data (RMS_a) recorded by the six sensors.

with the whole monitoring period (Figure 5.34). In normal operating conditions the values of the relative displacement are stable and consistent around a mean value of 3.56 10^{-5} m.

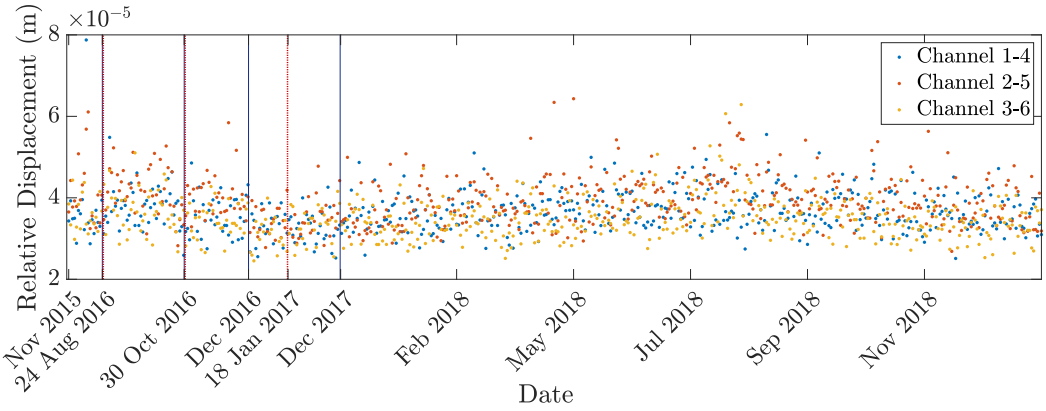

Figure 5.34: Relative displacement between channels.

5.6.2 Seismic Events

During the seismic events, the acceleration and the related RMS recorded by the six sensors reached maximum values of about 0.95 m/s^2 and 0.04 m/s^2 (Table 5.7), respectively, substantially higher than the values usually measured in the operational conditions. As expected, the sensors positioned on the mass of the TMD measured higher acceleration than those placed on the support. Also, the maximum displacement deviated from the values observed during operational conditions, reaching peaks of 2.4 mm both on the support floor and on the mass of

the TMD.

It can be stated that the TMD is activated and moves out of phase with respect to the rest of the structure by comparing the displacements derived from the measured accelerations on the sensors placed on the concrete mass with the corresponding ones on the support level (Figure 5.35b). This finding can also be easily derived looking at the relative displacement between the channels (Figure 5.35a). Right before and after the seismic event, the relative displacement results to be almost zero, proving an in-phase displacement recording between the channels. On the hand, during the earthquake, the relative displacement reaches values of 3.6 mm, showing a substantial "out of phase" behavior.

Table 5.7: Maximum acceleration, displacement and RMS of acceleration at the six channels during the seismic event of October 26^{th}, 2016.

	$\mathbf{Ch_1}$	$\mathbf{Ch_2}$	$\mathbf{Ch_3}$	$\mathbf{Ch_4}$	$\mathbf{Ch_5}$	$\mathbf{Ch_6}$
Max a (m/s^2)	0.3061	0.3504	0.3008	0.7217	0.9349	0.8755
RMS of a (m/s^2)	0.0178	0.0232	0.0180	0.0301	0.0387	0.0341
Max d (m)	0.0021	0.0022	0.0018	0.0019	0.0024	0.0020

The activation and movement of the TMD system during the seismic events is validated by comparing the recorded dynamic response with the one obtained by the FEM. The numerical model where the mass of the TMD is free to move has been considered by eliminating the rigid links between the tower and the TMD's mass, ensuring in this way the activation of the TMD system during the seismic event.

The analysis on the FEM is carried on applying at the base of the model the input acceleration time history of the seismic event occurred on October 26^{th}, 2016. The input was recorded at the base of the Prefecture, building located about 100 m away from the Civic Tower and erected on the same soil type; therefore it is acceptable to assume that the same input could be applied to the tower.

The displacement time histories derived from the measured accelerations at the sensor locations in the tower are then compared with the displacements given by the seismic analysis performed on the FEM.

Figure 5.36 shows the plot of the displacements of the six sensors numerically identified through the FE model and those obtained from integration of the acceleration recorded for event on October 26^{th}, 2016 (magnitude 5.4). It appears

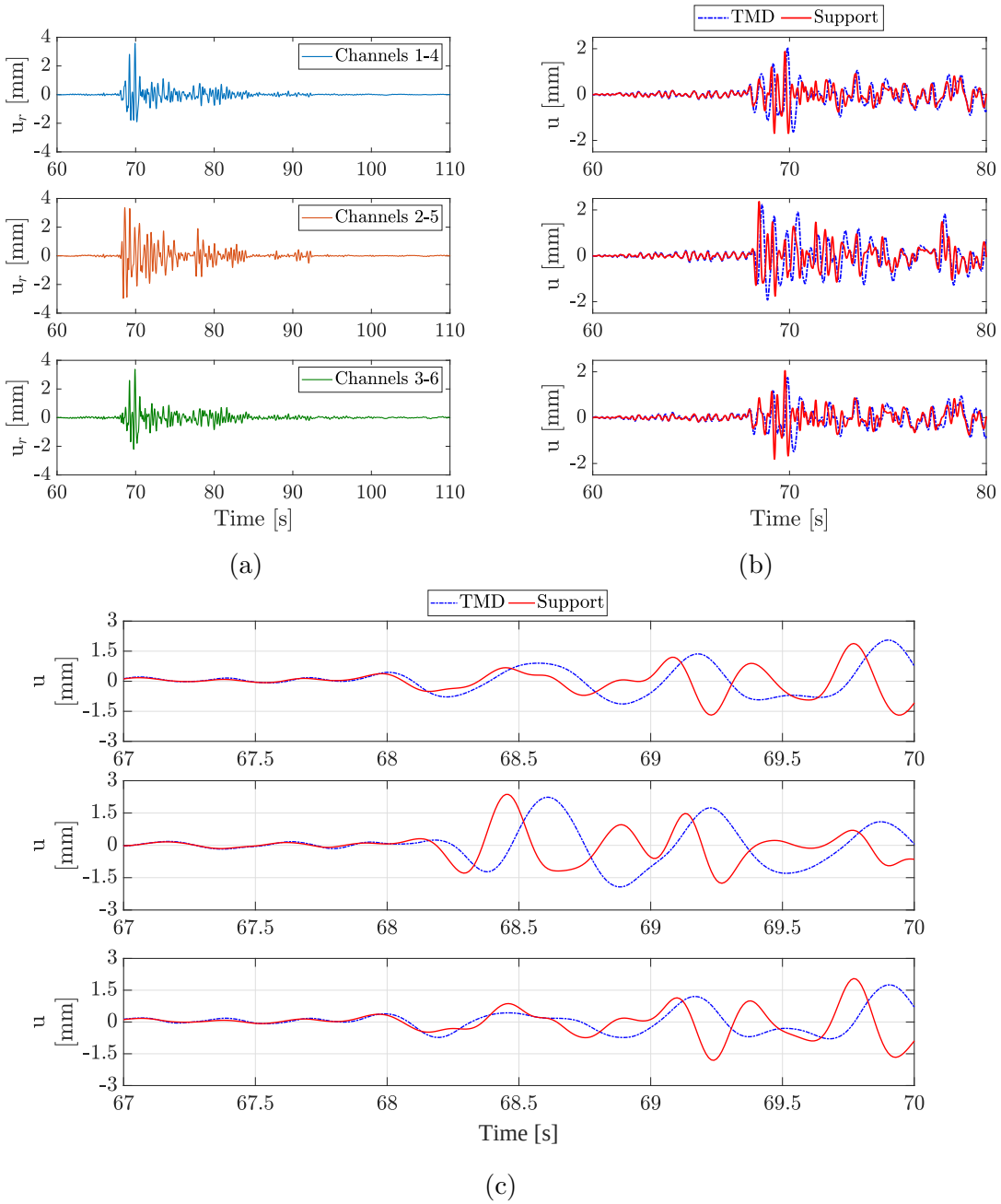

Figure 5.35: Displacement (earthquake October 26^{th} 2016): (a) relative, (b) absolute, (c) absolute zoomed.

that the response of the structure during the earthquake is well represented by the model with the passive control system non rigidly connected to the structure. These results confirm that, during the seismic event, the passive control system is moving out of phase with respect to the structure. The same analysis carried

on the original FEM leads to higher values of displacements, validating the fact that the FEM should be used for the representation of the structure during the operational conditions only, when the TMD can be considered connected to the structure.

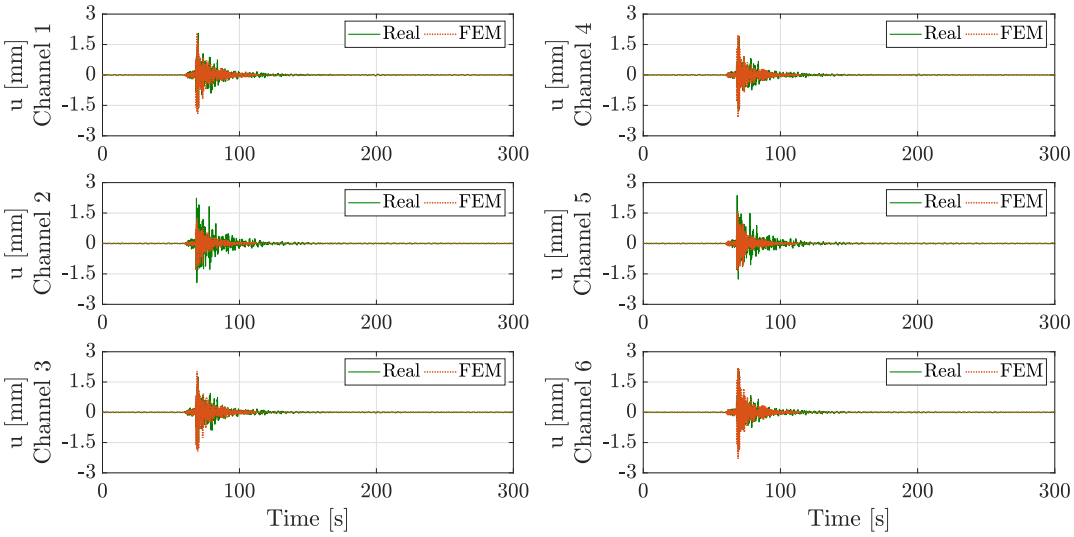

Figure 5.36: Comparison between the displacements of the six sensors experimentally identified and obtained by the FE model (earthquake October 26^{th} 2016).

5.6.3 Automated frequency tracking

Figure 5.37 shows the time histories of the identified natural frequencies obtained by applying the fully automated SSI output-only modal identification technique defined in Chapter 2. The time evolution of the modal frequencies is presented across the three monitoring phases, considering one record per day at midnight, with continuous vertical lines dividing the monitoring periods and dashed vertical lines indicate the three major seismic events which occurred within the monitoring campaigns.

Despite the low levels of vibration in operational conditions, five modes are successfully identified in most of the dataset: the first two translational modes, f_X and f_Y, the third and fourth coupled modes,f_{XT} and f_{YT} and finally the fifth torsional mode, f_T. An additional mode is spotted with less continuity (f^*), and it would correspond to the extra mode identified in the FVTs and the Peak Picking analysis cited in the dynamic reference state section however, because its

instability in the identification it was impossible to determine its nature (Table 5.8).

Table 5.8: Frequency Identification Rate

Mode	Phase 1			Phase 2			Phase 3		
	f (Hz)	Max σ_f	Rate (%)	f (Hz)	Max σ_f	Rate (%)	f (Hz)	Max σ_f	Rate (%)
1	3.06	0.023	100	2.97	0.027	98	2.98	0.013	69
2	3.48	0.049	100	3.28	0.088	75	3.25	0.026	73
*	3.64	0.025	17	3.41	0.098	43	3.41	0.023	25
3	4.61	0.035	100	4.42	0.062	94	4.40	0.014	98
4	4.97	0.051	83	4.77	0.045	58	4.79	0.024	35
5	5.65	0.052	100	5.38	0.063	97	5.37	0.021	98

The robustness of the frequency identification is supported by the value of the standard deviation (Figure 5.38) with respect to the mean values of each frequency that remains small along the monitoring period. Indeed the maximum values of the standard deviation along the monitoring campaign are below ±0.0980 (Table 5.8).

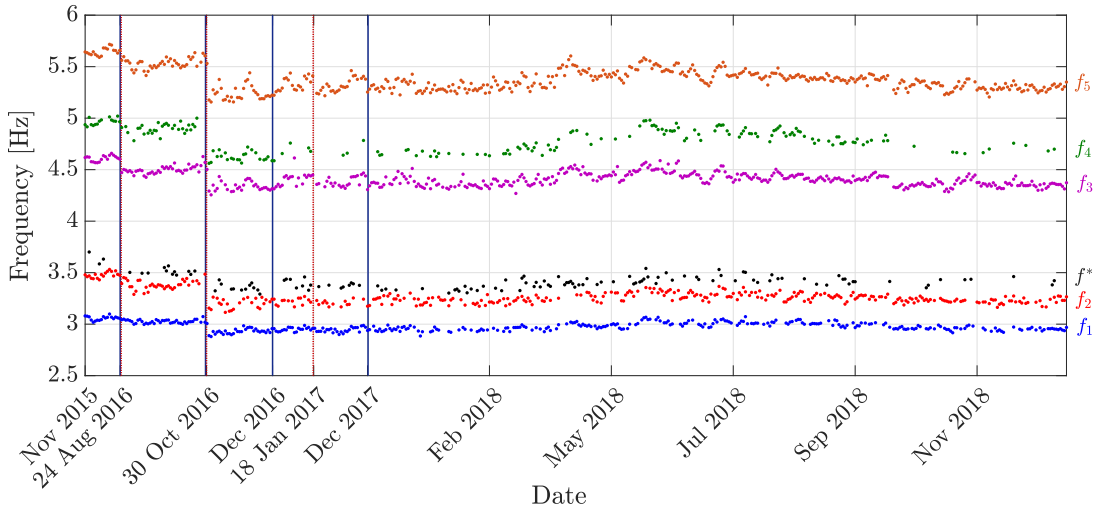

Figure 5.37: Identified natural frequencies along time.

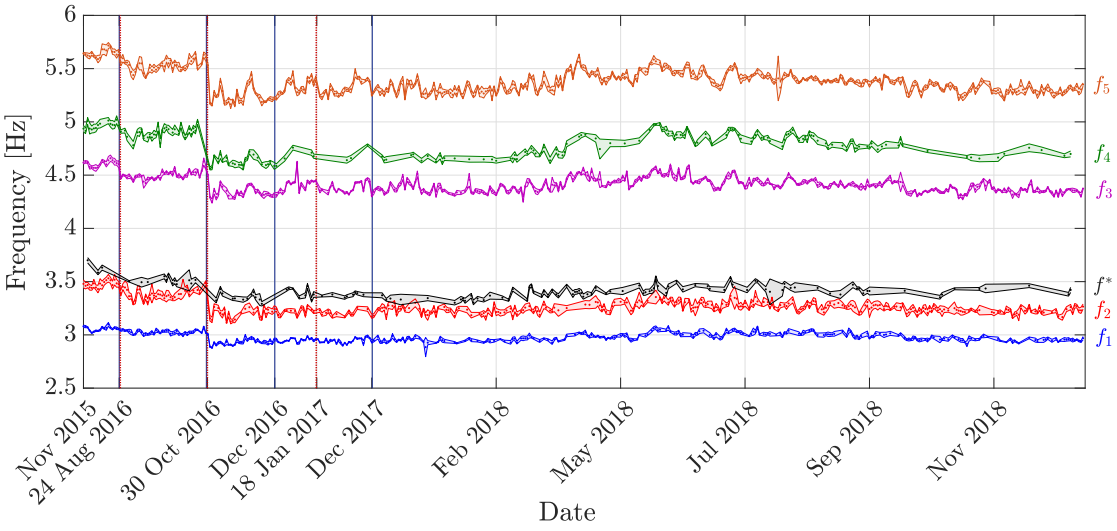

Figure 5.38: Identified natural frequencies and the standard deviation upper and lower bounds along time.

Significant reductions in the frequency value can be noticed comparing the mean values of the frequencies identified before and after the seismic events occurred in 2016 (Figure 5.37 and Figure 5.39). The earthquake that occurred on August 24^{th}, 2016, in Accumoli led to a substantial variation of the second frequency (3%). However, the series of seismic events that took place between October 26^{th} and 30^{th}, 2016, in Norcia reduced all the frequencies from 3% for the second frequency up to almost 6% for the fourth (Table 5.9). These reductions are consistent with the occurrence of localized small damages at the base of the tower, as the creation of small cracks or the coalescence of existing micro-cracks in the masonry structure, which would reflect in a loss of stiffness.

In addition, to confirm that the frequency reduction of the overall structure could be associated with small damage occurrence, a second FEM was calibrated on the basis of the new dynamic modal characteristics experimentally observed.

The mechanical properties assigned to the original FEM were obtained after a sensitivity analysis calibrated on the experimental structural modes identified in the first five monitoring campaigns. For this new model, the mechanical properties of the materials were varied to fit the new dynamic reference condition of the tower. Table 5.10 shows the selected values of mechanical properties assigned to the FEM before and after the new calibration. For converging to the new model, Young's modulus (E) of travertine and masonry was reduced differently along with the height of the tower. Masonry structures, subjected to earthquakes,

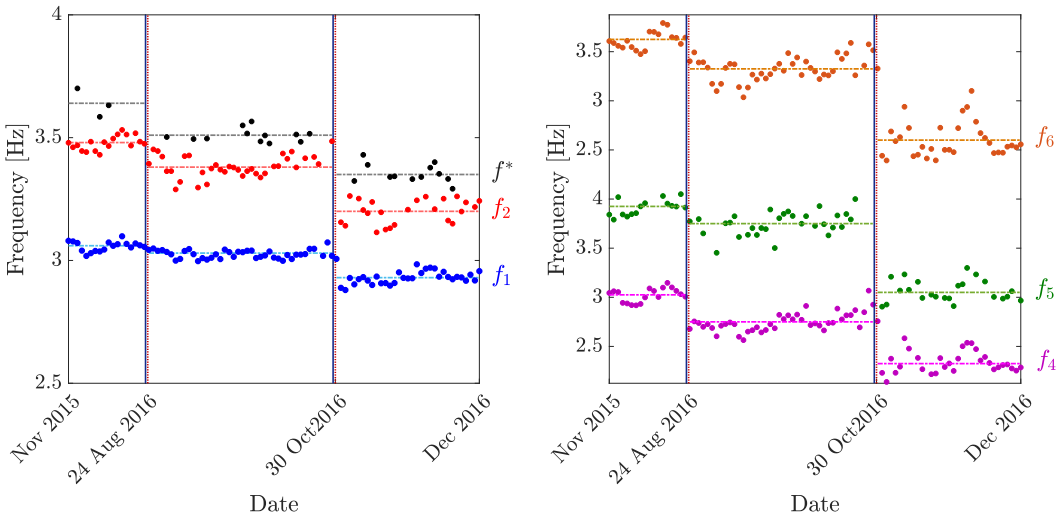

Figure 5.39: Time histories of identified natural frequencies before and after the earthquakes of August 24^{th}, 2016 and October 26-30^{th}, 2016.

Table 5.9: Reduction of the natural frequencies before and after the earthquakes of August 2016 and October 2016.

Mode No.	August 2016			October 2016		
	Before f (Hz)	After f (Hz)	Reduction Δf (%)	Before f (Hz)	After f (Hz)	Reduction Δf (%)
1	3.06	3.02	*1.31*	3.02	2.93	*2.98*
2	3.48	3.38	*2.87*	3.38	3.20	*5.32*
3	3.64	3.51	*3.57*	3.51	3.35	*4.56*
4	4.61	4.50	*2.39*	4.50	4.33	*3.78*
5	4.97	4.90	*1.41*	4.90	4.62	*5.71*
6	5.65	5.53	*1.95*	5.53	5.24	*5.24*

are more likely to present damage at the base, taking into account the cyclic nature of the seismic load that tends to worsen the micro-cracks configuration of masonry. Therefore the reduction in terms of the Young's modulus parameters was differentiated between the first level of the structure where the reduction was assumed higher, and the other levels of the tower (Table 5.10). The structural frequencies given by the re-calibrated FEM are 2.98 Hz, 3.29 Hz, 4.44 Hz, 4.83 Hz, and 5.39 Hz (Table 5.11). The re-calibrated FEM describes efficiently the new damaged reference conditions of the structure, with a maximum discrepancy

in terms of frequency of 1.2% for the second structural mode, while all the other structural modes remain within the 1% error (Table 5.11).

Table 5.10: Parameters assumed in the FEM after calibration.

Material	**Block**	**E** (N/mm^2) **First level** Before calibration	**First level** After calibration	**Other levels** After calibration
Travertine		1980	1830	1890
	Block 1	2000	1800	1860
Masonry	Block 2	1950	1820	1790
	Block CT	1940	1770	1790

Table 5.11: Natural frequencies experimentally identified (Automated DD-SSI) and numerically obtained through the damaged FEM.

Mode Number	**Automated DD-SSI** f (Hz)	**Finite Element Model** f (Hz)	**Delta** Δf [%]
1	2.98	2.98	0.0 %
2	3.25	3.29	1.2 %
*	3.41	-	-
3	4.40	4.44	0.9 %
4	4.79	4.83	0.8 %
5	5.37	5.39	0.4 %

5.7 Long-Term Monitoring of the Civic Tower

5.7.1 Environmental Effects

Modal properties of masonry structures are typically affected by changes in temperature and humidity. As already seen in the preliminary analysis of the dynamic response of the structure in section (5.5.1), a dependency of the Civic Tower from seasonal variations emerged. Here this trend is investigated forward, analyzing the data recorded during the last campaign (campaign X), in which the temperature sensor was installed (from July 13^{th}, 2018).

The environmental effect on the modal properties of the structure is inspected, carrying on two separate analyses. In the first one, a "seasonal" study is performed

where the effect of temperature on structural frequencies is studied on the long-time period range, considering one record per day at midnight. In the second analysis, a daily investigation, in which eight records per day are analyzed (two records recorded daily at 07:00 AM, 01:00 PM, 07:00 PM, and 01:00 AM), is performed to estimate the daily fluctuations of the natural frequencies.

Seasonal Variation

Significant seasonal increases in the structural frequencies from winter to summer are clearly visible in Figure 5.40: such increments are conceivably associated with changes in environmental conditions and, primarily, in ambient temperature. It is noted that the increase of natural frequencies with temperature is caused by a stiffening effect associated with the closing of microcracks within mortar layers due to thermal expansion. Consistently the reduction of frequencies related to a lower temperature is related to microcracks opening. This behavior is consistent with other literature findings outlining the same trend, especially for historical masonry towers Ramos et al. 2010; Saisi et al. 2015.

Figure 5.40 shows the six identified natural frequencies versus time and their oscillations around their mean values (continuous lines) for the entire campaign X. During that monitoring period, due to a failure in the monitoring system, from March 18^{th}, 2018 to April 12^{th}, 2018 no data were recorded.

Table 5.12: Maximum, minimum and mean values of modal identified frequencies during the seasonal study.

Mode Number	**Mean** f [Hz]	**Min** f [Hz]	**Max** f [Hz]	**DeltaMin** Δf [%]	**DeltaMax** Δf [%]	**Max Excursion** Δf [%]
1	2.98	2.89	3.07	*3.3*	*3.0*	*6.3*
2	3.25	3.16	3.37	*2.8*	*3.4*	*6.2*
*	3.41	3.30	3.54	*3.2*	*3.8*	*7.0*
3	4.40	4.27	4.59	*3.2*	*4.0*	*7.2*
4	4.79	4.63	4.98	*3.5*	*3.8*	*7.4*
5	5.37	5.21	5.60	*3.1*	*4.3*	*7.3*

Even if for the first seven months of 2018, no temperature data were recorded, the evolution of the natural frequencies clearly emerges. During winter (December 2017-February, 2018) the frequencies are under the annual average while, from

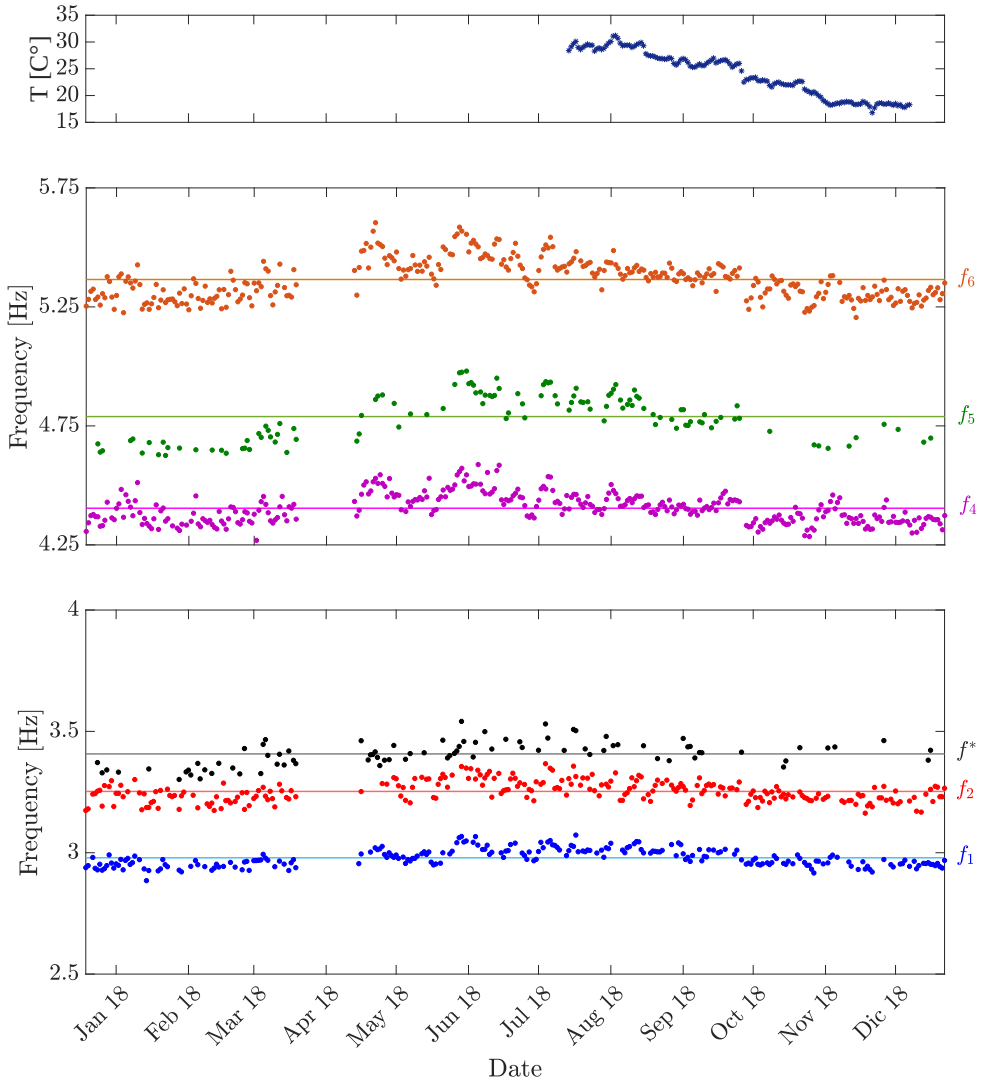

Figure 5.40: Time histories of the identified natural frequencies for campaign X.

March 2018, they increase. During summer, they stabilize above the average, while from mid-August, 2018, to the end of the year there is a decrease of all six frequencies. All the frequencies vary more than the ±3% around the mean values (Table 5.12) due to temperature, reaching in some cases also variations of 7.4% (Table 5.12). From July 2018, the installation of the temperature sensor made it possible to prove the correlation between frequency variation and temperature fluctuation. The temperature decreases from a maximum value of around 32°C during the summer season to a minimum of 16 C during winter, confirming the

same trend observed for the frequencies in Figure 5.40.

Daily Variation

The second study regarding the thermal effects on natural frequencies was conducted to investigate the sensitivity of the structure to the daily fluctuations of temperature. A period of 8 weeks, starting from July 13^{th}, 2018, was analyzed. In this monitoring period, the temperature varies from a maximum of 32°C to a minimum of 25°C, and it is worth noticing that the minimum temperature is usually registered at 07:00 AM, while the maximum one at 07:00 PM.

Looking at the identified natural frequencies-temperature plots in Figure 5.41, it is evident a strong correlation between the temperature and structural frequencies. For each mode, the maximum value of the identified daily frequency corresponds to the highest recorded temperature (record of 07:00 PM), while the minimum identified daily frequency is usually at the same time as the lowest minimum measured temperature (07:00 AM). For example, on July 15^{th}, 2018, at 07:00 AM (minimum value of temperature recorded for that day) the temperature sensor registered 29.3°C and the corresponding frequency associated to the second structural mode f_2 was equal to 3.22 Hz. Later on, at 07:00 PM, the recorded temperature (maximum daily value of temperature) was 31.4°C, and the corresponding frequency, f_2, was 3.45 Hz with a variation of 7.0 % (Table 5.13).

Table 5.13: Maximum, minimum and mean values of modal identified frequencies during the daily study.

Mode Number	**Mean** f [Hz]	**Min** f [Hz]	**Max** f [Hz]	**DeltaMin** Δf [%]	**DeltaMax** Δf [%]	**Max Excursion** Δf [%]
1	3.02	2.96	3.11	*2.1*	*3.0*	*5.0*
2	3.27	3.15	3.45	*3.7*	*5.2*	*8.6*
*	3.49	3.35	3.62	*4.2*	*3.6*	*7.4*
3	4.45	4.29	4.62	*3.5*	*3.8*	*7.0*
4	4.85	4.72	5.03	*2.7*	*3.7*	*6.2*
5	5.43	5.3	5.70	*2.2*	*4.6*	*6.7*

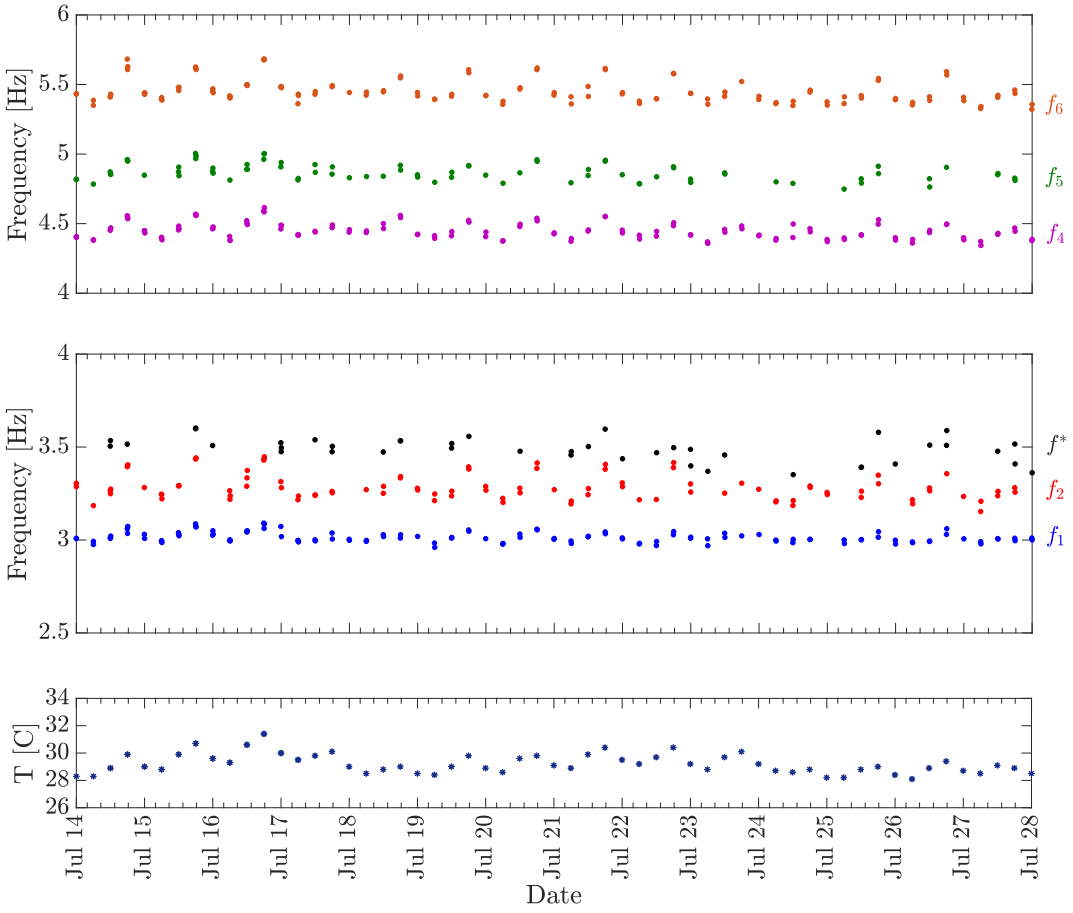

Figure 5.41: Time histories of temperature and frequencies f_1, f_2, f^*, f_3, f_4 and f_5 from July 13^{th}, 2018 to July 27^{th}, 2018.

Correlation analysis

Correlation coefficients between natural frequencies and temperature data are summarized in Table 5.14 both for the seasonal and daily study. These results show a high positive degree of correlation between natural frequencies f_1, f_2, f_3, f_4 and f_5 and temperature for the seasonal study, with values higher than 0.65. The same trend can be seen for the daily study, but, although the trend is clearly positive, the correlation between temperature and frequency appears less pronounced since computed on a shorter dataset. The relationship between frequencies and temperature is strongly linear. No correlation analysis has been carried on f^* because this mode is not consistently identified over time.

Figure 5.44 shows the correlation matrix computed between the natural fre-

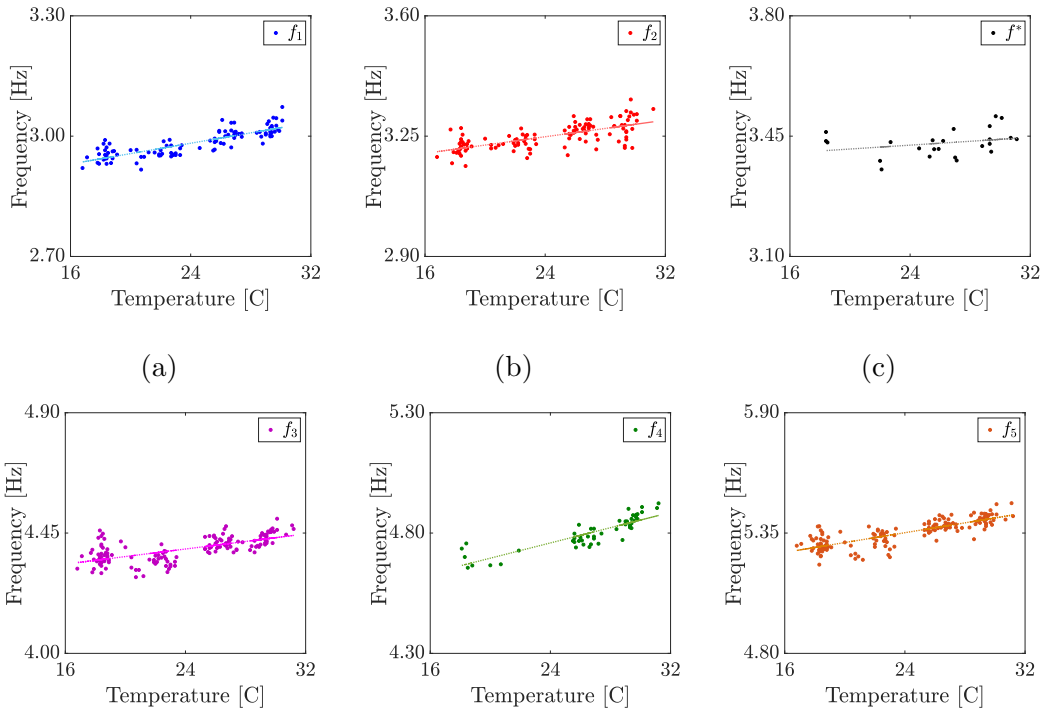

Figure 5.42: Correlation between temperature data and identified natural frequencies f_1, f_2, f^*, f_3, f_4 and f_5 for midnight data.

Table 5.14: Correlation coefficients between identified frequencies and temperature data.

Study	**Variable**	f_1	f_2	f^*	f_3	f_4	f_5
Seasonal	Temperature	0.84	0.69	0.29	0.67	0.87	0.81
Daily	Temperature	0.49	0.47	0.34	0.51	0.65	0.53

quencies. Histograms of the variables appear along the diagonal, while scattering plots of variable pairs appear in the off-diagonal, with the displayed values of the slopes of the least-squares reference lines. The natural frequencies f_1, f_2, f_3, f_4 and f_5 show a high degree of correlation within each other, which is related to their dependency on environmental parameters. All frequencies exhibit a positive linear correlation with temperature, indicating an increase in natural frequencies with increasing temperature, in agreement with other literary works (Gentile et al. 2016; Kita et al. 2019) and conceivably attributable to the closing of micro-cracks within mortar layers due to thermal expansion.

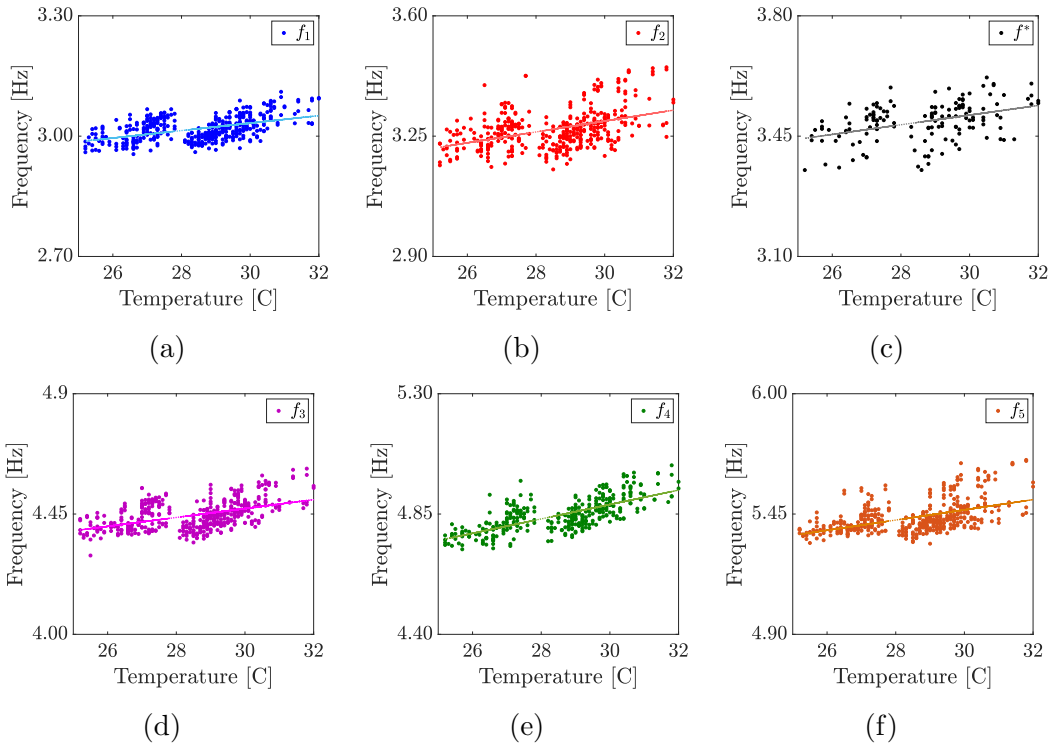

Figure 5.43: Correlation between temperature data and identified natural frequencies f_1, f_2, f^*, f_3, f_4 and f_5 for daily analysis.

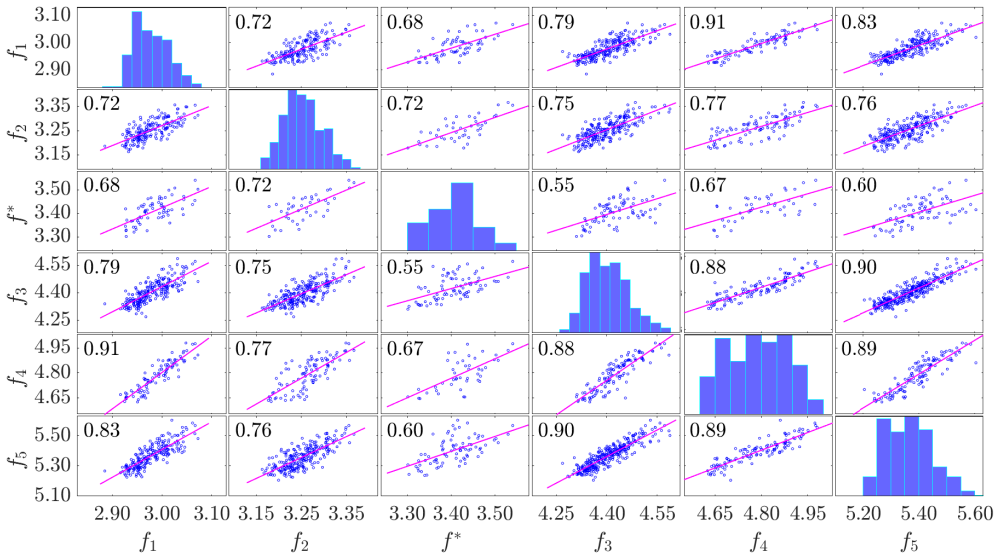

Figure 5.44: Correlation matrix between frequencies.

Cepstral Coefficients

The Cepstral Coefficients have been extracted as well from the monitoring data recorded during the past three years. Before applying the extraction procedure discussed in Section 3.1.1, the number of triangular filters must be selected with the value for the cutoff frequency. The number of filters can be set according to the Fraile et al. criterion presented in the Section 3.1.1 (Fraile Muñoz et al. 2008), since the sampling frequency adopted to simulate the system response is equal to 100 Hz, M is set to 13. Consequently, as mentioned in Section 3.1.1, the number of selected CCs $(D-1)$ is chosen equal to the number of frequency bands M.

Figure 5.45 show the time series of two coefficients extracted from channel 2. The coefficient c_3 presents a main drop right after the earthquake series of shocks on January, 18^{th} 2017. The epicenter of the seismic events was in Capitignano which is 38.5 Km far from Rieti. The variation is clear with the Cepstral Coefficients, while it did not emerge so evidently looking at the frequencies. Additionally, the third coefficient, exhibit a seasonal trend that matches the temperature fluctuation observed in the frequencies. On the other hand, the eleventh coefficient c_{11}, is consistently more stationary, revealing an important reduction after the earthquake occurred on August, 24^{th} 2016, and a smaller jump in correspondence of the one that took place on January, 18^{th} 2017. Unlike the third coefficient, c_{11}, does not exhibit any seasonal changes remaining substantially stationary.

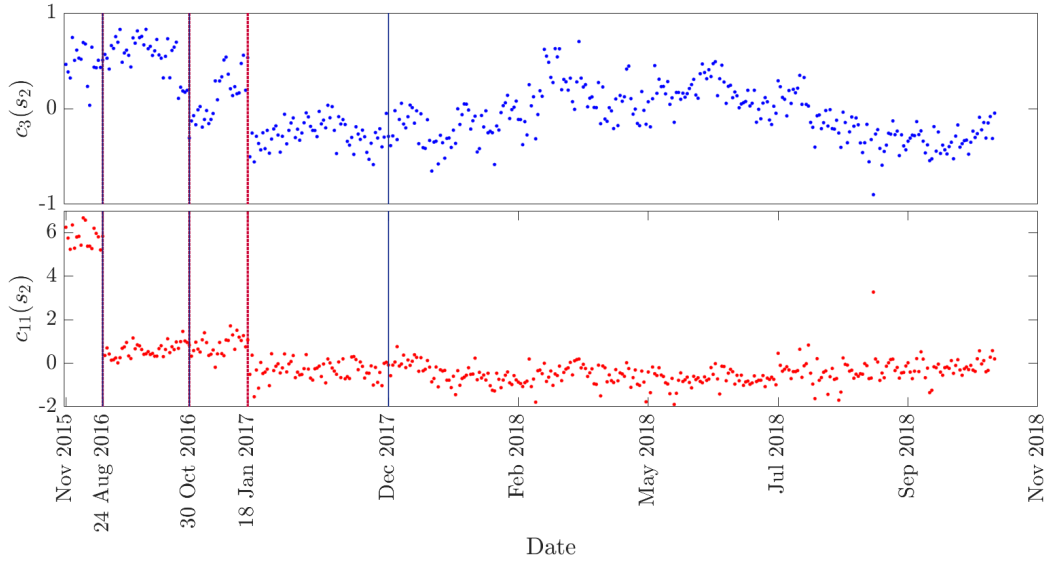

Figure 5.45: Cepstral Coefficients c_3 and c_{11} time series for channel 2

5.8 Conclusions

This chapter has introduced the comprehensive monitoring campaign of the Civic Tower of Rieti, which is led by professor Maurizio De Angelis and his research group at "Sapienza" University of Rome. The monitoring campaign provides a wealth of data that can now be used to make the first steps towards using real monitoring data for SHM. This structure forms the main case study in this thesis. In the next chapters the data from this campaign will be investigated in more depth and attempts will be made to understand what constitutes a normal structural response in the face of changing operational and environmental conditions. It will be analyzed also what kind of dynamic response the structure shows after the occurrence of low-magnitude earthquakes, investigating the consequent integrity level of the tower after the seismic shocks.

This section presents the development and results of the implementation of a simple vibration-based continuous SHM system installed in the historic Civic Tower in Rieti equipped with a NC TMD in order to dynamically characterize the structure and start a continuous real-time diagnostic process. The permanent SHM system comprises of six high-sensitivity accelerometers installed on the last floor of the tower and the mass of the TMD system, one temperature sensor, and a data acquisition system located inside the tower. A fully automated vibration-based SHM procedure has been proposed and implemented, based on Stochastic Subspace Identification, that allows tracking any variation of the modal characteristics over time.

The initial reference state of the structure is obtained by the analysis of the acceleration response recorded during the first five monitoring campaigns, considering two different types of test, AVTs and FVTs. The first five modes of vibration of the structure are identified in the frequency range up to 6 Hz. An additional frequency, f^*, around 3.5 Hz, turned out to be the least stable in the automated identification: this information is also confirmed by the low rate of successful identification associated with this frequency along the entire monitoring period. The introduction of a FEM has validated the model characterization of the structure derived from the AVTs. Such a model helped to optimize the monitoring system for the following campaigns and gave information about the modal behavior of the structure equipped with a TMD. The comparison between the structural experimental response and the corresponding one derived by the FEM confirmed that

in the operational conditions the mass of the passive control system is supported by two lateral walls, making the TMD system rigidly connected to the tower.

The use of an automated modal identification algorithm allowed to continuously identify the structural frequencies during the monitoring campaigns under operational conditions. The accuracy in the identification of the modal characteristics was consistently high making the identified frequencies a reliable, sensitive feature for damage assessment, strengthened by the capacity of spotting high variations of the frequency values after seismic events. Several variations have been noted in the dynamic behavior of the Civic Tower after the occurrence of the major seismic events in 2016.

Right after earthquake shocks, all natural frequencies exhibited consistent decays, which suggested that some damage occurred within the tower. Unfortunately, the structural conditions of the tower prior to the 2016 event were unknown, and so it was impossible to make any quantitative comparison of the two scenarios before and after the earthquakes. The FEM was re-calibrated on the basis of the new data recorded after the earthquake, introducing a reliable localized damage scenario at the base of the structure, which reinforced the hypothesis that those shifts in frequencies were due to damage occurrence. An additional investigation on the response of the structure during the seismic event revealed that the passive control system got activated and worked favorably towards the reduction of the structural vibrations.

Thanks to the great wealth of recorded data, it was also possible to investigate the effects of changes in environmental conditions on the natural frequencies. Two temperature-driven types of frequency variation phenomena have been observed: daily fluctuations and seasonal variations. It was highlighted how simple temperature fluctuations could cause pronounced frequency variations in structures that present masonry components due to the opening/closing of cracks. This trend is also observed in the statistical correlations between frequencies and temperature and between the frequencies themselves.

Part IV
Conclusions

Chapter 6

Conclusions

This dissertation addressed how choosing the correct DSFs, represents the key point in any damage detection strategy, to carry on robust vibration-based SHM campaigns. DSFs should be quickly derived from the vibration response of a structure, with low computational requirements and without any dependency from the users expertise. Additionally, these features need to be highly sensitive to damage to be considered efficient. However, at the same time, they should be insensitive as much as possible towards temporary or seasonally variation of the structural properties that fall into the common behavior of structural systems.

In this dissertation, two different families of DSFs were investigated, looking for suitable indicators to be used for vibration-based damage detection methodologies in civil structures.

The first group of DSFs, represented by the modal parameters, was discussed in Chapter 2. The original contribution of this section of the work was to develop an user-unsupervised automated approach for the extraction of modal parameters. The proposed approach gives similar results as in manual analysis, and it does not contain parameters that rely on the users expertise.

The proposed approach consists of five steps: (a) run of the DD-SSI for different values of users defined parameters; (b) hard validation criteria for certainly mathematical modes; (c) elimination of noise modes; (d) clustering of remaining modes & outliers removal; (e) selection of the representative modal quantities. The proposed methodology is built to minimize the interaction with the user and reduce the uncertainty in the parameters identification. Indeed, the user-dependent choices and parameters selection are driven by precise rules. Among

the automated procedures based on the SSI algorithm available in the literature, this is the first approach in which the asymmetric partition of the Hankel matrix is taken into account. The novel contribution stays, also, in the clustering step, where two alternatives are given to the user for clustering the structural modes. A blind k-means approach, where the Mahalanobis Square Distance is used to check the similarity between the modes is presented. Then, the DBSCAN algorithm is tested and adopted as an optimized choice to carry on the clustering step. These two approaches depend on very few parameters which do not depend on the user expertise at all, allowing to carry on an user-unsupervised methodology.

The proposed approach is tested in the final chapter of this dissertation, Chapter 5, where it is validated on monitoring data collected during the long-term monitoring of the Civic Tower located in Rieti. The tower is monitored by the research group supervised by professor Maurizio De Angelis, in the Department of Structural and Geotechnical Engineering at Sapienza University of Rome. Here, the unsupervised approach showed to have a great potential and offers all the right characteristics to be easily implemented within a long-term monitoring system, providing robust modal information.

The second group of DSFs was discussed in Chapter 3. Here the use of audio indicators, commonly adopted in the field of speech and speaker recognition, as novel damage sensitive feature in civil applications is investigated. An adaptation of Cepstral Coefficients and MPEG-7, which are commonly used to give a compact representation of the speechs signal, is presented. CCs coefficients have been rarely used for civil applications, and the MPEG-7 NASE features have never been adapted to civil structures before. The ease of extraction of these features, which requires minimal user expertise, represents an important advantage over other more popular features and makes the Cepstral features and the MPEG-7 NASE particularly convenient for implementations into automatic structural health monitoring routines. The potential of these features is here tested considering them within a damage detection algorithm that is developed according to the training and testing scheme, typical of pattern recognition applications. The damage detection algorithm employs the Mahalanobis Squared Distance to solve the Structural Health Monitoring assignment. The method was validated by using simulated data of a shear-type system. The performance of the proposed features was compared with frequencies, which have been largely used to solve the task of structural damage detection.

Results demonstrated that both Cepstral Coefficients and MPEG-7 NASE outperform frequencies for damage detection purposes when dealing with experimental data modeled to mimic the operational and environmental variability. Moreover, this optimal performance is given with a very low computational burden and a small number of user-dependent parameters that need to be set. On the other hand, the methodology adopted to extract the modal parameters tends to be computationally heavy or user-dependent. Additionally, within these two audio features, the Cepstral Coefficients showed to give a better performance.

Chapter 4 focused on the issue of the confounding influence of changing environmental and operational conditions on technology developed for SHM. This issue is widely considered as one of the largest stumbling blocks preventing the practical application of SHM to real-world structures. Here the cointegration is investigated to attempt to deal with the problem of environmentally-induced variation in measured structural response. The idea, which originates from econometrics, is to linearly combine response variables to create a stationary residual, whose stationarity represents the structures normal condition. When monitoring this residual, a departure from stationarity will indicate that the structure is no longer operating under its normal condition. This technique showed in the literature to work beautifully for the most common features adopted for SHM in civil structures, like modal parameters. The innovative contribution given in this chapter, is, first of all, the investigation of the dependency of Cepstral Coefficients from environmental variations given by temperature. It is shown how the application of the IDCT can actually help to reduce the effect of the long-term variation of some of these coefficients, making them more robust. The second original contribution is given by the application of the cointegration to the Cepstral features to remove the environmental dependency from those coefficients that vary with the temperature changes. This goal is here achieved adopting two different regression models the Support Vector Regression and the Relevance Vector Machine. These two algorithms allow building linear and nonlinear regression models, depending on the existing relationship between the analyzed features. They give the possibility of taking into account the common nonlinear relationships that usually occur in civil structure between DSFs and temperature.

Chapter 4 introduced the theory behind the Johansen procedure, which finds the most stationary linear combination of a set of variables under scrutiny. The ADF test has also been introduced as a stationarity test.

Although not used for its intended purpose, cointegration has provided a useful tool for inclusion in an SHM analysis/system. Its advantages lay in the simplicity of the idea. Moreover, there is a vast background of sophisticated research already carried out in the field of econometrics available for use. Finally, no information is being lost as features are created through a combination of monitored variables. The suggested cointegration procedure can also be implemented where no measurement of the environment/operational conditions are available. Indeed, the only stipulation is that the residual should be trained on data coming from the normal condition of a structure.

In the latter half of Chapter 4, the cointegration process is applied to simulated data and experimental data. Initially, the numerical study case of a steel cantilever beam subjected to temperature variation and also to different damage scenarios is addressed. Here the dependency of Cepstral Coefficients is investigated, and the application of nonlinear cointegration was able to remove the temperature dependent trend from Cepstral features successfully. Then, the benchmark Z24 case is used as a motivational example for showing how effective Cepstral Coefficients can be as DSFs and why the cointegration theory in its nonlinear formulation would be of benefit in real SHM applications.

The final chapter of the dissertation is dedicated to the structural health monitoring carried on the Civic Tower in Rieti. This structure represents a unique case study, being one of the few historical mixed structures (masonry-concrete) equipped with a non-conventional TMD. Moreover, the building is placed in the central region of Italy, which was affected by a relevant earthquake storm in 2016. Initially historical and geometrical information is given on the tower, followed by the description of the monitoring campaigns that were carried on. Here the unsupervised methodology presented in the first chapter is applied. Initially, the sensitivity of this approach is tested on a single record, to show how every parameter influenced the different steps of the methodology. Then the unsupervised technique is used to perform a long-term monitoring campaign on the structure, which results to be a robust tool to characterize the tower dynamically. The novel proposed DSFs proposed in Chapter 2, the CCs, are here extracted from the monitoring data of the investigated tower, showing a promising efficiency and robustness towards damage and environmental changes.

Chapter 7

Future Work

Automated Procedure

The implementation of the unsupervised approach to extract modal parameters from structural vibrations showed to be a robust tool to reduce the uncertainty usually present in the derivation of these parameters. The methodology proposed requires a considerable computational effort, especially in the first step of the procedure, when the DD-SSI algorithm is performed for different combinations of the parameters. It is therefore important to optimize the choice of the parameters driving DD-SSI, in order to reduce the computational requirements of the procedure and narrow the identification to meaningful combinations. Moreover, the third and fourth steps of the unsupervised approach could be merged into one single step. The noise removal could be performed at the same time as the cluster analysis where the noise modes are considered as additional outliers not belonging to any cluster. This idea requires further investigations.

Audio Features

Cepstral Coefficients showed to be a robust alternative to modal parameters, as damage sensitive feature. It presents most of the right characteristics that a damage indicator should have: compactness, the easy extraction process, and low computation requirements. The dependence of these coefficients from the temperature variation was studied, and the application of the IDCT showed a

benefit in the normalization of some of these coefficients towards temperature fluctuations. An additional effort should be put to investigate the dependency of CCs from other long-term environmental and operational changes, like humidity or variation of boundary conditions.

These coefficients happen to be derivable for each channel where the acceleration is recorded; therefore, Cepstral features can be considered local parameters. A local feature seems a natural and smart choice not only for damage detection purposes but also for damage localization. However, the ability of these indexes to give information about damage location has not been investigated yet. This idea requires further research.

Civic Tower in Rieti

This dissertation is one of the first works investigating data coming from a real historical tower equipped with a non-conventional Tuned Mass Damper for SHM. The main aim, as far as data from the tower is concerned, was to learn how the structure typically responds to the changing environmental and operational conditions.

The lower modal frequencies are now known and understood well enough to be able to predict their fluctuation to a reasonable degree of accuracy. These features could be used to carry on a data normalization approach following the approach described in Chapter 4. Once an larger amount of data will be available and processed, it will be possible to construct a regression model and apply the cointegration technique to build robust DSFs. That model error could then be used to spot anomalous behavior. At this initial stage of development, the signs are encouraging that the construction of an SHM system that works in the face of environmental and operational variations is possible.

At this point, it would be feasible to implement online novelty detectors for modal frequencies and Cepstral Coefficients. Several novelty detectors for each measurement type could be applied. For example, the use of response surface model errors and classic control charts could be explored. The Gaussian process regression with confidence interval type controls charts or the use of classic control charts with cointegrated residuals could be an alternative option. Multiple novelty detectors on the same measurements would enhance confidence in any anomaly

detection and may help to avoid issues with false-positive identifications of unusual behavior. Although the detection of anomalous behavior is a positive step in the right direction, it is only an initial step as far as the aims of SHM or performance monitoring are concerned. A detection of novelty alone is uninformative; indeed, novelty may occur due to sensor failure, an extreme weather condition, a performance anomaly, or damage. The next stage in the development of an SHM system for the civic tower is to be able to identify the causes of an anomaly, or to be able to detect specific changes in structural condition. Generally, such challenges require a supervised learning approach and a step away from novelty detection. This is a challenge in the face of a lack of data available for supervised learning for the kind of events one may be interested in identifying.

The author envisages that the ability to identify the causes of anomalous behavior or structural response, or particular structural behavior, will take considerable effort and time to develop. One way to progress to the next step could be to use a high fidelity FEM of the tower. The definition of a FEM will allow to simulate specific damage or performance-related scenarios and, also to simulate the response of the structure under environmental variations, providing data for supervised learning.

The scope for further work on the development of a working SHM system for the Civic Tower in Rieti is broad. Additionally, an obvious limitation when using modal parameters as DSFs arises from the fact that natural frequencies are well known to be insensitive to localized damages. This situation is further limited by the fact that only the first five frequencies are available, as greater sensitivity to damage scenarios may be gained from higher modes.

Bibliography

Hamid Ahmadian, John E Mottershead, and Michael I Friswell. Substructure modes for damage detection. *Structural Damage Assessment Using Advanced Signal Processing Procedures, Proceedings of DAMAS 97, University of Sheffield, UK*, pages 257–268, 1997.

Nasir Ahmed, T_ Natarajan, and Kamisetty R Rao. Discrete cosine transform. *IEEE transactions on Computers*, 100(1):90–93, 1974.

Sharada Alampalli. Influence of in-service environment on modal parameters. In *Proceedings-SPIE The International Society For Optical Engineering*, volume 1, pages 111–116. Citeseer, 1998.

Sharada Alampalli, Sandeep Alampalli, and Mohammed Ettouney. Big data and high-performance analytics in structural health monitoring for bridge management. In *Sensors and Smart Structures Technologies for Civil, Mechanical, and Aerospace Systems 2016*, volume 9803, page 980315. International Society for Optics and Photonics, 2016.

Douglas HW Allan. *Statistical quality control: an introduction for management.* Reinhold Pub. Corp., 1959.

Randall J Allemang, David L Brown, and Phillips Allyn W. *Survey of Modal Techniques Applicable to Autonomous/Semi-Autonomous Parameter Identification.* 2010.

Luciana Balsamo, Raimondo Betti, and Homayoon Beigi. Structural damage detection using speaker recognition techniques. In *Proceedings of the 11th international conference on structural safety and reliability (ICOSSAR), Columbia University, New York, NY, USA*, 2013.

Luciana Balsamo, Raimondo Betti, and Homayoon Beigi. A structural health monitoring strategy using cepstral features. *Journal of Sound and Vibration*, 333(19):4526–4542, 2014.

Homayoon Beigi. *Fundamentals of speaker recognition*. Springer Science & Business Media, 2011.

Christopher M Bishop. *Pattern recognition and machine learning*. springer, 2006.

Bruce P Bogart. The quefrency analysis of time series for echoes: cepstrum, pseudo-autocovariance, cross-cepstrum and saphe cracking. *Time Series Analysis*, pages 209–243, 1963.

Rune Brincker, Palle Andersen, and Niels-Jørgen Jacobsen. Automated frequency domain decomposition for operational modal analysis. In *Proceedings of The 25th International Modal Analysis Conference (IMAC), Orlando, Florida*, volume 415, 2007.

Peter E Carden and Akira Mita. Challenges in developing confidence intervals on modal parameters estimated for large civil infrastructure with stochastic subspace identification. *Structural Control and Health Monitoring*, 18(1):53–78, 2011.

Shashank Chauhan and Dmitri Tcherniak. On the number of rows and columns in subspace identification methods. In *13th, IFAC Symposium on System Identification; SYSID '03; Rotterdam, Netherlands*, 2003.

Shashank Chauhan and Dmitri Tcherniak. Clustering approaches to automatic modal parameter estimation. In *Proceedings, International Modal Analysis Conference (IMAC)*, 2008.

Qian Chen, Uwe Kruger, and Andrew YT Leung. Cointegration testing method for monitoring nonstationary processes. *Industrial & Engineering Chemistry Research*, 48(7):3533–3543, 2009.

Allan Churchward and Yehuda J Sokal. Prediction of temperatures in concrete bridges. *Journal of the Structural Division*, 107(ST11), 1981.

Giorgia Coletta. *Nonlinear Cointegration using Statistical Learning Theory with Applications to Structural Health Monitoring.* Master Thesis, Polytechnic of Turin, 2017.

Giorgia Coletta, Gaetano Miraglia, Marica L Pecorelli, Rosario Ceravolo, Elizabeth Cross, Cecilia Surace, and Keith Worden. Use of cointgration strategies to remove environmental effects from data acquired on historical buildings. *Engineering Structures*, 183:1014–1026, 2019.

Elizabeth J Cross, Keith Worden, and Qian Chen. Cointegration: a novel approach for the removal of environmental trends in structural health monitoring data. *Proceedings of the Royal Society A: Mathematical, Physical and Engineering Sciences*, 467(2133):2712–2732, 2011.

Steven Davis and Paul Mermelstein. Comparison of parametric representations for monosyllabic word recognition in continuously spoken sentences. *IEEE transactions on acoustics, speech, and signal processing*, 28(4):357–366, 1980.

Maurizio De Angelis, Salvatore Perno, and Anna Reggio. Dynamic response and optimal design of structures with large mass ratio tmd. *Earthquake Engineering & Structural Dynamics*, 41(1):41–60, 2012.

Arnaud Deraemaeker, Edwin Reynders, Guido De Roeck, and Jyrki Kullaa. Vibration-based structural health monitoring using output-only measurements under changing environment. *Mechanical systems and signal processing*, 22(1): 34–56, 2008.

David A Dickey and Wayne A Fuller. Distribution of the estimators for autoregressive time series with a unit root. *Journal of the American statistical association*, 74(366a):427–431, 1979.

David A Dickey and Wayne A Fuller. Likelihood ratio statistics for autoregressive time series with a unit root. *Econometrica: Journal of the Econometric Society*, pages 1057–1072, 1981.

Scott W Doebling, Charles R Farrar, and Randall S Goodman. Effects of measurement statistics on the detection of damage in the alamosa canyon bridge. Technical report, Los Alamos National Lab., NM (United States), 1996a.

Scott W Doebling, Charles R Farrar, Michael B Prime, and Daniel W Shevitz. Damage identification and health monitoring of structural and mechanical systems from changes in their vibration characteristics: a literature review. Technical report, Los Alamos National Lab., NM (United States), 1996b.

Harris Drucker, Christopher JC Burges, Linda Kaufman, Alex J Smola, and Vladimir Vapnik. Support vector regression machines. In *Advances in neural information processing systems*, pages 155–161, 1997.

Robert F Engle and Clive WJ Granger. Co-integration and error correction: representation, estimation, and testing. *Econometrica: journal of the Econometric Society*, pages 251–276, 1987.

Martin Ester, Hans-Peter Kriegel, Jörg Sander, Xiaowei Xu, et al. A density-based algorithm for discovering clusters in large spatial databases with noise. In *Kdd*, volume 96, pages 226–231, 1996.

Charles R Farrar and Thomas A Duffey. Vibration-based damage detection in rotating machinery. In *Key engineering materials*, volume 167, pages 224–235. Trans Tech Publ, 1999.

Charles R Farrar and Keith Worden. *Structural health monitoring: a machine learning perspective*. John Wiley & Sons, 2012.

Charles R Farrar, Phillip J Cornwell, Scott W Doebling, and Michael B Prime. Structural health monitoring studies of the alamosa canyon and i-40 bridges. Technical report, Los Alamos National Lab., NM (US), 2000.

Charles R Farrar, Scott W Doebling, and David A Nix. Vibration–based structural damage identification. *Philosophical Transactions of the Royal Society of London. Series A: Mathematical, Physical and Engineering Sciences*, 359(1778): 131–149, 2001.

Rubén Fraile Muñoz, Nicolas Sáenz Lechón, Juan Ignacio Godino Llorente, Víctor Osma Ruiz, and Pedro Gómez Vilda. Use of mel frequency cepstral coefficients for automatic pathology detection on sustained vowel phonations: Mathematical and statistical justification. 2008.

Wayne A Fuller. *Introduction to statistical time series*, volume 428. John Wiley & Sons, 1996.

Yujin Gao and Robert B Randall. Determination of frequency response functions from response measurementsi. extraction of poles and zeros from response cepstra. *Mechanical systems and signal processing*, 10(3):293–317, 1996.

Carmelo Gentile, Marco Guidobaldi, and Antonella Saisi. One-year dynamic monitoring of a historic tower: damage detection under changing environment. *Meccanica*, 51(11):2873–2889, 2016.

Bart Vanluyten Goethals, Ivan and Bart De Moor. Reliable spurious mode rejection using self learning algorithms. pages 991–1003, 2004.

Johanna Hardin and David M Rocke. The distribution of robust distances. *Journal of Computational and Graphical Statistics*, 14(4):928–946, 2005.

Haibo He and Edwardo A Garcia. Learning from imbalanced data. *IEEE Transactions on Knowledge & Data Engineering*, (9):1263–1284, 2008.

Donald O Hebb. The organization of behaviour new york, 1949.

Ah Lum Hong. *Weighting matrices and model order determination in stochastic system identification for civil infrastructure systems*. Columbia University, 2010.

Ah Lum Hong, Filippo Ubertini, and Raimondo Betti. Wind analysis of a suspension bridge: identification and finite-element model simulation. *Journal of Structural Engineering*, 137(1):133–142, 2010.

Søren Johansen. *Likelihood-based inference in cointegrated vector autoregressive models*. Oxford University Press on Demand, 1995.

Erik A Johnson, HF Lam, LS Katafygiotis, and JL Beck. A benchmark problem for structural health monitoring and damage detection. In *Structural control for civil and infrastructure engineering*, pages 317–324. World Scientific, 2001.

J-N Juang and Richard S Pappa. An eigensystem realization algorithm for modal parameter identification and model reduction. *Journal of guidance, control, and dynamics*, 8(5):620–627, 1985.

Jer-Nan Juang. Applied system identification. 1994.

Katarina Juselius. *The cointegrated VAR model: methodology and applications*. Oxford university press, 2006.

Junhee Kim and Jerome P Lynch. Subspace system identification of support-excited structurespart i: theory and black-box system identification. *Earthquake engineering & structural dynamics*, 41(15):2235–2251, 2012a.

Junhee Kim and Jerome P Lynch. Subspace system identification of support excited structurespart ii: gray-box interpretations and damage detection. *Earthquake Engineering & Structural Dynamics*, 41(15):2253–2271, 2012b.

Alban Kita, Nicola Cavalagli, and Filippo Ubertini. Temperature effects on static and dynamic behavior of consoli palace in gubbio, italy. *Mechanical Systems and Signal Processing*, 120:180–202, 2019.

C Krämer, CAM De Smet, and Guido De Roeck. Z24 bridge damage detection tests. In *IMAC 17, the International Modal Analysis Conference*, volume 3727, pages 1023–1029. Society of Photo-optical Instrumentation Engineers, 1999.

Jyrki Kullaa. Damage detection of the z24 bridge using control charts. *Mechanical Systems and Signal Processing*, 17(1):163–170, 2003.

Jong Jae Lee and Masanobu Shinozuka. A vision-based system for remote sensing of bridge displacement. *Ndt & E International*, 39(5):425–431, 2006.

Lennart Ljung. *System identification: theory for the user*. Prentice-hall, 1987.

Stuart Lloyd. Least squares quantization in pcm. *IEEE transactions on information theory*, 28(2):129–137, 1982.

Hilmi Luş, Maurizio De Angelis, Raimondo Betti, and Richard W Longman. Constructing second-order models of mechanical systems from identified state space realizations. part i: theoretical discussions. *Journal of Engineering Mechanics*, 129(5):477–488, 2003.

Jerome P Lynch, Aaron Partridge, Kincho H Law, Thomas W Kenny, Anne S Kiremidjian, and Ed Carryer. Design of piezoresistive mems-based accelerometer for integration with wireless sensing unit for structural monitoring. *Journal of Aerospace Engineering*, 16(3):108–114, 2003.

Gangadharrao S Maddala and In-Moo Kim. *Unit roots, cointegration, and structural change*. Number 4. Cambridge university press, 1998.

Johan Maeck and Guido De Roeck. Dynamic bending and torsion stiffness derivation from modal curvatures and torsion rates. *Journal of Sound and Vibration*, 225(1):153–170, 1999.

Filipe Magalhaes, Alvaro Cunha, and Elsa Caetano. Online automatic identification of the modal parameters of a long span arch bridge. *Mechanical Systems and Signal Processing*, 23(2):316–329, 2009.

Prasanta Chandra Mahalanobis. On the generalized distance in statistics. National Institute of Science of India, 1936.

Bangalore S Manjunath, Philippe Salembier, and Thomas Sikora. *Introduction to MPEG-7: multimedia content description interface*. John Wiley & Sons, 2002.

Claudio Modena, Devis Sonda, and Daniele Zonta. Damage localization in reinforced concrete structures by using damping measurements. In *Key engineering materials*, volume 167, pages 132–141. Trans Tech Publ, 1999.

Mary M Moya, Mark W Koch, and Larry D Hostetler. One-class classifier networks for target recognition applications. *NASA STI/Recon Technical Report N*, 93, 1993.

K Krishnan Nair and Anne S Kiremidjian. Derivation of a damage sensitive feature using the haar wavelet transform. *Journal of Applied Mechanics*, 76(6):061015, 2009.

K Krishnan Nair, Anne S Kiremidjian, and Kincho H Law. Time series-based damage detection and localization algorithm with application to the asce benchmark structure. *Journal of Sound and Vibration*, 291(1-2):349–368, 2006.

Alan V Oppenheim and Ronald W Schafer. From frequency to quefrency: A history of the cepstrum. *IEEE signal processing Magazine*, 21(5):95–106, 2004.

Alan V Oppenheim, John R Buck, and Ronald W Schafer. *Discrete-time signal processing. Vol. 2*. Upper Saddle River, NJ: Prentice Hall, 2001.

Richard S Pappa, George H James, and David C Zimmerman. Autonomous modal identification of the space shuttle tail rudder. *Journal of Spacecraft and Rockets*, 35(2):163–169, 1998.

Bart Peeters and Guido De Roeck. Reference-based stochastic subspace identification for output-only modal analysis. *Mechanical systems and signal processing*, 13(6):855–878, 1999.

Bart Peeters and Guido De Roeck. One-year monitoring of the z24-bridge: environmental effects versus damage events. *Earthquake engineering & structural dynamics*, 30(2):149–171, 2001.

Bart Peeters and CE Ventura. Comparative study of modal analysis techniques for bridge dynamic characteristics. *Mechanical Systems and Signal Processing*, 17(5):965–988, 2003.

Bart Peeters, Johan Maeck, and Guido De Roeck. Vibration-based damage detection in civil engineering: excitation sources and temperature effects. *Smart materials and Structures*, 10(3):518, 2001.

Brad A Pridham and John C Wilson. An application example illustrating the practical issues of subspace identification. In *Proceedings of the 21st International Modal Analysis Conference*, 2003.

Carlo Priori, Maurizio De Angelis, and Raimondo Betti. On the selection of user-defined parameters in data-driven stochastic subspace identification. *Mechanical Systems and Signal Processing*, 100:501–523, 2018.

Carlo Rainieri and Giovanni Fabbrocino. Influence of model order and number of block rows on accuracy and precision of modal parameter estimates in stochastic subspace identification. *International Journal of Lifecycle Performance Engineering 10*, 1(4):317–334, 2014.

Luis F Ramos, Leandro Marques, Paulo B Lourenço, Guido De Roeck, A Campos-Costa, and J Roque. Monitoring historical masonry structures with operational modal analysis: two case studies. *Mechanical systems and signal processing*, 24 (5):1291–1305, 2010.

Anna Reggio and Maurizio De Angelis. Optimal energy-based seismic design of non-conventional tuned mass damper (tmd) implemented via inter-story isolation. *Earthquake Engineering & Structural Dynamics*, 44(10):1623–1642, 2015.

Edwin Reynders and Guido De Roeck. Continuous vibration monitoring and progressive damage testing on the z 24 bridge. *Encyclopedia of structural health monitoring*, 2009.

Edwin Reynders, Jeroen Houbrechts, and Guido De Roeck. Fully automated (operational) modal analysis. *Mechanical Systems and Signal Processing*, 29: 228–250, 2012.

Edwin Reynders, Kristof Maes, Geert Lombaert, and Guido De Roeck. Uncertainty quantification in operational modal analysis with stochastic subspace identification: validation and applications. *Mechanical Systems and Signal Processing*, 66:13–30, 2016.

Guido De Roeck. The state-of-the-art of damage detection by vibration monitoring: the simces experience. *Journal of Structural Control*, 10(2):127–134, 2003.

Antonella Saisi, Carmelo Gentile, and Marco Guidobaldi. Post-earthquake continuous dynamic monitoring of the gabbia tower in mantua, italy. *Construction and Building Materials*, 81:101–112, 2015.

Marco Scionti and Jeroen P Lanslots. Stabilisation diagrams: Pole identification using fuzzy clustering techniques. *Advances in Engineering Software*, 36(11-12): 768–779, 2005.

Haichen Shi, K Worden, and EJ Cross. A nonlinear cointegration approach with applications to structural health monitoring. In *Journal of Physics: Conference Series*, volume 744, page 012025. IOP Publishing, 2016.

Hoon Sohn. Effects of environmental and operational variability on structural health monitoring. *Philosophical Transactions of the Royal Society A: Mathematical, Physical and Engineering Sciences*, 365(1851):539–560, 2006.

Hoon Sohn, Mark Dzwonczyk, Erik G Straser, Kincho H Law, Teresa H-Y Meng, and Anne S Kiremidjian. Adaptive modeling of environmental effects in modal

parameters for damage detection in civil structures. In *Smart Structures and Materials 1998: Smart Systems for Bridges, Structures, and Highways*, volume 3325, pages 127–139. International Society for Optics and Photonics, 1998.

Hoon Sohn, Charles R Farrar, Norman F Hunter, and Keith Worden. Structural health monitoring using statistical pattern recognition techniques. *Journal of dynamic systems, measurement, and control*, 123(4):706–711, 2001.

Wieslaw J Staszewski, S Gareth Pierce, Keith Worden, Wayne R Philp, Geoffrey R Tomlinson, and Brian Culshaw. Wavelet signal processing for enhanced lamb-wave defect detection in composite plates using optical fiber detection. *Optical Engineering*, 36(7):1877–1889, 1997.

Michael E Tipping. Sparse bayesian learning and the relevance vector machine. *Journal of machine learning research*, 1(Jun):211–244, 2001.

Filippo Ubertini, Carmelo Gentile, and Annibale Luigi Materazzi. Automated modal identification in operational conditions and its application to bridges. *Engineering Structures*, 46:264–278, 2013.

Filippo Ubertini, Gabriele Comanducci, Nicola Cavalagli, Anna Laura Pisello, Annibale Luigi Materazzi, and Franco Cotana. Environmental effects on natural frequencies of the san pietro bell tower in perugia, italy, and their removal for structural performance assessment. *Mechanical Systems and Signal Processing*, 82:307–322, 2017.

Herman Van der Auweraer and Bart Peeters. Discriminating physical poles from mathematical poles in high order systems: use and automation of the stabilization diagram. In *Instrumentation and Measurement Technology Conference, 2004. IMTC 04. Proceedings of the 21st IEEE*, volume 3, pages 2193–2198. IEEE, 2004.

Peter Van Overschee and Bart L De Moor. *Subspace identification for linear systems: Theory, Implementation, Applications*. Springer Science & Business Media, 2012.

Kim J Vandiver. Detection of structural failure on fixed platforms by measurement of dynamic response. In *Offshore Technology Conference*. Offshore Technology Conference, 1975.

Steve Vanlanduit, Peter Verboven, Patrick Guillaume, and Joannes Schoukens. An automatic frequency domain modal parameter estimation algorithm. *Journal of Sound and Vibration*, 265(3):647–661, 2003.

Vladimir N Vapnik. *Statistical Learning Theory*. Wiley, 1998.

Peter Verboven, Eli Parloo, Patrick Guillaume, and Marc Van Overmeire. Autonomous structural health monitoringpart i: modal parameter estimation and tracking. *Mechanical Systems and Signal Processing*, 16(4):637–657, 2002.

Peter Verboven, Bart Cauberghe, Eli Parloo, Steve Vanlanduit, and Patrick Guillaume. User-assisting tools for a fast frequency-domain modal parameter estimation method. *Mechanical systems and signal processing*, 18(4):759–780, 2004.

Dimitrios Ververidis and Constantine Kotropoulos. Information loss of the mahalanobis distance in high dimensions: Application to feature selection. *IEEE Transactions on Pattern Analysis and Machine Intelligence*, 31(12):2275–2281, 2009.

Dejan V Vranic, Dietmar Saupe, and Jörg Richter. Tools for 3d-object retrieval: Karhunen-loeve transform and spherical harmonics. In *2001 IEEE Fourth Workshop on Multimedia Signal Processing (Cat. No. 01TH8564)*, pages 293–298. IEEE, 2001.

Keith Worden, Graeme Manson, and Nick RJ Fieller. Damage detection using outlier analysis. *Journal of Sound and Vibration*, 229(3):647–667, 2000.

Yong Xia, Yozo Fujino, Masato Abe, and Jun Murakoshi. Short-term and long-term health monitoring experience of a short highway bridge: case study. *Bridge Structures*, 1(1):43–53, 2005.

Hae Young Noh, K Krishnan Nair, Dimitrios G Lignos, and Anne S Kiremidjian. Use of wavelet-based damage-sensitive features for structural damage diagnosis using strong motion data. *Journal of Structural Engineering*, 137(10):1215–1228, 2011.

Ka-Veng Yuen and Sin-Chi Kuok. Ambient interference in long-term monitoring of buildings. *Engineering Structures*, 32(8):2379–2386, 2010.

Gang Zhang, Ronald S Harichandran, and Pradeep Ramuhalli. Application of noise cancelling and damage detection algorithms in nde of concrete bridge decks using impact signals. *Journal of Nondestructive Evaluation*, 30(4):259–272, 2011.